End-Capped Oligothiophene Dimers Incorporating TTF, Metal Dithiolene and Spirocentric Cores

Submitted by

Iain A. Wright

A thesis submitted in fulfilment of the requirements for the degree of Doctor of Philosophy in Department of Pure and Applied Chemistry, University of Strathclyde

2011

Signed:

Date:

Acknowledgements:

I thank Prof. Peter Skabara for the chance to work in his research group, the freedom and flexibility I've been given in my work, and the support and opportunities which have been available throughout the duration of my studies in his group. I also owe a great deal of thanks to the postdoctoral researchers in the group, Dr. Filipe Vilela Dr. Alex Kanibolotsky, and Dr. Neil Findlay for the help and advice they have always been happy to provide.

The group has always been a fun place to work and so I would like to personally acknowledge the other members of the group I have worked alongside for helping to make my PhD studies an enjoyable as well as productive experience: Dr. John Forgie, Irina Afonina, Greg McEntee, Diego Cortizo-Lacalle, Sandeep Kaur, Saad-eldin Elmasly, Clara Orofino, Zuzana Vobecka, and Neil Thompson.

I would like to extend further thanks to Prof. Ifor Samuel and Dr. Salvatore Gambino (University of St. Andrews) for performing time-of-flight studies on my materials, Dr. Dmitrii Perepichka and Andrey Moiseev (University of McGill) for EPR and OFET studies, and Dr. Will Skene (Université de Montréal) for the time spent in his group.

Abstract:

The field of organic conductors and semiconductors has grown rapidly. The development of devices based on this technology, and the insights it provides into molecular electronics have led it to the forefront of materials research both industrially and academically.

Electroactive organic species can have wildly varied properties and take on two main different forms:

i. conjugated macromolecules, including polymers and metallopolymers and oligomers thereof

ii. molecular systems, such as small organic molecules and metal complexes with functional ligands

Compared to traditional inorganic materials, semiconducting polymer and oligomer systems have the potential to demonstrate major practical benefits, including tunability, cost effectiveness, ease of manipulation in processing and flexibility. Molecular systems tend to have very well defined electronic characteristics and careful design allows access to highly varied topologies and functionalities.

Chapter 1 incorporates a description of band theory and the development of organic semiconducting technologies, particularly those based on oligothiophenes and small molecules, including characterisation and device structures. Chapter 2 describes the synthesis, design and characterisation of oligothiophene precursors for unique tetrathiafulvalene, metal dithiolene, and spirocyclic dimers, the synthesis and properties of which are discussed in chapters 3, 4, and 5 respectively.

Abbreviations:

2D	two dimensional
3D	three dimensional
A	ampere / area
a.u.	arbitrary units
BEDT-TTF	bis(ethylenedithio)tetrathiafulvalene
BHJ	bulk-heterojunction
BODIPY	boron-dipyrromethene
BTZ	benzothiadiazole
C	capacitance / Coulomb
c	concentration
CE	colouration efficiency
CIE	Commision Internationale de L'Eclairage
CGL	charge generation layer
cm	centimetre
CT	charge transfer
CV	cyclic voltammmetry
D	diffusion coefficient
DB-TTF	dibenzo-tetrathiafulvalene
DFT	density functional theory
dm	decimetre
dmit	1,3-dithiole-2-thione-4,5-dithiolate
DPP	diketopyrrolopyrrole
DPV	differential pulse voltammetry
DSSC	dye-sensitised solar cell
DT-TTF	dithiophene-tetrathiafulvalene
E	electrode potential
E^0	standard electrode potential

EL	electroluminescent
Et	ethyl
F	Faraday’s constant
Fc	ferrocene
Fc^+	ferrocenium
FF	fill factor
FTO	fluorine-doped tin oxide
HOMO	highest occupied molecular orbitals
I	intensity of transmitted light / current
I_0	intensity of incident light
I_a	anodic current
I_c	cathodic current
iR	internal resistance
I_{SD}	source-drain current
ITO	indium tin oxide
IUPAC	International Union of Pure and Applied Chemists
J	Joule
K	Kelvin
kbar	kilobar
kJ	kilojoule
l	cuvette path length / litre
LDA	lithium diisopropylamide
LUMO	lowest unoccupied molecular orbitals
M	molarity / metal
m	metre / electroactive material
Me	methyl
mol	mole
mV	millivolt

n	non-bonding orbital / number of electrons
n-Bu	*n*-butyl
NIR	near infra-red
nm	nanometre
O	oxidised species
OFET	organic field effect transistor
OLED	organic light emitting diode
OSC	organic solar cell
P3HT	poly(3-hexylthiophene)
PCBM	[6,6]-phenyl-C_{61}-butyric acid methyl ester
PCE	power conversion efficiency
PEDOT	poly(3,4-ethylenedioxythiophene)
Ph	phenyl
P_{in}	incident light intensity
P_{out}	maximum output electrical power
PSS	polystyrene-sulfonate
Q	counter-ion
R	reduced species / substituent group
RGB	red, green and blue
s	second
S	Siemens
S.E.	solvation energy
SEC	spectroelectrochemistry
SWV	square-wave voltammetry
T	temperature
TCNQ	7,7',8,8'-tetracyano *p*-quinodimethane
TD	thiophene-dithiolene
T_{dedop}	transmittance in the dedoped state

T_{dop}	transmittance in the doped state
THF	tetrahydrofuran
TMTSF	tetramethyltetraselenafulvalene
TOF	time-of-flight
TTF	tetrathiafulvalene
UV	ultra-violet
V	Volt
V_G	gate voltage
vis	visible
V_{mpp}	voltage at maximum power point
V_{OC}	open circuit voltage
V_{SD}	source-drain voltage
V_T	threshold voltage
W	Watt / channel width
WOLED	white organic light emitting diode
X	halide substituent

Greek

α	1st position on heterocycle / transfer coefficient
β	2nd position on heterocycle / crystal phase
μ	charge-carrier mobility
δ	chemical shift
κ	crystal phase
ε	dielectric constant / molar extinction coefficient
Φ	flux
π	pi bonding orbital
σ	sigma bonding orbital
θ	torsion angle

π^*	pi anti-bonding orbital
σ^*	sigma ant-bonding orbital
μA	microampere
∂c_m	concentration gradient
∂x	change in distance
ΔA	change in optical absorbance
ΔE	difference between energy levels
ΔG	Gibb's free energy
ΔG^0	standard Gibb's free energy
λ	wavelength
λ_{max}	absorption maximum
η_{ext}	external quantum efficiency
η_{int}	internal quantum efficiency
η_{lum}	luminous efficiency
η_{pow}	power efficiency
η_s	power conversion efficiency
v	frequency

Symbols

c	speed of light
d	film thickness
e	charge of an electron
e^-	electron
$E_{1/2}$	half-wave potential
E_a	acceptor energy level
E_d	donor energy level
E_f	Fermi level
E_g	HOMO-LUMO energy gap

E_{Int}	interchain/intermolecular coupling energy
E_{ox}	solution oxidation potential
E_{P}	energy of emitted photons
E_{red}	solution reduction potential
E_{Res}	aromatic resonance energy of a monomer unit
E_{Sub}	substituent influence on the HOMO-LUMO gap
eV	electron volts
$E_{\delta r}$	bond length alternation
E_{θ}	distortions from planarity in a polymer chain
h	Planck's constant
I	current
I_{mpp}	current at maximum power point
I_{SC}	short circuit current density
k	rate constant
k^0	standard rate constant
L	channel length
n	refractive index
P_c	critical pressure
Q_d	charge passed in electrochromic devices
R	gas constant
S	eye sensitivity curve
T_c	critical temperature
t_{tr}	transit time

Contents:

List of Figures:

List of Tables:

List of Schemes:

Chapter 1: An Introduction to Organic Molecular Electronics – Oligothiophenes, Tetrathiafulvalenes and Dithiolene Complexes

1.1. Band Theory

Band theory is a model used to describe the conductance of solids. It describes bulk systems as having a valence band and a conductance band which (in semiconductors and insulators) is separated by a band gap with energy E_g.[1]

In metals there are large numbers of atoms. The overlap of the atomic orbitals of neighbouring atoms results in "bands" of energy levels pertaining to each shell of atomic orbitals. This overlap of atomic orbitals allows electrons to flow freely through the metal lattice. Figure 1.1 demonstrates the construction of these bands for the half full 2s band in metallic lithium. The Pauli Exclusion Principle forces additional electrons into progressively higher and higher energy levels, leading eventually to the Fermi level. The Fermi level, E_f, is the highest occupied state of the valence band at 0 K.[1, 2]

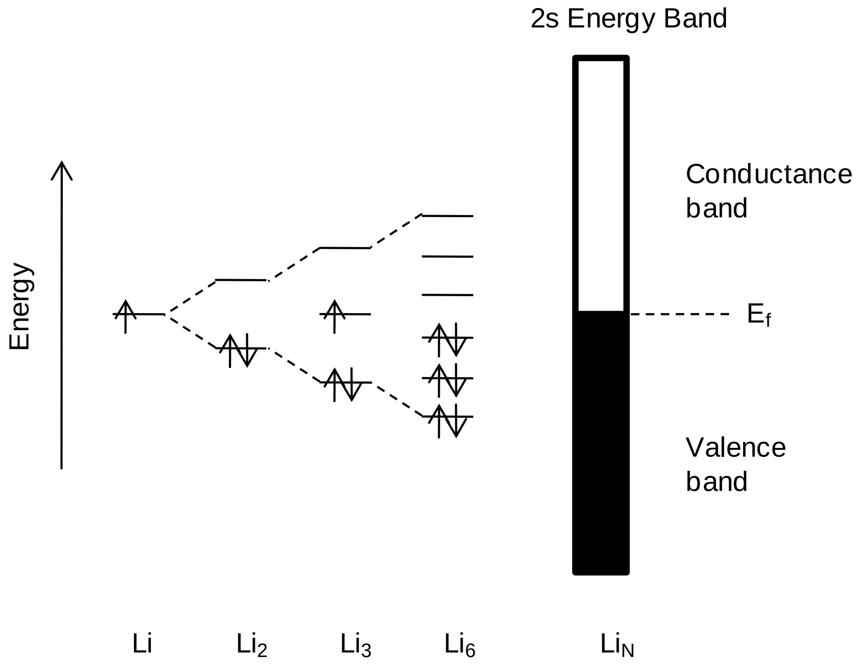

Figure 1-1 Band composition of lithium.

In non-metallic systems, molecular orbitals form from the overlap of the atomic orbitals of the atoms in the molecule and are delocalised over the entire molecule. In semiconductors and insulators, the valence band is made up of the combined occupied molecular orbitals of each species in the material culminating in the *highest occupied molecular orbital* (HOMO). The higher energy conductance band begins with the *lowest unoccupied molecular orbital* (LUMO) of each species and is a combination of the unoccupied molecular orbitals in the system. The valence band is separated by the band gap from the higher energy empty conductance band, and above the full bands pertaining to lower energy orbitals which do not take part in electrical conduction.[1, 2] Figure 1.2 highlights the differences in the band structure of the three main different classes of materials: metals, semiconductors and insulators.[3]

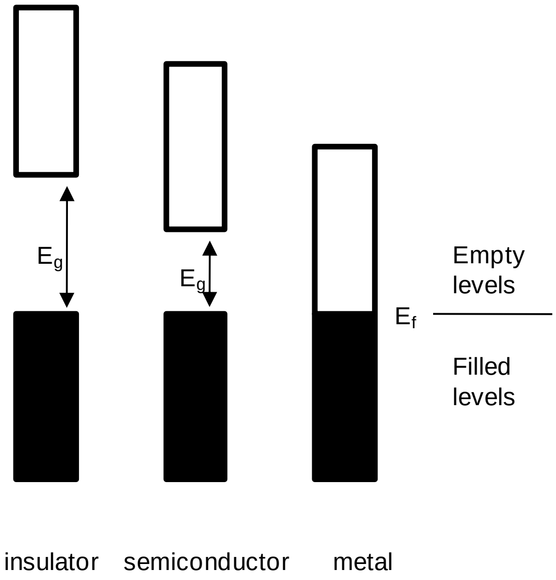

Figure 1-2 Comparative band structures of insulators, semiconductors and metals.

In order for a material to conduct, electrons must be excited from the valence to the conductance band. Metals are conductors due to the fact that there is an overlap of the valence and conductance bands, therefore electrons can flow freely through the bulk material. The valence electrons are mobile due to the strong interactions between neighbouring atoms, and are essentially delocalised throughout the metal lattice. Insulating materials have a full valence band and the energy difference between the HOMO and LUMO is very large, therefore thermal excitation is not sufficient to induce conductivity in the materials. Semiconductors have a much smaller band gap which can be overcome *via* thermal excitation, allowing conductivity to be observed. When the electrons are promoted to the conductance band they become mobile and able to sustain electrical current. When promoted they also leave behind a partially filled band; the vacancies left behind can be envisaged as positively charged "holes" which can also sustain electrical current.[1, 2]

The semiconducting mechanism described above is that of *intrinsic* conduction (based solely on thermal excitation of electrons). A key feature of semiconductors which can be used to decrease the band gap is doping, and results in *extrinsic* conductivity. In traditional semiconductors, doping can be achieved by the introduction of atoms with a different valence to the lattice material, and can be either *n*-type or *p*-type depending on the dopant used. The principle of extrinsic doping is well demonstrated by silicon. Silicon is in group 14 and has 4 valence electrons; therefore if it is doped with a group 15 element, which has 5 valence electrons, the extra electrons in the valence band will be easily promoted to the conductance band leaving behind a positive ion. The impurity is said to act as a donor and the excess of electrons in the conductance band allow *n*-type conductivity. Similarly, if silicon is doped with a group 13 element, with 3 valence electrons, this gives rise to positively charged holes and leads to *p*-type conductivity. Organics can be chemically doped, however they also can be electrochemically doped through either oxidation or reduction of the valence band. Doping using this method is achieved using an electrochemical cell: a working electrode coated in the material to be doped is held in an electrolyte solution (which the material is insoluble in) alongside counter and reference electrodes. Doping is induced by the creation of a potential difference to create a charge in the electrolyte which either removes electrons from the material, *p*-doping, or adds electrons, *n*-doping. *n*-Type doping results in the formation of a new donor level below the conductance band, E_d, whereas *p*-type doping creates a new acceptor level, E_a, as shown in figure 4.[1, 2]

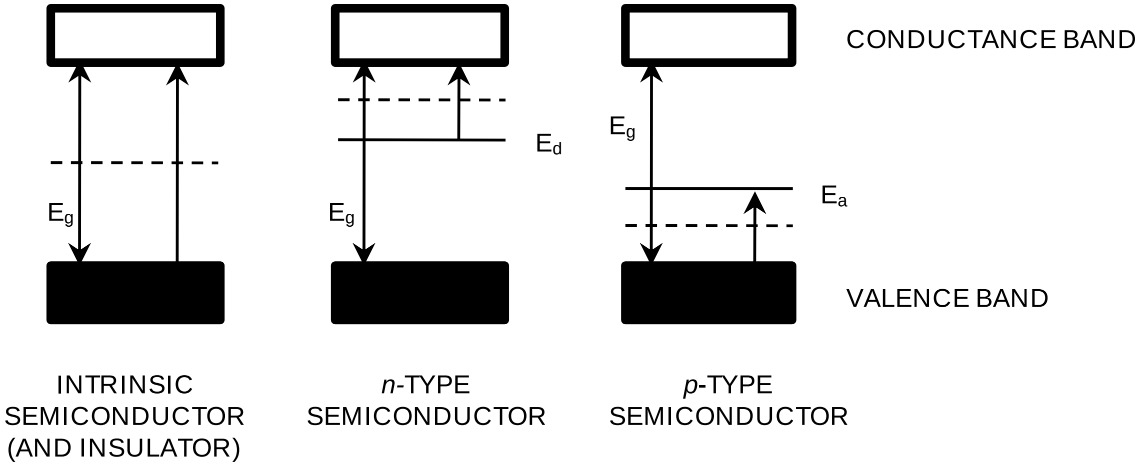

Figure 1-3 Effects of doping on energy levels of semiconductors.

1.2. Organic Semiconductors and Oligothiophenes

Conductivity in polymers was first reported in 1973, when metallic conductivity, then superconductivity, were noticed in the inorganic polymer poly(sulfur nitride).[4, 5] It was later noted that the conductivity of the polymer could be increased by an order of magnitude by doping *via* exposing to oxidising agents.[6] This inspired the discovery of the conductivity of doped poly(acetylene) in 1977,[7] initiating the investigations of the unique electronic properties of semiconducting, organic, conjugated polymers and oligomers, and the synthetic design of new functional systems which have continued to the present day. Those responsible for this discovery and subsequent development of the field, Alan J. Heeger, Alan G. MacDiarmid and Hideki Shirakawa, would go on to share the Nobel Prize for Chemistry in 2000.

As the name implies, conjugated polymers (and the oligomers thereof) have a backbone consisting of alternating single and double bonds. Other than the simplest, poly(acetylene) **1**, this is achieved by the use of conjugated cyclic, polycyclic and heterocyclic systems. Some of the most popular examples are derivatives of poly(thiophene) **2**, poly(pyrrole) **3**, poly(p-phenylenevinylene) **4**, poly(fluorene) **5**, poly(p-phenylene) **6** to name a few.

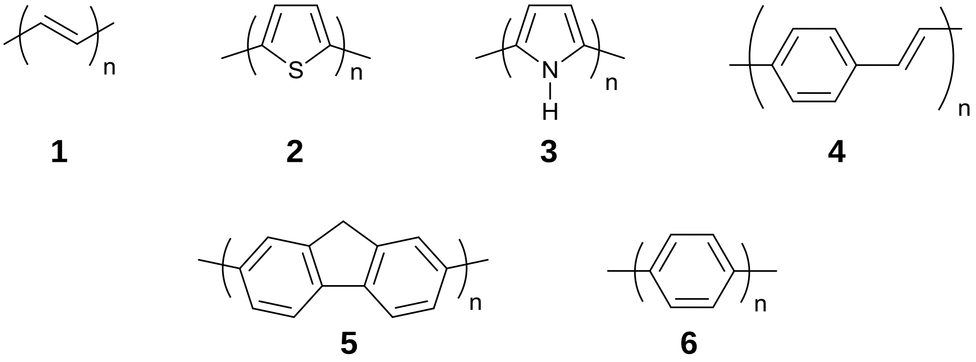

Figure 1-4 Illustrative semiconducting conjugated polymers.

Organic semiconducting materials are lighter and cheaper than their traditional inorganic counterparts and have the potential for processing and manufacturing using cost effective and/or straightforward methods such as spin coating, ink-jet printing, and stamping. The inherent flexibility of polymeric systems allows them to be deposited onto a wide variety of substrates, or alternatively cast as sheets themselves. A large range of applications for these materials subsequently evolved including: electrochromic devices,[8-10] organic field effect transistors (OFETs),[11-13] organic solar cells (OSCs),[14-18] organic light emitting diodes (OLEDs),[19] and sensors.[20]

In these molecules conductivity stems from the delocalised π-electrons. In polymers these electrons occupy the many molecular orbitals which merge into a valence band, beneath the conductance band comprised of the unfilled molecular orbitals, allowing band theory to be applied well to these systems. In oligomeric and small molecule systems, molecular orbitals are both smaller in number and more well-defined, thus true band formation cannot occur, so for discussion of these systems at a molecular level E_g is referred to as the HOMO-LUMO gap.[21, 22]

Linear π-conjugated molecules have various factors which contribute to E_g and can be used to estimate the magnitude of this property. These are:

i. the solution oxidation potential of the molecule, E_{ox}

ii. the solution reduction potential of the molecule, E_{red}

iii. the solvation energy, S.E., which is derived from the solvation energy of the ionised molecule minus that of the neutral molecule

iv. the dielectric constants of the solution and the solid which are ε_1 and ε_2 respectively

Consideration of these influences can be used to assist the design of low band gap systems. These factors can be described using the following approximation:[21]

$$E_g \approx (E_{ox} - E_{red}) + (\mathrm{S.E.}^{+} + \mathrm{S.E.}^{-})\left[1 - \left[[1-(1/\varepsilon_2)]/[1-(1/\varepsilon_1)]\right]\right] \quad (1)$$

Conjugated polymers and oligomers are essentially insulators when in their neutral, non-doped state. However, when doped they can demonstrate both very high conductivity and also unique electroactive properties. These materials allow tuning of their physical properties *via* alteration of their band gap or HOMO-LUMO gap which can be achieved by careful consideration and modification of their structural motifs, or by adding further functionalisation. In polymers, these modifications can be achieved simply by adopting a different monomer, whereas for molecular systems (and the design of new monomers themselves) careful synthetic design may be required.

The magnitude of the band gap in polymers is a consequence of five factors (illustrated for poly(thiophene) in figure 1-5):[21]

i. bond length alternation due to aromaticity (bond length alternation resulting from Peierl's distortion), $E_{\delta r}$
ii. the distortions from planarity of the polymer chains, E_{θ}
iii. the aromatic resonance energy of the monomer unit, E_{Res}
iv. the substituents on the monomer cycle, E_{Sub}
v. the interchain or intermolecular coupling in the solid state, E_{Int}

An estimation of E_g can therefore be attained from:[21]

$$E_g = E_{\delta r} + E_{\theta} + E_{Res} + E_{Sub} + E_{Int} \tag{2}$$

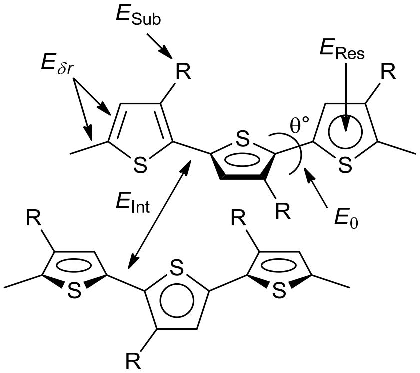

Figure 1-5 Factors which affect band-gap magnitude in poly(thiophene).

The factors listed above indicate how taking structural factors into account can allow for a more strategic approach to the development and evaluation of new low band gap organic semiconductors.[21] Though developed primarily to improve the design of long chain polymeric systems, these rules are also worth considering when evaluating the design or properties of oligomers and other small molecules.

Conjugated oligomers have attracted an increasing amount of interest over the past 20 years, most notably oligoacenes[23-25] and oligothiophenes.[25-28] Oligomers provide excellent model compounds for the development of new conjugated polymers as they are monodisperse and structurally defined, resulting in few or no defects in their conjugation. Many are crystalline and so can be characterised by X-ray crystallography revealing how the molecules self-assemble and improving explanations of redox behaviour. Their responses to electrochemical and spectroscopic studies are generally very well-defined revealing greater insight into the molecules electronics, and allowing more precise conclusions to be drawn.[29] Though more demanding synthetically and often requiring more complex and/or expensive processing, semiconducting oligomers are much more than just useful models.

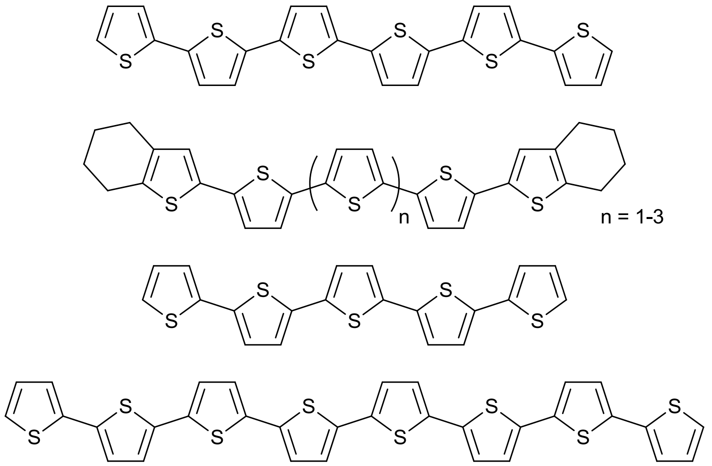

7

8

9

10

Figure 1-6 Early functional oligothiophenes.

Poly(thiophene) had been shown to function as an active component in an OFET in 1986.[30] This was followed in 1989 by Garnier's demonstration that sexithiophene **7** could also function in an OFET device.[31] This inspired increased investigations into these systems in a range of technologies leading to oligothiophene **8** based OLEDs[32] and OSCs[33] based around **9** and **10** in 1993 and 1995 respectively. These early studies of oligothiophenes revolved around relatively simple α-linear systems. As the field has developed, careful design has opened up access to multi-dimensional systems contrasting with traditional linear conjugation.[27]

Oligothiophenes are often synthesised *via* an iterative approach revolving around transition metal catalysed cross-coupling reactions between functionalised thiophenes. Stille (organotin), Negishi (organozinc), Suzuki (organoboron) and Kumada (organomagnesium) couplings are some of the most commonly used thanks to their flexibility, reliability, and the high yields which are often obtained (scheme 1-1).[27, 34]

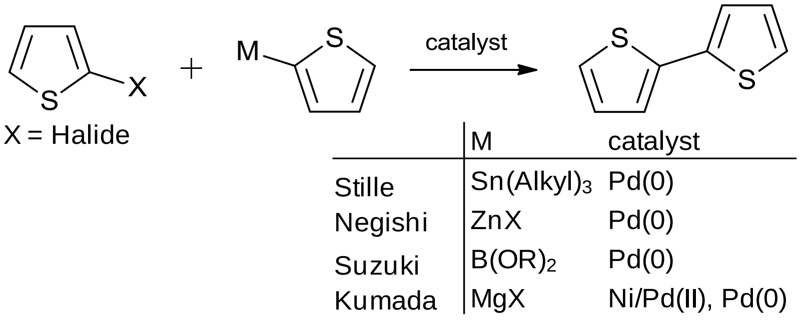

	M	catalyst
Stille	Sn(Alkyl)$_3$	Pd(0)
Negishi	ZnX	Pd(0)
Suzuki	B(OR)$_2$	Pd(0)
Kumada	MgX	Ni/Pd(II), Pd(0)

Scheme 1-1 Transition metal catalysed cross-coupling of thiophenes.

The fact that there are a number of these cross-coupling approaches to choose from and a wealth of catalysts available provides great scope for the development or further optimisation of new synthetic pathways.

In efforts to improve their properties, new oligothiophenes have become increasingly complex often bearing solubilising alkyl chains, novel functional groups, being composed of a variety of heterocycles, incorporating metals and semi-metals, or featuring branched or multi-dimensional architectures.[27] Thanks to the structural flexibility allowed by these moieties, high mobility oligothiophenes have become one of the most widely studied and intensively developed materials for a range of applications, most notably OFETs,[11-13, 25, 28, 35] OLEDs,[36-39] and OSCs.[14, 40-43]

In the solid state these materials tend to overlap extensively, maximising intra-chain non-covalent interactions. These non-bonding interactions help to induce co-planarity between molecules in the solid state, potentially increasing dimensionality and the charge carrier mobility of the bulk phase.[11] These are both very attractive characteristics for use in various organic electronic devices. The majority of oligothiophenes are electron donors and function as *p*-type semiconductors; oxidation of these species will most often result in the formation of a radical cation (or polaron) then a dication (or bipolaron) with a semi-quinoidal structure.[27] The reversibility of these oxidations varies from one system to another. Most thiophene based materials are less susceptible to *n*-doping, the radical anion which results from reduction of the molecule is unstable and readily reacts in unwanted side reactions such as dimerisation.

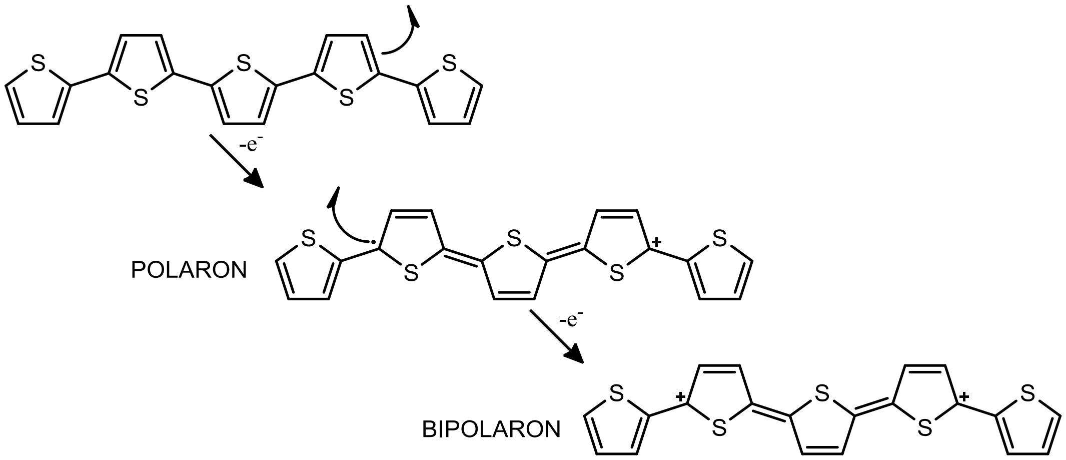

Figure 1-7 *p*-Doping behaviour of thiophene chains.

Though most simple oligothiophenes function as electron donors, electron accepting oligothiophenes have also been developed.[44, 45]

Incorporation of electron accepting units such as benzothiadiazole (BTZ, **11**),[46] diketopyrrolopyrrole (DPP, **12**),[47] or boron-dipyrromethene (BODIPY, **13**)[48] into the oligothiophene chain can allow access to single entity donor-acceptor species with a reduced HOMO-LUMO gap.[49]

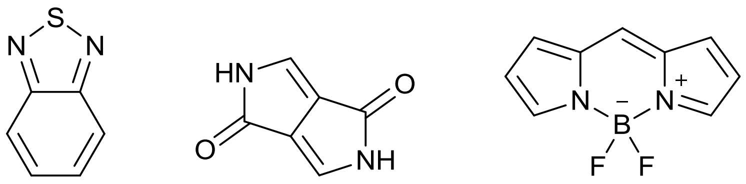

11 **12** **13**

Figure 1-8 Commonly used acceptor moeities in donor-acceptor molecules.

By generating and comparing a series of related oligomers with varying chain lengths or substituents, structure-property relationships can be investigated allowing educated design and evaluation of new materials.[27, 50]

1.3. Tetrathiafulvalene and Dithiolene Complexes

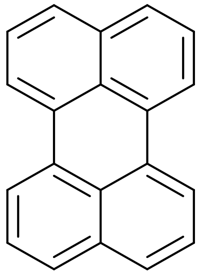

14

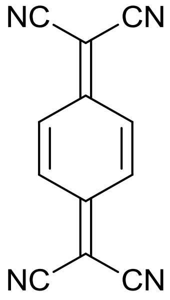

15

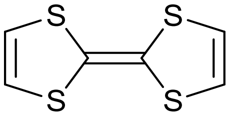

16

Figure 1-9 Small molecules key to the development of organic electronics.

Electrical conductivity in an organic solid was first noticed by a Japanese team in the 1950s with the conductivity of the bromide salt of the polycyclic aromatic hydrocarbon perylene (**14**).[51] Subsequently, in 1962, the π-acid 7,7',8,8'-tetracyano *p*-quinodimethane (TCNQ) (**15**) was synthesised and the semiconductivity of many of its salts was reported with E_g values between 0.05 and 0.2 eV.[52, 53] Chloride salts of the electron donor tetrathiafulvalene (TTF) (**16**) were first reported in 1970 showing it to be readily oxidised in stepwise fashion to form stable radical cations and dications (figure 1-10).[54] TTF is composed of two non-aromatic five-membered rings and has a total of 14 π-electrons; each ring of TTF can be seen as having 7 π-electrons. By losing electrons TTF gains aromaticity through the formation of aromatic dithiolium rings. As a result of this, these charged species exhibit far higher stability than would otherwise be expected.

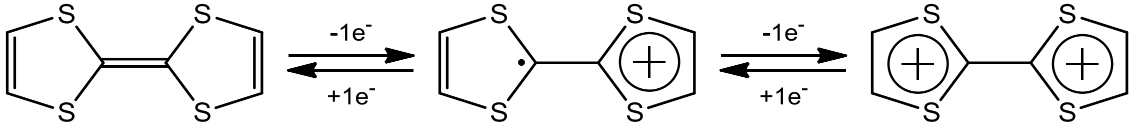

Figure 1-10 Stepwise oxidation of TTF.

Many salts of TTF were then developed and characterised, eventually leading to the discovery of metallic conductivity in the 1:1 charge transfer (CT) complex formed between TTF and TCNQ at low temperature (66 K).[55]

CT salts are constructed of highly ordered arrays of an electron donating species (usually a small molecule) complexed to an electron accepting species (either a small molecule or a transition metal complex) with at least one of them being a stable radical ion.[3] The charge transfer not only binds the salt together, it also acts as a dopant by causing the occurrence of holes, a prerequisite for conduction in these materials.[56] Organic or molecular metals are observed when the charge transferred from donor to acceptor is of a non-integer value. The TTF-TCNQ salt has 1:1 stoichiometry although the amount of charge transferred from the TTF to the TCNQ molecules is 0.59.[57] In a similar fashion to the oligomers described previously crystalline molecular conductors show great structural regularity and so relationships between the structure and properties of these systems can often be readily identified.

For a long time, studies into the properties of structures containing the TTF moiety revolved around development of these new organic metals, leading to the synthesis of more highly conducting CT salts of the organoselenium donor tetramethyltetraselenafulvalene (TMTSF) (**17**).

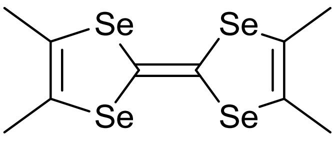

17

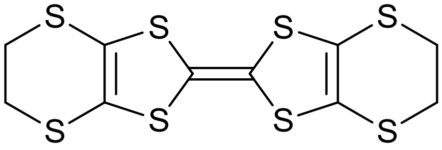

18

Figure 1-11 TMTSF **17** and BEDT-TTF **18**.

The materials with the general form $(TMTSF)_2X$, where X = $[PF_6]^-$, $[AsF_6]^-$, $[SbF_6]^-$, $[BF_4]^-$ etc are commonly known as the Bechgaard salts. The salt $(TMTSF)_2PF_6$ was the first reported organic superconductor with a critical temperature, T_c, of 0.9 K under 12 kbar of pressure.[58] Consideration of the size and geometry of the counteranion led to the generation of a salt with a smaller anion (tetrahedral rather than octahedral) in the complex

$(TMTSF)_2ClO_4$, which was the first ambient pressure organic superconductor with a T_c of 1.4 K.[59]

Development of a wealth of conducting and superconducting CT salts featuring TTF and its homologues took place from then onwards. This eventually led to the synthesis of the sulfur-rich TTF derivative bis(ethylenedithio)tetrathiafulvalene (BEDT-TTF) (**18**).[60] Salts of BEDT-TTF gave rise to another large family of conducting and superconducting salts featuring some of the highest T_c values observed for organic superconductors (table 1-1).[61]

	T_c (K)	P_c (kbar)	Ref.
κ-$(BEDT\text{-}TTF)_2Cu[N(CN)_2]Br$	11.6	0	62
κ-$(BEDT\text{-}TTF)_2Cu[N(CN)_2]Cl$	12.8	0.3	63
β'-$(BEDT\text{-}TTF)_2ICl_2$	14.2	82	64

Table 1-1 Critical temperatures and pressures of some superconducting salts of BEDT-TTF.

In CT salts the donor and/or acceptor species are typically planar or nearly planar molecules. This results in the crystal lattice being comprised of stacks or sheets of molecules adjacent to each other.[3]

Orbital overlap of the π-electron systems of neighbouring molecules allows for metallic delocalisation of electrons along the stacking direction and therefore conductance. This stacked structure of CT salts leads to dimensionality and anisotropy in its conductivity as the electrons can only travel through the π-orbital system of the stacks.[3, 56, 57]

CT salts provide a clean environment for the study of many aspects of electronic conductivity, as such there is a wealth of fundamental electronic and solid state chemistry and physics contained in these substances.[56, 65] However, the crystals are brittle and fragile which presents handling and fabrication problems, while defects or grain boundaries in the crystals can prove detrimental to charge transport meaning batch homogeneity can also prove problematic.[65]

Metal bis(dithiolene)s (figure 1-12) are another high profile electroactive species which began to be investigated in the early 1960s.[66]

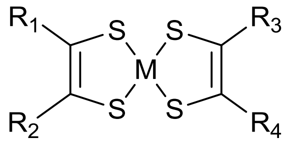

$R_1=R_2=R_3=R_4$ - Symmetric/Homoleptic Dithiolene
$R_1=R_2$; $R_3=R_4$ - Mixed ligand/Heteroleptic Dithiolene
$R_1=R_3$; $R_2=R_4$ - (Unsymmetrically substituted) symmetric *cis*-dithiolene
$R_1=R_4$; $R_2=R_3$ - (Unsymmetrically substituted) symmetric *trans*-dithiolene

Figure 1-12 Structure of metal bis(dithiolene) complexes.

Key to this interest was the realisation that the ligands were redox active leading to the "non-innocent" redox behaviour shown in figure 1-13.[66-69]

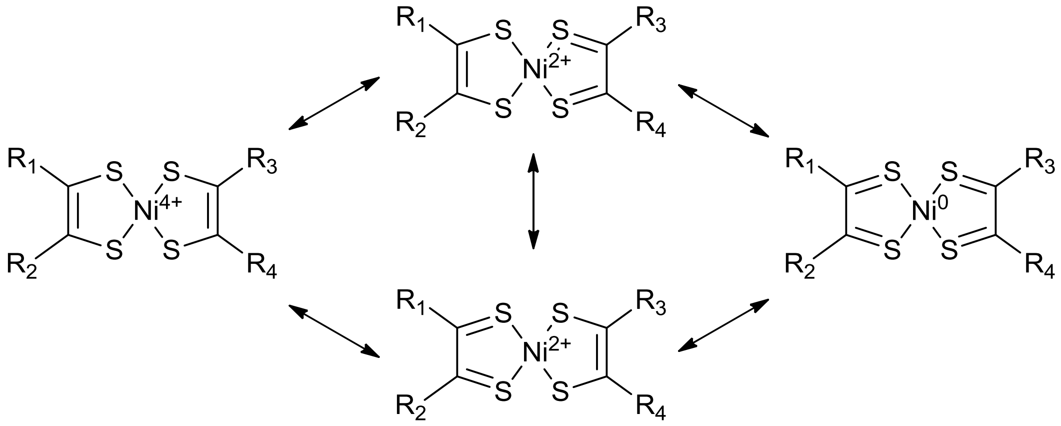

Figure 1-13 Multiple oxidation states of Ni available through the non-innocence of the dithiolene ligand.

Metal bis(dithiolene) complexes have a square planar geometry with an electronically delocalised MS_4C_4 core. The extent of delocalisation of the complex can be modified by careful choice of the other substituents on the alkenyl bond and directly influences the electrochemical and spectroscopic properties of the complex. Owing to the extensive delocalisation and the presence of the electron rich metal centre, the frontier orbitals are distributed over all or most of the MS_4C_4 core.[69-71]

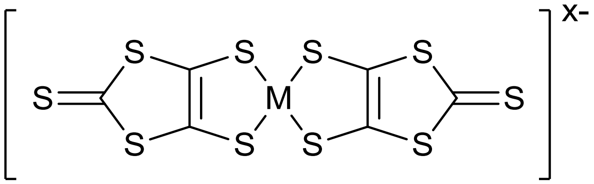

Figure 1-14 Generic $M(dmit)_2$ complex.

In 1975 the ligand 1,3-dithiole-2-thione-4,5-dithiolate (dmit) was reported. The acronym dmit is derived from the old nomenclature of dimercaptoisotrithione.[57, 72] Complexes of this ligand have the general formula $[M(dmit)_2]^{x-}$ (figure 1-14). From a structural viewpoint, the $M(dmit)_2$ molecule is broadly analogous to BEDT-TTF; both are planar with an electron rich centre and tend to stack in the crystal lattice, maximising the inter- and intra-stack S•••S interactions of their peripheral sulfur atoms.[73]

Complexes of dmit were intensively studied for reasons similar to those which inspired development of the many TTF derivatives; the conductivity and superconductivity observed in its CT salts.[57, 73, 74] In 1983 conductivity was observed in the salt $[Ni(dmit)_2]_7(n\text{-}Bu_4N)_2.2CH_3CN$.[75] Subsequently it was discovered that the complex $[TTF][Ni(dmit)_2]_2$ is a molecular metal at ambient conditions and a superconductor at 1.62 K under 7 kbar of pressure.[76]

As will be shown below, the highly functional and reliable electronic and structural characteristics of species such as TTF and metal bis(dithiolene)s affords us the potential to access many new and exciting technologies or improve upon existing benchmarks.

Single component TTF species are increasingly being investigated for device applications owing to their reliable redox behaviour, the high conductivity observed in their salts, and their propensity to stack in the solid state (which maximises orbital overlap allowing for efficient charge carrier mobility). For these reasons TTFs are seen as some of the most promising candidates for *p*-type OFETs.[11, 77-79]

The fused ring systems dithiophene-tetrathiafulvalene (DT-TTF) **19** and dibenzo-tetrathiafulvalene (DB-TTF) **20** illustrate well the potential that TTF based systems offer.

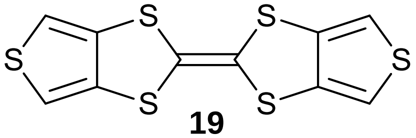

19

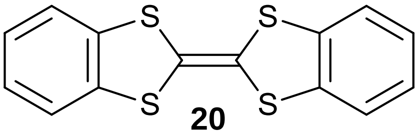

20

Figure 1-15 DT-TTF **19** and DB-TTF **20**.

The charge-carrier mobilities (*μ*) observed in commercial field-effect transistors based upon amorphous silicon are in the range of 0.1 – 1 cm^2 V^{-1} s^{-1}.[78] In order to be viable alternatives, OFETs should be able to at least match these values. A variety of organic molecules including the acene derivatives pentacene **21** and rubrene **22** have demonstrated mobilities greatly exceeding this threshold.[24, 80, 81] Rubrene has demonstrated the highest known mobility in a single crystal OFET device of ~15-20 cm^2 V^{-1} s^{-1}.[82, 83]

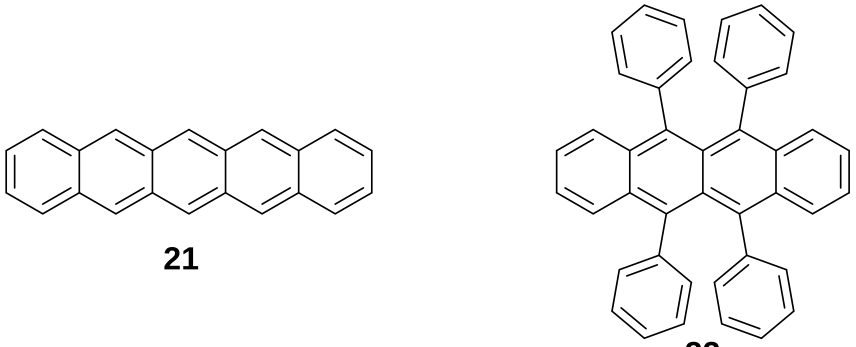

21

22

Figure 1-16 Pentacene **21** and rubrene **22**.

The studies of Rovira, Mas-Torrent and co-workers into OFET devices based upon DT-TTF have given rise to some of the highest mobilities observed from solution processed organic materials.[84, 85] OFET devices based on single crystals of DT-TTF initially demonstrated high mobilities of up to 1.4 cm^2 V^{-1} s^{-1},[84] and have subsequently been improved to 3.6 cm^2 V^{-1} s^{-1} with a high ON/OFF ratio of *ca.* 10^6.[85] Devices using films of DT-TTF, cast *via* the solution based zone casting technique, yielded devices with an average mobility of approximately 0.05 cm^2 V^{-1} s^{-1} and a respectable maximum mobility of 0.17 cm^2 V^{-1} s^{-1}.[86] Following the conclusions from a study of the relationships between the crystal structure and mobilities of DT-TTF, and a selection of structurally similar TTF species,[87] work by the same group on single crystal devices of DB-TTF cast from solution yielded mobilities ranging from 0.01 – 1 cm^2 V^{-1} s^{-1}.[88]

Elsenbaumer *et al.* have recently developed new methods for the functionalisation of the DT-TTF precursor thieno[3,4-*d*]-1,3-dithiole-2-one **23** and have succeeded in incorporating the DT-TTF core into soluble thienylenevinylene oligomers such as **24** (figure 1-17), featuring a variety of R groups. These oligomers also have the potential for polymerisation through the α-position of the pendant thiophenes to generate DT-TTF cross-linked macromolecules.[89, 90]

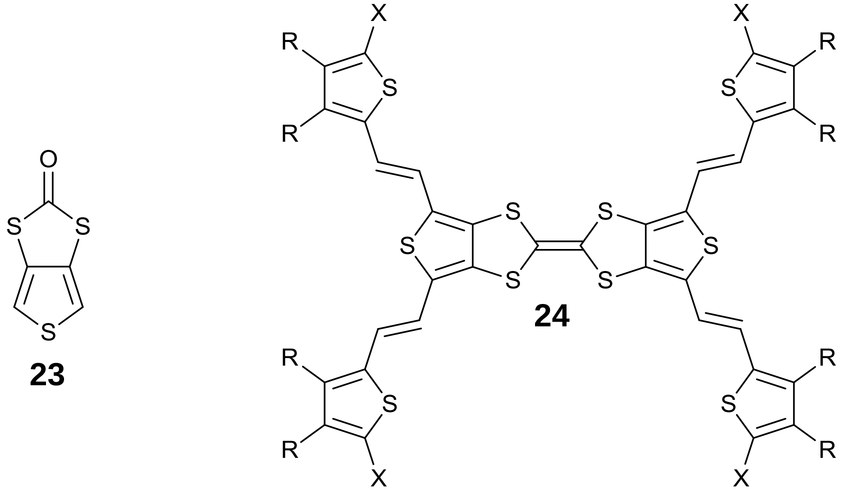

23

24

Figure 1-17 DT-TTF precursor **23** and the general structure of the thienylenevinylene oligomers of Elsenbaumer **24**.

The approach of direct incorporation of species such as TTFs into more process-friendly semiconducting polymers and oligomers has the potential to overcome the handling and manufacturing problems inherent with brittle crystalline materials while also making use of their appealing electronic characteristics.

Over the past decade, the Skabara group has developed a variety of new hybrid TTF-poly(thiophene)s and oligo(thiophenes) (figure 1-18) featuring through-bond fusion of TTF either directly onto the conjugated poly(thiophene) backbone **25-27**, or *via* a non-planar, non-conjugated 1,4-dithiin ring **28-29**.[91-94]

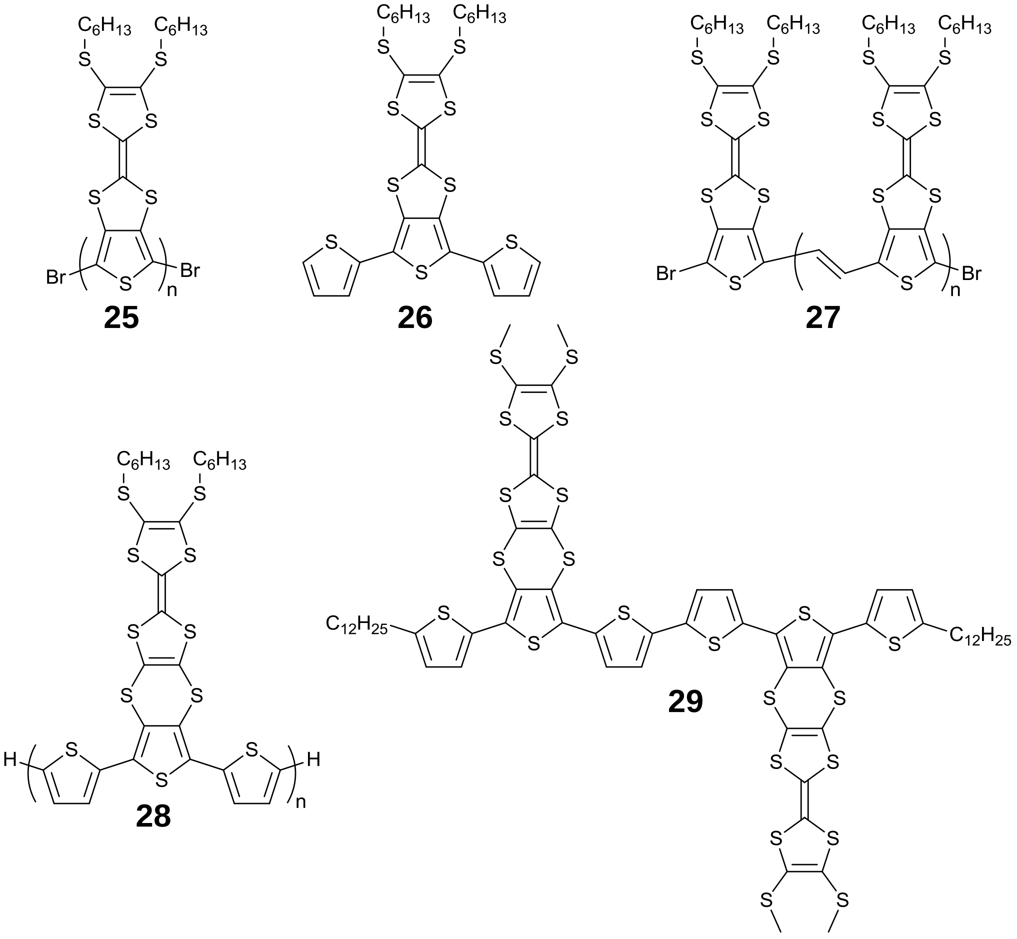

25 **26** **27** **28** **29**

Figure 1-18 A selection of fused TTF poly(thiophene)s and oligothiophenes previously developed in the Skabara group.

Through the study of these species, the fulvalene unit has been observed to either dominate the polymers electroactivity, or to participate in unique hybrid redox states with complex electrochemical characteristics.[91-94] An OSC device based on poly(thienylenevinylene) **27** demonstrated a power conversion efficiency of 0.13%.[93]

In dithiolene complexes the extensively delocalised MS_4C_4 core gives rise to characteristic near infra-red (NIR) $\pi \rightarrow \pi^*$ absorptions,[71, 95] therefore judicious choice of the metal or ligand(s) used, or further ligand design, allows for tuneable absorptivity, making them appealing candidates for a variety of optical applications including OSCs,[96-98] near infra-red dyes,[99] and nonlinear optics.[100, 101] Furthermore, a rare example of an ambipolar (both *p*-type and *n*-type) and air-stable OFET, based upon the neutral dithiolene complex, **30**, was reported by Anthopoulos *et al.*; this device displayed mobilities up to the order of 10^{-4} cm^{2} V^{-1} s^{-1}.[102] This discovery has helped to encourage the investigation of a variety of new neutral dithiolene complexes with charge transport applications in mind.[96, 103, 104]

A different application for dithiolene complexes, within a similar context, was recently demonstrated by Marder *et al.*. The introduction of molybdenum tris-[1,2-bis(trifluoromethyl)ethane-1,2-dithiolene] **31** as a dopant (1:1 ratio) in OFETs based on pentacene served to increase mobilities by significantly reducing the contact resistance of the devices studied, with little impact on device stability or ON/OFF ratios.[105]

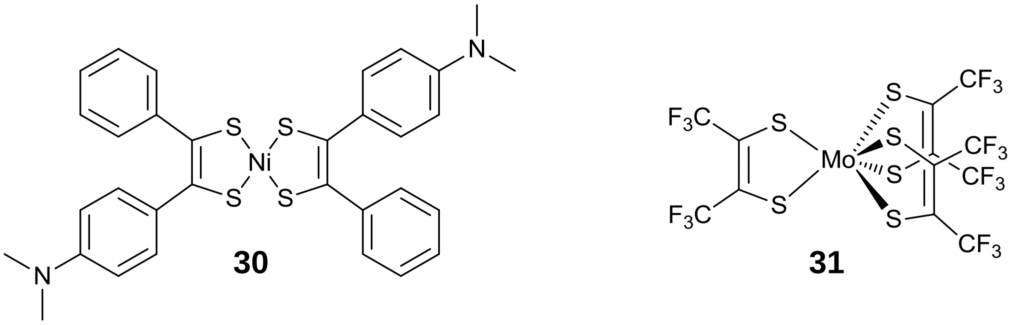

Figure 1-19 Ambipolar dithiolene complex **30** and OFET dopant **31**.

By incorporating a metal into a conjugated polymer we can develop systems with hybrid electronics featuring the *d*-electrons of the metal centre being incorporated within the π-system of the polymer backbone.[106, 107] The dithiolene moiety has also been incorporated into organic semiconductors as an active component in conjugated metallopolymers and oligomers.[67]

In 2001 Pickup *et al.* reported the first electro-polymerisable nickel dithiolene complex **32** featuring pendant 2-thiophene cycles. The resulting metallopolymer poly(**32**) displayed low conductivities of 10^{-6}-10^{-4} S cm^{-1}, which was attributed to the presumed network nature of the polymer and to limited conjugation length.[108]

In an effort to confirm this, Pickup *et al.* conducted more detailed studies into the nature of the electronic and structural properties of the system by comparison to the related structures **33-35**.[109] These studies illustrate well how incorporation of dithiolene centres into a polymer can have marked effects on its properties.

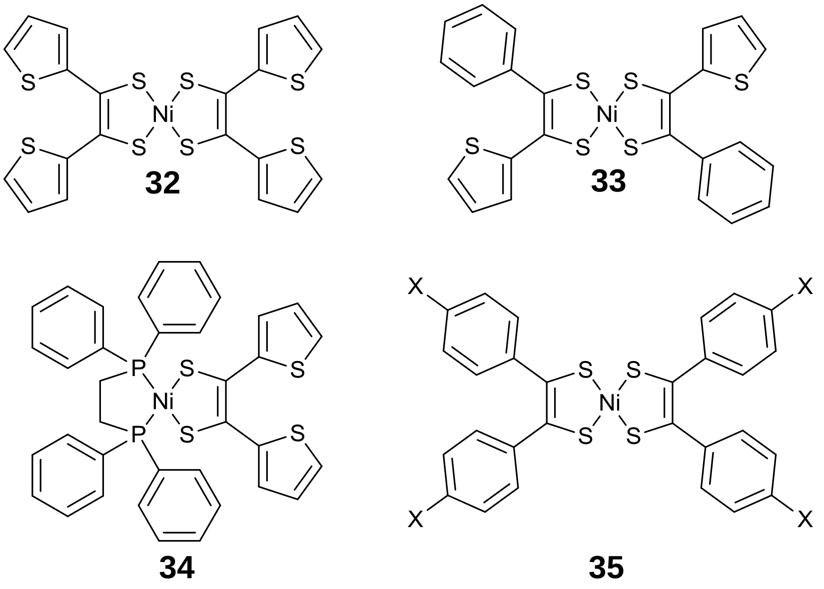

Figure 1-20 First electropolymerisable dithiolene complex **32** and complexes **33-35** as used for comparative studies.

Complex **32** displayed two reversible reduction processes and a single reversible oxidation. After electropolymerisation to poly(**32**), the reduction processes were maintained, but the reversible oxidation observed in the monomer had been lost. This was attributed to the lower oxidation potential of the connecting oligothiophenes formed during polymerisation preceding and masking that of the dithiolene centre. This conclusion was strengthened by similar observations in **33**, and the lack of an oxidation wave in this region for the tetraphenyl analogue **35** confirmed a thiophene-based oxidation. Comparison of the visible absorption spectra of these structures also served to demonstrate that the introduction of thiophene substituents served to reduce the HOMO-LUMO gap. The properties of poly(**34**) were significantly different from the other materials as the Ni atoms are bound stemming off from a single poly(dithienylvinylene) conjugated backbone. As such, they were shown to be less intimately involved with the linear conjugation of the polymer.[109]

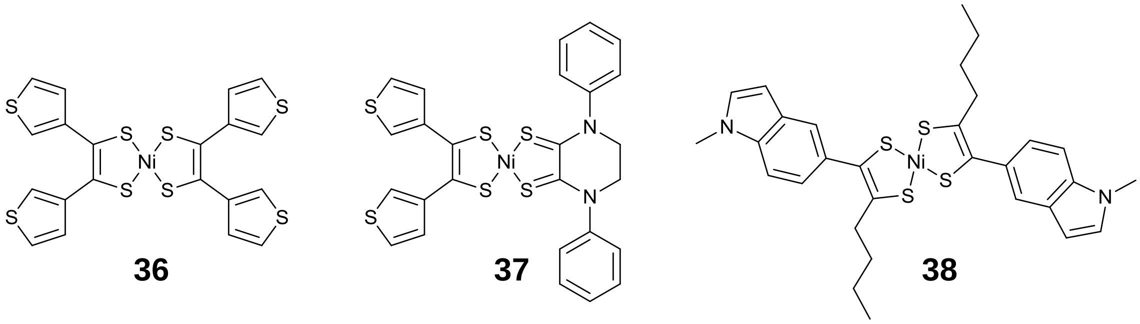

Figure 1-21 Electropolymerisable nickel dithiolenes reported by Anjos *et al.* **36** and Robertson *et al.* **37** and **38**.

Anjos *et al.* expanded on this work by switching from pendant 2-thienyl groups to 3-thienyl **36**, to allow the possibility of poly(thiophene) chains being grown featuring the dithiolene complex as a pendant group, as opposed to direct incorporation of the dithiolene into the polymer conjugation. An electrodeposited film of neutral **36** displayed conductivity, however, upon electropolymerisation, an insulating dichloromethane soluble film was formed. This indicates limited polymerisation which was attributed to the poor solubility of the monomer and loss of conjugation due to twisting of any thiophene chains formed. Interestingly, co-polymerisation with thiophene improved the polymerisation and generated a conducting film, demonstrating a promising approach to the development of new hybrid polymers with unique properties.[110] Further work by Robertson's group demonstrated this in the heteroleptic system **37**. Electropolymerised poly**37** on fluorine-doped tin oxide (FTO) generated a polymer with a very broad NIR absorption (1200-2000 nm, λ_{max} = 1550 nm). Co-polymerisation again with thiophene resulted in a hybrid film which retained the broad NIR absorption (though shifted to 1400nm).[111]

Robertson's group have also developed the indole dithiolene complex **38**, the polymer of which displayed reliable and reversible two stage NIR electrochromism with a red-shift and decrease in intensity of the NIR absorption moving from the neutral to the mono-reduced form, before eventual complete loss of signal in the doubly-reduced form. Materials like this could have applications in telecommunications.[112]

Thiophene-dithiolene (TD) ligands feature thiophene rings fused to the dithiolene moiety, similar to DT-TTF. The extended conjugation of these structures encourages π-π interactions between neighbouring molecules and increasing the sulfur count encourages S•••S interactions, both of which serve to improve the electronic properties of the bulk material.[113-115]

Previous work within the Skabara group involved the development of a number of new conjugated oligocyclic TD ligands featuring the MS_4 core fused onto the central thiophene of either a polymerisable or end-capped oligocyclic chain. Anionic complexes (figure 1-22) of these ligands featuring a variety of metals and counterions were prepared.[97, 98]

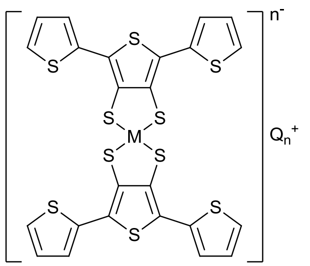

39

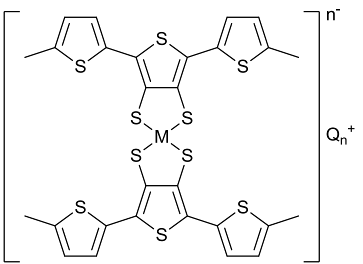

40

	M	Q	n
39a	Ni(II)	Bu_4N	2
b	Pd(II)	Et_4N	2
c	Au(III)	$N(PPh_3)_2$	1
d	Au(III)	Bu_4N	1
40	Ni(II)	Bu_4N	2
41a	Ni(III)	Et_4N	1
b	Au(III)	Bu_4N	1
c	Au(III)	$N(PPh_3)_2$	1
d	Pd(III)	Et_4N	1

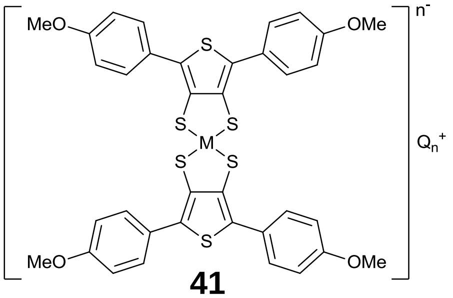

41

Figure 1-22 Electropolymerisable metal complexes **39a-d** and capped complexes **40** and **41a-d** as studied by Skabara *et al.*.

Monomer **39a** was compared to both its corresponding polymer poly(**39a**) (figure 1-23i) and to its methyl-capped analogue **40** (figure 1-23ii). Structure **40** cannot polymerise and so serves as an excellent model complex for comparison, allowing for an improved understanding of the observed properties. This is demonstrated in the cyclic voltammetry studies of these systems.

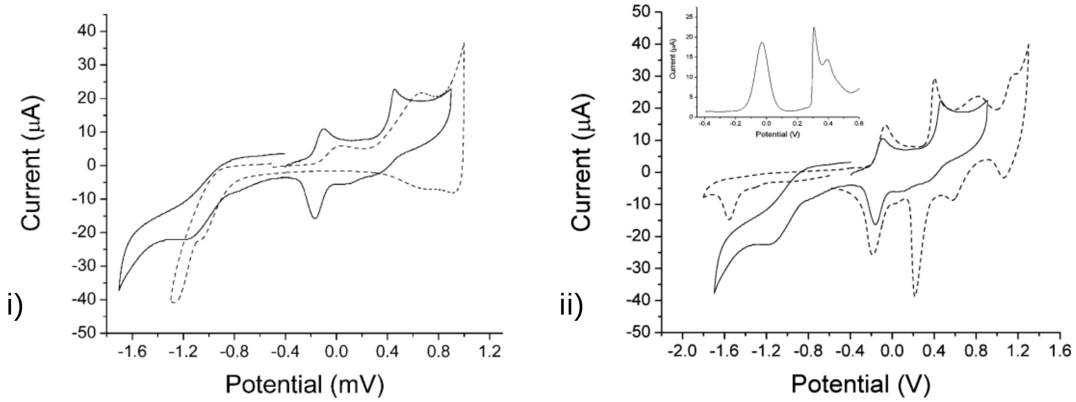

Figure 1-23 Cyclic voltammetry studies of i) **39a** (solid line) and poly(**39a**) (dotted line) and ii) **39a** (solid line) and **40** (dotted line).

Poly(**39a**) maintained the low first oxidation potential of the dithiolene centre, though the reversibility demonstrated in the monomer had been lost. The polymer shows two further reversible oxidation processes at +0.66 V and +0.97 V, attributed to the dithiolene centre and thiophene chains respectively. In the monomer only a single further oxidation attributed to oxidation of the terthiophene chains can be observed at +0.46 V owing to the onset of polymerisation.[97] Subsequent comparison of **39a** and **40** served to confirm the assignments given above and also revealed two further oxidation processes attributed to second oxidations of the dithiolene centre and the terthiophene chains. The shift of the single reversible reduction seen in **39a** to lower potential in **40** (owing to the inductive effect of the terminal methyl groups) allowed positive identification of a thiophene-based reduction.[98]

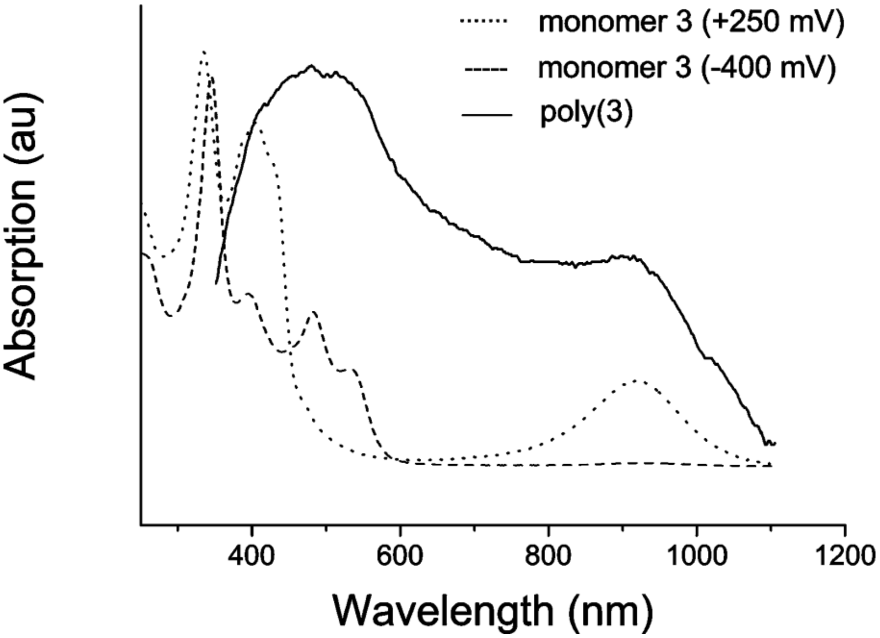

Figure 1-24 UV/vis absorption spectroscopy of **39a** showing the differences between the monoanionic (dotted line, +250 mV) and dianionic (dashed line, -400 mV), and the broad absorption demonstrated by poly(**39a**) (solid line).

Unlike **39a**, in the cyclic voltammogram of the palladium and gold containing monomers (**39b-d**) no electroactivity attributable to the dithiolene centre could be seen. This was maintained in the polymers which all demonstrated behaviour typical of poly(thiophene)s (sequential reversible/quasi-reversible formation of radical cations then dications) with no input from the metal centres. Absorption spectra of the polymers also showed that charged species formed on the polythiophene chains.[98] A thin film of cross-linked poly(**39a**) demonstrated very broad absorption over the entire visible spectrum (shown as poly(3) in figure 1-23). An absorption wave of this breadth is very rare and indicates that materials of this kind could be well employed as light-harvesters in OSC devices.[97]

An appealing factor in the development of both TTFs and dithiolene complexes is the synthetic freedom and structural variation allowed by the routes commonly used when developing new derivatives.

For TTFs, base or phosphite induced coupling of pre-functionalised 1,3-dithiole-2-chalcones, or 1,3-dithiolium salts are commonly used approaches (scheme 1-2).[26, 116, 117] Though ideal for homocouplings, this approach allows little control when attempting to generate asymmetrical TTF systems due to the potential for forming a mixture of two homocoupled TTFs and the desired heterocoupled TTF, often resulting in difficult purification and/or low yields. More direct heterocoupling can be obtained *via* Wittig or Horner-Wadsworth-Emmons reactions. [26, 116]

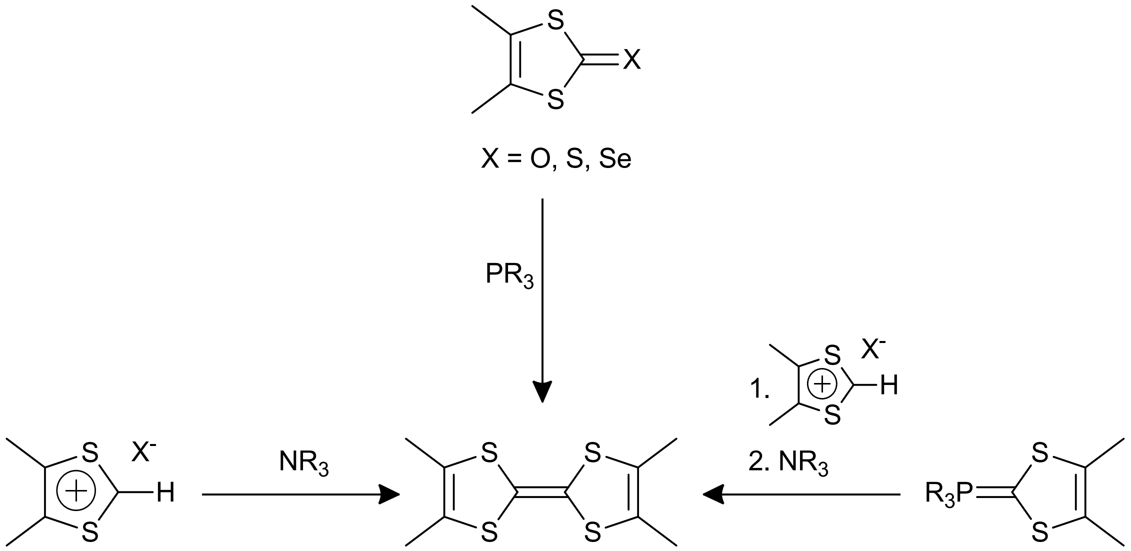

Scheme 1-2 Common approaches to the synthesis of TTFs.

Another approach is the functionalisation of TTF itself. Two of the most reliable approaches to this are the deprotection of S-*β*-cyanoethyl groups,[117, 118] or lithiation with LDA followed by treatment with an electrophile (figure 1-3).[119, 120]

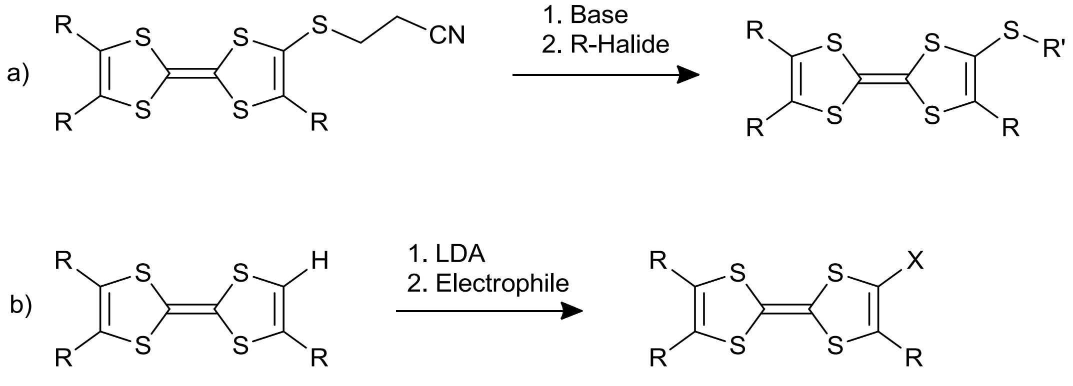

Scheme 1-3 Methods of functionalisation of TTF.

The 1,3-dithiole-2-chalcone TTF precursors are also precursors for dithiolene complexes. Base induced cleavage of the carbonyl/thiocarbonyl group, prior to addition of a salt of the desired metal and a counterion, if required, can be employed (often tetraalkylammonium) (scheme 1-4).[97, 98, 108-111, 113, 114] If isolated as a salt, neutral complexes can often be obtained by exposure to a variety of oxidising agents including iodine,[108-110, 113, 114] silica,[112] and air.[110, 114]

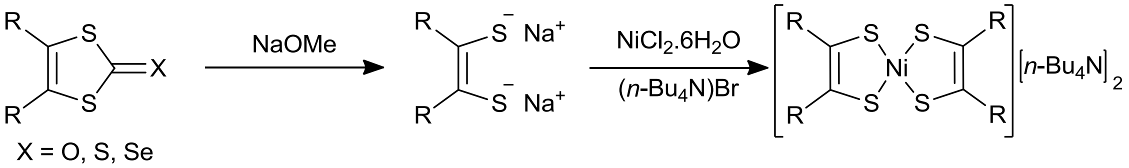

Scheme 1-4 Synthesis of nickel dithiolene complexes from 1,3-dithiole-2-one/thione/selenones.

1.4. Methods of Characterisation

1.4.1. Ultra-Violet/Visible Absorption Spectroscopy.

Upon irradiation with light of the correct energy, absorbance by organic molecules causes electrons to be excited into higher electronic energy levels.

UV/vis spectra are taken using very dilute solutions of the analyte in a cuvette, which is made from a material which does not absorb UV light and is usually of 1 centimetre path length. A matched reference cuvette containing pure solvent is mounted next to the sample cell in the spectrophotometer. The cuvettes are then irradiated simultaneously with separate beams of UV or visible light and the intensities of the transmitted beams from each cell are compared over the entire range of wavelengths to obtain the absorption spectrum of the analyte.[121, 122]

The spectra obtained are generally broad and other than the absorbance maxima (λ_{max}), little fine structure is observed. This is due to the existence of vibrational and rotational energy levels, which broaden the peaks due to transmissions between their own discrete energy levels. Interactions with solvent molecules also tend to blur any fine structure and lead to the broad, smooth peaks characteristic of UV/vis spectra.[121, 122]

The features of a molecule which absorb incident light are referred to as chromophores. Both the chromophores and the transitions they undergo are classified according to the molecular orbitals involved such as n (non-bonding orbitals containing heteroatom lone pairs), σ, or π. Anti-bonding orbitals are denoted by superscript asterisks.[121, 122]

The energy differences between these levels ΔE can be calculated using:

$$\Delta E = hv = \frac{hc}{\lambda} \tag{3}$$

Where h is Planck's constant (6.63×10^{-34} J s), v is the frequency of the incident light, c is the speed of light (3×10^{8} m s^{-1}), and λ is the wavelength of the incident light. It should be noted that as λ increases the magnitude of ΔE decreases.[121, 122]

Transitions observed from non-conjugated chromophores (for example $\sigma \rightarrow \sigma^*$, $n \rightarrow \sigma^*/\pi^*$) are observed at higher energy (low λ_{max}) and are not usually seen in standard UV/vis spectra. Though isolated carbon-carbon double bonds also have a low λ_{max} (~180 nm) conjugated multiple double bond systems, such as the conjugated polymers described previously, give rise to a significant bathochromic shift (red-shift to longer λ_{max}) of the $\pi \rightarrow \pi^*$ transition to the lower energy, visible region of the UV/vis spectrum.[121, 122]

Estimation of the optical HOMO-LUMO gap from UV/vis spectra can therefore be obtained from equation 3 by using the onset of the longest wavelength (lowest energy) absorption edge, and converting to electron volts by dividing by the charge of an electron e ($e = 1.602 \times 10^{-19}$ C). As h, c and e are all constants, the equation simplifies to:

$$E_{\mathrm{g}} = \frac{1240.68}{\lambda} \tag{4}$$

The Fieser-Woodward rules are an empirical set of rules which describe how as the conjugation length increases, the $\pi\rightarrow\pi^*$ transition lowers in energy, and how substituents can influence the $\pi\rightarrow\pi^*$ transition depending on their electron-withdrawing or -donating nature with regard to the conjugated chain. Manipulation of these effects gives rise to the tunable colours and electronic properties of these species.[21, 121, 122]

The absorption laws use for characterisation using UV/vis spectra are:

Lambert's Law: The fraction of incident light absorbed is independent of the intensity of the source.

Beer's Law: the absorption of light is proportional to the number of absorbing molecules.

These two laws are the foundations of the *Beer-Lambert Equation*:[122]

$$\mathrm{A} = \log_{10}\frac{\mathrm{I}_0}{\mathrm{I}} = \varepsilon l c \qquad (5)$$

Where I and I_0 are the intensities of the transmitted and incident light respectively, the $\log_{10}$ of I_0/I is the absorbance, ε is the molar extinction coefficient with units of 1000 $\mathrm{cm}^2\ \mathrm{mol}^{-1}$ (which by convention are often not included when quoting values of ε). The value l is the path length of the absorbing solution in centimetres (the use of a 1 cm path length cuvette further simplifies the equation), and c is the concentration in mol dm^{-3}. The spectra are usually plotted as absorbance against λ.[121, 122]

The magnitude of intensity of absorption, the molar extinction coefficient, is largely dependent on the allowed or forbidden nature of the electronic transitions. Allowed transitions give rise to much more intense absorptions and therefore higher values of ε than those due to forbidden transitions.[121, 122]

1.4.2. Electrochemical Analysis - Cyclic Voltammetry

Upon application of a potential difference across an electrochemical cell containing an analyte and electrolyte, reactions occur at the working electrode and the counter electrode.[123-125]

The reactions which can occur are oxidation (the loss of electron(s)) and reduction (the gain of electron(s)), where *n* is the number of electrons lost or gained:

Oxidation: $R \rightarrow O + ne^-$

Reduction: $O + ne^- \rightarrow R$

The relationships between the applied potential, the redox current and the concentrations of the components of the redox couple are described by a number of important laws. Two of the most important are the Nernst equation and the Butler-Volmer equation.[124]

The free energy, ΔG (kJ mol^{-1}), is related to the concentrations of the oxidised species [O] (mol l^{-1}) and the reduced species [R] (mol l^{-1}) by:

$$\Delta G = \Delta G^0 + RT \ln \frac{[\mathrm{O}]}{[\mathrm{R}]} \tag{6}$$

where R is the gas constant (8.314 J mol^{-1} K^{-1}), and T is the temperature (K). The Gibbs free energy and the electrode potential, E (V), of the redox couple are related by:

$$\Delta G = -nFE \tag{7}$$

Where *n* is the number of electrons involved and F is Faraday's constant (96485 C mol^{-1}). The standard Gibb's free energy (ΔG^0) and standard electrode potential, E^0, are related by the similar equation:

$$\Delta G^0 = -nFE^0 \tag{8}$$

From these equations the Nernst equation is derived which describes the relationship between potential, and concentration:[123-125]

$$E = E^0 + \frac{RT}{nF} \ln \frac{[\mathrm{O}]}{[\mathrm{R}]} \tag{9}$$

Another important relationship which links the current, I (A), potential and concentration is the Butler-Volmer equation.

If the overall current is viewed as the difference between the cathodic (reduction) current I_c (A) and the anodic (oxidation) current I_a (A) then:

$$I = I_c - I_a \tag{10}$$

These currents are proportional to their corresponding rate constants:

$$I_c = FAk_f[\mathrm{O}] \tag{11}$$

$$I_a = FAk_b[\mathrm{R}] \tag{12}$$

Where A is the area of the electrode (cm^2), and [O] and [R] are the concentrations of the oxidant and reductant at the electrode surface. At a certain potential, $E^{0'}$, the values of k_f and k_b will be equal; this value is the standard rate constant k^0. The forward and reverse rate constants can be written as functions of k^0:

$$k_f = k^0 e^{-\alpha f(E-E^{0'})} \tag{13}$$

$$k_b = k^0 e^{(1-\alpha)f(E-E^{0'})} \tag{14}$$

Where f = F/RT and α is the transfer coefficient, a dimensionless value which can range from 0 to 1. Combining equations 8 – 12 gives the complete current-potential characteristic, the Butler-Volmer equation:[123, 125]

$$I = nFAk^0\left\{[\mathrm{O}]e^{-\alpha f(E-E^{0'})} - [R]e^{(1-\alpha)(E-E^{0'})}\right\} \tag{15}$$

Another important parameter is the mass transport or flux of the electroactive material (m) to the electrode surface (Φ). This is described by Fick's law of diffusion:

$$\Phi = -AD_m\left(\frac{\partial c_m}{\partial x}\right) \qquad (16)$$

Where D_m is the diffusion coefficient of new material to the electrodes surface and ($\partial c_m/\partial x$) is the concentration gradient per unit distance x. Other factors in mass transport are convection and migration, though these have a much smaller influence.[124]

Cyclic voltammetry (CV) is an electrochemical technique which can be used to probe the electronic characteristics of a material. It is highly informative and can be used to disclose the material's HOMO and LUMO levels (thereby its HOMO-LUMO gap), and the number of redox processes that the material undergoes.

In potential sweep methods such as CV the current response of an analyte is recorded while the electrode potential is changed linearly with time from one potential to another. In linear sweep voltammetry, the potential only moves from one value to another in a forwards direction. In CV the potential moves in a forwards then backwards direction. Therefore a plot of applied voltage against time has a triangular profile (figure 1-25).

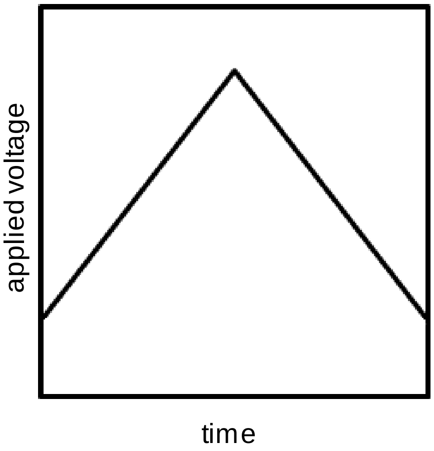

Figure 1-25 Potential sweep form used in CV experiments

When an electron transfer takes place, the current response will increase to a peak which then diminishes as the oxidised material near the electrode diffuses into solution. The experimental results are plotted as current against applied voltage and give rise to smooth wave-forms. Peaks in the forward direction indicate oxidation and those in the reverse direction indicate reduction. As each electron is lost/gained, the potential required to remove/add another electron increases as more energy is required. Provided the redox processes are reversible, they will be seen as waves of similar size and shape upon reversal of potential.[123, 125, 126]

Typical electrochemical cells for CV experiments consist of three electrodes: a working electrode, a counter electrode, and a reference electrode.

The electrodes are connected to a potentiostat and suspended in an electrolyte. The potentiostat controls the potential of the working electrode with respect to the reference electrode solution, and compensates for as much of the internal resistance of the cell as possible. The electrolyte is required to allow conductivity and is chosen upon consideration of the solvent to be used and its non-reactivity with respect to the analyte.[123-126]

The working electrode is where the redox process being examined occurs, and can be various metals including gold, silver, and platinum, or inert substances such as glassy carbon. To probe the redox characteristics of a material in the solid state, the material can be cast or grown onto the working electrode itself or coated onto an ITO coated glass slide, with the ITO slide functioning as the working electrode. The counter electrode has a polarity opposite to that of the working electrode, and ensures that current does not flow through the reference electrode. The counter electrode is typically a highly conducting metal such as silver or platinum wire. The reference electrode is an electrode with a stable redox potential which can be set to zero and used as a baseline..[123, 125]

Common reference electrodes include the standard hydrogen electrode, the saturated calomel electrode, and the Ag/AgCl electrode. When using a non-aqueous solvent, pseudo-reference electrodes are often employed, typically a metal wire such as silver or platinum calibrated to a known redox couple.[123]

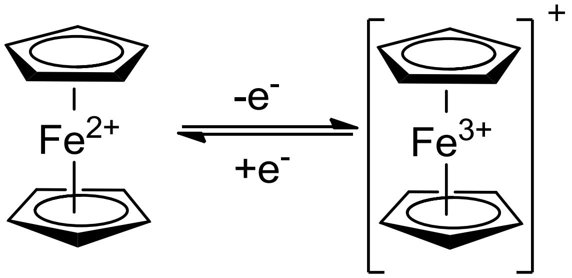

Figure 1-26 Structures of the ferrocene/ferrocenium redox couple.

Following studies by Strehlow, the ferrocene/ferrocenium (Fc/Fc$^+$) redox couple (figure 1-26) is recommended by IUPAC as a calibrating redox couple based on the following requirements:[127]

1) The ions or molecules forming the reference redox system should be spherical with as large a radius as possible.
2) The ions should carry a low charge.

3) The equilibrium at the electrode should be fast and reversible.
4) Both forms of the redox couple should be soluble.
5) No change in the geometry of the ligands should occur.
6) The redox potential should be accessible in a very wide range of solvents.
7) Both forms should be stable enough to permit potentiometric measurements.

The Fc/Fc$^+$ couple satisfies all but the first of these requirements.

By calibrating the results to the Fc/Fc$^+$ redox couple, the HOMO and LUMO levels of the analyte can be calculated by subtracting the onset of the first oxidation and reduction processes from the HOMO of ferrocene which has a known value of -4.8 eV. The value of E_g can therefore be calculated as the difference between the HOMO and LUMO value.

Convoluted voltammograms can often be simplified by using step techniques such as differential pulse voltammetry (DPV) or square-wave voltammetry (SWV). These techniques hold the potential constant for a short while before measuring the current, minimising the influence of any charging current, and improve sensitivity by subtracting current values sampled at two different times, as shown by the arrows in figure 1-27.[125]

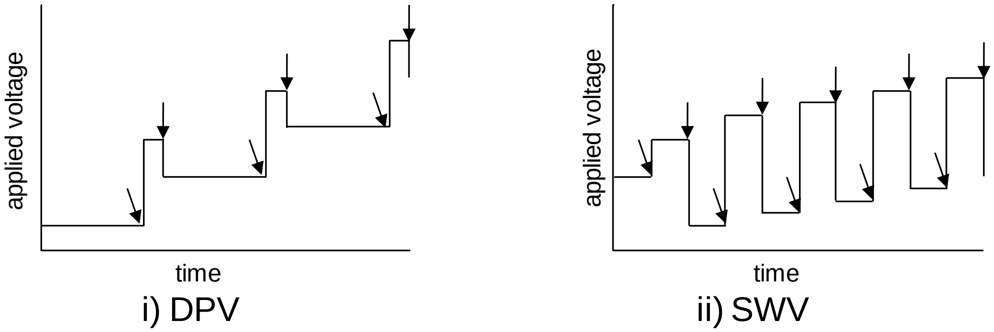

i) DPV ii) SWV

Figure 1-27 Variation of applied voltage with time in DPV and SWV experiments; arrows indicate the position of current measurements used to take an average.

1.4.3. Spectroelectrochemistry

Spectroelectrochemistry (SEC) is the combination of spectroscopic techniques and linear sweep voltammetry and reveals how the spectral properties of a material change upon oxidation or reduction. Various types of spectroscopy can be implemented into SEC, though the most relevant for the work presented here is UV/vis SEC. SEC involves electrolysis of an analyte combined with simultaneous or subsequent *in situ* spectroscopic investigation. Small quantities of analyte are used in order to minimise the time taken for the cell to reach equilibrium at a given applied potential.[125]

Three-electrode electrochemical cells are used, in a similar way to CV, and they must be able to fit inside the cuvette holder of the UV/vis spectrophotometer.

By casting or growing a film onto a conductive transparent substrate, such as an ITO coated glass slide, solid state SEC experiments can be performed routinely. The ITO slide functions as the working electrode and fits in the back of a cuvette. In order to ensure complete electrolysis the counter electrode must have a high surface area; commonly platinum gauze is used, and it must fit into the cell without disrupting the light path. Silver wire functions as a pseudo-reference electrode and again must not disrupt the light path. The cuvette is filled with an electrolytic solution to complete the circuit. The solvent must be chosen so as not to dissolve the film from the ITO slide.[125, 128]

Solution state SEC requires more specialised cells which can accommodate high surface area metal working and counter electrodes, and the reference electrode whilst remaining airtight. Stirring is also required unless the SEC experiment is carried out in a thin film cell.[125, 128]

The results of SEC are usually plotted as either the individual scans of different voltages plotted together on a 2D plot of absorbance against wavelength or as 3D graphs with wavelength, absorbance and potential as the x, y, and z axes respectively.

Typical observations of linear conjugated systems are that upon increasing the oxidation potential, a decrease in the intensity of the aromatic π-π^* transitions occurs, together with the emergence of a radical cation wave at a higher wavelength. The intensity of the π-π^* transition decreases as the conjugation is disrupted by the formation of the radical cations. As the potential is increased further, radical cations will be oxidised to dications, resulting in loss of intensity of the radical cation band and the emergence of a new band pertaining to the dication. Dication bands are of higher wavelength again and usually broad owing to increasing conductivity.[128]

1.5. Operating Principles of Organic Electronic Devices

1.5.1. Organic Field Effect Transistors

Field effect transistors function as on/off switches in electronic circuits. The structure of an OFET is comprised of an insulating layer (often SiO_2) sandwiched between the gate electrode and substrate underneath, and a layer of semiconductor between the source and drain electrodes on top (figure 1-25). These can be arranged in either a top-contact or bottom-contact fashion depending on whether the source and drain contacts are deposited (usually *via* vacuum evaporation) on top of the semiconducting layer, or the semiconducting layer is cast over pre-patterned contacts.[25, 45, 78]

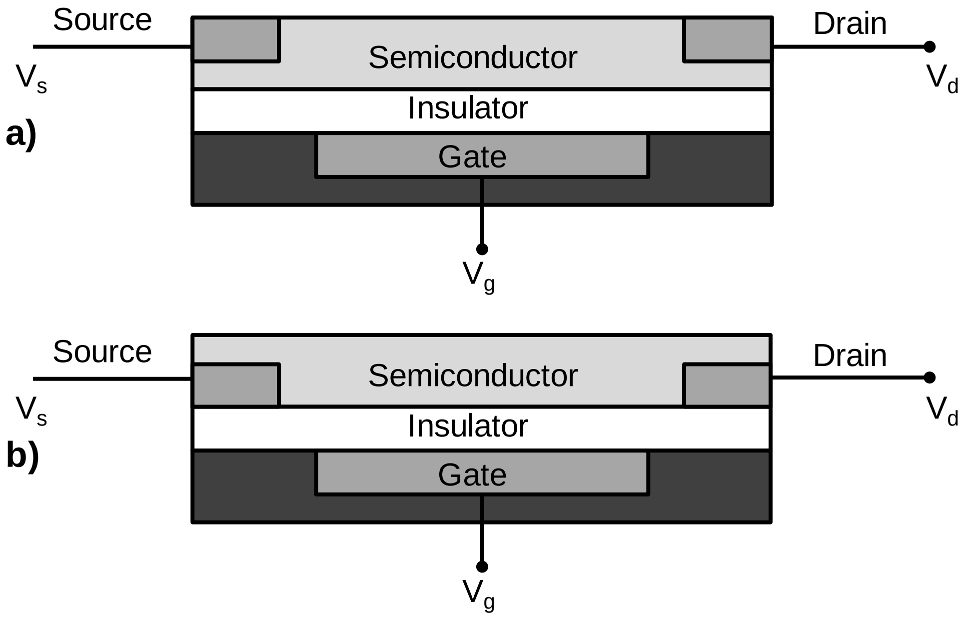

Figure 1-28 Layered structure of an OFET device in a) top-contact and b) bottom-contact configurations.

When a positive voltage is applied to the gate, it accumulates positive charge with a corresponding negative charge induced on the interface between the semiconductor and the gate, forming a conduction channel. When a voltage is then applied between the source and drain electrode, the induced charge can flow. If the gate voltage is removed, then the drain current is also stopped. When positive voltage is applied to the gate, electrons are the charge carriers and we have an *n*-channel FET, if negative potential is applied, holes are the charge carriers and the system is a *p*-channel FET.[25, 28, 45, 78]

The typical output characteristics of an OFET are shown as a plot of the current between the source and drain electrodes (I_{SD}) against the source-drain voltage (V_{SD}). The variation of I_{SD} with increasing V_{SD} is measured at a variety of gate voltages (V_G) and is described by two regimes. In the linear regime, I_{SD} increases linearly with V_{SD} until high V_{SD} is reached and the signal begins to curve and resolves as a horizontal line, the saturation regime. In the saturation regime V_{SD} is greater than or equal to V_G therefore I_{SD} cannot increase as the amount of charge induced in the semiconducting layer cannot further increase.[28, 45, 78]

The most important characteristics of a candidate material in an OFET configuration are its charge carrier mobility (μ) ON/OFF ratio, and threshold voltage (V_T).

V_T is the gate voltage at which the conduction channel begins to form, applying $V_G<V_T$ will not generate enough free charge carriers for conduction.[25, 28, 45, 78]

The charge carrier mobility (μ) is a measure of the average charge carrier drift velocity per unit of electric field. The magnitude of μ can be calculated from two equations which relate to the linear and saturated regimes of the graph.

Linear regime:

$$I_{SD} = \frac{W\mu C}{L}\left((V_G - V_T)V_{SD} - \frac{1}{2}V_{SD}^2\right) \quad (17)$$

Saturated regime:

$$I_{SD} = \frac{W\mu C}{2L}(V_G - V_T)^2 \quad (18)$$

Where W is the channel width, L is the channel length and C is the capacitance of the gate.[28, 45, 78]

The ON/OFF ratio is the ratio of the drain current measured under applied V_G, over the drain current under no applied V_G. A larger ON/OFF ratio gives cleaner switching characteristics.[25, 28, 45, 78]

1.5.2. Organic Solar Cells

Photovoltaic or solar cell devices convert light into electrical energy and are one of the key technologies in the search for more efficient renewable energy sources. At present the power conversion efficiency (PCE) of organic systems remain lower than that of traditional silicon based systems, but if their efficiencies can be raised to a level comparable with those of inorganic devices (>10%) then OSCs will become viable for adoption into widespread use.[129, 130]

Solar cells require an active layer containing electron donating and accepting components. A general structure for an OSC device features an active layer containing the donor and acceptor components between a transparent electrode (often ITO on glass) and a metal electrode (figure 1-29).[15, 16]

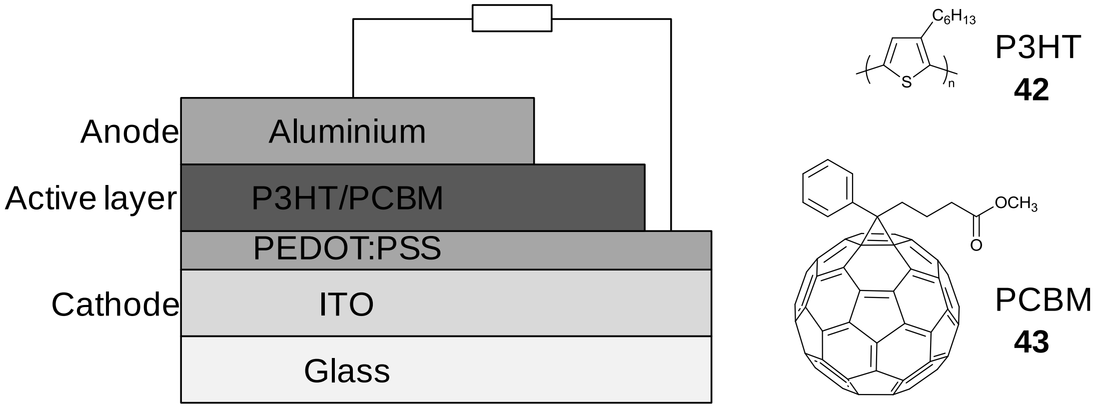

Figure 1-29 Layer structure of a bulk-heterojunction OSC device, showing the structures of the commonly used donor P3HT **42** and PCBM **43**.

The basic working principles of an OSC are demonstrated below in figure 1-30. Absorption of a photon by the donor material leads to photoexcitation of an electron from the HOMO to LUMO, leaving behind a hole. This photogenerated hole-electron pair is held together by Coulombic attraction as an exciton. Excitons are charged species with limited stability, if they have to travel far, recombination back to the ground state can occur, so the exciton must be long-lived enough to survive migration towards the donor-acceptor interface without undergoing recombination. Upon reaching the interface the excited electron is then transferred to the LUMO of the acceptor, leaving a donor radical-cation behind and generating an acceptor radial anion. These charged species can then take part in charge transport in their respective phases eliciting a current response.[15]

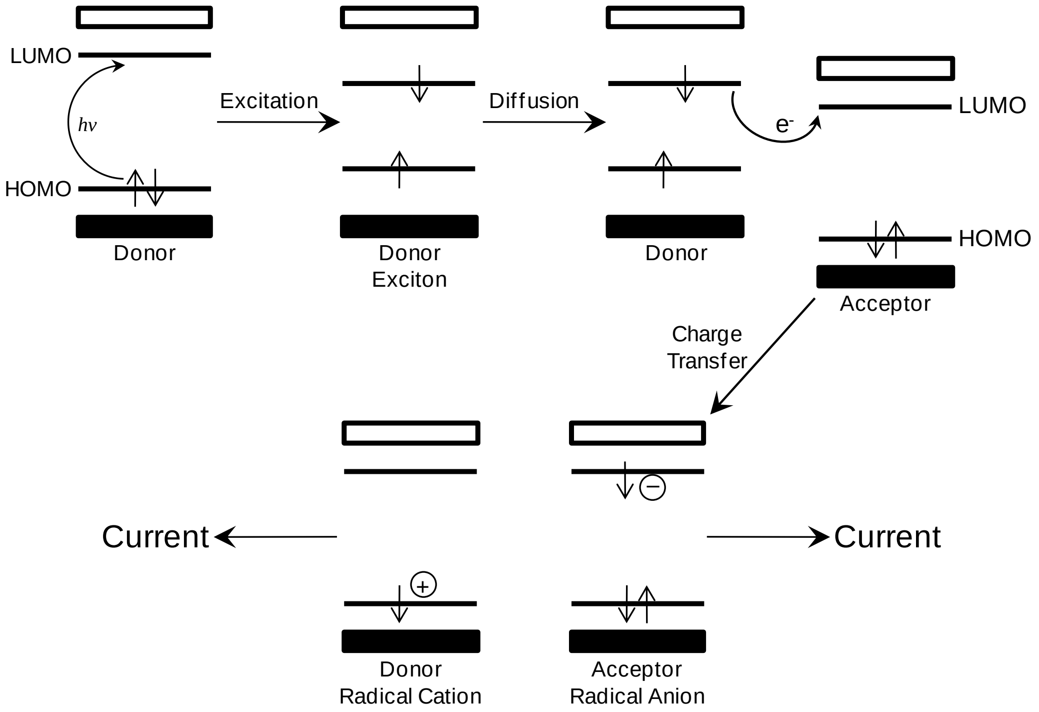

Figure 1-30 Basic operating principles of an OSC device.

Flat-heterojunction OSCs are biphasic and feature a layer of acceptor cast directly on top of a layer of donor. This is problematic as the contact area between layers is small and only excitons formed close to the interface are able to undergo charge separation and generate a photocurrent.[16]

OSC device efficiencies were improved dramatically by the development of bulk-heterojunction (BHJ) solar cells first reported in 1995.[131] BHJ solar cells employ a blend of donor and acceptor as the single active layer. This serves to increase the contact area between donor and acceptor, minimise exciton diffusion lengths and improve processing as a blend in solution can be cast from solution in one step.[14, 16, 129, 130]

The donors used most often are conjugated polymers such as poly(3-hexylthiophene) (P3HT, **42**), and the acceptors typically fullerene derivatives, such as [6,6]-phenyl-C_{61}-butyric acid methyl ester (PCBM, **43**). Indeed PCBM was one of the first acceptors to be used in a BHJ arrangement and remains both the most widely used and one of the most effective components used today.[18, 129-131] A number of methods to further improve the efficiencies in BHJ devices have been implemented. These include coating the ITO-glass electrode with a transparent and conductive polymer such as poly(3,4-ethylenedioxythiophene):polystyrene-sulfonate (PEDOT:PSS) (as shown in figure 1-29), which serves to improve the interface between the active layer and the ITO electrode, improving efficiencies,[16, 132] and thermal annealing of the devices.[129, 133]

OSCs with a PCE of 8.13% have now been reported bringing efficiencies closer to those seen in inorganic devices.[134]

The AM 1.5 solar spectrum corresponds to the terrestrial solar irradiance with the sun 45° above the horizon, the solar photon flux displays that the number of photons per unit area and time is much greater at longer wavelengths. At 500 nm, only 8% of the solar photon flux is available, compared to 53% at 1000 nm.[17] In order to maximise solar absorptivity it is therefore desirable to increase the breadth of absorption, the molar absorptivity and decrease the band gap of candidate materials (increase λ_{max}).[17]

However, by decreasing the band gap of the donor, the open circuit voltage (V_{OC}, voltage at zero current and proportional to the difference between the HOMO of the donor material and the LUMO of the acceptor material, figure

1-31) also decreases, limiting the PCE of the device.[17, 18, 130] The LUMO level of the donor should also be at least 0.3 eV higher than that of the acceptor in order to make electron transfer from exciton to acceptor an energetically favourable process.[15, 18]

The factors listed show that careful control over the HOMO and LUMO levels of both the donor and acceptor is therefore required in order to maximise efficiency.

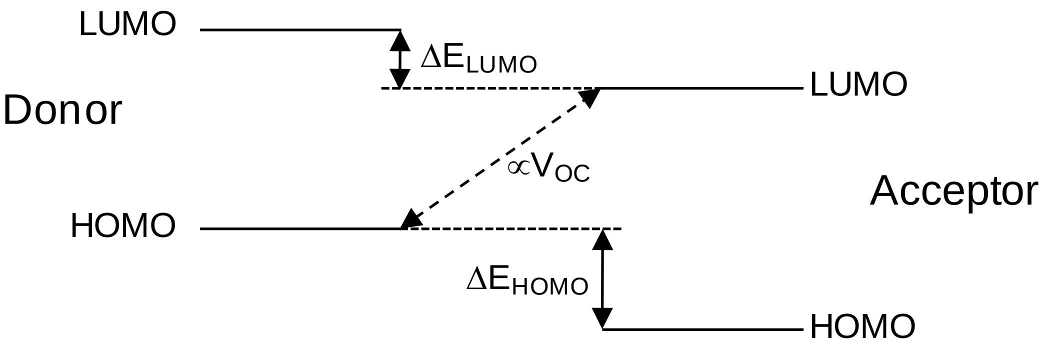

Figure 1-31 Illustration of the reliance of the open circuit voltage (V_{OC}) on the energy level differences of the donor and acceptor. The LUMO of the donor is also higher than that of the acceptor to ensure efficient charge transfer.

The PCE of a solar cell, η_s, is the ratio of the maximum output electrical power P_{out} (in W m^{-2}) of the device under irradiation, to the light intensity incident on the device P_{in} (also in W m^{-2}), standardised to simulated AM 1.5 solar light and is calculated using the following equation:

$$\eta_s = \frac{\mathrm{P_{out}}}{\mathrm{P_{in}}} = \frac{\mathrm{I_{SC}V_{OC}(FF)}}{\mathrm{P_{in}}} \tag{19}$$

I_{SC} is the short circuit current density (current density at 0 V in A m^{-2}), V_{OC} is the open circuit voltage as described previously. FF is the fill factor which is affected by charge carrier resistance and recombination and indicates the quality of the diode.[135] It is defined by the equation:

$$\mathrm{FF} = \frac{V_{mpp} I_{mpp}}{V_{OC} I_{SC}} \tag{20}$$

where V_{mpp} and I_{mpp} are the voltage and current at the maximum power point obtained from a plot of I_{SC} against V_{OC} (an I-V curve).[16]

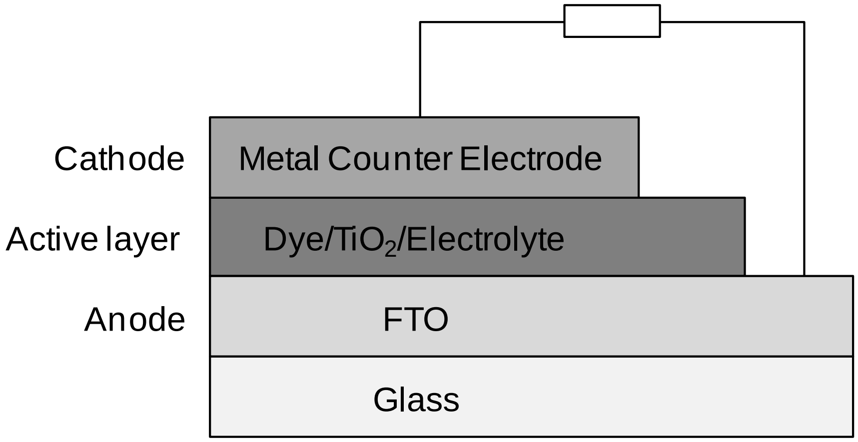

Figure 1-32 Layered structure of a dye-sensitised solar cell.

Another type of OSC device is dye-sensitised solar cells (DSSCs), also known as Graetzel cells after their inventor.[136]

DSSCs are comprised of a conducting fluorine-doped tin oxide (FTO) coated glass substrate covered with TiO_2 nanoparticles which are then coated with a dye monolayer from solution before being completely coated in an electrolyte or hole-transporting material, and a metal counter-electrode (figure 1-32).[16, 137]

In these devices, the dye molecules absorb light before an electron is transferred from the excited dye molecule to the conduction band of the TiO_2 nanoparticle, and subsequently migrates towards the FTO electrode then the counter electrode. The electrolyte/hole-transporting material serves to regenerate the dye sensitizers, and transport the resulting positive charges to the counter electrode.[16, 137]

DSSCs with liquid electrolytes are the most efficient OSCs with PCEs of over 11%.[138, 139] However the liquid electrolytes present problems such as leakage and toxicity and all solid-state DSSCs are yet to display such high efficiencies.[16]

1.5.3. Organic Light Emitting Diodes

OLEDs work on the principle that recombination of holes and electrons in an electroluminescent (EL) material causes emission of photons.

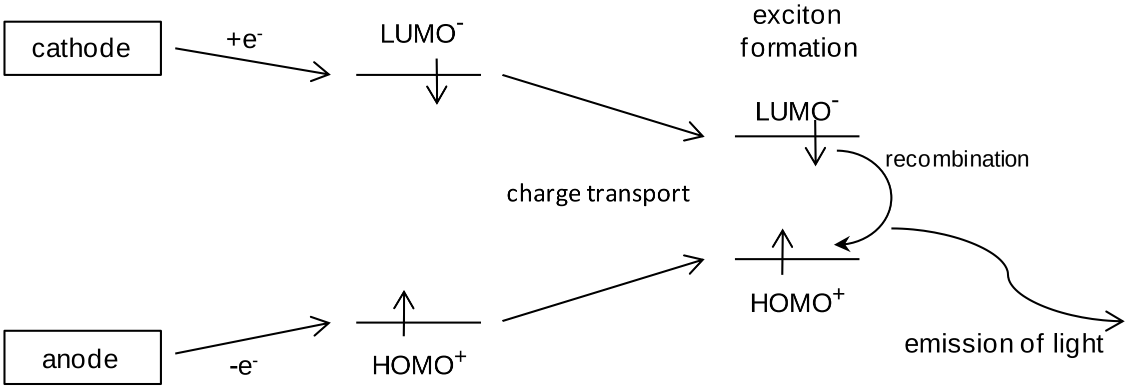

Figure 1-33 Operating principles of an OLED.

Application of a potential difference across the cell results in the injection of holes and electrons from the anode and cathode respectively. They pass through hole and electron transport layers respectively before meeting and forming an exciton in the emissive layer which subsequently recombines to the ground state *via* radiative decay, releasing a photon of light (figure 1-33).[19, 140, 141] Singlet and triplet excitons are both possible with the singlet state giving rise to fluorescence upon recombination and the triplet state (which is slower to recombine and less emissive) to phosphorescence. The ratio of singlet to triplet excitons is considered to be 1:3 which could limit the achievable external quantum efficiencies for electrofluorescent OLEDs.[19, 140, 142]

A typical multi-layer device is shown in figure 1-34. The anode must be transparent therefore is often a film of ITO on glass.

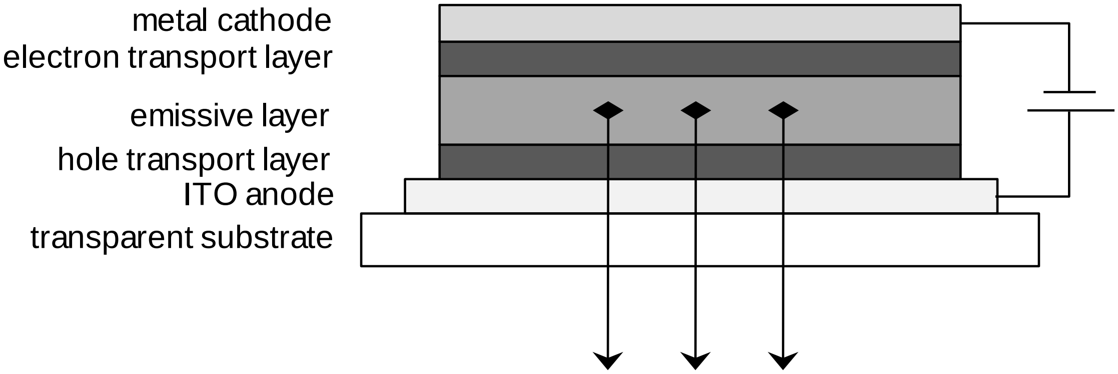

Figure 1-34 Layered structure of an OLED device.

The colour of the electroluminescence is dependent upon the HOMO-LUMO gap of the active material. Shorter conjugation length leads to blue-shifted emission and longer conjugation gives red-shifting of emissions, allowing for tuning of the colour by structural modifications of the active semiconductor.[141, 143]

The internal EL quantum efficiency (η_{int}) of an OLED device is the ratio of photons emitted to electrons injected and can be calculated from the measured external quantum efficiency (η_{ext}) using:

$$\eta_{\mathrm{int}} = 2\mathrm{n}^2\eta_{\mathrm{ext}} \tag{21}$$

Owing to refraction a portion of the photons emitted from the semiconductor cannot be observed externally, thus the external efficiency is diminished by $2n^2$ (n is the refractive index of the organic layer).

The power efficiency (η_{pow}) of the OLED is the ratio of the output light power to the input electrical power. It can also be calculated from η_{ext} using the values of the applied voltage V and the average energy of the emitted photons E_P.

$$\eta_{\mathrm{pow}} = \eta_{\mathrm{ext}} \mathrm{E_P} \mathrm{V}^{-1} \tag{22}$$

Finally, the luminous efficiency (η_{lum}) is determined as the product of the power efficiency and the eye sensitivity curve (S), defined by the Commision Internationale de L'Eclairage (CIE). The eye sensitivity curve is a function which factors in the varying sensitivity of the human eye to different colours of light.[140]

$$\eta_{\mathrm{lum}} = \eta_{\mathrm{pow}} \mathrm{S} \tag{23}$$

The use of OLEDs in multicoloured displays has already begun to be employed in commercial applications such as televisions. White organic light emitting diodes (WOLEDs) are excellent candidates for cheap high area lighting.[144, 145] Using more advanced multi-component device structures[19, 144] or improving the efficiency of electrophosphorescence based devices, could serve to improve overall efficiency of both OLEDs and, in particular, WOLEDs.[19, 144, 145]

1.5.4. Organic Electrochromic Devices

Electrochromic substances are those which exhibit at least one reversible colour change upon the application of a potential difference. The colour of the material will change either between a transparent bleached state and coloured states, or between two or three differently coloured states.[9, 141, 146]

The optical band gap of these materials in their doped and undoped states dictate the colours which they display. When E_g is higher than 3 eV the materials tend to be transparent in the undoped state and absorbing in the visible region when doped, when E_g is less than 1.5 eV the material will be highly absorbing when undoped and more transparent upon doping.[146]

Examples of electrochromic materials include P3HT **42** which is orange/red in the undoped state and transmissive blue in the doped state, PEDOT **44**, which undergoes a transition from deep-blue in the neutral state to a highly transmissive pale blue state upon oxidation, and poly(2,3-di(thien-3-yl)-5,7-di(thien-2-yl)thieno[3,4-*b*]pyrazine) **45**, which changes from green to transmissive upon oxidation (figure 1-35). Devices of these polymers represent some of the first steps towards red, green and blue (RGB) display applications for electrochromic devices.[8, 147, 148]

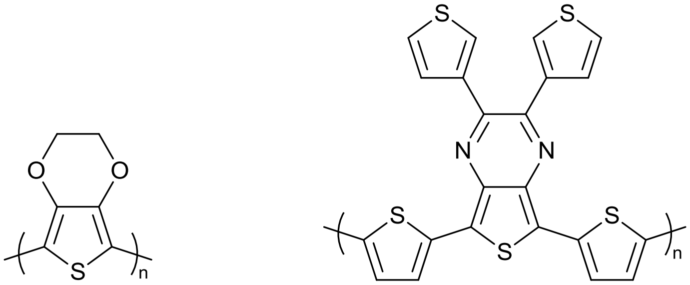

44 **45**

Figure 1-35 Structures of the blue electrochromic material **44** and the green electrochromic material **45**.

Electrochromic devices have a multi-layer structure, an example of a classical seven layer device structure is shown in figure 1-36.[141] Upon application of a potential, the electrochromic material will be oxidised or reduced and will change colour, with counter-ions in the electrolyte layer balancing the developed charge. Upon reversal of polarity, the material will revert back to its ground state colour.[141]

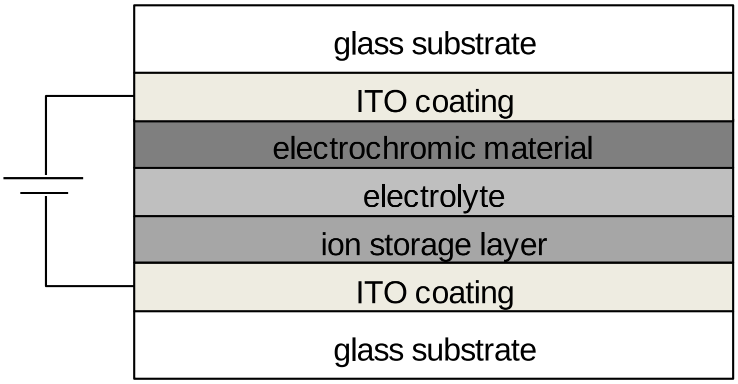

Figure 1-36 Structure of a seven-layer electrochromic device.

Plastic substrates can be used instead of glass allowing for flexible devices to be created and many electrochromic materials can be readily processed from solution allowing for facile processing using techniques such as spray coating, spin-coating, or inkjet printing.[10, 141, 146]

Some important properties which characterise an electrochromic device are its switching time, colouration efficiency and colour coordinates.

The switching time is the time needed for the polymer to switch from one redox state to another. It is dependent on various properties of the device such as the ability of the electrolyte to conduct counter-ions and the ease of diffusion of these counter-ions into the active layer of the device. Different applications have different requirements of the switching time.[10]

The colouration efficiency (CE) relates the change in optical absorbance at a given wavelength (ΔA), to the density of electrochemical charge necessary to induce a full switch (Q_d), as shown in equation 22. The value of ΔA is obtained from the logarithm of the ratio of the transmittance in the doped (T_{dop}) and dedoped (T_{dedop}) states.[10]

$$CE = \frac{\Delta A}{Q_{\mathrm{d}}} = \frac{\log_{10}\left(\frac{T_{\mathrm{dop}}}{T_{\mathrm{dedop}}}\right)}{Q_{\mathrm{d}}} \tag{24}$$

Since 2000, the colours presented by electrochromic devices are commonly described by using the 1931 and/or 1976 CIE representations of colour space which allows for precise definition of the colour. In the 1976 CIE-defined $L^*a^*b^*$ representation, the $L^*a^*b^*$ values are calculated using the 1931 Yxy values (as determined using a colorimeter), where Y is the luminance and x and y are the two dimensional set of coordinates which define the colour state at a given Y.[10, 149]

Chapter 2: The Development of New Methyl-Capped Oligothiophene Precursors to Hybrid Tetrathiafulvalenes and Metal Bis(dithiolene) Complexes

2.1. Abstract

Soluble methyl-capped ter-, quinque- and septithiophene chains have been synthesised in good yields. The oligothiophene chains feature 1,3-dithiol-2-one rings fused to the central thiophene, making them ideal precursors for the synthesis of new, highly conjugated tetrathiafulvalene (TTF) compounds and dithiolene complexes. As such they will also serve as excellent model compounds for the study of these systems.

The electronics of the oligothiophene series has been investigated using cyclic voltammetry (CV), and absorption spectroscopy. The series displays electronic and spectral characteristics typical of a series of oligothiophenes, with the HOMO-LUMO gap decreasing as the chain length, and therefore extent of conjugation, increases.

The influence of the fused 1,3-dithiol-2-one moiety can be seen in the discrepancies between the optical and electronic HOMO-LUMO gaps.

Some results described herein have already been published as:

Electronic, redox and charge transport properties of an unusual hybrid structure: a bis(septithiophene) bridged by a fused tetrathiafulvalene (TTF)

I. A. Wright, P. J. Skabara, J. C. Forgie, A. L. Kanibolotsky, B. Gonzalez, S. J. Coles, S. Gambino and I. D. W. Samuel

Journal of Materials Chemistry, 2011, **21**, 1462-1469.

2.2. Introduction

Oligothiophenes are semiconducting molecules which have been intensively studied towards the development of many new organic electronic devices, including light emitting diodes, field effect transistors and solar cells.[22, 25, 27, 43, 150] End-capped oligothiophenes are particularly attractive materials to study as they generally give well-defined redox signatures and stable charged intermediates, allowing for more precise analysis of the complex electrochemical behaviour typical of these hybrid systems.[94, 151]

In recent years, the Skabara group has been interested in hybrid oligothiophenes (and poly(thiophene)s) possessing electronically active systems such as TTFs,[92-94, 152, 153] metal bis(dithiolene) centres,[97, 98] and other redox active species,[154-156] fused directly to the backbone of the conjugated chain. This has given rise to unique and complex redox behaviour resulting from the merging of two highly redox active components.

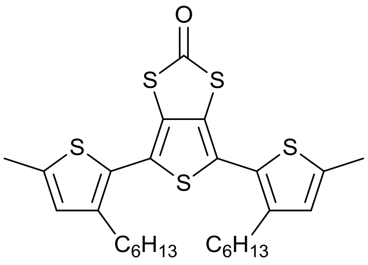

46

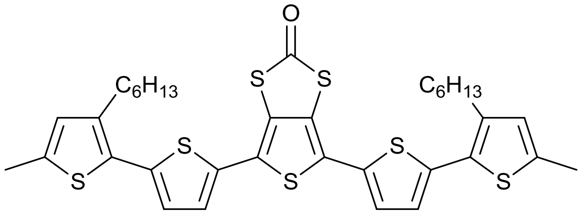

47

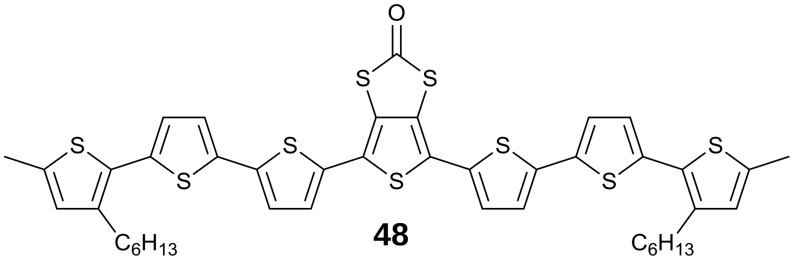

48

Figure 2-1 Structures of the new oligothiophenes.

Here the synthesis of a new series of functionalised methyl end-capped oligothiophenes **46**, **47**, and **48** (figure 2-1) is reported. These oligomers bear a central 1,3-dithiole-2-one cycle which opens up access to the synthesis of a number of hybrid oligothiophenes containing redox active centres (such as TTFs or metal bis(dithiolene)s) fused between two chains. The chains also bear hexyl groups on the 3-position of the terminal thiophene rings to improve solubility.

2.3. Synthesis

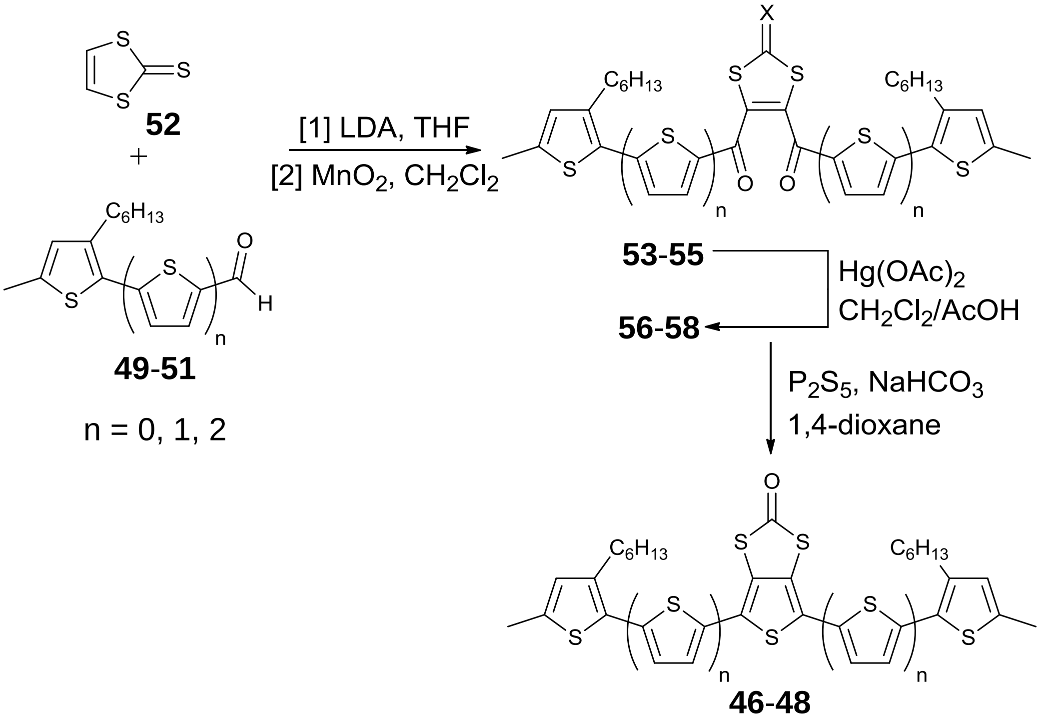

Scheme 2-1 Synthetic route used for the development of oligothiophenes **46** (n = 0), **47** (n = 1), and **48** (n = 2).

The synthesis of the oligothiophenes follows a common path (scheme 2-1). Two-fold sequential lithiation of vinylene trithiocarbonate (VTC, **52**), followed by the addition of pre-functionalised thiophene-2-carbaldehyde **49**, **50**, or **51** gave the corresponding diol intermediate, which was oxidised immediately with MnO$_2$ to afford the 1,3-dithiole-2-thiones **53**, **54**, and **55**.

Transchalcogenation of the 1,3-dithiole-2-thiones to the oxone derivatives (**56**-**58**) was achieved in excellent yields with mercuric acetate. Paal-Knorr thiophene synthesis using P_2S_5 was applied to yield the desired oligothiophenes **46**-**48**, yields are shown in table 2-1.

Table 2-1

	n	Yield (%)
53	0	53
54	1	52
55	2	60
56	0	88
57	1	84
58	2	~99
46	0	75
47	1	75
48	2	69

VTC, **52**, is obtained by the treatment of salt **61** with sodium hydrogen sulphide monohydrate in a 3:1 mixture of DMF/acetic acid (DMF = *N,N*-dimethylformamide). Salt **61** can be readily obtained in large quantities from the efficient synthetic pathway to TTF devised by Bryce and Moore, as shown in figure 2-3.[157]

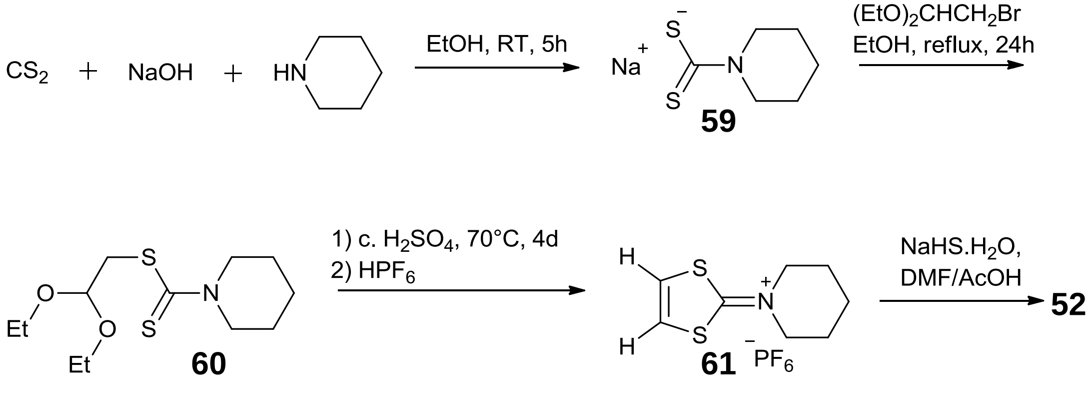

Scheme 2-2 Synthetic path taken to obtain VTC, **52**.

The aldehyde precursors were synthesised in two distinct ways.

Monothiophene aldehyde **49** was generated *via* palladium(0) catalysed Negishi coupling of 3-bromo-5-methylthiophene-2-carbaldehyde (**63**) with hexylzinc bromide (53% yield). Compound **63** was synthesised using a slight modification of the halogen migration reaction pathway as outlined by Fröhlich *et al.*[158] Using this approach, 2-bromo-5-methylthiophene (**62**) was synthesised *via* bromination of 2-methylthiophene using *N*-bromosuccinimide (NBS) in DMF (83% yield), and was used immediately following purification *via* vacuum distillation. Lithiation of **62** with LDA prior to addition of an electrophile, in this case DMF, results in migration of the bromide to the 3-position and addition of the electrophile at the 2-position, to yield **63** (63% yield).

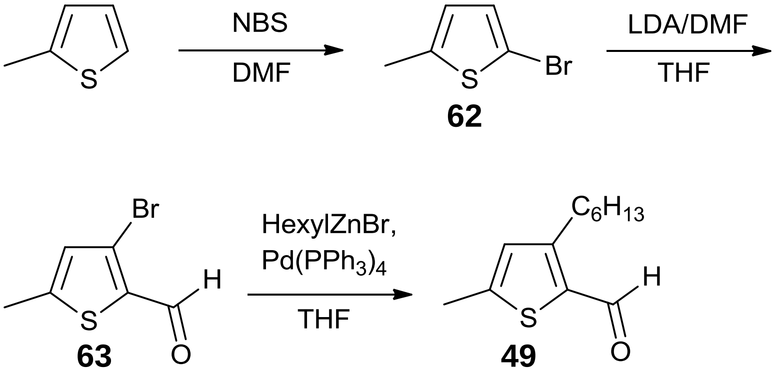

Scheme 2-3 Synthesis of monothiophene aldehyde **49** *via* halogen migration followed by Negishi Coupling.

The bi- and terthiophene aldehydes, **50** and **51** were synthesised using more conventional iterative approaches (shown in scheme 2-4). 2-Bromo-3-hexyl-5-methylthiophene (**64**) was made by treating 3-hexylthiophene (synthesised according to the method of Chaloner *et al.*[159]) first with NBS to give 2-bromo-3-hexylthiophene (98% yield),[160] followed by methylation using LDA/iodomethane to give **64** in 91% yield. This procedure differs from that reported by Sato and Kamine,[161] who performed methylation of 3-

hexylthiophene before bromination, to obtain an overall yield of 36% for compound **64**. Negishi coupling of **64** with 2-thienylzinc bromide affords bithiophene **65**, an intermediate for both **50** and **51**, in 67% yield.

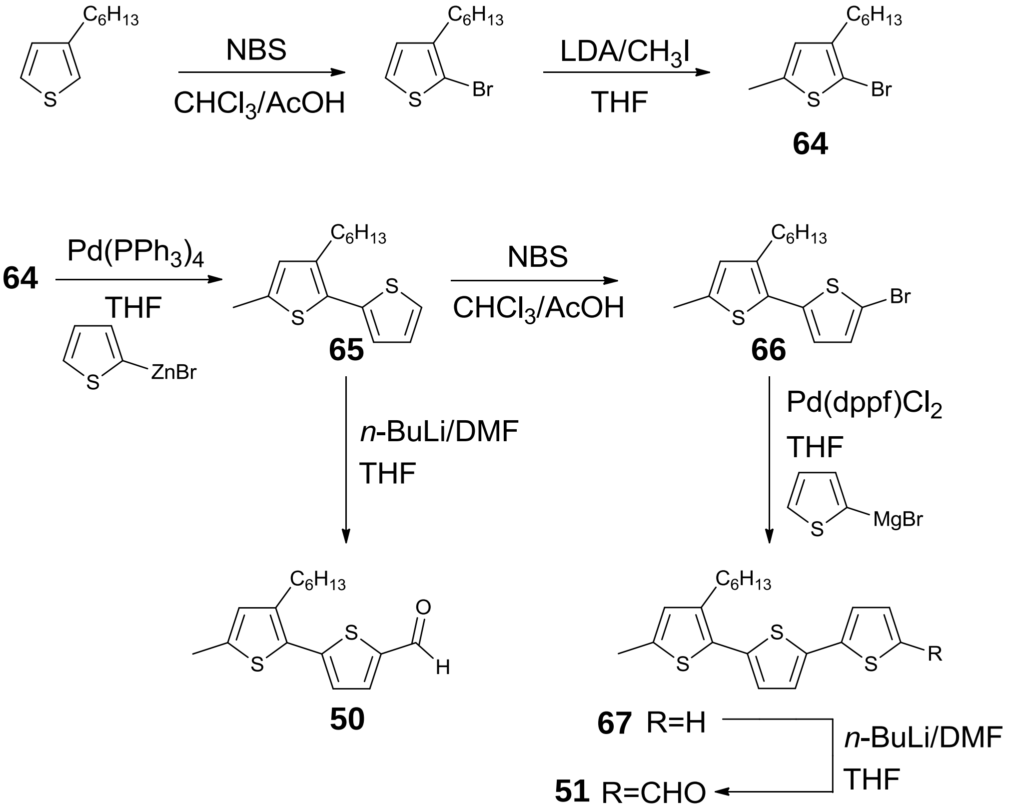

Scheme 2-4 Synthesis of bithiophene and terthiophene aldehydes **50** and **51** *via* common intermediate **65**.

Compound **50** is formed *via* carbonylation of **65** with *n*-butyllithium (*n*-BuLi)/DMF to give bithiophene aldehyde **50** in 59% yield. For the terthiophene **51**, bromination with NBS (96% yield) gives bithiophene **66**, which is subjected to Kumada coupling with thiophen-2-yl magnesium bromide to obtain terthiophene **67** in 88% yield. Carbonylation with *n*-BuLi/DMF generates the desired terthiophene aldehyde **51** in 83% yield.

2.4. Absorption Spectroscopy and Electrochemistry of Oligothiophenes 46-48

Absorption spectra were recorded in dichloromethane solution using a UNICAM UV300 instrument. CV measurements were taken on a CH Instruments 660A potentiostat with *iR* compensation and performed using glassy carbon, platinum wire and silver wire as the working, counter, and reference electrodes respectively. Substrates were dissolved in anhydrous dichloromethane solution (*ca.* 10^{-4} M) containing n-Bu_4NPF_6 as the supporting electrolyte and all solutions were degassed with argon. All measurements are referenced against the $E_{1/2}$ of the Fc/Fc^+ redox couple. Spectroelectrochemical experiments were conducted on ITO coated glass suspended in a solution of n-Bu_4NPF_6 in acetonitrile.

2.4.1. Absorption Spectroscopy

The absorption spectra of oligothiophenes **46**, **47**, and **48** (figure 2-2) demonstrate peak maxima at 345 nm, 436 nm and 467 nm respectively. These peaks correspond to the π-π* transition of the oligothiophene chains, with the red shifting of the value of the peak maxima across the series corresponding to the increase in conjugation length. The peaks at shorter wavelengths (274, 304, and 338 nm in **46**, **47**, and **48** respectively) have been attributed to the influence of the 1,3-dithiole-2-one moeity.[92] Peaks at lower wavelengths do not resolve in the UV/vis window for **46**, peaks at 258 nm in **47** and 262 nm in **48** are apparent though are more difficult to assign.

Using the onset of the π-π* absorption edge, the optical HOMO-LUMO gap for the oligomers **46**, **47**, and **48** were calculated as 3.03 eV, 2.44 eV and 2.10 eV respectively (table 2-2).

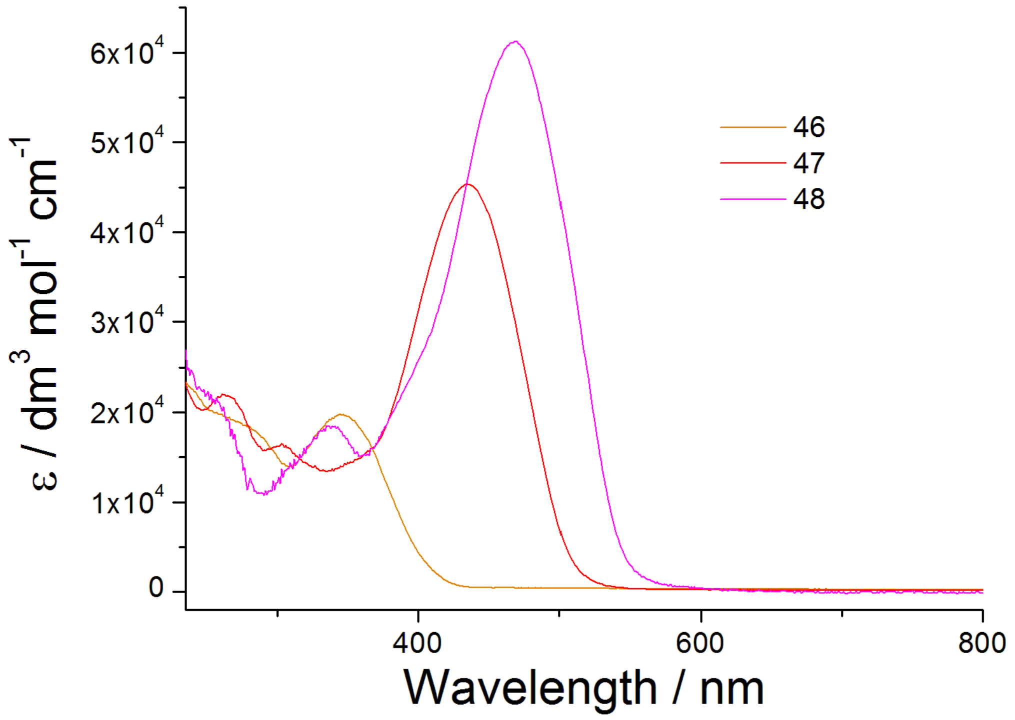

Figure 2-2 Solution state electronic absorption spectra for oligothiophenes **46-48**.

Table 2-2 Electronic absorption data for oligothiophenes **46-48**.

	λ_{max} / nm	HOMO-LUMO gap / eV
46	345	3.03
47	435	2.44
48	467	2.29

2.4.2. Electrochemistry

The electrochemistry of the oligomers was probed using cyclic voltammetry and the oxidation and reduction of the systems are shown in figure 2-3. The oxidations of both **46** and **47** show two sequential oxidation waves and that of **48** shows three. In all cases the first oxidation is reversible and attributed to the formation of a radical cation, this occurs at half-wave potentials of +0.62 V in **46**, +0.50 V in **47**, and +0.44 V in **48**, whereas the second oxidations corresponding to the formation of a dication occur at half-wave potentials of +0.94, +0.62, and +0.64 V respectively.

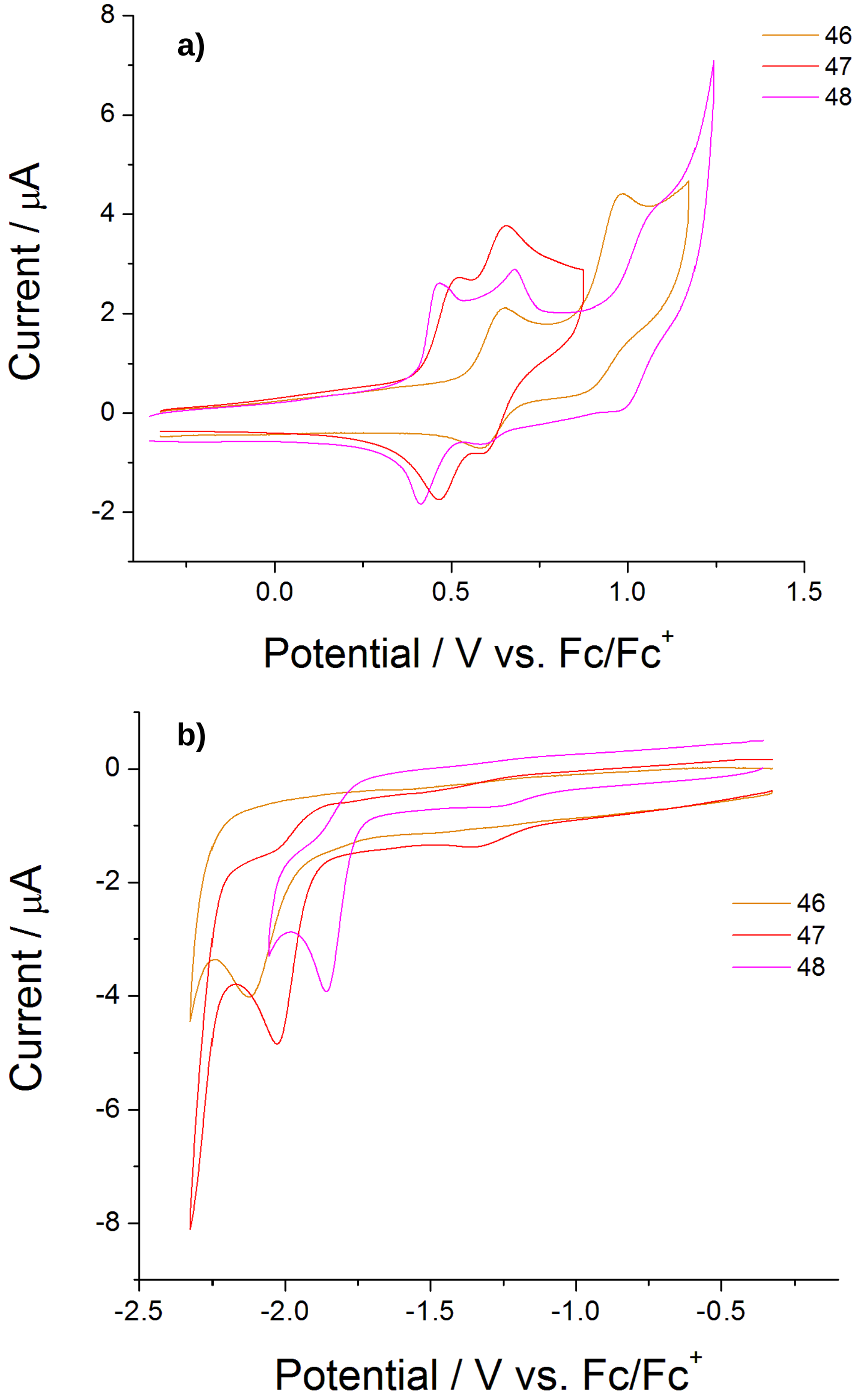

Figure 2-3 Cyclic voltammograms of **46**-**48** showing a) oxidation and b) reduction.

In the oxidation of septithiophene **48** a third oxidation wave appears at +1.02 V affording a radical trication. All of these redox processes are either reversible or quasi-reversible. This electrochemical stability can be attributed to the terminal methyl groups impeding any coupling reactions to generate polymeric species.

Compared to end-capped sexithiophenes **68** and **69** (figure 2-5) made previously in the group, extending the chain length to a septithiophene has given access to an additional redox state.

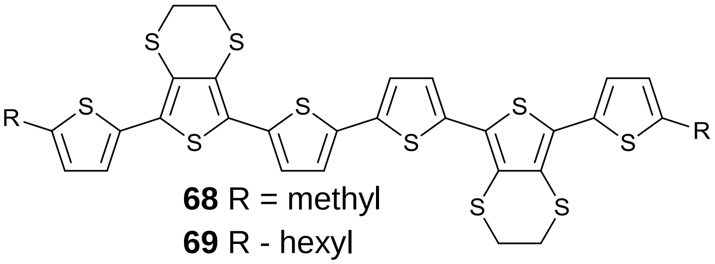

68 R = methyl
69 R - hexyl

Figure 2-4 End-capped sexithiophenes developed previously in the Skabara group.

The cyclic voltammograms for the reduction of **46**, **47**, and **48** all show a single irreversible peak at -2.12, -2.03 and -1.80 V respectively, due to the formation of radical anions in the oligothiophene chains. The small peaks at *ca.* -1.3 V are due to the presence of oxygen in the electrolytic solution.

The electrochemical HOMO-LUMO gaps of the materials were obtained from the difference in the onsets of the first oxidation and reduction peaks (figure 2-5 and table 2-3). Using data referenced to the ferrocene/ferrocenium redox couple, HOMO and LUMO energies were calculated by subtracting the onsets from the HOMO of ferrocene, which has a known value of -4.8 eV. The electrochemical HOMO-LUMO gaps of **46**, **47**, and **48** were found to be 2.50, 2.33, and 2.10 eV, respectively, with the E_g values decreasing as the conjugation length increases.

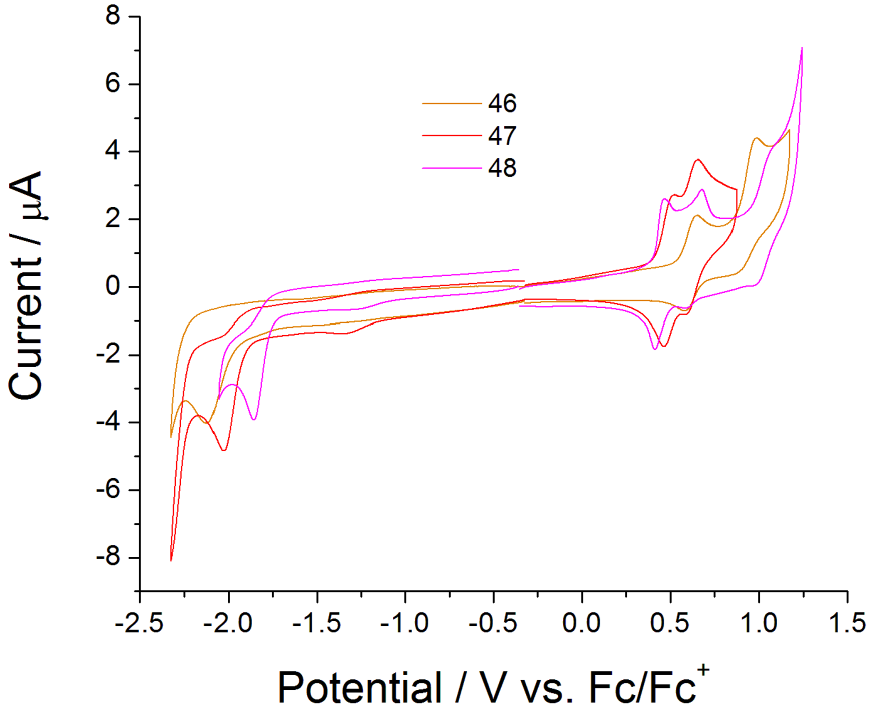

Figure 2-5 Cyclic voltammograms of **46-48** for energy level determination.

Table 2-3 Electrochemical data obtained for oligothiophenes **46-48**.

	E_{1ox} / V	E_{2ox} / V	E_{3ox} / V	E_{red} / V	HOMO / eV[a]	LUMO / eV	HOMO-LUMO gap / eV[b]
46	+0.65/+0.58	+0.99/+0.88[q]		-2.12[irr]	-5.34	-2.84	2.50
47	+0.52/+0.47	+0.66/+0.58[q]		-2.03[irr]	-5.21	-2.88	2.33
48	+0.47/+0.41	+0.68/+0.59[q]	+1.05/+0.98[q]	-1.86[irr]	-5.18	-3.08	2.10

[a] HOMO and LUMO levels are calculated from the onset of the first peak of the corresponding redox wave and are referenced to ferrocene which has a HOMO of -4.8 eV. [b] Electrochemical HOMO-LUMO gap is the energy gap between the HOMO and LUMO levels. [q] Quasi-reversible peak. [irr] Irreversible peak.

The optical HOMO-LUMO gaps are larger than the electrochemical HOMO-LUMO gaps of all the compounds, particularly **46**.

Despite being fused *via* a common sp^2-sp^2 bond, the aromaticity and extended conjugation of the oligothiophene chains will encourage electron density to remain on the oligothiophene. It is therefore reasonable to assume that the 1,3-dithiole-2-one will have little influence on the tendency of the π-π^* transition of the oligothiophene chains to dominate both the absorbance spectrum, and the optical HOMO-LUMO gap of the material. The 1,3-dithiole-2-one unit has a larger influence on the first oxidation potential, decreasing the electrochemical HOMO-LUMO gap in relation to the optical. By losing an electron the aromaticity of the 1,3-dithiole-2-one moeity increases and a radical cation is formed (similar to the effects illustrated for TTF in figure 1-10), delocalisation then allows for subsequent formation of a dication on the oligothiophene chain. Similar effects could account for the very close first and second oxidation potentials observed in **47** and **48**. On increasing the chain length to the quinquethiophene **47** and septithiophene **48** the disparity between the optical and electrochemical HOMO-LUMO gaps appears to begin to resolve.

Though synthetically demanding, the development of a nonithiophene analogue could serve to confirm the observed trends.

2.4.3. Spectroelectrochemistry

Films of **47** and **48** were dropcast onto an ITO coated glass slide from dichloromethane solution. Due to its low melting point and tendency to form oils, suitable films of **46** could not be achieved.

The absorption band of the solid state spectrum of **47** (figure 2-6) is slightly red-shifted with respect to the spectrum in solution with a peak at 448 nm which tails over several hundred nm. Upon oxidation, the material begins to dissolve into the supporting electrolyte solution, as shown by the blueshift of the main band back to 436 nm. Despite this, the beginning of the growth of a broad peak centred at 736 nm, and a peak >1100 nm can be observed once potentials above +0.9 V are reached, before complete dissolution occurs above +1.2 V. These characteristics are similar to that of end-capped sexithiophenes **68-69** studied previously within the Skabara group.[151]

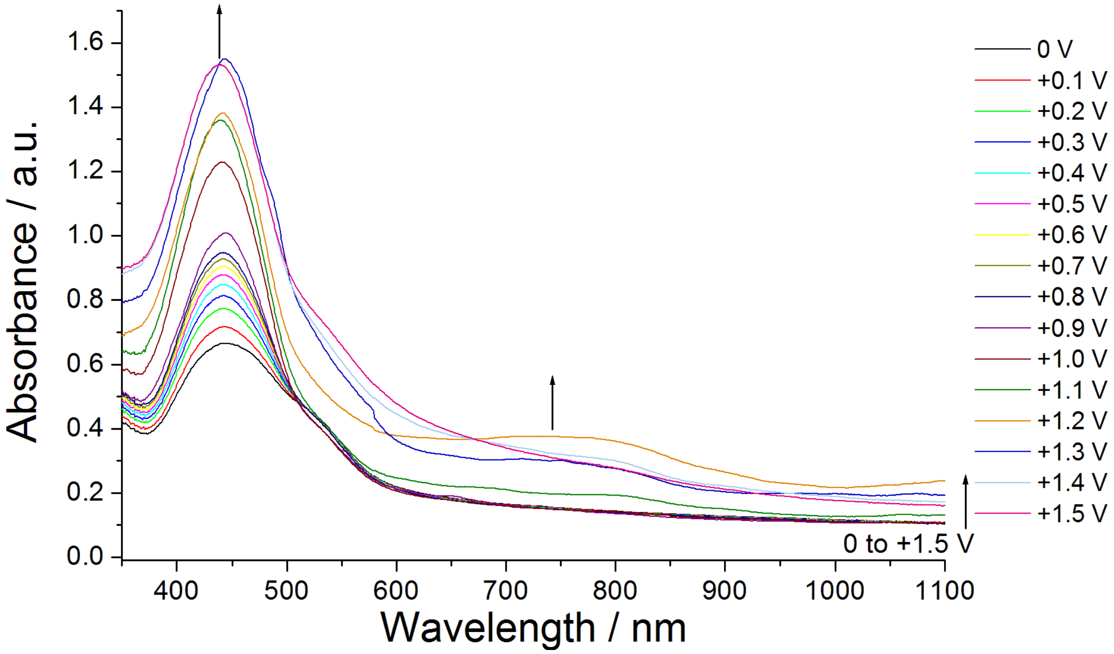

Figure 2-6 Solid state SEC of **47**. Arrows indicate band growth upon increasing potential.

The solid state spectrum of **48** (figure 2-7) is much less ambiguous thanks to the improved insolubility of its charged intermediates.

Again, the solid state spectrum of **48** displays characteristics similar to those of the materials we have studied previously. The absorption band is red-shifted compared to the solution state spectrum to a greater extent than **47**, with peaks at 495 and 561 nm, and the tail of the absorption band extends over several hundred nm. Solid state UV/vis SEC of **48** also follows similar trends. At potentials higher than +0.5 V, a broad band forms between 670 and 930 nm accompanied with a band >1100 nm. Throughout the experiment, the main π-π* band remains unchanged, but the broad band that evolves on oxidation superimposes the original band.

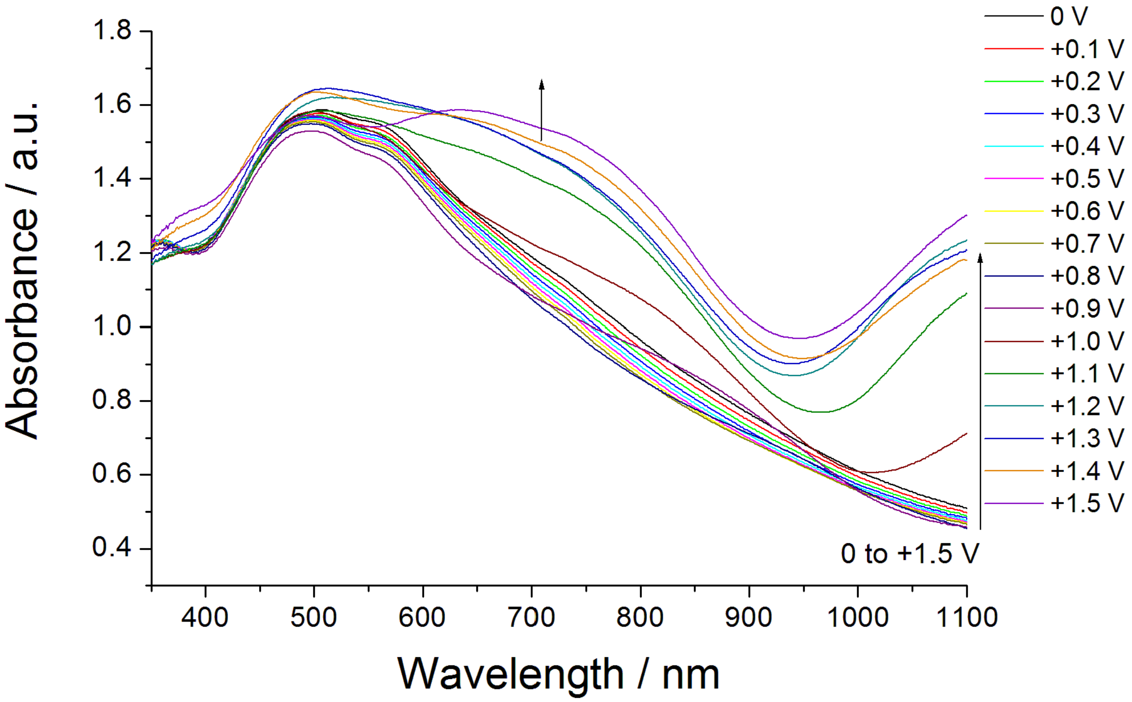

Figure 2-7 Solid state SEC of **48**. Arrows indicate band growth upon increasing potential.

2.5. X-Ray Crystallography

X-ray crystallography measurements were performed and solved by Simon Coles (University of Southampton).

Crystals of **48** were obtained from a hot CH_2Cl_2/hexane solution. The septithiophene chain adopts an all-*anti* conformation with the exception of one terminal thiophene ring (figure 2-8). The dihedral angles between the *anti*-thiophenes range from 6-19°, and the angle between the two *syn*-thiophenes is 26°. The molecule packs in a stacked herringbone pattern (figure 2-9) and within the stacks, the 1,3-dithiole ring is associated with ring-over-bond overlap with one adjacent molecule with an interplanar distance of 3.57 Å, and π-π overlap with the terminal *syn*-thiophene ring of the second adjacent molecule (interplanar distance of 3.38 Å, figure 2-10).

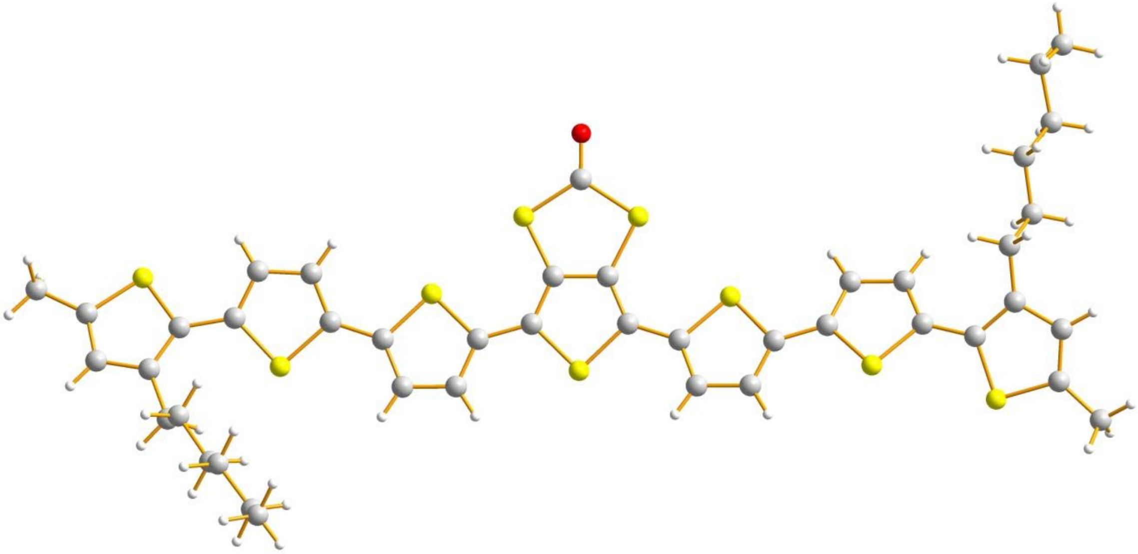

Figure 2-8 Molecular structure of compound **48**.

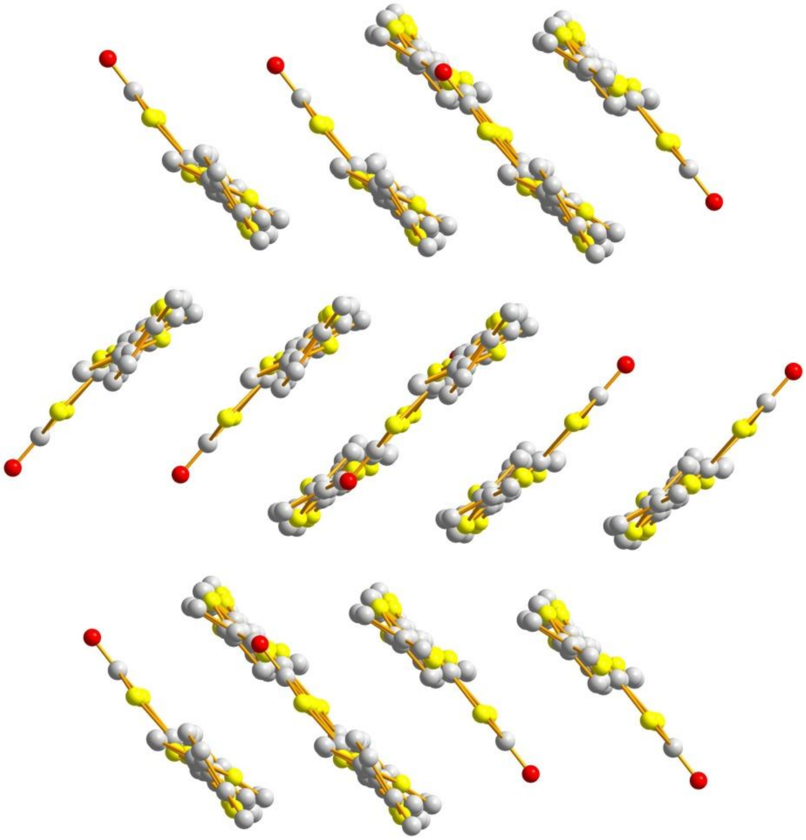

Figure 2-9 Herringbone orientation of stacks of **48**.

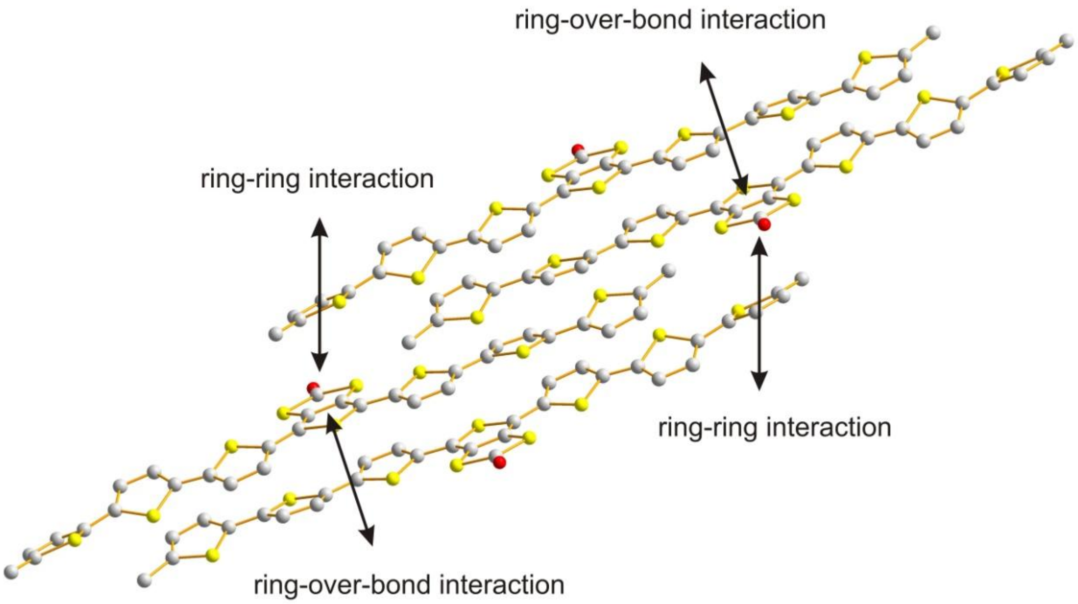

Figure 2-10 Overlap of chains within the stacks.

2.6. Conclusions and Further Work

Three new soluble 1,3-dithiole-2-one functionalised oligothiophenes with chain lengths of three, five and, seven thiophenes have been synthesised efficiently using metal catalysed cross-coupling reactions.

The molecules of this series have demonstrated discrepancies between their individual optical and electrochemical HOMO-LUMO gaps, the differences between which decrease as the chain length increases. The terthiophene and quinquethiophene systems have demonstrated two sequential oxidation processes whilst increasing the chain length to a septithiophene has given access to a third oxidation state.

The new molecules have been developed as precursors for novel high molecular weight hybrid oligothiopene/TTF and oligothiophene/metal bis(dithiolene) compounds and will also be used as model compounds for evaluation of these hybrid materials.

Chapter 3: Electronic and Redox Properties of Hybrid Tetrathiafulvalene Structures: Bis(oligothiophene)s Bridged by Fused TTFs

3.1. Abstract

Hybrid tetrathiafulvalene-oligothiophene compounds have been synthesised from oligothiophenes **46**, **47**, and **48** in which the fulvalene unit is fused between two end-capped ter-, quinque-, or septithiophene oligomers. All have been studied using cyclic voltammetry and UV/vis spectroelectrochemistry, and compared with their respective precursor. The molecules have demonstrated unique and complex oxidative behaviour.

The largest of the series, a bis(septithiophene) TTF, has also been subject to X-ray crystallography. Charge generation layer time-of-flight and OFET measurements on this molecule give maximum hole mobilities of *ca.* 1×10^{-5} $cm^2 V^{-1} s^{-1}$ and 1.5×10^{-4} $cm^2 V^{-1} s^{-1}$ respectively.

Some results described herein have already been published as:

Electronic, redox and charge transport properties of an unusual hybrid structure: a bis(septithiophene) bridged by a fused tetrathiafulvalene (TTF)

I. A. Wright, P. J. Skabara, J. C. Forgie, A. L. Kanibolotsky, B. Gonzalez, S. J. Coles, S. Gambino and I. D. W. Samuel

Journal of Materials Chemistry, 2011, **21**, 1462-1469.

3.2. Introduction

TTF derivatives have been studied as components in OFETs and there are several examples of materials with high mobilities,[77, 78] including fused TTF-thiophene hybrids such as DT-TTF as described in chapter 1.[84, 85]

In our own previous work on fused TTF-thiophene oligomers and polymers (examples of which are shown in figure 1-18), the molecules bore TTF units stemming from the poly(thiophene) chain.[91-94, 152, 153] From these studies, it has been shown that, depending on the nature of the polymer, the fulvalene unit can either dominate the electroactivity of the polymer or participate in a hybrid redox state.[92, 93]

In all these cases the TTF system was fused directly to the conjugated chain through only one of the 1,3-dithiole rings, thereby retaining the signature oxidation of the second dithiole ring as an independent redox-active moiety. Here, using the soluble oligothiophenes **46-48**, a series of new hybrid molecules featuring a TTF core fused at both ends between two methyl end-capped ter- (**70**), quinque- (**71**), or septithiophene (**72**) chains have been synthesised. TTFs **70-72** have been studied using absorption spectroscopy and voltammetric techniques. Crystallographic analysis was obtained for the largest of the series **72**, which has also been subjected to DFT analysis.

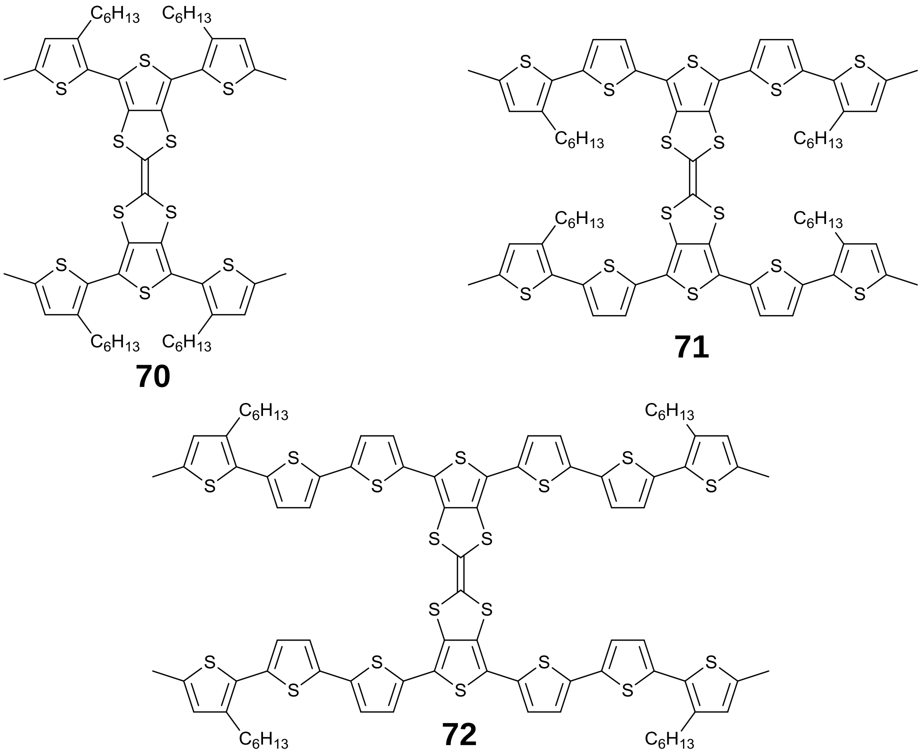

70

71

72

Figure 3-1 New hybrid TTF structures **70**, **71**, and **72**.

As mentioned previously, TTF derivatives are some of the most promising materials for charge transport applications, therefore mobility measurements have been performed on **72** using charge generation layer time of flight measurements. A similar study has been performed on half-unit **48** for comparison with TTF **72**.

3.3. Synthesis

The hybrid TTFs were made *via* homocoupling of the corresponding oligothiophene precursor in freshly distilled triethylphosphite at 125°C (scheme 3-1).

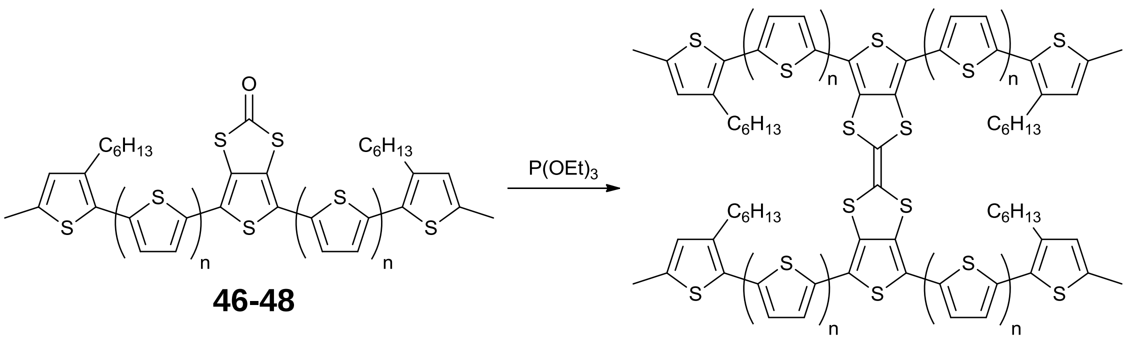

70-72

Scheme 3-1 Synthesis of TTF **70** from precursor **46** (n = 0), **71** from **47** (n = 1), and **72** from **48** (n = 2).

TTF **70** was obtained in 77% yield, **71** in 84% yield and **72** in a considerably lower 39% yield.

3.4. Absorption Spectroscopy and Electrochemistry of Hybrid TTFs 70-72

Absorption spectra were recorded in dichloromethane solution using a UNICAM UV300 instrument. CV measurements were taken on a CH Instruments 660A potentiostat with *iR* compensation and performed using glassy carbon, platinum wire and silver wire as the working, counter, and reference electrodes respectively. Substrates were dissolved in anhydrous dichloromethane solution (*ca.* 10^{-4} M) containing *n*-Bu_4NPF_6 as the supporting electrolyte and all solutions were degassed with argon. All measurements are referenced against the $E_{1/2}$ of the Fc/Fc^+ redox couple. Spectroelectrochemical experiments were conducted on ITO coated glass suspended in a solution of *n*-Bu_4NPF_6 in acetonitrile.

3.4.1. Absorption Spectroscopy

The absorption spectra for TTFs **70**, **71**, and **72** (figure 3-2) display peak maxima at 351 nm, 431 nm, and 461 nm respectively which correspond to the π-π* transition of the oligothiophene chains. The onset of the longest wavelength absorption edges gave optical HOMO-LUMO gaps of **70**, **71**, and **72** as 2.92 eV, 2.45 eV, and 2.20 eV respectively.

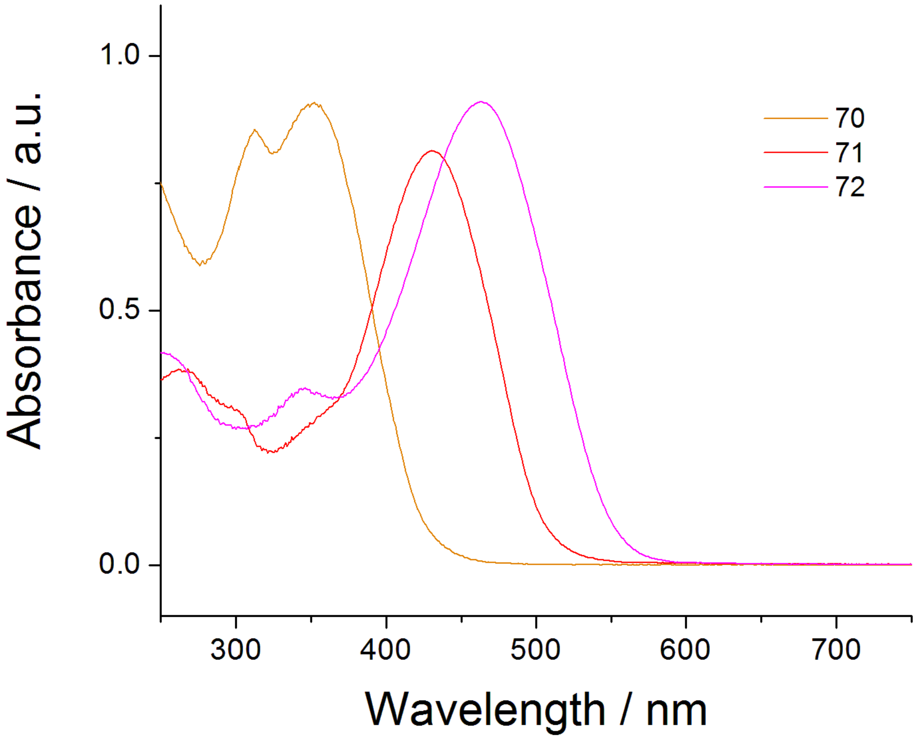

Figure 3-2 UV/vis absorption spectra for TTFs **70**-**72**.

Table 3-1 Electronic absorption data obtained for TTFs **70**-**72**.

	λ_{max} / nm	HOMO-LUMO gap / eV
70	351	2.92
71	431	2.45
72	461	2.20

The absorption maxima of the ter- and septithiophene TTFs **70** and **72** are both redshifted by 6 nm in comparison with their precursors **46** and **48**, indicating some weak interactions exist between the oligothiophene chains in these molecules when in solution. In contrast, the absorption maximum of the quinquethiophene TTF **71** is blueshifted by 5 nm compared to that of its precursor **47**. This can be explained by considering the likely disruptions of the planarity in the thiophene chains caused by the close proximity of the 3-hexyl chains on the terminal thiophenes, impinging upon any aggregation. Peaks at lower wavelength are observed and have been attributed to the influence of the TTF core.[92]

Despite these small differences, the similarity between the peak maxima of the TTF species and their respective half-unit precursors indicates that the extent of conjugation has not been changed greatly by moving from a single oligothiophene chain to the fused TTF structure. This is perhaps to be expected due to the fact that the fused TTF unit does not provide a conjugated link between the oligothiophene chains.

When compared to a series of unsubstituted swivel-cruciform bis(oligothiophene)s reported by Scherf *et al.*,[162] and featuring thiophene chain lengths identical to those discussed here, the longer chain TTFs **71** and **72** display redshifts of 5 nm and 10 nm respectively which have been attributed to the electronic effects of the alkyl and sulfur substituents. Terthiophene TTF **70** on the other hand displays a blueshift of 10 nm, which is due to the presence of the TTF core stabilising the HOMO of the molecule.

3.4.2. Electrochemistry

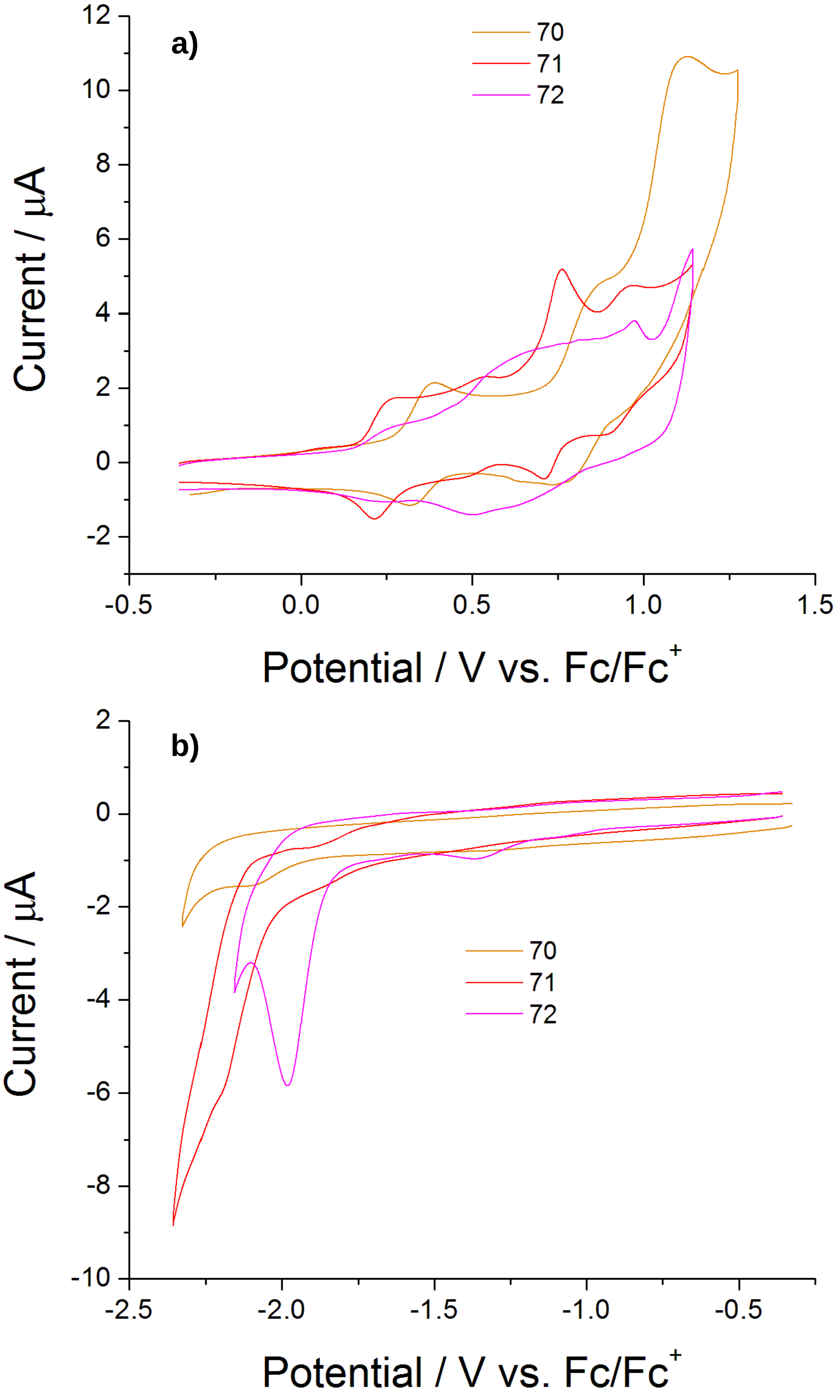

Figure 3-3 Cyclic voltammograms of **70**-**72** showing a) oxidation and b) reduction.

Cyclic voltammograms for the oxidation and reduction of TTFs **70-72** are shown in figure 3-3. In all cases, the first oxidation potentials are very low when compared to those of their respective precursors and access to multiple oxidation states has been achieved. The electrochemical results are summarised in table 3-2. The oxidative behaviours of **70** and **71** are much more well-defined than that of **72**, which demonstrates a number of redox processes occurring over a wide potential range, making peak-picking complex (the distinguishable parts of the voltammogram are noted in the table). Differential pulse voltammetry experiments carried out in an attempt to resolve the oxidations of **72** did not provide any further clarity (figure 3-4).

Table 3-2 Electrochemical results obtained for TTFs **70-72**.

	E_{1ox} / V	E_{2ox} / V	E_{3ox} / V	E_{4ox} / V	E_{red} / V	HOMO / eV[a]	LUMO / eV[a]	HOMO-LUMO gap / eV[b]
70	+0.39/ +0.32	+0.86/ +0.75	+1.13/ +1.02[q]		-2.12[irr]	-5.06	-2.92	2.14
71	+0.27/ +0.21	+0.54/ +0.48[q]	+0.76/ +0.71[q]	+0.97/ +0.89[q]	-2.19[irr]	-4.96	-2.81	2.15
72	+0.26/ +0.23	+0.66/ +0.49[q]	+0.97/ +0.94[q]		-1.98[irr]	-4.95	-3.00	1.95

[a]HOMO and LUMO levels are calculated from the onset of the first peak of the corresponding redox wave and are referenced to ferrocene which has a HOMO of -4.8 eV. [b]Electrochemical HOMO-LUMO gap is the energy gap between the HOMO and LUMO levels. [q]Quasi-reversible peak. [irr]Irreversible peak.

Terthiophene TTF **70** demonstrates two reversible oxidations at half-wave potentials of +0.36 V and +0.81 V and a third quasi-reversible oxidation at +1.08 V. The third oxidation appears to be a multi-electron process owing to the very high current response.

The quinquethiophene TTF **71** exhibits four well-defined oxidation processes, a single reversible oxidation at a half wave potential of +0.24 V followed by three quasi-reversible oxidations occurring at +0.51 V, +0.74 V, and +0.92 V.

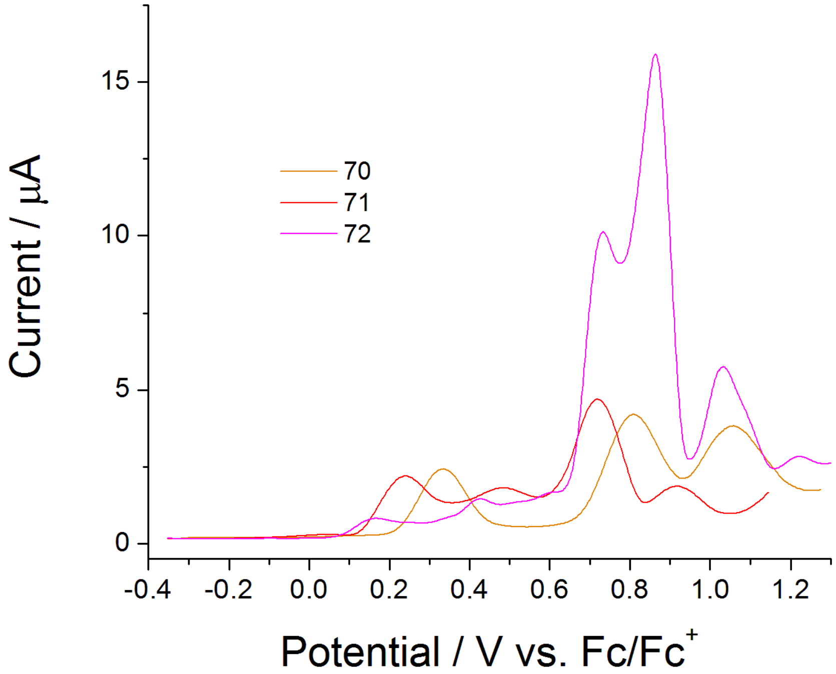

Figure 3-4 Differential pulse voltammograms for compounds **70**, **71**, and **72**.

Despite the complex electrochemical behaviour shown by **72** a number of peaks can be discerned, most notably the reversible first oxidation at +0.25 V, which is almost identical to that of **71**, and the quasi-reversible second oxidation at +0.58 V. The DPV exhibits at least six oxidation waves with a very large current response between +0.65 and +0.95 V, indicating a multi-electron process. This was not observed in the oxidative CV scan and is the result of the material being held at constant potentials throughout the DPV experiment (the stepwise nature of the waveform for DPV experiments was shown in figure 1-27). This could induce multiple oxidations of each molecule at the electrode interface (similar to bulk electrolysis), or an alternative explanation is that as the material readily aggregates, aggregates with differing conformations will have slightly different oxidation potentials, resulting in extensive overlap of the individual current response from each aggregate of molecules.

The much lower first oxidation potentials observed across the series **70-72**, when compared to their respective precursors **46-48** as well as the similarity of those results for **71** and **72**, suggests initial oxidation of the TTF unit. The proximity of the first to the second oxidation potentials, and the fact that the second oxidation potential decreases as the chain length increases tends to indicate that the second oxidation occurs over the oligothiophene chains. Assigning the subsequent oxidations is more difficult.

Within the potential window observed, it is reasonable to assume that of the four peaks observed in **71**, two have arisen from the presence of the TTF unit, and two from the oligothiophene chains. Similar conclusions can be drawn for **70** owing to the multi-electron third oxidation stated above. However, owing to the extended nature of these molecules, and the fact that we are considering excited states, it is difficult to make confident assignment of the later oxidations.

All three systems demonstrated a single irreversible reduction at -2.12 V in **70**, -2.19 V in **71**, and -1.98 V **72**. The small peaks at *ca.* -1.3 V are due to the presence of oxygen in the electrolytic solution.

The electrochemical HOMO-LUMO gaps of the materials were obtained from the difference in the onsets of the first oxidation and reduction peaks (figure 3-5 and table 3-2). The electrochemical HOMO-LUMO gaps of **70**, **71**, and **72** were 2.14, 2.15, and 1.95 eV, respectively, with E_g varying little with increasing conjugation when compared to the trend observed in the oligothiophene precursors.

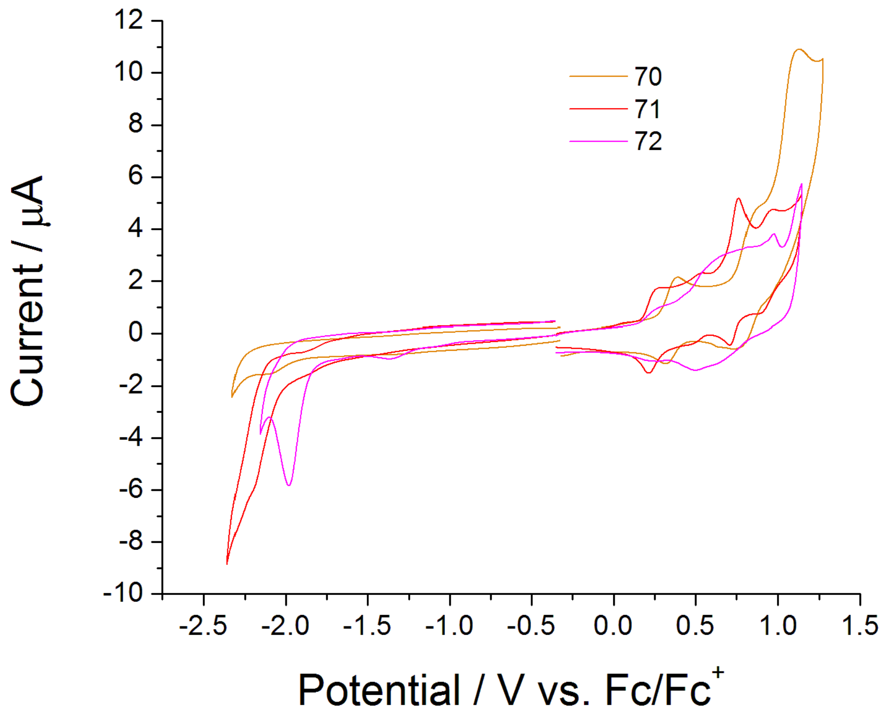

Figure 3-5 Cyclic voltammograms of **70-72** for energy level determination.

The close values of E_g observed add weight to the argument that the TTF core is responsible for the first oxidation process. As observed for **46-48**, there is a noted difference between the optical and electrochemical HOMO-LUMO gap probably due to similar reasons: the TTF dominates the electrochemical behaviour, while the more extended chromophore of the oligothiophene arms dominates the absorbance spectra.

3.4.3. Spectroelectrochemistry

Films of **71** and **72** were dropcast onto an ITO coated glass slide from dichloromethane solution. Films of **70** were obtained, but its high solubility in all solvents tested rendered SEC plots unobtainable.

The solid state absorption spectrum of **71** (figure 3-6) demonstrates an absorption maxima at 463 nm, a redshift of 25 nm compared to the precursor

47 due to the π-π*transitions of the oligothiophene chains, and a shoulder on the main peak at 507 nm. The absorption band is redshifted by 32 nm compared to the solution spectrum and tails off over several hundred nm. As the potential is increased to *ca.* +0.6 V, two bands begin to appear. One at 581 nm and another at >1100 nm, and the intensity of the π-π* band drops slightly. As the potential increases over +0.7 V the higher wavelength peak blueshifts and resolves at 1009 nm. At potentials above 1.0 V, the film dissolves into solution due to the solubility of the multi-charged states.

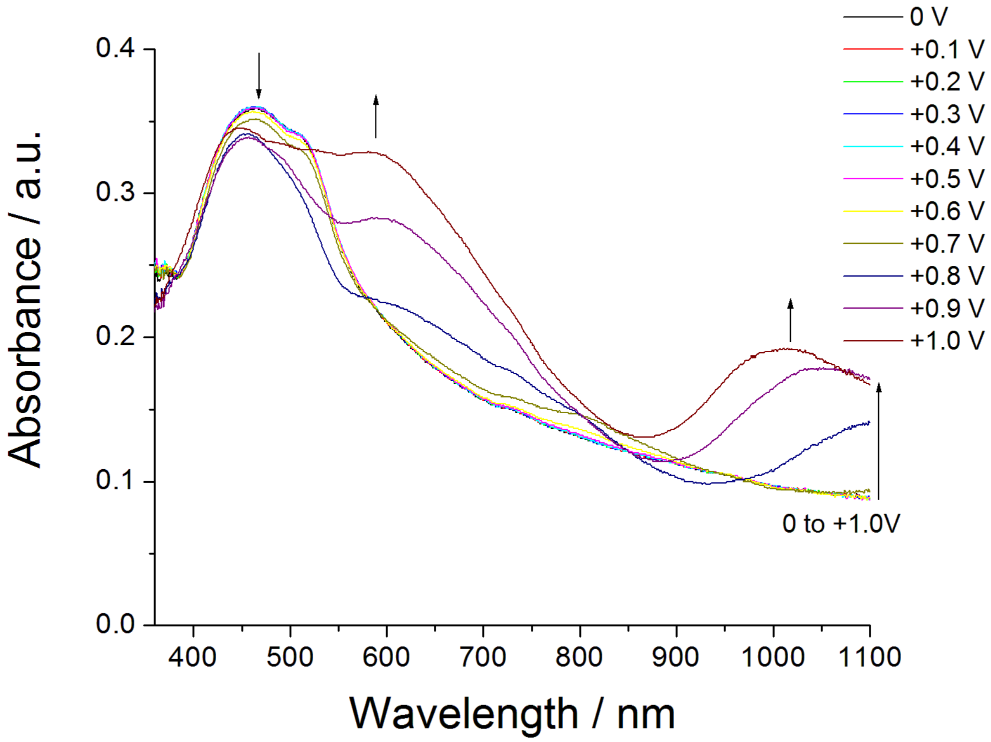

Figure 3-6 SEC plot of a thin layer of **71**.

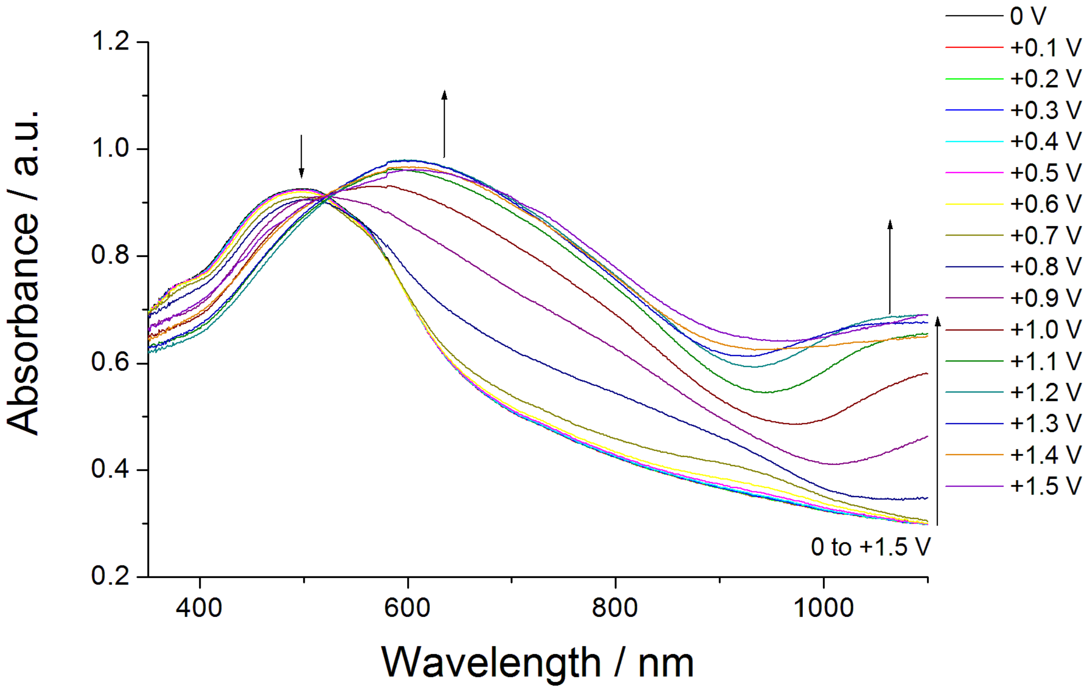

Figure 3-7 SEC plot of **72**.

The absorption spectrum for the film of compound **72** (figure 3-7) shows a peak at 496 nm, a bathochromic shift of 29 nm compared to the solution state spectrum. Upon oxidation, a small band appears at 933 nm at *ca.* +0.3 V. This peak is typical for the oxidation of a TTF species to the radical cation and can be assigned to intermolecular charge transfer between TTF radical cation dimers.[92] Interestingly, this was not observed in **71**. The peak is quickly lost upon further oxidation and is eclipsed by a band with a peak maximum at 597 nm and a second band at >1100 nm. The trough which was observed for compound **48** is not evident in **72** due to the signature of the oxidised TTF over this region. Furthermore the π-π* band for the neutral compound diminished upon oxidation, and there is a clear isosbestic point at 521 nm. The film dissolves into solution at higher potentials.

These results, in combination with the CV data, indicate that the site of the first oxidation in these hybrid TTF-oligothiophene molecules involves the TTF unit.

Electron Paramagnetic Resonance (EPR) experiments were carried out by Andrey Moiseev of the University of McGill.

Although the solution and solid state absorption spectra did not show any signs of doping, EPR spectra were obtained for compound **72** and its precursor **48** to investigate the presence of radicals. Peaks were obtained at g = 2.0046 for **72** and 2.0050 for **48**, indicating that the materials carry residual radical cations. In comparison to these values, thiophene radicals have g values of 2.002-2.003, whilst for TTF radical cations $g \approx 2.008$.[163] Previous work on hybrid TTF-poly(thiophene) materials, in which the electroactivity is concentrated solely within the TTF units, gave $g = 2.0078$,[92] and values of around 2.005 for structures in which the radical cation is delocalised over the thiophene-dithiol units.[93] The results obtained for both **72** and **48** are commensurate with hybrid electroactivity.

3.5. X-Ray Crystallography

X-ray crystallography measurements were performed and solved by Simon Coles (University of Southampton).

Crystals of the septithiophene TTF derivative **72** were grown by slow evaporation from a 3:1 chloroform-carbon disulfide solution and isolated as a 1:1 carbon disulfide solvate. The molecular structure of **72** is shown in figure 3-8. The asymmetric unit is defined by the ring systems labelled A-H and the molecule has an inversion centre around the central double bond of the TTF moiety. The dithienoTTF fragment is essentially planar, though significant twisting is observed at one end of the septithiophene chain, with a dihedral angle of 33° between rings A and B which adopt a *syn* conformation and is due to packing forces between molecules. Conjugation is weakest in this portion of the molecule and the dihedral angles between ring B-C and C-D are 11° and 16° respectively. In contrast, the dihedral angles between thiophenes D-G are in the range 4-10°. Though twisting out of plane was not observed in the crystal structure of the septithiophene precursor **48**, once more it was observed that a terminal thiophene of the septithiophene chain adopts a *syn* conformation. The sexithiophene fragment represented by B-G adopts an *anti* conformation. The stacked packing structure of **72** is shown in figure 3-9 and the overlap between chains within each stack, identifying the closest interactions, is depicted in figure 3-10. The angle between the two planes of rings D and F is 5.79(12)° and the distance between these planes is 3.738(2) Å. The angle between the planes of thiophenes C and G (18.36(21)°) is larger, but the two sulfur atoms of the corresponding rings show a weak non-covalent interaction with a S•••S distance of 3.811(1) Å. Given the extent of the twist between A and B, these rings do not participate in the stacking mode of compound **72**.

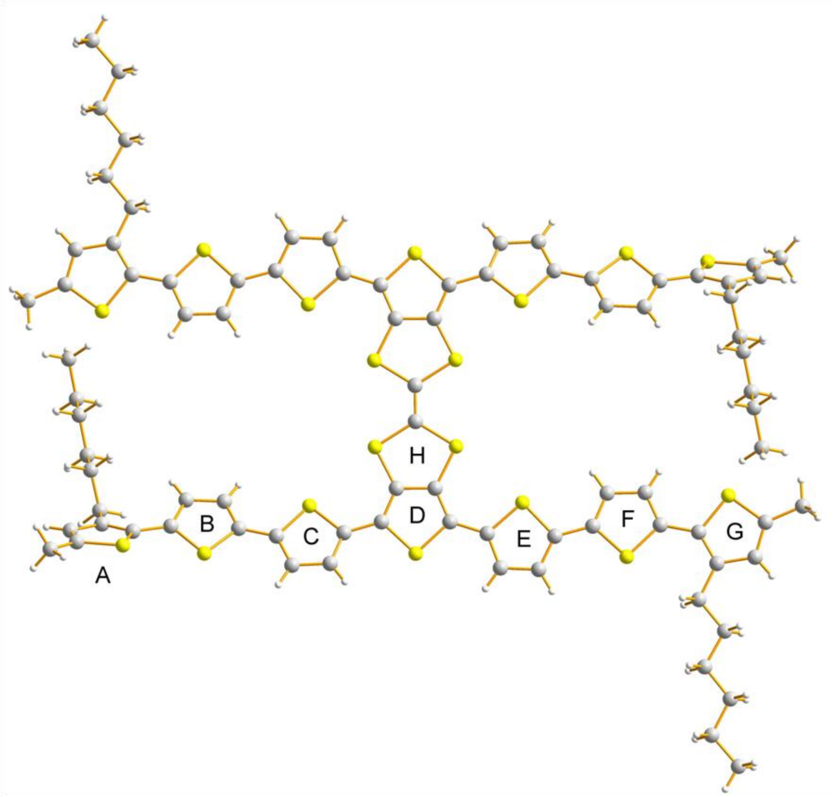

Figure 3-8 Molecular structure of crystalline **72**. The asymmetric unit is defined by the ring systems labelled A-H.

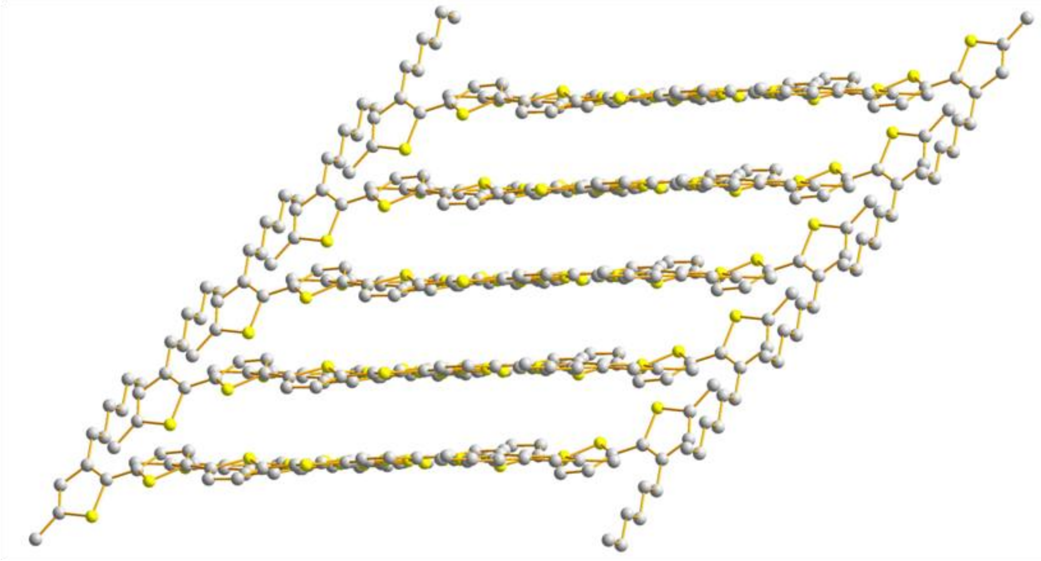

Figure 3-9 Stacked structure observed in crystals of **72**.

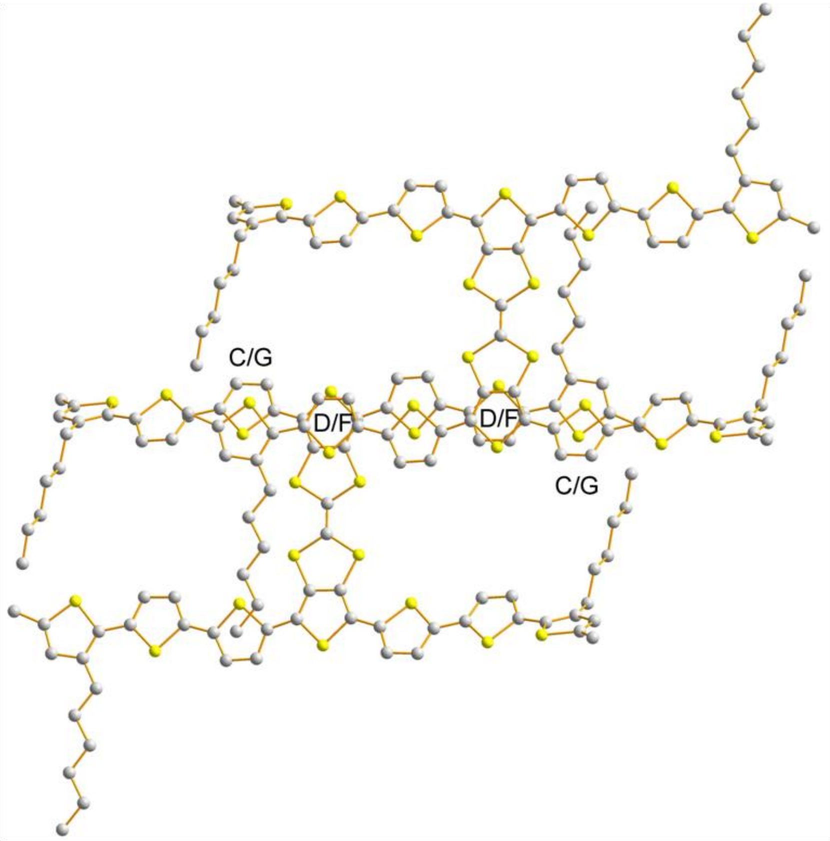

Figure 3-10 Stacking mode of molecules **72**.

Attempts have been made to generate a charge transfer salt of donor **72** with the acceptor PCBM *via* electrocrystallisation, though no crystals were formed.

3.6. DFT Calculations

Density functional theory (DFT) has been applied to **72** in order to gain a stronger understanding of the electronic energy levels within the compound. DFT calculations were performed by Peter Skabara with Spartan 08, using the B3LYP hybrid functional with a 6-31G* basis set.

Initially, a single point energy calculation was performed on the structure obtained by X-ray analysis, with the hexyl groups replaced by methyl groups. Secondly, the terminal bithiophene units that exist in the *syn* conformation were twisted to an *anti* conformation and this structure was allowed to relax to a local minimum.

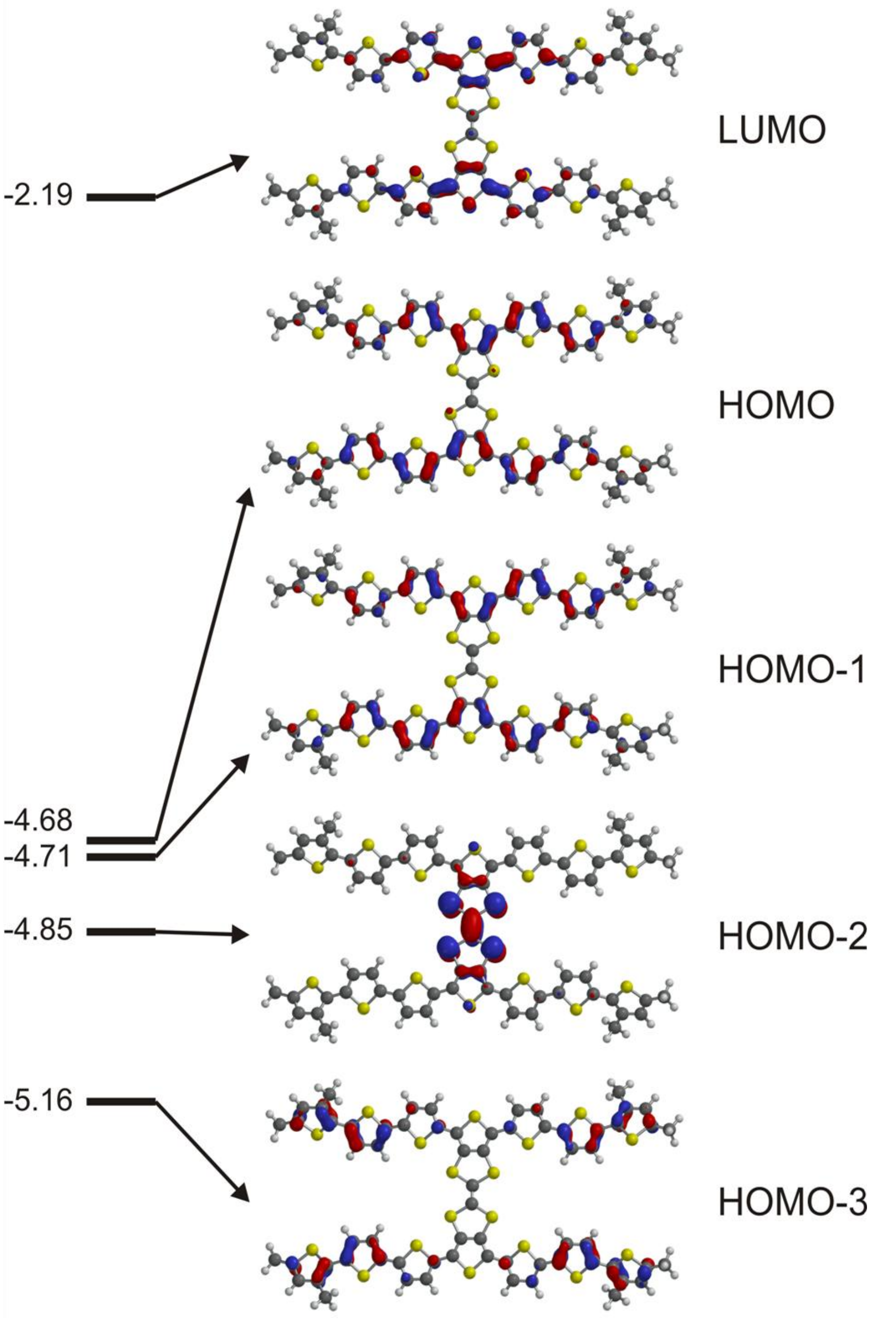

Figure 3-11 Results of DFT calculations.

The calculated HOMO-LUMO gap for the all-*anti* conformer (2.49 eV) was found to be closer to the experimental HOMO-LUMO gap (see table 3-2) than the structure obtained from crystallography (2.70 eV). Also, the all-*anti* conformer was lower in energy, showing that this is the preferred geometry in the gas phase. The orbitals of **72** as the all-*anti* conformer are shown in figure 3-11 and show the HOMO to be derived from the oligothiophene chain. The TTF was shown to be involved with the HOMO-2 orbital, but this energy level is only 0.17 eV lower than the HOMO. Though this seems to contradict some of the observations made from the electrochemical studies, it is feasible that the first oxidation state of this material involves both components of the molecule acting in a truly hybrid fashion.

3.7. Time-of-flight Measurements

Time-of-flight measurements were carried out and interpreted by Salvatore Gambino in the group of Ifor Samuel at the University of St Andrews.

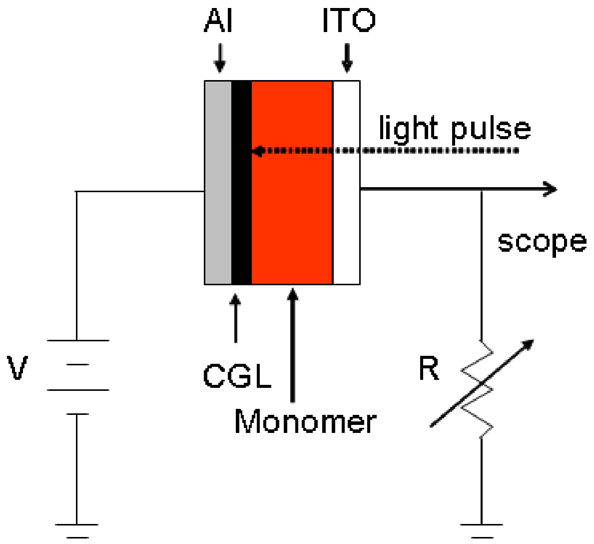

Figure 3-12 Schematic of CGL-TOF experimental setup.

Charge generation layer time-of-flight (CGL-TOF) measurements are made by depositing a layer of the analyte onto a transparent conductor, such as an ITO coated glass slide, followed by a charge generation layer and finally a metal electrode. The charge generation layer is an absorptive dye which can be excited with a laser pulse to generate charge carriers. In the studies presented here, holes are the charge carriers being studied. The aluminium electrode was biased positively and the photocurrent signal was detected from the ITO. The applied bias led to the electrons photogenerated in the dye layer being removed from the device at the aluminium electrode and the holes being injected into the oligothiophene layer and swept across the device to be collected at the ITO electrode (figure 3-12).

Hole mobilities, μ, were deduced from the transit times, t_{tr} *via* the relationship:

$$\mu = \frac{d^2}{V t_{\mathrm{tr}}} \tag{25}$$

Where d is the film thickness and V the applied voltage.

CGL-TOF measurements were carried out on compounds **48** and **72**. For these measurements, solutions of the two compounds were made at concentrations of about 40 mg ml^{-1} in a 1:1 chlorobenzene-carbon disulfide solution. The use of carbon disulfide has been necessary to overcome the problems associated with the highly aggregating nature of these sulfur rich species, particularly **72**. Films were spin-coated onto an ITO substrate at speeds of 1000 rpm to obtain films around 200-230 nm thick. The samples were then transferred to an evaporator where, under high vacuum, a 10 nm layer of the absorptive dye (Squaraine) followed by 100 nm of aluminium, were deposited through a shadow mask to define the active area of approximately 6 mm^2.

Figure 3-13 shows the hole photocurrent transient on linear and log-log scales for a film of compound **72**, at room temperature and an applied electric field $E = 2.5 \times 10^5$ V cm^{-1}. The absence of a clear plateau in the photocurrent transient on the linear scale indicates highly dispersive charge transport behaviour. In order to estimate the transit time (t_{tr}), a log-log plot was necessary, which allowed measurement of the transit time from the change of slope at the photocurrent transient, t_{tr} = 18 μs. The transit time corresponds to a mobility 4.4×10^{-6} cm^2 V^{-1} s^{-1}.

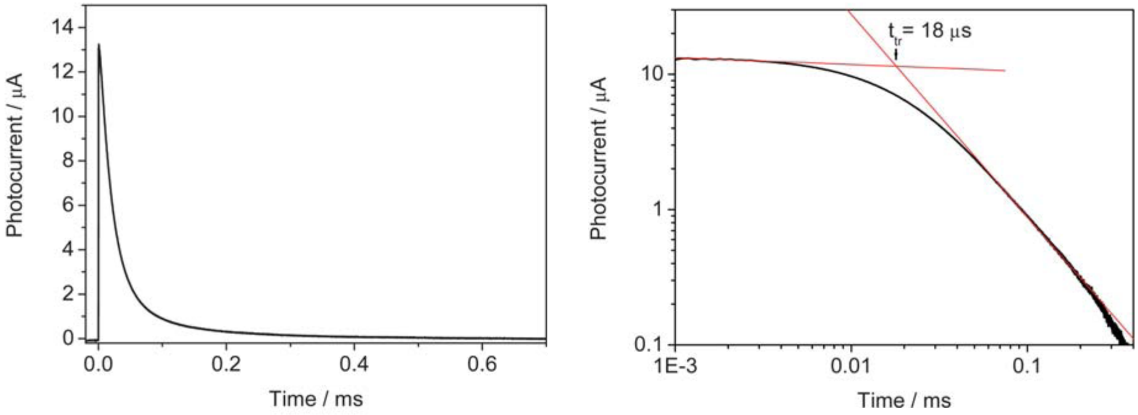

Figure 3-13 TOF results for bis(septithiophene)-TTF **72**. Linear scale plot is shown on the left, log-log scale plot is shown on the right.

For direct comparison, CGL-TOF measurements were performed on compound **48** under the same conditions, such as temperature and electric field. Figure 3-14 shows the hole photocurrent transient on linear and log-log scales for a film of compound **48**. Again, the absence of a clear plateau in the photocurrent transient on a linear scale indicates dispersive charge transport behaviour and a log-log plot was used to estimate the transit time, t_{tr} = 62 μs. The transit time corresponds to a mobility of 1.4×10^{-6} cm^2 V^{-1} s^{-1}.

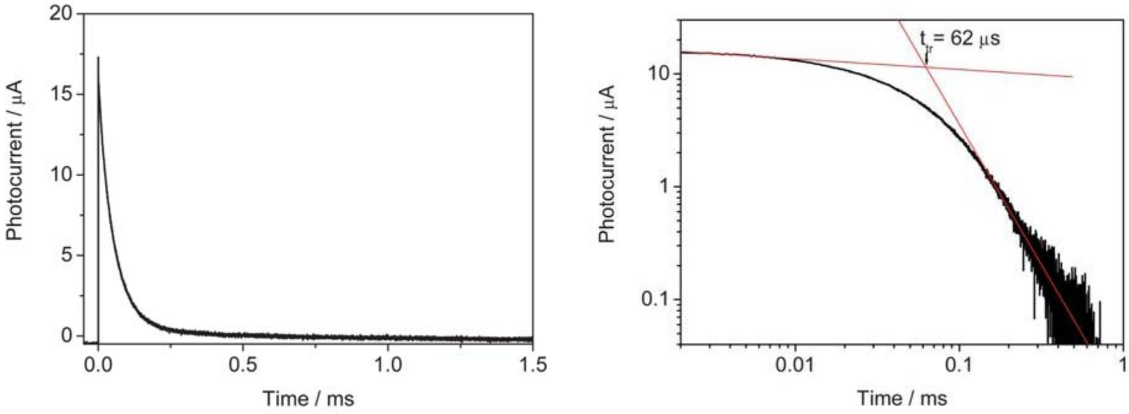

Figure 3-14 TOF results for septithiophene TTF precursor **48**. Linear scale plot is shown on the left, log-log scale plot is shown on the right.

TTF **72** shows hole mobility values three times higher than compound **48** under the same electric field. This is consistent with improved molecular orbital overlap between the larger TTF-oligothiophene molecules.

In the literature, much attention has focussed on improving the mobility of OFETs based on TTF devices, such as the studies on DT-TTF described in chapter 1.[77] In OFETs, charge transport occurs in the direction parallel to the substrate. Less attention has been placed on measuring charge-transport in the direction perpendicular to the substrate. Solar cells and organic memory devices based upon TTF-based materials have already been reported,[93, 164] and devices of this sort require efficient charge transport in the perpendicular direction.

The measurements quoted above give the hole mobility in the direction perpendicular to the substrate, and the dependence of the mobility on the electric field has also been subject to investigation (figure 3-15). As the electric field is increased from 2.5×10^5 to 7.4×10^5 V cm^{-1}, the hole mobility increases from 1.4×10^{-6} to 1.3×10^{-5} cm^2 V^{-1} s^{-1} for **48**. For **72**, as the electric field is increased from 1×10^5 to 4×10^5 V cm^{-1}, the hole mobility increases from 1.4 × 10^{-6} to 1.1 × 10^{-5} $cm^2 V^{-1} s^{-1}$. Figure 3-15 shows that both materials exhibit similar electric field dependence.

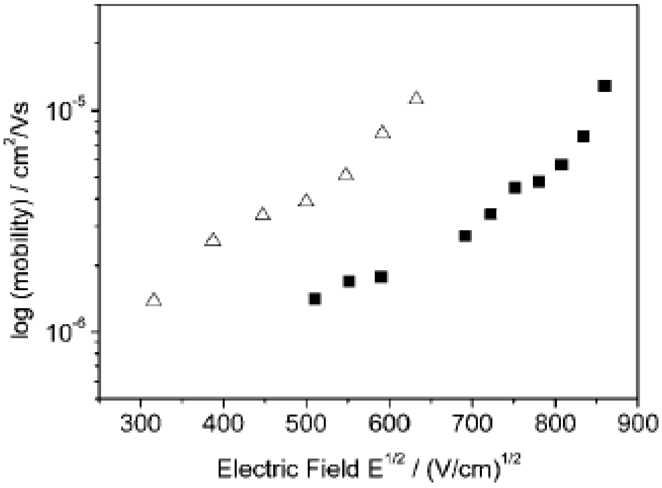

Figure 3-15 Electric field dependancies on the hole mobilities of **72** (triangles) and **48** (squares).

It is clear that the mobility values are several orders of magnitude less when charge transport is measured in the direction perpendicular to the substrate instead of parallel to the plane. It is difficult to compare charge transport properties between the two methods, because these compounds clearly differ in size and complexity from the ones previously reported for FET mobility measurements. Furthermore, as has been reported for poly(3-hexylthiophene), TOF mobility values can be orders of magnitude lower than FET mobilities.[165-167]

The mobility values shown here are consistent with others reported using TOF and related techniques on a related family of thiophene based conjugated materials.[168-170] The CGL-TOF results have shown that it is possible to tune the HOMO-LUMO levels of materials without inhibiting the charge transport properties of the thiophene oligomers.

3.8. OFET Measurements

OFET devices based on compounds **48**, and **72** have been fabricated and characterised in the lab of Dmitrii Perepichka at McGill University.

Preliminary results are shown in figure 3-16 for compound **48** and in figure 3-17 for compound **72**.

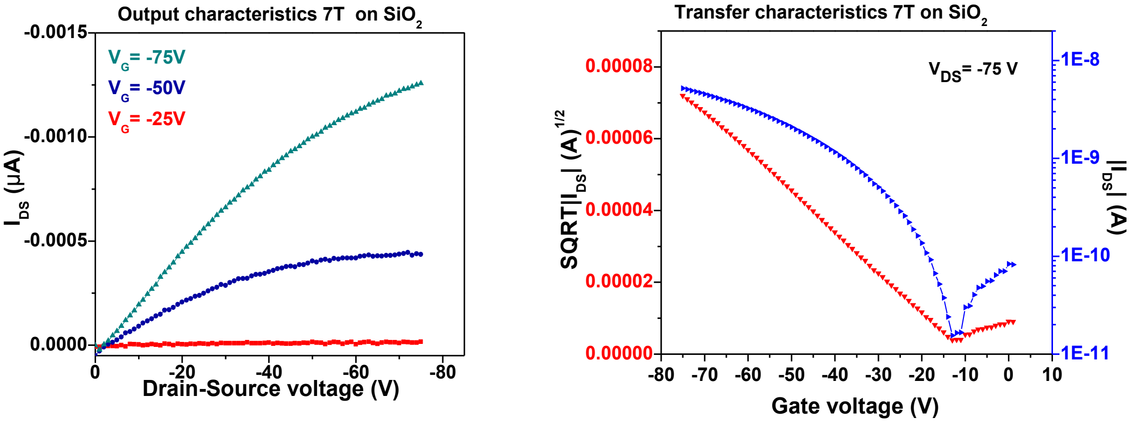

Figure 3-16 OFET results for septithiophene **48**.

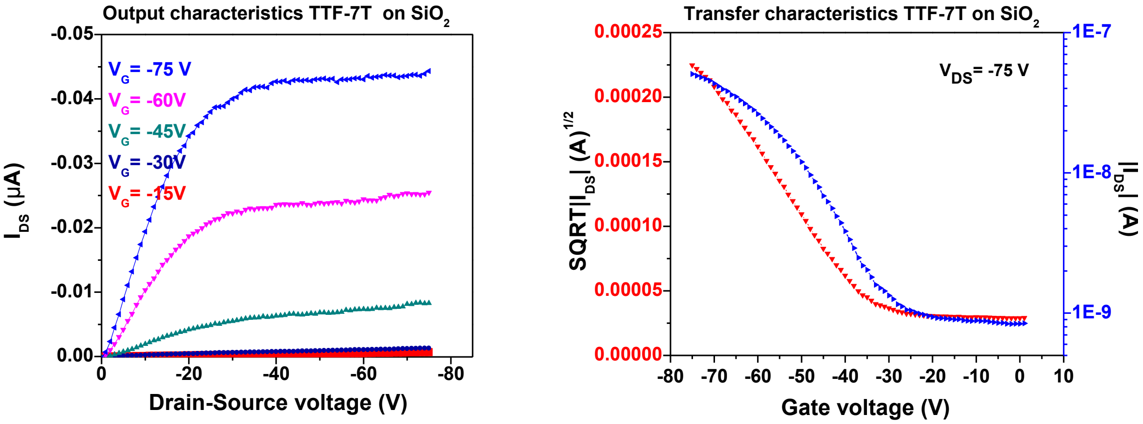

Figure 3-17 OFET results for bis(septithiophene) precursor **72**.

From these results, the mobility of the septithiophene half-unit **48** has been calculated as 2.5×10^{-5} cm^2 V^{-1} s^{-1} and that of TTF **72** as 1.5×10^{-4} cm^2 V^{-1} s^{-1}.

Whilst still low, the OFET mobilities for **48** and **72** are increased with respect to their CGL-TOF results, confirming that charge-transport is more efficient in the direction parallel to the substrate

3.9. Conclusions and Further Work

Three new hybrid TTF-thiophene materials **70**, **71**, and **72** have been synthesised and their electrochemical and electronic properties have been investigated and compared to their corresponding half-unit precursors **46**, **47**, and **48**. A close association of the TTF unit and the oligothiophene chain has been observed leading to hybrid electroactivity and complex redox behaviour.

The presence of the TTF unit in compounds **70**, **71**, and **72** affords access to additional redox states and multi-electron processes, and appears to be responsible for at least the first oxidation in these molecules.

The charge transport properties of compound **72** and its precursor **48** have been investigated and compared using CGL-TOF measurements. The charge transport properties do not differ greatly, but the HOMO energy level of the TTF compound is closer to vacuum than the dithiole derivative as the former is a stronger electron donor. Results of CGL-TOF experiments showed that compound **72** has a mobility three times higher than compound **48** (at a field of 2.5×10^5 V cm^{-1}) due to improved molecular orbital overlap. Early results from OFETs fabricated using these molecules have demonstrated higher mobilities.

Further work imaging the structure of the active layer using scanning tunnelling microscopy is underway in order to improve the understanding of carrier flow in these systems.

Collaboration within the group has begun towards the development of asymmetrically substituted TTFs, featuring an end-capped oligothiophene fused to one side of the TTF unit, and a non-capped terthiophene chain (see structure **73**) or 2,5-dibromothiophene (see structure **74**) fused to the other (examples are shown in figure 3-18). These molecules could allow access to uniquely arranged polymeric structures (for example **75**) featuring extensive overlap between the longer oligothiophene chains.

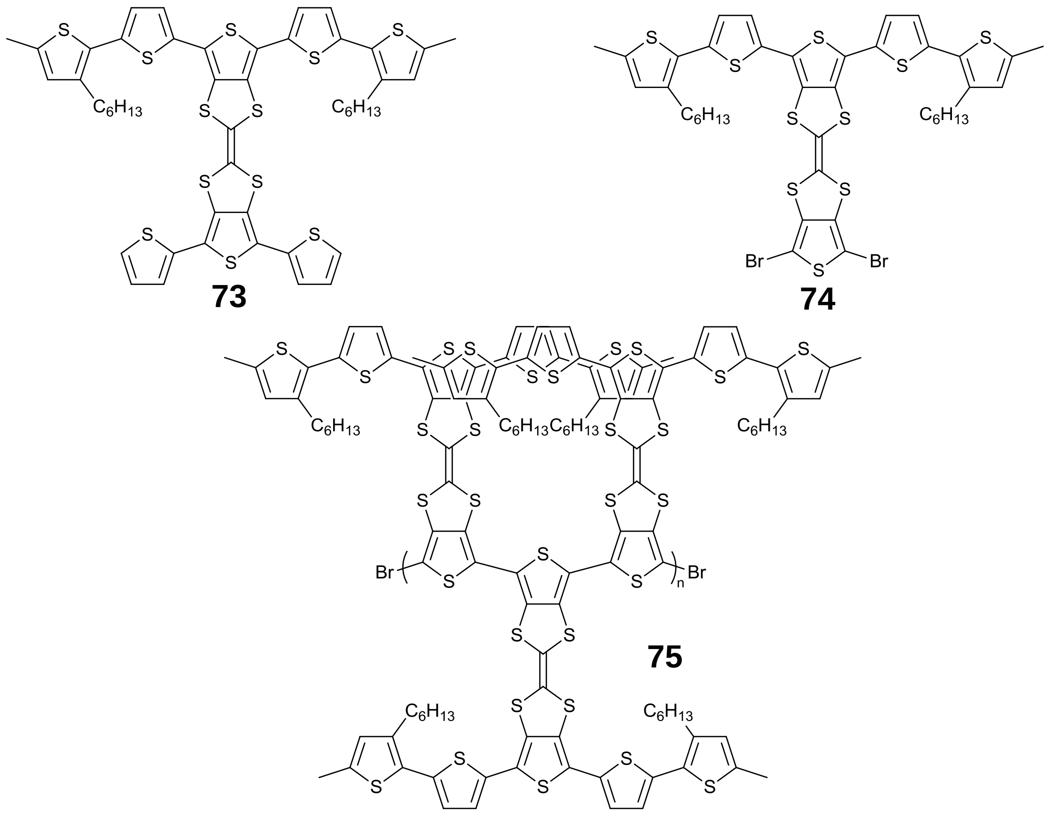

73

74

75

Figure 3-18 Structures **73** and **74**; currently in development towards the synthesis of overlapping polymers such as **75**.

Stemming from work on oligofluorene substituted truxene molecules that have given rise to very efficient lasing materials,[171-174] investigations have begun on the synthesis of the oligofluorene-dithienoTTF **76** (figure 3-19).

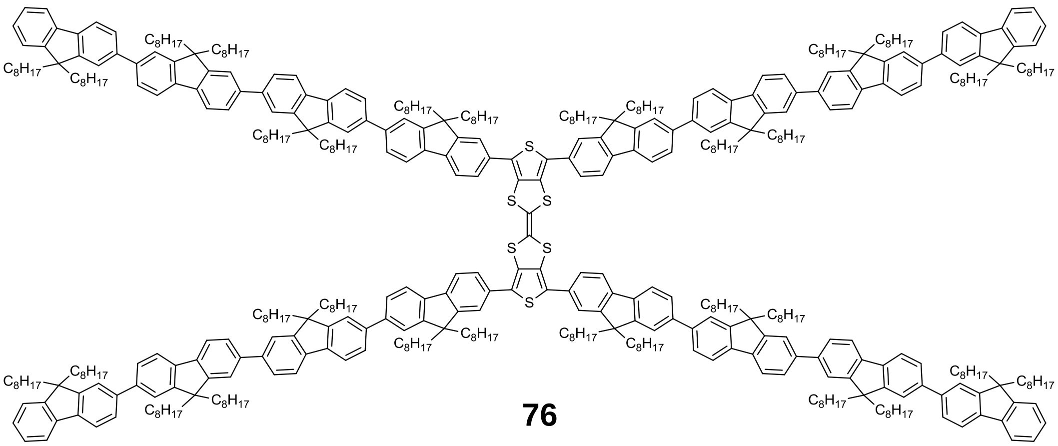

76

Figure 3-19 Oligofluorene-dithienoTTF structure **76**, currently in development.

Early investigations on Negishi coupling of two equivalents of quaterfluorene **77** (bearing solubilising octyl chains) with 4,6-dibromo[3,4-*d*][1,3]dithiol-2-one **78** under microwave irradiation to generate the TTF precursor **79** (scheme 3-2) have so far proved unsuccessful.

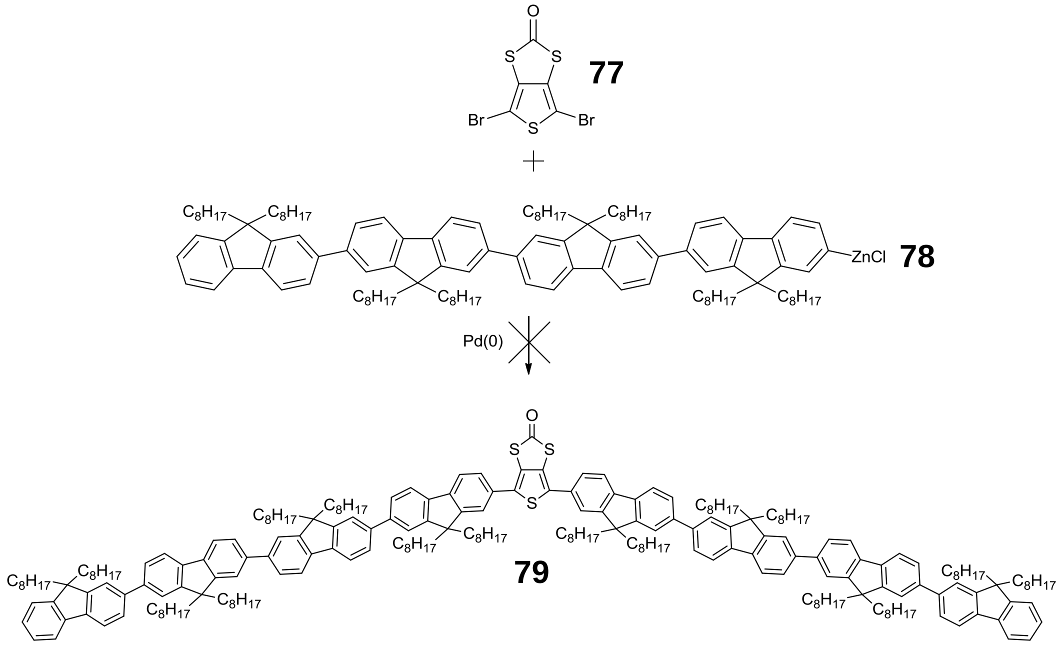

Scheme 3-2 First attempt towards the synthesis of TTF precursor **79**.

Chapter 4:Highly Redox Active Homoleptic Nickel (II/III) and Gold (III) Bis(dithiolene) Complexes Featuring End-Capped Oligothiophene Ligands

4.1. Abstract

Using methyl end-capped oligothiophenes **46-48** as ligands, two new series of highly soluble, extensively conjugated, metal bis(dithiolene) complexes featuring nickel and gold centres have been synthesised. The electrochemical properties of these complexes and the effects of the incremental increase in the ligand chain length have been studied using cyclic voltammetry and UV/vis spectroelectrochemistry.

All the complexes have displayed hybrid redox activity involving both the non-innocent dithiolene centre, and the conjugated ligand. The Ni complexes have demonstrated very low first oxidation potentials and very intense colouration, with molar extinction coefficients exceeding 100,000 dm^3 mol^{-1} cm^{-1}, and films of the Au complexes have demonstrated dramatic changes in their absorption behaviour upon oxidation.

4.2. Introduction

Metal dithiolene complexes have a long and rich history of useful materials properties, notably the metallic and superconductivity observed in their charge transfer salts.[57, 70, 73, 74] Applications for dithiolene complexes include ambipolar OFETs,[102] NIR dyes for lasers[175, 176] and liquid crystal devices,[99] and conductive metal-organic frameworks of dithiolene complexes were reported recently.[177]

Studies of thiophene rich dithiolene ligands were stimulated by the inaugural work on electropolymerisable thiophene bearing dithiolene complexes (figure 1-20) by Kean and Pickup,[108, 109] and the studies by Belo, Almeida and others on thiophene-dithiolene (TD) ligands.[113-115, 178]

Electropolymerisable dithiolene complexes have been used to generate polymers that demonstrated interesting electrochemical and optical properties,[67] however electropolymerisation is not a suitable process for preparation of bulk quantities of material. Furthermore, the robustness of metal dithiolene centres to more conventional polymerisation techniques is questionable and remains largely unexplored.[67]

Au complexes of TD ligands have given rise to a number of interesting species, notably an example of a single component molecular metal.[113]

Another intriguing aspect of TD ligands is the possibility of extending the conjugation of the ligand by the use of aromatic substituents in place of the protons on the ligating thiophene Using thiophenes as the substituents gives rise to hybrid oligothiophene-dithiolene molecules featuring direct fusion of the dithiolene centre to either the terminus or backbone of the oligothiophene chain(s).[97, 98, 179]

Previous work in the Skabara group on dithiolene complexes (using a number of metals, figure 1-22) has included extended TD ligands, featuring the S donor atoms stemming from the 3- and 4-positions of the central thiophene of a methyl-capped or non-capped (and therefore polymerisable) terthiophene chain (complexes **40** and **39a-d** in figure 1-22, respectively).[97, 98]

An electropolymerised film of poly(**39**) demonstrated very broad absorption (figure 1-24) indicating potential for light harvesting in OSC devices. This work indicates the potential benefits of incorporating both a dithiolene centre and extended conjugation into a single entity.

Here, the development of two new families of metal bis(dithiolene) complexes using oligothiophenes **46-48** is described. The complexes are homoleptic and feature either nickel (**80-82**) or gold (**83-85**) metal centres bound between methyl end-capped terthiophene, quinquethiophene or septithiophene chains bearing solubilising hexyl groups (figure 4-1).

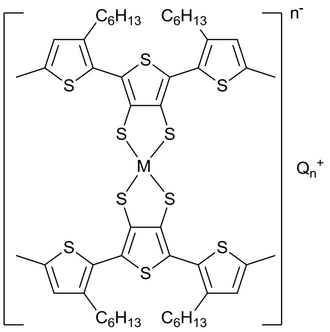

80 and **83**

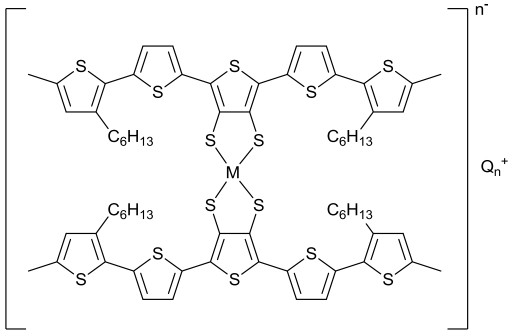

81 and **84**

	M	Q	n
80	Ni(III)	Et_4N	1
81	Ni(II)	Et_4N	2
82	Ni(II)	Et_4N	2
83	Au(III)	Bu_4N	1
84	Au(III)	Bu_4N	1
85	Au(III)	Et_4N	1

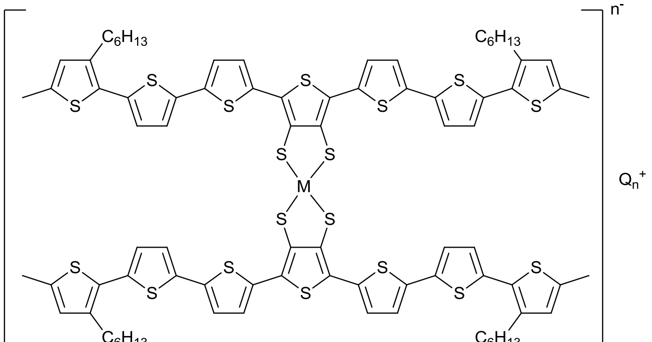

82 and **85**

Figure 4-1 Structures of the new Ni dithiolene complexes **80-82** and Au dithiolene complexes **83-85**.

4.3. Synthesis

The complexes were synthesised according to a route previously developed within the Skabara group (scheme 4-1).[97, 98] Oligothiophene precursor, **46**, **47** or **48**, was dissolved in tetrahydrofuran (THF) and treated with 2 equivalents of freshly made sodium methoxide under reflux, to generate dithiolate intermediate **86**, **87**, and **88**. Addition of $NiCl_2.6H_2O$ and Et_4NBr gave the corresponding nickel bis(dithiolene) complexes **80**-**82**, isolated *via* precipitation from hot THF solution with EtOH. The Au(III) complexes **83** and **84** were synthesised analogously using $KAuCl_4$ as the metal salt with *n*-butylammonium counterions, and were isolated from THF/MeCN solutions. Bis(septithiophene) Au(III) complex **85** was made in exactly the same fashion as the Ni complexes. Yields are shown in table 4-1.

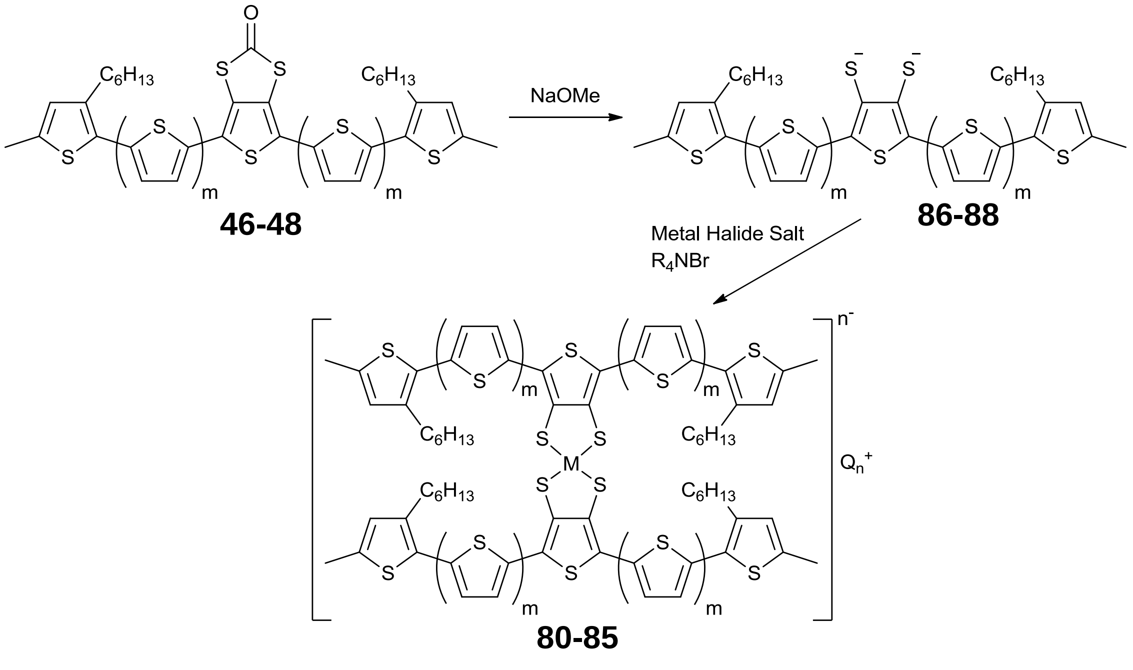

Scheme 4-1 Synthesis of complexes **80** and **83** from precursor **46** (m = 0), **81** and **84** from **47** (m = 1) and **82** and **85** from **48** (m = 2). For **80**-**82** metal halide salt $NiCl_2.6H_2O$ was used and for **83**-**85** $KAuCl_4$ was used.

Table 4-1 Yields of complexes **80**-**85**.

	Yield (%)
80	33
81	70
82	78
83	43
84	48
85	74

Though all the complexes are highly coloured, the longer chain dianionic nickel complexes **81** and **82** are very intensely coloured, appearing almost black in the solid state.

4.4. Absorption Spectroscopy and Electrochemistry of Dithiolene Complexes 80-85

Absorption spectra were recorded in dichloromethane solution using a Shimadu UV-1800. CV measurements were taken using a BAS CV-50W potentiostat with *iR* compensation and performed using glassy carbon, platinum wire and silver wire as the working, counter, and reference electrodes respectively. Substrates were dissolved in anhydrous dichloromethane solution (*ca.* 10^{-4} M) containing n-Bu_4NPF_6 as the supporting electrolyte and all solutions were degassed with argon. All measurements are referenced against the $E_{1/2}$ of the Fc/Fc^+ redox couple. Spectroelectrochemical experiments were conducted using a UNICAM UV300 instrument and a CH Instruments 660A potentiostat. Measurements were taken of films drop-cast onto ITO coated glass and suspended in a solution of n-Bu_4NPF_6 in acetonitrile, or in dichloromethane solution (*ca.* 10^{-4} M) containing n-Bu_4NPF_6 as supporting electrolyte with constant stirring.

4.4.1. Absorption Spectroscopy

The absorption spectra of Ni complexes **80-82** are shown in figure 4-2, and the peaks observed summarised in table 4-2. All demonstrate an absorption at the NIR region of the visible spectrum arising from the low energy HOMO to LUMO transition of the paramagnetic Ni dithiolene monoanion.

The presence of this peak at lower intensity in the spectra of **81** and **82** indicates partial oxidation of the complexes **81** and **82** upon dissolution. This peak undergoes slight redshifting as the oligothiophene chain length increase as shown in table 4-2.

By comparison with its precursor **46** (λ_{max} = 345 nm), the hybrid bis(terthiophene)-TTF **70** (λ_{max} = 351 nm, structure of hybrid TTFs shown in figure 3-1) and other similar systems,[97, 98] the peak at 338 nm in **80** can be attributed to the π-π* transition within the terthiophene chains. This implies that the broad shoulder peaking at 388 nm arises from electronic communication between the delocalised dithiolene core and the conjugated ligands.

The complex **80** demonstrates an extinction coefficient of ε = 44,289 dm^3 mol^{-1} cm^{-1}, whilst complexes **81** and **82** are much more highly absorbing with very large extinction coefficients of 112,033 and 170,835 dm^3 mol^{-1} cm^{-1} respectively.

Table 4-2 Peak maxima in the absorbance spectra of **80-82**.

	λ_{max} / nm
80	228(sh), 296(sh), 338, 388(sh), 906
81	249(sh), 304, 373, 438, 514, 922
82	247(sh), 336, 422(sh), 523, 544(sh), 939

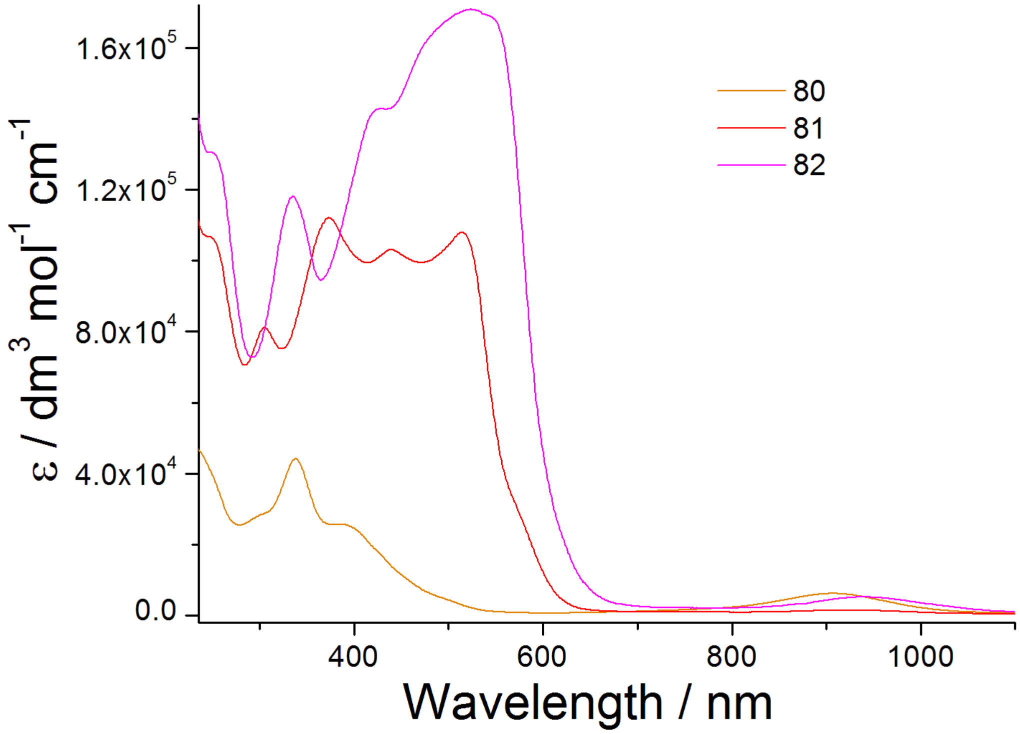

Figure 4-2 Solution state absorbance spectra of Ni dithiolene complexes **80**-**82**.

The spectrum of **81** consists of the NIR absorption, an intense band with a sharp onset and multiple peaks covering the entire spectral window below 620 nm. Again, comparison to the precursor **47** and the hybrid bis(quinquethiophene)-TTF **71** allows for identification of the π-π* transition over the quinquethiophene chain at 438 nm, and the overlapping absorption at 514 nm demonstrates the influence of the dithiolene core on the oligothiophene chain. The numerous discrete peak maxima of similar intensity could arise from the expected deviations from planarity induced in the quinquethiophene chains by the hexyl groups on opposing terminal thiophenes. Crystallographic studies are underway which will provide a better understanding of the geometry of complex **81**.

The highest intensity band of the absorption spectrum of bis(septithiophene) complex **82** has a sharp onset, with a peak maximum at 523 nm and a slightly less intense shoulder at 544 nm. Unlike **81** the main band does reach a definite peak maximum and the subsequent shoulders and peaks exist at considerably lower intensities. Again we observe considerable redshifting of the main absorption band when compared to the precursor **48** and bis(septithiophene)-TTF **72** owing to the effects of the Ni dithiolene core. The small peak at 336 nm, exists at an almost identical wavelength to the terthiophene based transition observed in **80** indicating excited states of more localised conjugation.

Optical energy gaps have been calculated for these complexes from the onsets of both the low energy dithiolene monoanion absorptions (the optical HOMO-LUMO gap of the complexes) and the higher energy transitions occurring over the oligothiophene chains (table 4-3).

Table 4-3 Calculated transition energies for complexes **80**-**82**.

	λ_{max} / nm	HOMO-LUMO gap / eV	λ_{max} / nm	Transition energy / eV
80	906	1.21	388	2.35
81	922	1.17	514	2.01
82	939	1.15	523	1.96

As mentioned earlier, the energy of the long wavelength absorption is observed to decrease gradually as the conjugation length of the ligands increases, whilst the energy of the initial transitions over the oligothiophene chains decreases considerably moving from the terthiophene complex **80** to the quinquethiophene **81** (a similar effect was seen in the studies in chapters 2 and 3), but decrease only slightly moving from **81** to **82**. This decrease is certainly less than would be expected with an increase from five to seven thiophenes, demonstrating again the power of the delocalised Ni dithiolene core in modulating the spectral characteristics of these systems.

Absorption spectra of the Au(III) complexes **83-85** are shown in figure 4-3.

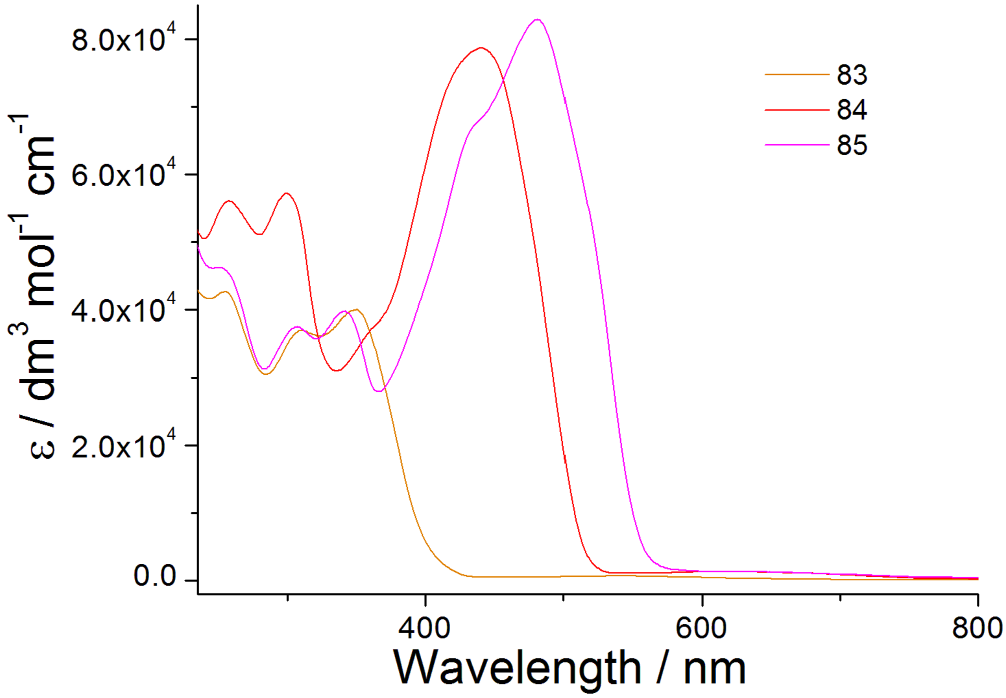

Figure 4-3 Solution state absorbance spectra of Au dithiolene complexes **83-85**.

The monoanionic, Au(III) complexes have distinctly different characteristics to the Ni complexes described above. The characteristic low energy NIR absorption of the paramagnetic monoanionic d^7 Ni complexes is not observed in the visible spectrum of diamagnetic monoanionic d^8 Au(III) complexes.[180-182] Instead, only large intense bands at lower wavelengths are observed, reminiscent of purely organic materials.

Complex **83** displays its longest wavelength peak at 349 nm, (a value typical for terthiophene systems), whereas complexes **84** and **85** have λ_{max} values of 439 and 479 nm respectively. These values are all comparable to those of the precursor oligothiophenes, although they are slightly redshifted in all cases showing that the presence of the Au dithiolene centre has lowered the

LUMO making it more accessible. All of these complexes display multiple peak maxima at lower wavelengths, attributed to the presence of the Au dithiolene centre.

These spectra allow for calculation of the optical HOMO-LUMO gap of these molecules from the onset of the highest wavelength absorption (table 4-4). The optical HOMO-LUMO gaps of Au complexes **83-85** are all decreased by 0.04 – 0.07 eV with respect to their precursors **46-48**, indicating much more limited influence of the diamagnetic Au centre on the HOMO and LUMO levels of the complexes, compared to the effects observed with the paramagnetic Ni complexes.

Whilst still large, the extinction coefficients of the Au complexes are considerably lower than those of the Ni complexes, with **83**, **84**, and **85** demonstrating values of ε = 42,642, 78,660, and 83,169 dm^3 mol^{-1} cm^{-1}, respectively.

Table 4-4 Optical HOMO-LUMO gaps for Au dithiolene complexes **83-85**.

	λ_{max} / nm	HOMO-LUMO gap / eV
83	349	2.99
84	439	2.37
85	479	2.24

4.4.2. Electrochemistry

Cyclic voltammograms of the oxidation of Ni complexes **80-82** are shown in figures 4-4. As shown, other than the first oxidation the peaks are poorly defined, though SWV scans give better definition of peaks at lower potentials (figure 4-5). Reduction scans are shown in figure 4-6.

Surprisingly, the redox signatures of these end-capped Ni complexes, particularly at higher potentials, are not particularly well-defined, as would be expected based upon past observations.[97, 98]

As expected, the redox behaviour of the dithiolene core dominates the first oxidation and reduction potentials. Owing to the larger current responses observed, the results for **82** have been plotted on separate graphs for clarity.

The oxidation plots are all complex and feature very low reversible first oxidation potentials (table 4-5), attributed to the oxidation of the complex from the monoanionic to charge neutral state, effectively moving from Ni(III) to Ni(IV). The influence of incrementally increasing the conjugation length of the ligand can be seen in the concomitant decrease of this first oxidation potential.

The nature of subsequent oxidations is harder to ascertain. Based on previous observations, the second oxidation could be expected to be due to the formation of radical cations on the oligothiophene chains. However, the very low second oxidation potentials of complexes **80-82** (table 4-5), compared to the first oxidation potentials of the precursors **46-48** (table 2-3), may cast doubt on this assignment.

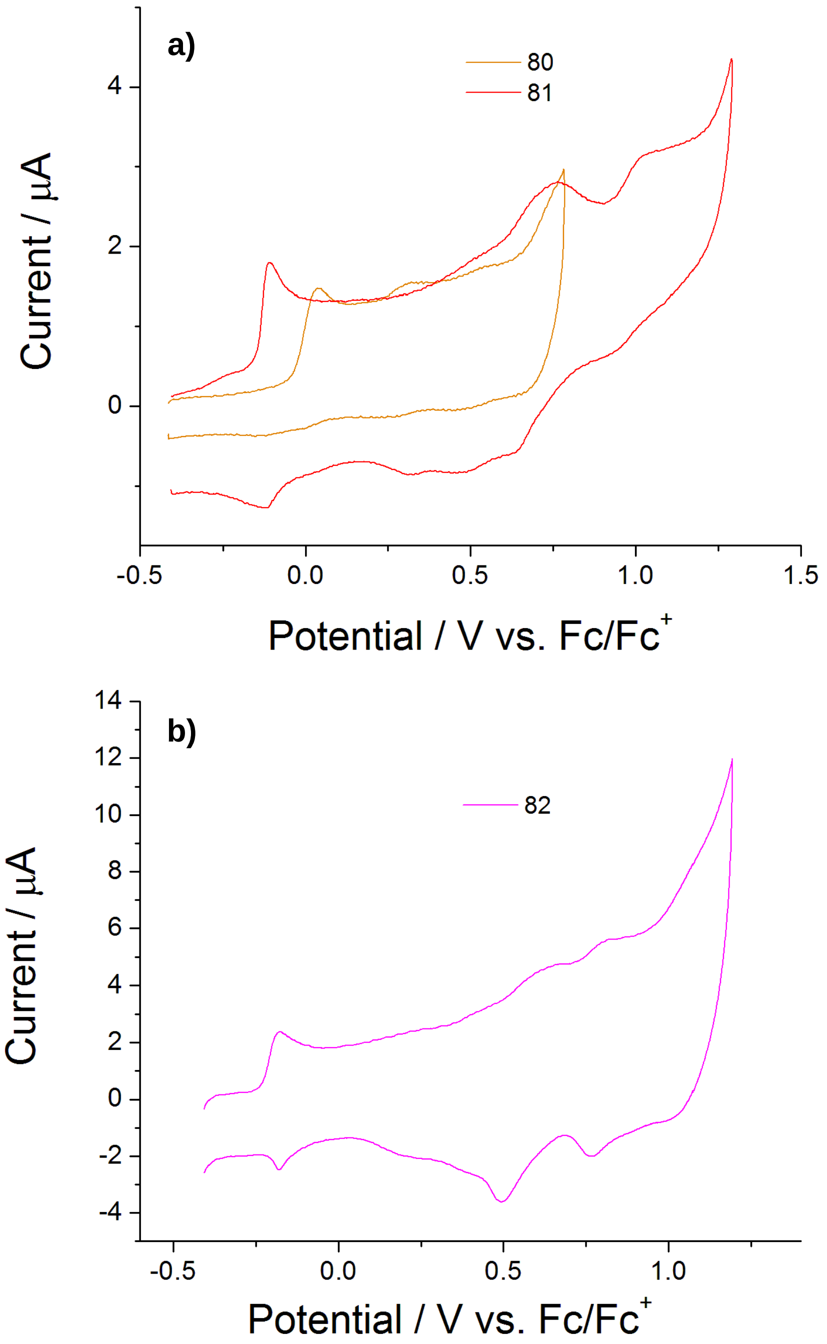

Figure 4-4 Oxidative CV scans of a) bis(terthiophene) Ni complex **80** and bis(quinquethiophene) Ni complex **81**, and b) bis(septithiophene) Ni complex **82**.

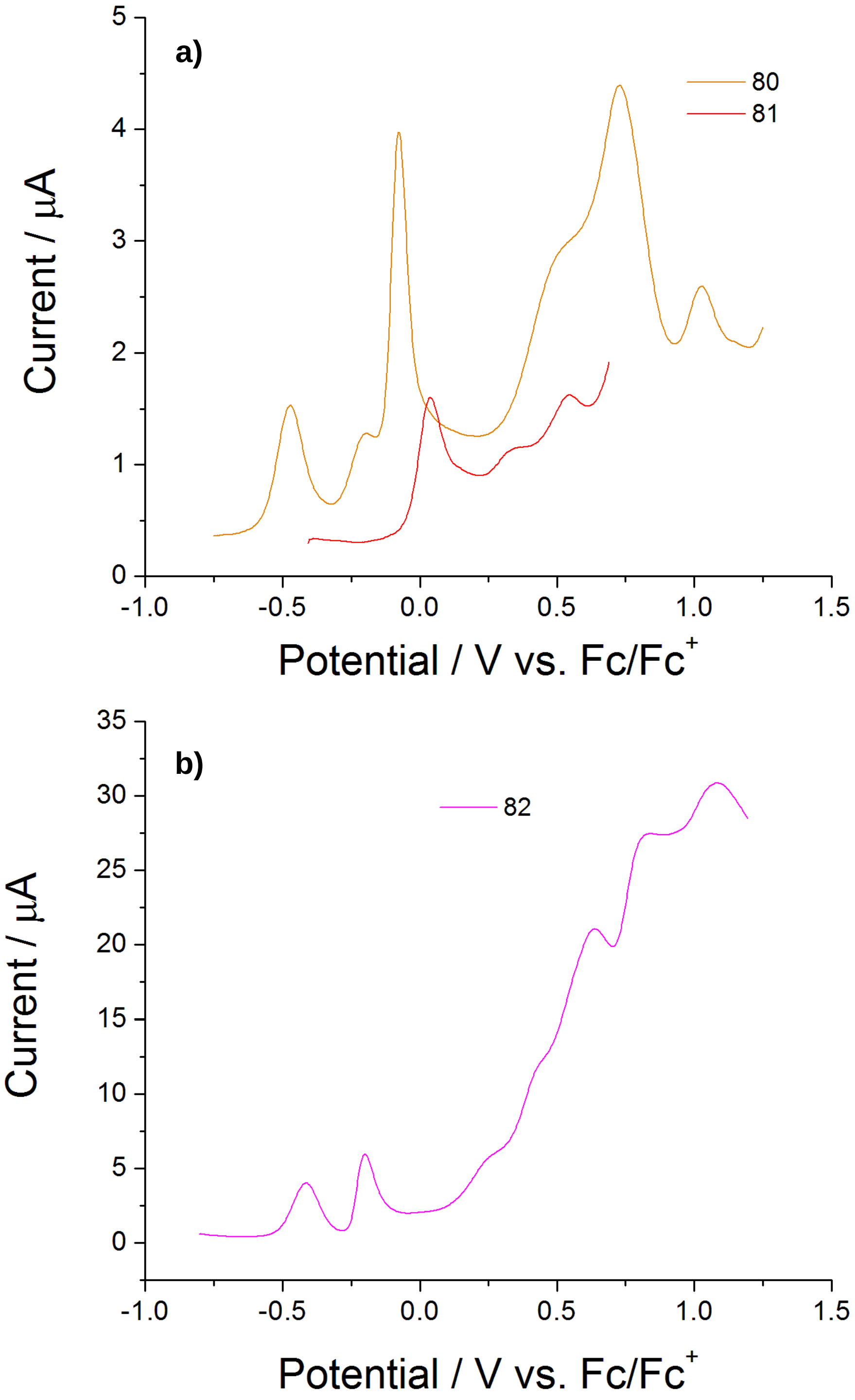

Figure 4-5 SWV scans of a) bis(terthiophene) Ni complex **80** and bis(quinquethiophene) Ni complex **81**, and b) bis(septithiophene) Ni complex **82**.

Table 4-5 Redox processes observed for Ni dithiolene compexes **80**-**82**.

	E_{1ox} / V	E_{2ox} / V	E_{3ox} / V	E_{4ox} / V	E_{1red} / V	E_{2red} / V
80	+0.04/-0.01^{q}	+0.31/0.27^{q}	+0.55/0.47^{q}		-0.74/0.65	-1.51^{irr}
81	-0.11/0.13	+0.51/0.46^{q}	+0.76/0.65^{q}	+1.05/0.95^{q}	-0.52/0.44	-1.51^{irr}
82	-0.18/0.18	+0.26/0.18^{q}	+0.61/0.49	+0.81/0.76	-0.51/0.44	-1.50^{irr}

^{q}Quasi-reversible peak. ^{irr}Irreversible peak

Subsequent oxidations are the results of either radical cation or dication formation on the oligothiophene chains, or even further oxidation forming a radical trication.

The reversibility of many of the oxidation processes has been rendered more quasi-reversible by the presence of the dithiolene core, an effect that decreases in magnitude as the oligothiophene chain length increases from terthiophene **80** through to septithiophene **82**. All oxidations display either limited or no reversibility and, if the potential is increased further the reversibility of these processes either decreases or is lost completely.

The reduction scans (figure 4-6) are much more well defined than the oxidation scans with each complex demonstrating a single reversible reduction at high potential, stemming from reduction of Ni(III) to Ni(II). Again, the influence of increasing ligand conjugation length can be seen in the redox potential of this reduction as it increases upon moving from terthiophene complex **80** through to septithiophene complex **82**.

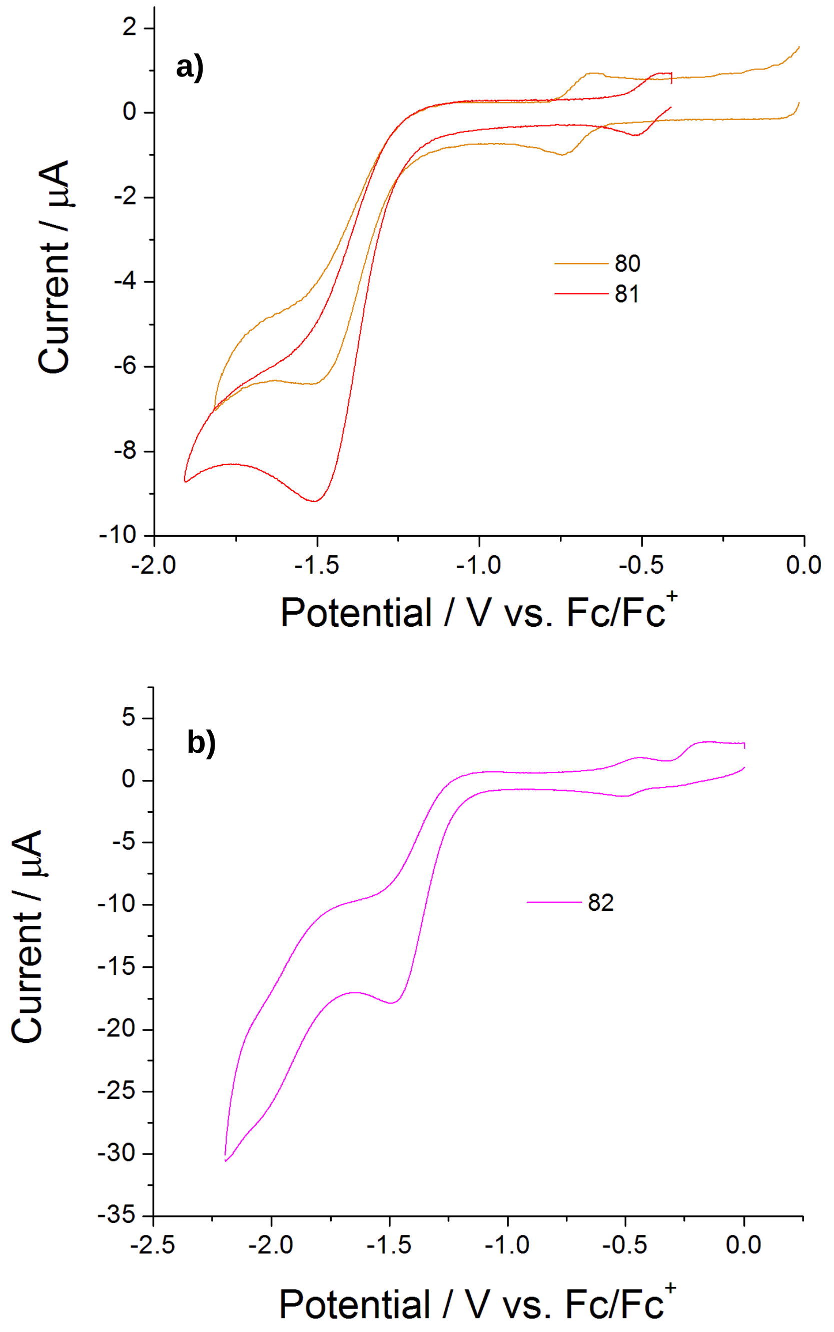

Figure 4-6 Reductive CV scans of a) bis(terthiophene) Ni complex **80** and bis(quinquethiophene) Ni complex **81**, and b) bis(septithiophene) Ni complex **82**.

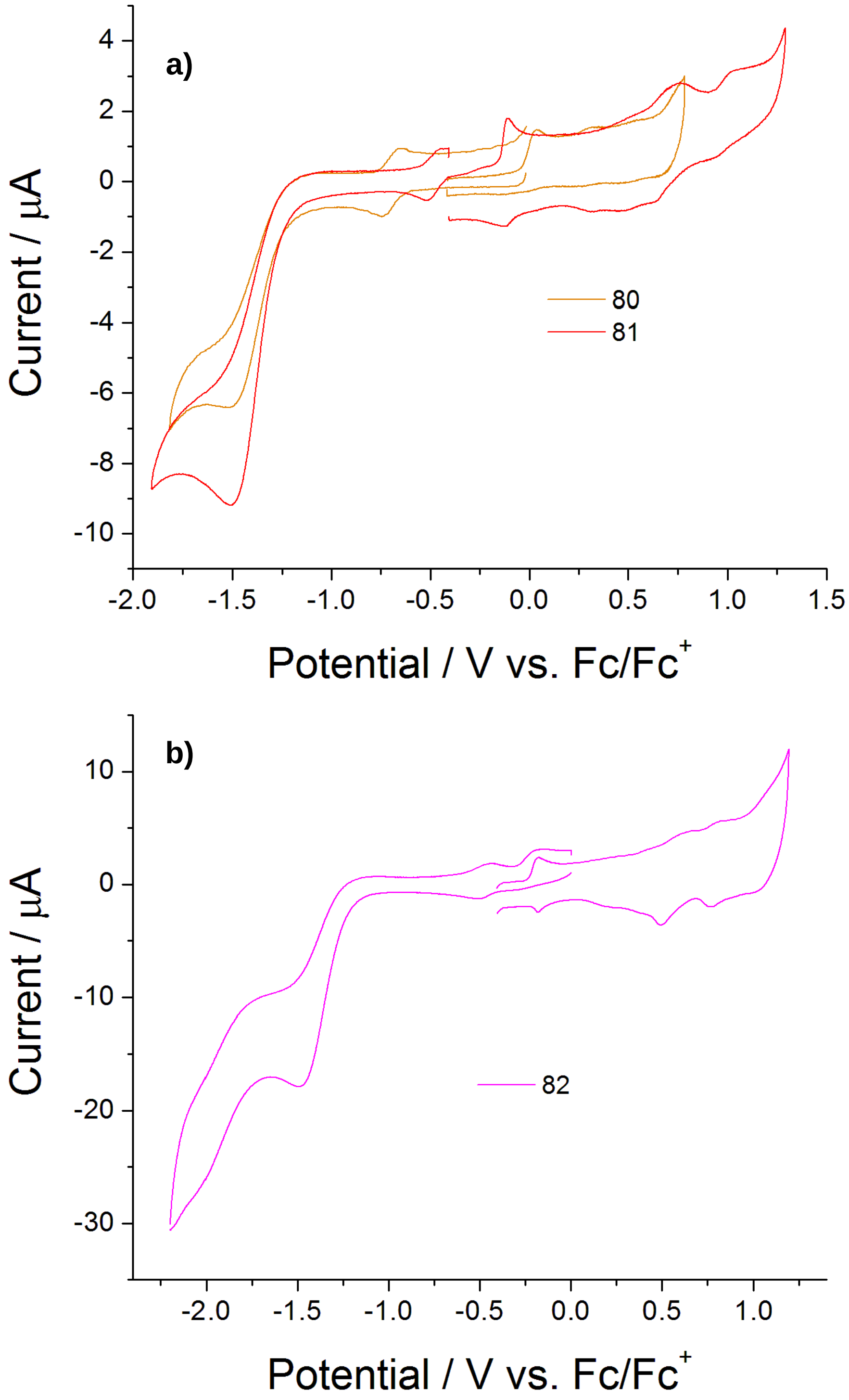

Figure 4-7 Combined oxidation and reduction CV scans for a) **80** and **81** and b) **82** used for HOMO-LUMO gap calculation.

The HOMO and LUMO levels and electrochemical HOMO-LUMO gap were calculated using figure 4-7 and are shown in table 4-6. The LUMO levels of the five- and seven-thiophene complexes **81** and **82** have been calculated as lying at almost the same energy, demonstrating that the effect of extending the conjugation has a more limited effect on lowering the LUMO energy. Interestingly, the HOMO levels continue to rise as the conjugation length increases, indicating greater electronic influence of the oligothiophenes on the HOMO of the dithiolene core, than the LUMO.

Table 4-6 Calculated energy levels for Ni dithiolene complexes **80**-**82**.

	HOMO / eV[a]	LUMO / eV	HOMO-LUMO gap / eV[b]
80	-4.75	-4.18	0.57
81	-4.64	-4.42	0.22
82	-4.56	-4.41	0.15

[a]HOMO and LUMO levels are calculated from the onset of the first peak of the corresponding redox wave and are referenced to ferrocene which has a HOMO of -4.8 eV. [b]Electrochemical HOMO-LUMO gap is the energy gap between the HOMO and LUMO levels.

As a result of the influence of the oligothiophene chains on the HOMO and LUMO levels of the dithiolene core, these complexes demonstrate remarkably low electrochemical HOMO-LUMO gaps (figure 4-7 and table 4-6), which, when coupled with the high reversibility of the redox processes of the dithiolene centre, gives access to low potential NIR switching. A second irreversible reduction occurs at lower potentials due to the formation of unstable radical anions on the oligothiophene chains.

The oxidation and reduction scans of the Au(III) complexes **83**-**85** are shown in figure 4-8 and 4-9, and summarised in table 4-7. All demonstrate multiple oxidation processes stemming from both the dithiolene centre and the oligothiophene chains. The oxidation scans are much more well-defined for the Au complexes **83-85** compared to the Ni complexes **80-82**, and demonstrate greater reversibility.

All the complexes demonstrate reversible first oxidations to form the neutral complexes, attributed to the oxidation of the dithiolene core by comparison with other aromatic Au(III) dithiolene complexes.[181, 182] The first oxidation potential decreases steadily in energy as the oligothiophene chain length increases along the series, occurring at half wave potentials of +0.08 V in **83**, -0.10 V in **84** and -0.21 V in **85**. Again, despite changing from Ni to Au, the chain length has a dramatic effect on the HOMO level of the dithiolene core.

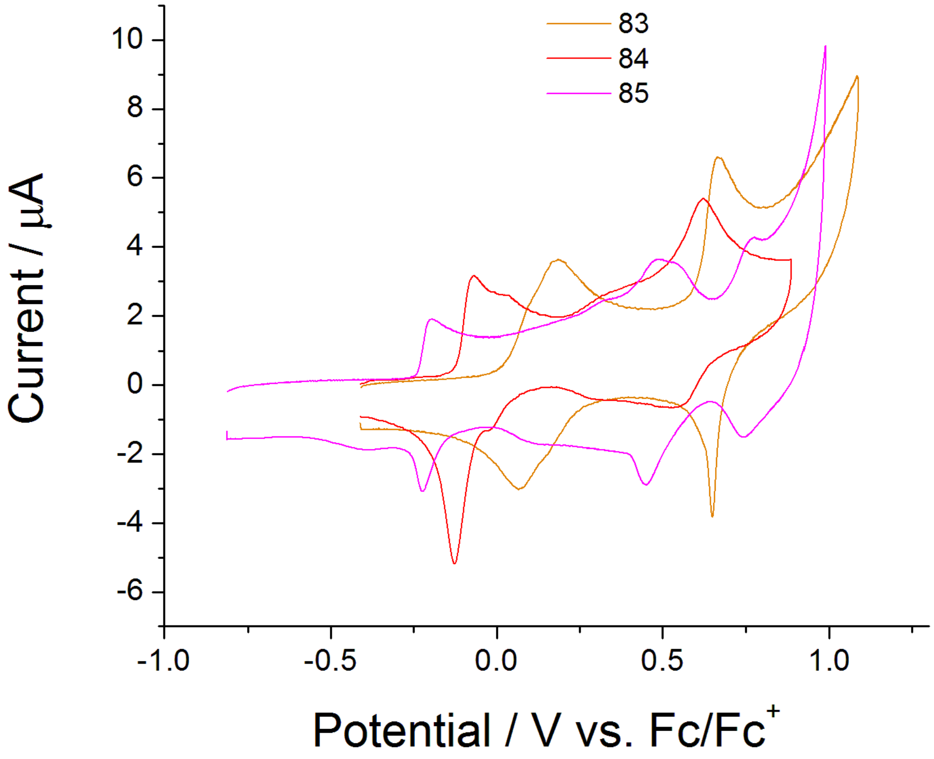

Figure 4-8 Oxidative CV scans of bis(terthiophene) Au complex **83**, bis(quinquethiophene) Au complex **84**, and bis(septithiophene) Au complex **85**.

There is a second reversible oxidation closely associated with the first in the scans of **83** and **84**. This is demonstrated more clearly by the peak at +0.12 V (the first oxidation exists as a shoulder at +0.06 V) in the DPV of the terthiophene complex **83** and the peak at +0.01 V in the SWV of quinquethiophene complex **84** as shown in figure 4-9. Neither of these techniques served to deconvolute the voltammogram of the septithiophene complex **85**.

The very low potential of this peak renders it unlikely to be attributable solely to the oligothiophene. If extensive electronic communication is occurring between the oligothiophene chains and the Au dithiolene core as expected, then the dithiolene centre appears to give access to a delocalised radical cation state at unprecedentedly low oxidation potentials.

In the oxidation scan of **83**, a third narrow reversible oxidation occurs at $E_{1/2}$ of +0.66 V. Though this compares well with the first oxidation to form a radical cation in the terthiophene precursor **46** (table 2-3), the high reversibility and narrow peak profile indicates oxidation centered over the dithiolene core when compared with the literature.[180, 182] A fourth wave is seen in the DPV at +1.01 V corresponding to a second thiophene based oxidation. This wave is not observed in the standard CV scan.

In complex **84**, the early peaks are similar to those observed for complex **83**, though they occur at lower potentials due to the more extended conjugation. A third broad quasi-reversible oxidation is observed at +0.33 V corresponding to the formation of a second radical cation on quinquethiophene arms. This is followed by a fourth reversible peak centred at +0.58 V owing to formation of the cationic complex. In a similar fashion to the observations made for the fourth oxidation in the DPV for **83**, a fifth wave is observed at higher potential, +1.14 V, in the SWV of complex **84** due to the dication formation.

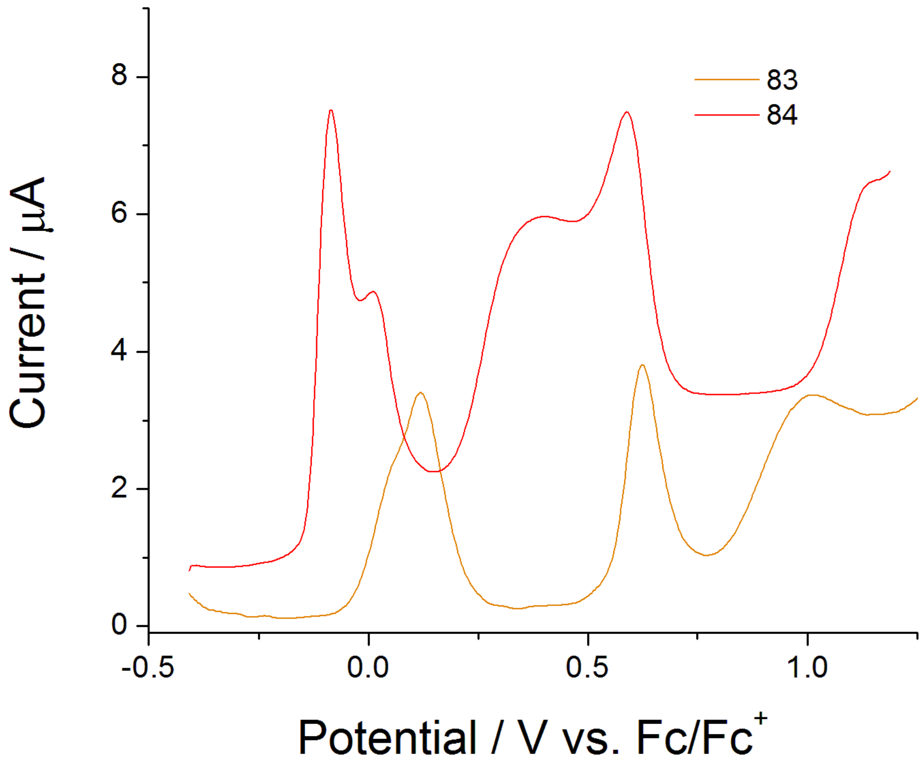

Figure 4-9 DPV results for bis(terthiophene) Au complex **83** and SWV results for bis (quinquethiophene) Au complex **84**.

In the largest of these complexes, septithiophene based complex **85**, the low potential reversible oxidation to the neutral complex is observed again, centred at -0.21 V, and the reversible oxidation to the cationic complex is centred at +0.47 V. There appears to be at least one quasi-reversible oxidation evident occurring in the broad waveform between these two dithiolene focussed oxidations. There is a shoulder at +0.54 V representing quasi-reversible formation of a dication, prior to the final reversible formation of a second dication at +0.76 V. Again, the shifts of peaks to lower potentials observed in the shorter chain complexes **83** and **84** are induced by the increase in conjugation length.

Reduction scans for **83**-**85** are shown in figure 4-10. Complexes **83** and **84** display reversible oxidations to produce a dianionic complex at half-wave potentials of -1.75 and -1.50 V respectively. In **85** an irreversible reduction of one or both of the septithiophene chains at -1.51 V is observed, followed by a quasi-reversible reduction of the Au dithiolene centre with the peak centred at -1.92 V. Though -1.51 V seems high for radical anion formation along the septithiophene chain (especially when compared to the septithiophene precursor **48**, table 2-3), and -1.92 V seems low for reduction of the dithiolene core, a dithiolene based reduction is expected to be reversible, as observed for the other members of the series, and so the waves have been assigned in this fashion.

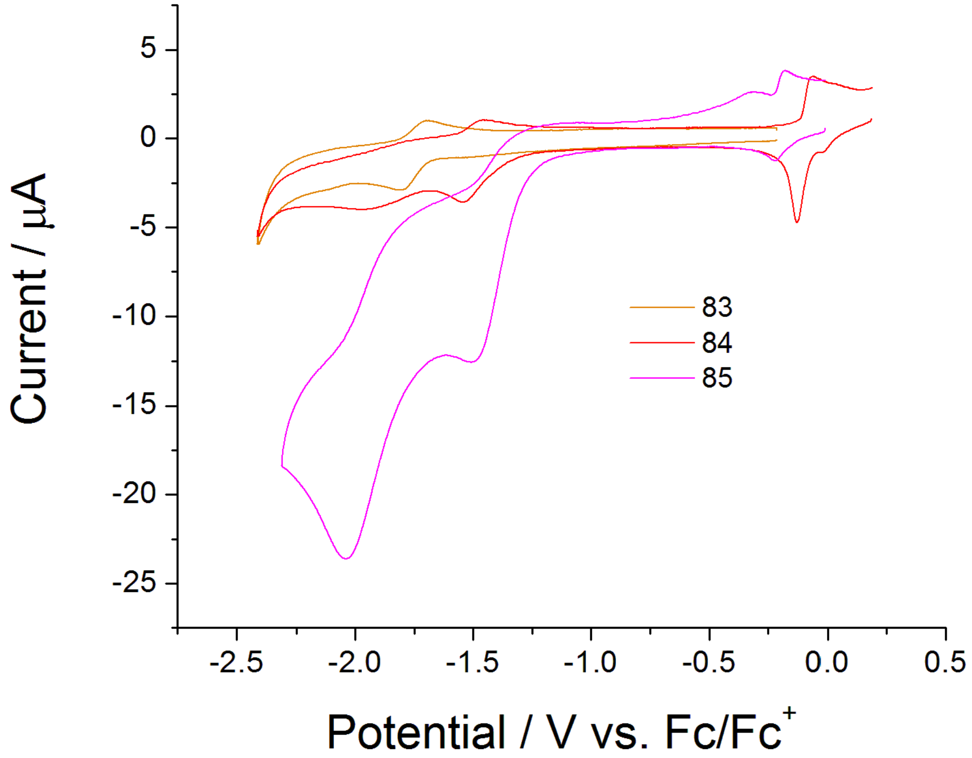

Figure 4-10 Reductive CV scans of bis(terthiophene) Au complex **83**, bis(quinquethiophene) Au complex **84**, and bis(septithiophene) Au complex **85**.

The complexes all display a single irreversible reduction process below -2.0 V corresponding to the formation of radical anions on the oligothiophene chains.

Table 4-7 Redox processes observed for Au dithiolene compexes **83**-**85**.

	E_{1ox} / V	E_{2ox} / V	E_{3ox} / V	E_{4ox} / V	E_{5ox} / V	E_{1red} / V	E_{2red} / V
83	+0.10/0.07	+0.19/0.15	+0.67/0.65			-1.81/1.69	-2.13^{irr}
84	-0.07/0.13	-0.00/0.02	+0.36/0.30^{q}	+0.62/0.54		-1.54/1.45	-1.97^{irr}
85	-0.20/0.22	+0.32/0.20^{q}	+0.49/0.45	+0.55^{irr}	+0.78/0.74	-1.51^{irr}	-2.04/1.81

^{q}Quasi-reversible peak. ^{irr}Irreversible peak

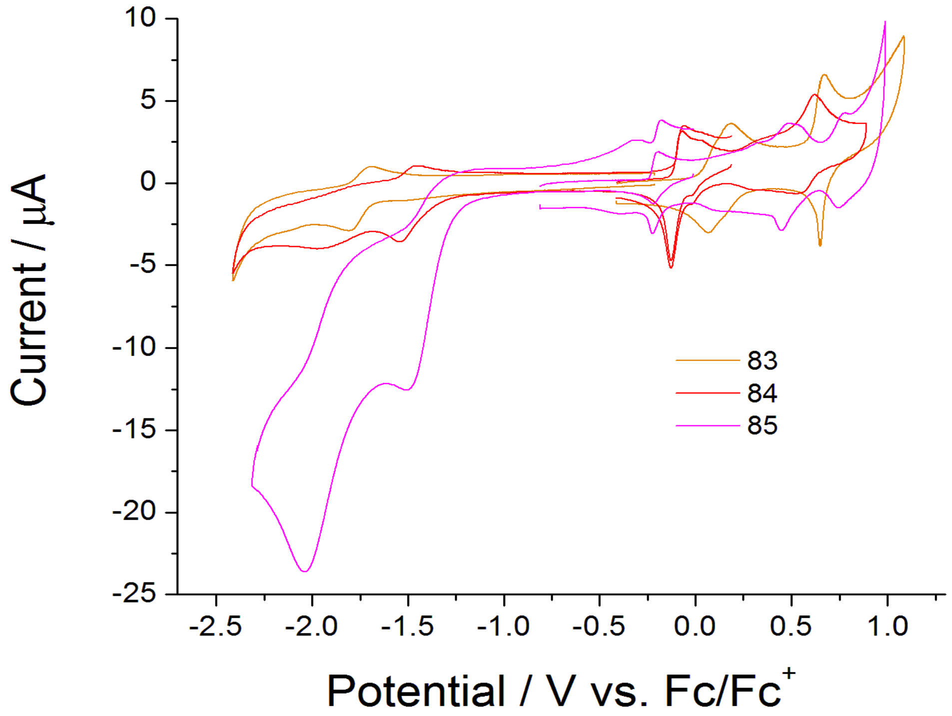

Figure 4-11 Combined oxidative and reductive scans for complexes **83**-**85** as used for HOMO and LUMO level determination.

The electrochemical HOMO-LUMO gaps for these materials were obtained from the difference in the onsets of the first oxidation and reduction peaks (figure 4-11, and table 4-8). The electrochemical HOMO-LUMO gaps of **83**, **84**, and **85** were calculated as 1.68, 1.19, and 1.04 eV respectively. These are as much as 1 eV lower than the values obtained for the oligothiophene precursors (table 2-3), mainly owing to the easily oxidised HOMO over the Au(III) dithiolene centre.

Table 4-8 HOMO and LUMO levels for complexes **83**-**85** and HOMO-LUMO gaps.

	HOMO / eV[a]	LUMO / eV[a]	HOMO-LUMO gap / eV[b]
83	-4.81	-3.13	1.68
84	-4.68	-3.49	1.19
85	-4.58	-3.54	1.04

[a]HOMO and LUMO levels are calculated from the onset of the first peak of the corresponding redox wave and are referenced to ferrocene which has a HOMO of -4.8 eV. [b]Electrochemical HOMO-LUMO gap is the energy gap between the HOMO and LUMO levels.

Despite being considerably lower than the calculated optical HOMO-LUMO gaps (table 4-4) which are dominated by the extensively conjugated oligothiophene chains, the electrochemical HOMO-LUMO gaps display similar trends. They feature differences of similar magnitudes between the individual HOMO-LUMO gaps of the complexes, indicating cooperation between the dithiolene core and oligothiophene chains.

4.4.3. Spectroelectrochemistry

The absorption spectra of thin films of the quinquethiophene Ni(II) dithiolene complex **81** and septithiophene Ni(II) dithiolene complex **82** are shown in figure 4-12 and described in table 4-9. A suitable film of the terthiophene Ni(III) complex **80** could not be formed.

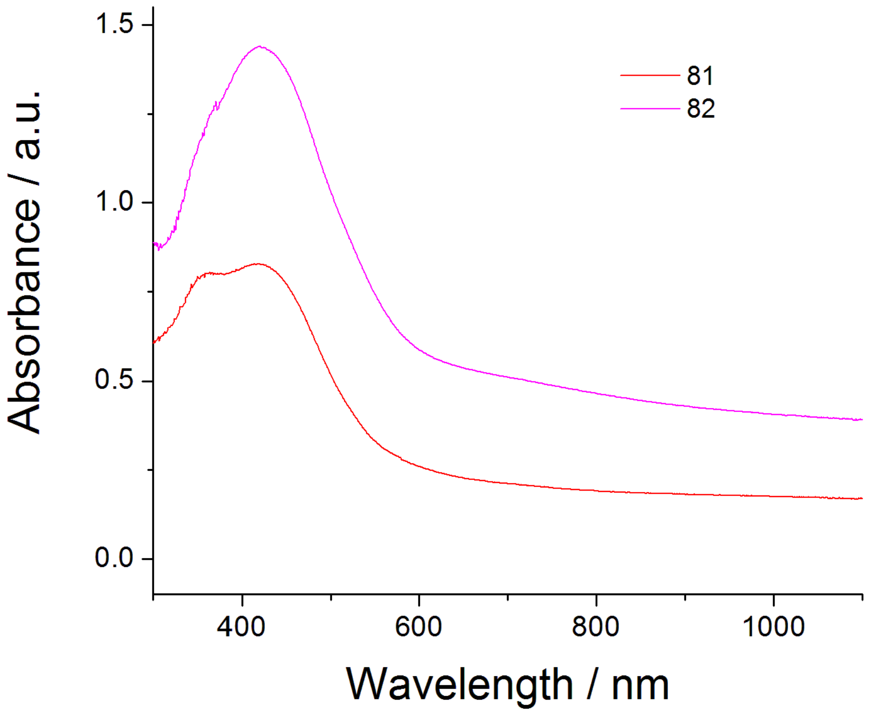

Figure 4-12 Thin film absorption spectra for Ni complexes **81** and **82**.

Table 4-9 Peak maxima observed for thin films of Ni complexes **81** and **82**.

	λ_{max} / nm
81	419, 360
82	421

The quality of the films is surprising given that these complexes exist as salts. Both films demonstrate a λ_{max} at *ca.* 420 nm stemming from the π-π* absorption of the oligothiophene chains and a long tail which covers the entire visible region. The secondary absorbance at 360 nm in the spectrum of complex **81** can be attributed to the non-planarity of the quinquethiophene chains in this complex within the film. These films are highly soluble and did not allow for solid-state SEC characterisation, however solution-state SEC plots were obtained for both complexes using a solution cell.

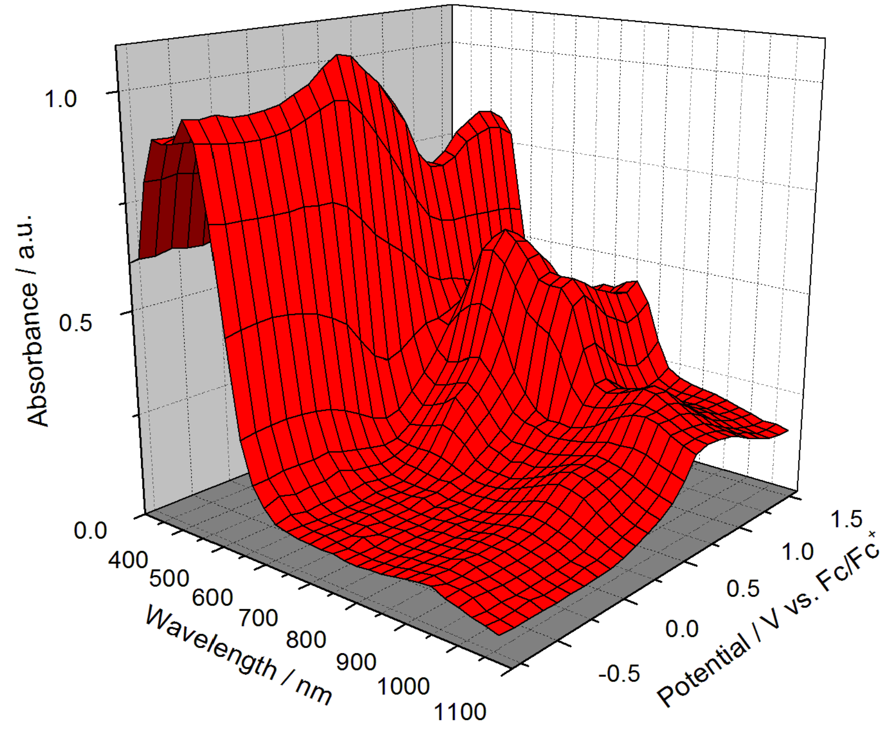

Figure 4-13 Solution state SEC of bis(quinquethiophene) Ni complex **81**.

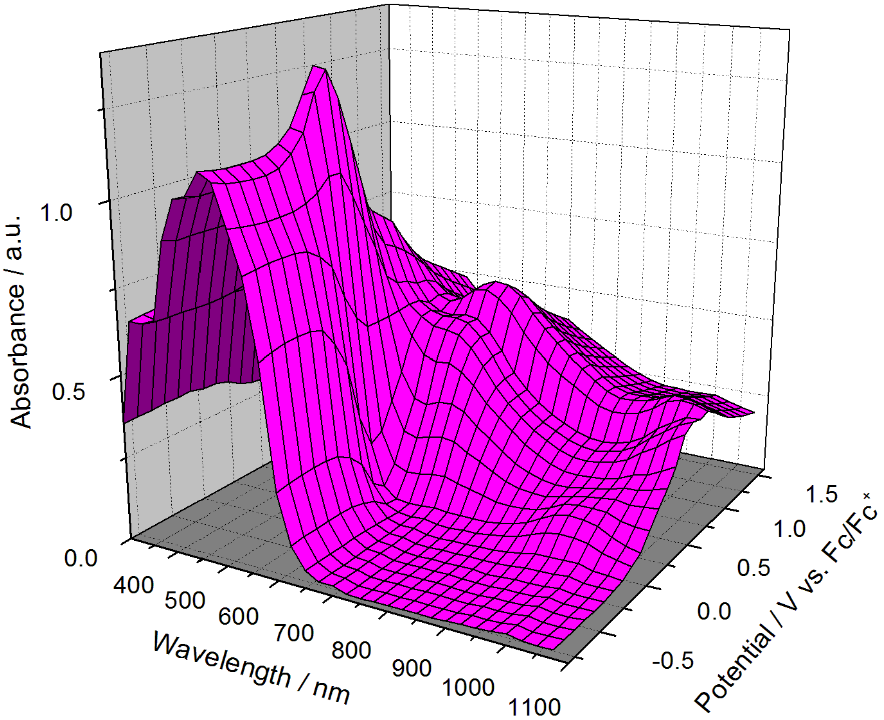

Figure 4-14 Solution state SEC of bis(septithiophene) Ni complex **82**.

Figure 4-13 shows the SEC plot for a dichloromethane solution of quinquethiophene nickel dithiolene complex **81** and figure 4-14 shows the SEC plot for the septithiophene nickel complex **82**, also a dichloromethane solution. Both materials are initially held at a reducing potential allowing the dianionic complex to stabilise in solution and resulting in the loss of the NIR band from the visible spectrum.

Upon increasing potential past +0 V both **81** and **82** demonstrate the growth of the NIR band corresponding to the monoanionic Ni(III) complex at 934 nm and 963 nm respectively. The near identical onset potentials support the hypothesis that this band is derived from the dithiolene centre. As the potential increases beyond +0 V, a growth in the intensity of the π-π* band of the oligothiophene chains in both complexes is observed.

Above +0.25 V in complex **81** the growth of a band at 635 nm corresponding to radical cation formation on the quinquethiophene arms is observed. At +0.6 V a band corresponding to dication formation, peaking at 749 nm begins to grow and the intensity of the π-π* band falls. At this potential, a second more intense NIR band emerges at 948 nm stemming from the now neutral dithiolene core. Beyond +1.0 V the band pertaining to the radical cation is lost as these species are all converted to dications at this high potential. The intensities of the dication and NIR bands obtain more constant values and the intensity of the oligothiophene π-π* band increases slightly.

At potentials of +0.1 to +0.6 V in septithiophene complex **82** the growth of a band at 636 nm pertaining to radical cation formation occurs, and the NIR dithiolene band of the monoanionic complex diminishes as the NIR absorbance of the neutral dithiolene complex begins to grow at wavelengths >1100 nm. Increasing the potential past +0.6 V results in dication formation on the septithiophene chains as can be seen by the emergence of the band which peaks at 662 nm and the shifting of the NIR dithiolene absorption to higher energy. Throughout these processes the intensity of the π-π* absorption falls and remains low at the end of the experiment.

The SEC results indicate that the absorbances pertaining to the oligothiophene radical cation and the monoanionic dithiolene centre, and the absorbances from the oligothiophene dication and neutral dithiolene band grow at the same time in **81**. This coupled with the shifting of the dithiolene absorbance upon oxidation of the septithiophene chains in **82** indicates extensive electronic interplay between the dithiolene core and oligothiophene chains in these Ni complexes.

The absorption spectra for thin films of the Au(III) complexes **83**, **84**, and **85** are plotted in figure 4-15 and summarised in table 4-10. Like the films of the Ni complexes, the films formed by all three Au complexes, especially the higher molecular weight complexes **84** and **85**, were of surprisingly high quality given their salt nature. The π-π* transition of the film of the terthiophene Au complex **83** occurs outwith the observable region. The spectra of **84** and **85** are dominated by the absorption of the π-π* transitions of the oligothiophene chains, and feature long tails that absorb across the entire visible range.

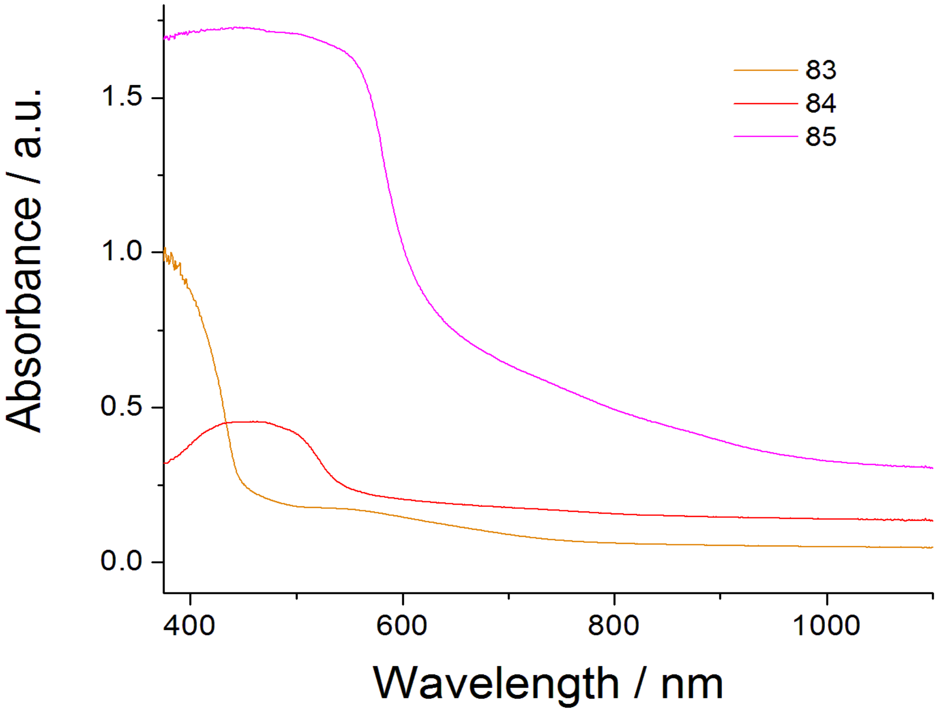

Figure 4-15 Thin film absorption spectra for Au complexes **83**-**85**.

Table 4-10 Peak maxima observed for Au complexes **83**-**85**.

	λ_{max} / nm
83	527(sh) , <377
84	468
85	460 (br)

The solid state SEC of bis(terthiophene) Au dithiolene complex **83** is shown in figure 4-16. It is clear that upon increasing the potential from -0.4 to +0 V the intensity of absorption drops slightly, before oxidation begins to occur at +0 V eliciting a very large increase in the absorptivity of the film across the entire visible spectrum, with peaks at 515 and 734 nm. The oxidation occurs at a low potential and is therefore attributable to radical cation formation over the dithiolene centre, though the spectral response occurs where bands associated with the terthiophene based radical cation would be expected.

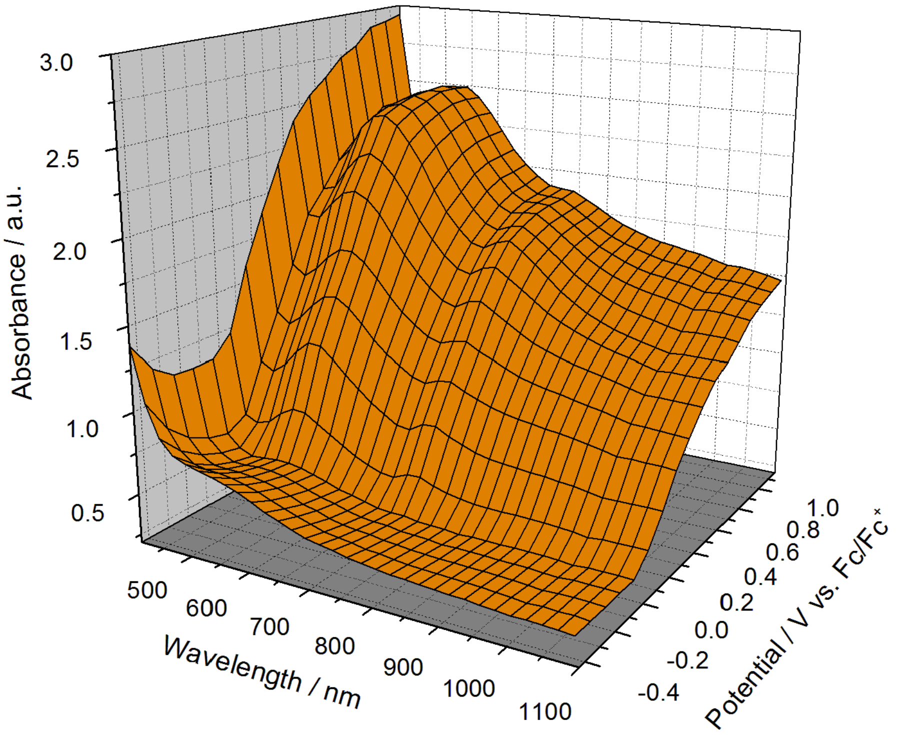

Figure 4-16 Solid state SEC plot for bis(terthiophene) Au complex **83**.

This demonstrates again that hybrid electronic behaviour is occurring combining the low first oxidation potential of the dithiolene centre with the optical properties of the oligothiophene chains. The intensity of the λ_{max} absorption band begins to resolve at potentials >+0.7 V.

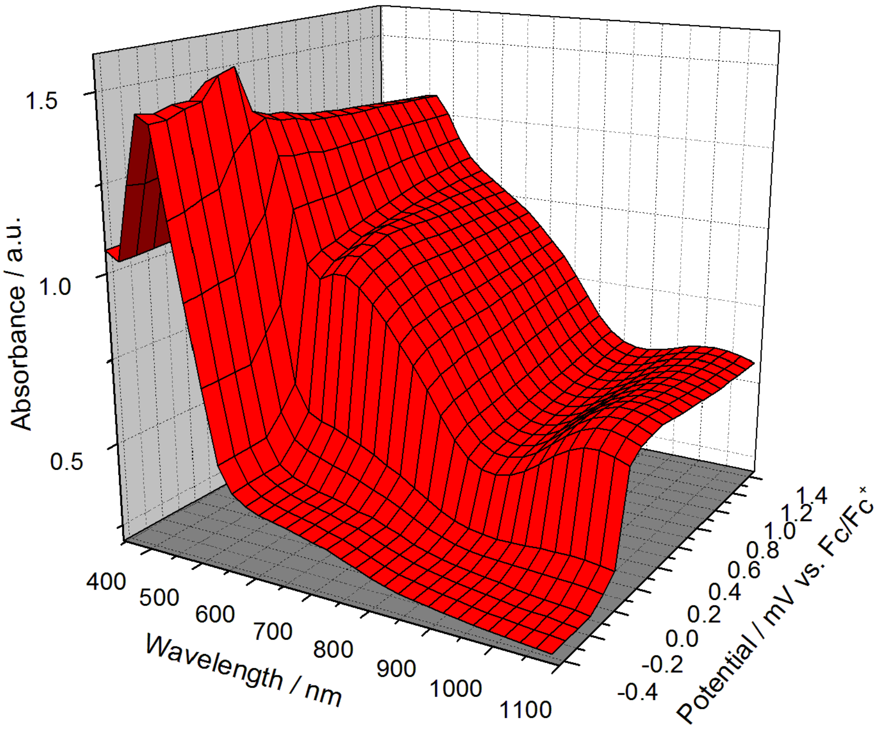

Figure 4-17 Solid state SEC plot for bis(quinquethiophene) Au complex **84**.

The SEC plot for the quinquethiophene complex **84** is shown in figure 4-17. The spectral characteristics are very similar to those observed in **83**, though now the effect of oxidation on the π-π* absorption of the film is clear. Above +0.1 V, oxidation to form a radical cation occurs over the Au dithiolene core, eliciting a large and sudden spectral response. The π-π* absorption drops in intensity and is redshifted from 429 to 459 nm, while the intensity of absorption over the entire visible spectrum is raised greatly with peaks at 602 nm and 1036 nm. The lower wavelength absorption is the π-π* transition of the quinquethiophene radical cation, and the NIR absorption can be attributed to the dithiolene centre. Again, these results indicate hybrid electronic behaviour.

The low potential radical cation formation observed in both **83** and **84**, induced by the Au dithiolene centre may explain the overlapping peak forms recorded for the first oxidations in the CV of these complexes.

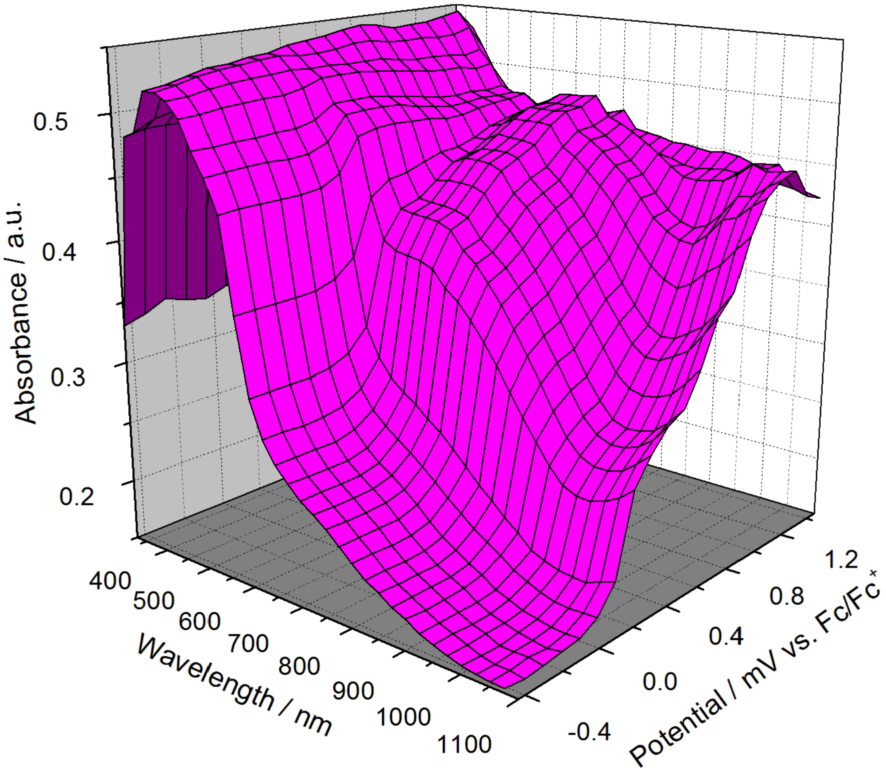

Figure 4-18 Solid state SEC plot for bis(septithiophene) Au complex **85**.

The SEC plot of the septithiophene complex **85** shows similar behaviour to that seen for the complexes **83** and **84**. Upon oxidation to +0.2V sudden development of a septithiophene and Au dithiolene radical cation wave appear at 679 and >1100 nm respectively. The intensity of these bands continues to grow as the potential is continually increased. Additionally, there is less impact on the π-π* absorption of the septithiophene chains when compared to the changes observed for complexes **83** and **84**. A smoother waveform for **85** may be obtained by improving the casting technique to obtain a more uniform film.

4.5. Conclusions and Further Work

In conclusion, six new homoleptic bis(dithiolene) complexes featuring nickel or gold metal centres bound between highly extended end-capped oligothiophene ligands with chain lengths of three, five and seven thiophenes, have been synthesised.

The Ni complexes are highly soluble and have demonstrated very high extinction coefficients. In each complex, the characteristic NIR absorption of the Ni dithiolene core has been apparent, and this redox active centre has granted very small HOMO-LUMO gaps to the complex as a whole, making them highly active and resulting in multiple redox processes being observed in the oxidation CV scans. Solution SEC studies of the quinquethiophene complex **81** and the septithiophene complex **82** have shown delocalisation of excited states over the whole molecule. Crystals have been obtained for all three Ni complexes and have been submitted for crystallographic analysis. This will provide a useful insight into the molecular structure and the ordering of these large molecules in the solid state.

The monoanionic Au(III) complexes are also soluble and have demonstrated highly reversible redox properties. SEC results for thin films of these complexes have shown that in all cases oxidation to the neutral Au(IV) radical cationic complex results in a large and sudden increase in the intensity of absorption across the entire visible window, which persists at higher potentials. The absorptions observed result from the NIR absorption of the neutral Au dithiolene centre, and the π-π^* transitions of the oligothiophene radical cation. UV/vis/NIR spectroscopy studies of all of these complexes would be useful to refine the understanding of their optical properties, and would allow for quantification of the NIR absorptions of the Au complexes which are often very intense.[182]

Neutral complexes of thiophene-dithiolene ligands have been reported and have demonstrated interesting conductive and magnetic properties,[113-115] so future work with these complexes should involve efforts towards the development of charge neutral Ni(IV) and Au(IV) complexes by treatment of the salts described here with an oxidising agent such as iodine. Most examples of charge neutral TD complexes have been highly insoluble polycrystalline precipitates[113-115] though it is hoped that the hexyl chains in these complexes will maintain solubility. Assuming the intense and broad absorptivities are maintained, the resulting complexes could then be studied for device applications such as OSCs.

Similarly to the Ni complexes, single crystals of all three Au complexes have been obtained and have recently been sent for crystallographic analysis. Obtaining crystal structures of these complexes would also serve to simplify future DFT calculations (similar to those performed for the hybrid septithiophene-TTF in chapter 3.6), which could give a greater understanding of the energy level ordering of these complex systems.

Chapter 5: Oligothiophene Dimers Featuring Spirocyclic Germanium Centres – Novel Highly Absorbing Solution Processable Materials

5.1. Abstract

Using the soluble 1,3-dithiole-2-one functionalised, methyl end-capped, oligothiophenes **46-48**, three new spirocyclic compounds (**89**, **90**, and **91**) featuring two oligothiophene chains fused across a spirobi([1,3,2]dithiagermole) centre have been developed. The effects of both the electron rich spirocentre and the incremental increases in the oligothiophene chain length, on the electrochemical and spectroscopic properties of these compounds, have been studied using cyclic voltammetry and UV/vis spectroelectrochemistry.

These species have demonstrated very large extinction coefficients and are exciting new candidates for light harvesting applications in OSCs.

5.2. Introduction

Spirocyclic compounds have been widely studied for materials applications and have demonstrated promising properties for use in a number of organic electronic devices[183, 184] notably as hole transport mediums in highly efficient solid-state dye-sensitized solar cells.[185, 186] Spiro-linked conjugated molecules feature two conjugated chains which are connected orthogonally *via* a common tetrahedral sp^3-hybridised atom (figure 5-1).[183]

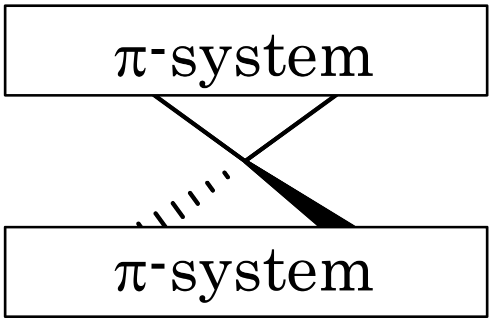

Figure 5-1 Generic spirocentric structure.

Despite the perpendicular arrangement of the two halves of the molecule brought about by the sp^3 spirocentre there is evidence of electronic communication between the two spiro-linked π-systems.[183] If the extent to which the two halves of the molecule interact can be improved, then the benefits of longer effective conjugation lengths, such as reduced and tunable HOMO-LUMO gaps can be accessed. One way to achieve this could be to increase the electron density around the spirocentre.

With this in mind, the use of a tetrathiolato germanium spirocentre in place of the traditional solely carbon based spirocentres has been explored. The electron rich and non-innocent nature of the chelating dithiolene moiety, and the conductivity and superconductivity observed from its transition metal complexes, has been widely and continuously explored for almost 50 years.[57, [66, 70, 73] However, "complexes" using main group elements have been much less widely explored.[187]

The use of a group 14 element in place of a metal centre can give access to purely covalent compounds featuring electron rich 1,3-dithiole rings bound *via* a neutral, tetrahedral sp^3 centre, an area that is largely overlooked for the development of unique and useful new materials.

By using elements from lower down the group, electron density at the spiro-centre can be increased and so the extent of electronic communication across the spiro-centre could be enhanced.

A small number of aromatic or extensively unsaturated/conjugated spirocyclic bis(dithiolate) compounds featuring C[188-190] and Si[191] centres have been developed. Similar compounds containing spirocyclic bis(dithiolate) Ge, centres,[189, 192] referred to as spirobi([1,3,2]dithiagermole), are rarer still with only a handful of examples reported since the first synthesis of molecules of this class, using Si, Ge, Sn and Pb spirocentres, in 1966.[193, 194] Ge is the first of the group 14 elements to possess a full *d*-shell and so is much more electron rich than either C or Si, as such it could be expected to support an increased level of spiro-conjugation.

For these reasons, spirobi([1,3,2]dithiagermoles) **89-91** (figure 5-2), featuring soluble and end-capped oligothiophene chains fused to the spirocentre, have been developed. Chain lengths of three, five, and seven thiophenes have been created, using the oligothiophene precursors **46-48**.

Similarly linked bis(oligothiophenes), fused to a common all carbon spiro[4,4]nonane or Si centred 5-silaspiro[4,4]nonane (not the sulfur rich centres described here) have been reported in the past, allowing for useful comparisons to be made.[195, 196] The highly electron-rich spirobi([1,3,2]dithiagermole) centre has had a marked influence on the optical and electrochemical behaviour of the oligothiophenes, demonstrating that despite the orthogonal centre, electronic communication between the two oligothiophene chains across this electron-rich centre is occurring.

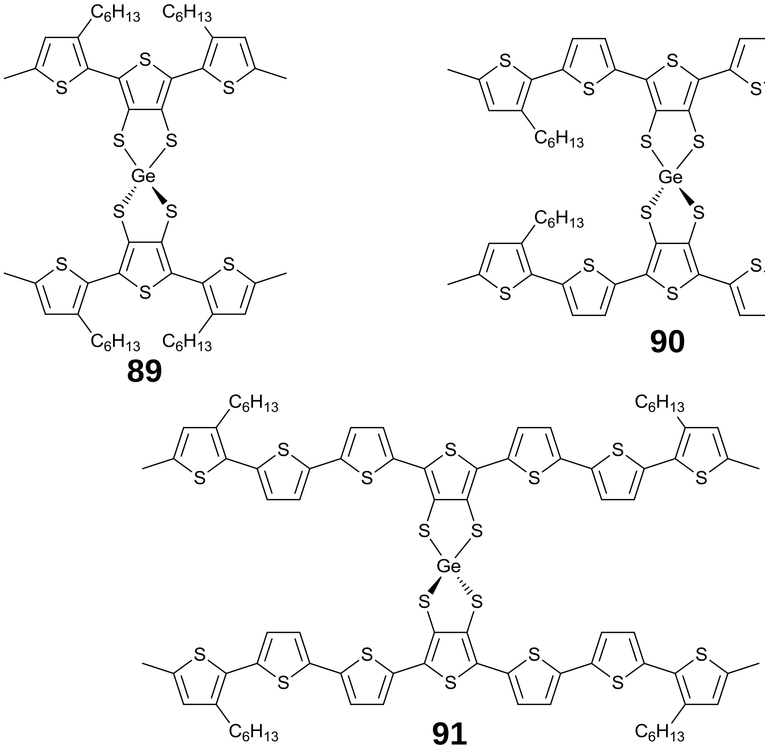

89 **90** **91**

Figure 5-2 New spirobi([1,3,2]dithiagermole molecules **89**-**91**.

Studies on germafluorene polymers were published after commencing this work which demonstrated promising OFET and OSC properties,[197] reinforcing that Ge containing compounds are a highly underexplored avenue for the development of new materials, the potentials of which are only now beginning to be determined.

5.3. Synthesis

The compounds were synthesised in the same fashion as the dithiolene complexes in chapter 4, again involving the generation of intermediates **86**, **87** or **88** prior to treatment with $GeBr_4$ (scheme 5-1). No counterion is necessary as covalent bonding dominates and tetrahedral Ge centres are to be expected. As the compounds are diamagnetic, NMR analysis was possible, though the materials **90** and **91** demonstrated strong aggregation effects owing to π-π and S•••S interactions. This could be overcome in part by the addition of carbon disulfide to the NMR sample. Single crystals of **90** and **91** suitable for X-ray crystallographic analysis have been obtained and have been sent for analysis.

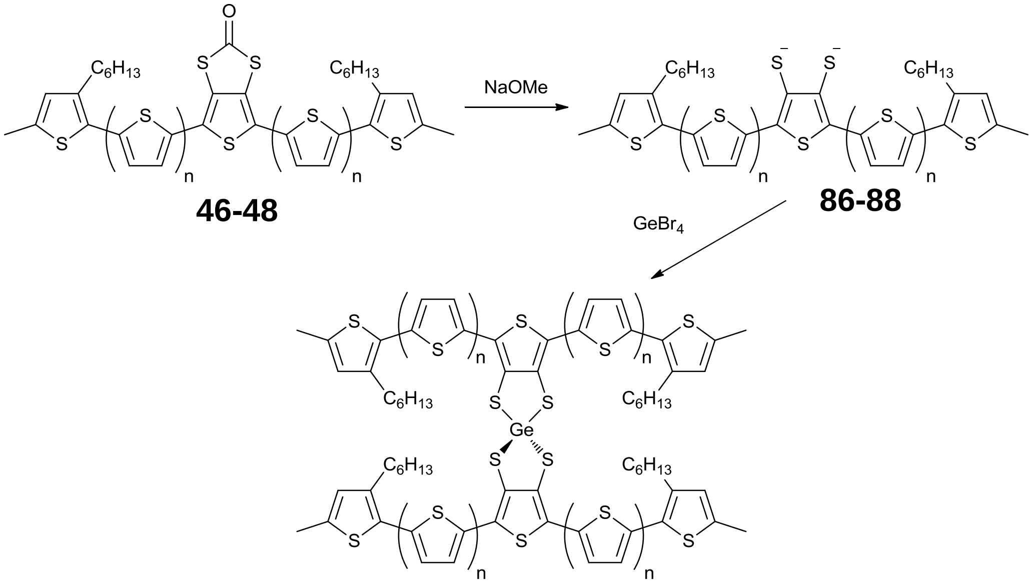

46-48

86-88

89-91

Scheme 5-1 Synthetic route followed for the synthesis of compounds **89-90**.

5.4. Absorption Spectroscopy and Electrochemistry of Spirocyclic Compounds 89-91

Absorption spectra were recorded in dichloromethane solution using a Shimadu UV-1800. CV measurements were taken using a BAS CV-50W potentiostat with *iR* compensation and performed using glassy carbon, platinum wire and silver wire as the working, counter, and reference electrodes respectively. Substrates were dissolved in anhydrous dichloromethane solution (*ca.* 10^{-4} M) containing *n*-Bu_4NPF_6 as the supporting electrolyte and all solutions were degassed with argon. All measurements are referenced against the $E_{1/2}$ of the Fc/Fc^+ redox couple. Spectroelectrochemical experiments were conducted using a UNICAM UV300 instrument and a CH Instruments 660A potentiostat. Measurements were taken of films drop-cast onto ITO coated glass and suspended in a solution of *n*-Bu_4NPF_6 in acetonitrile.

5.4.1. Absorption Spectroscopy

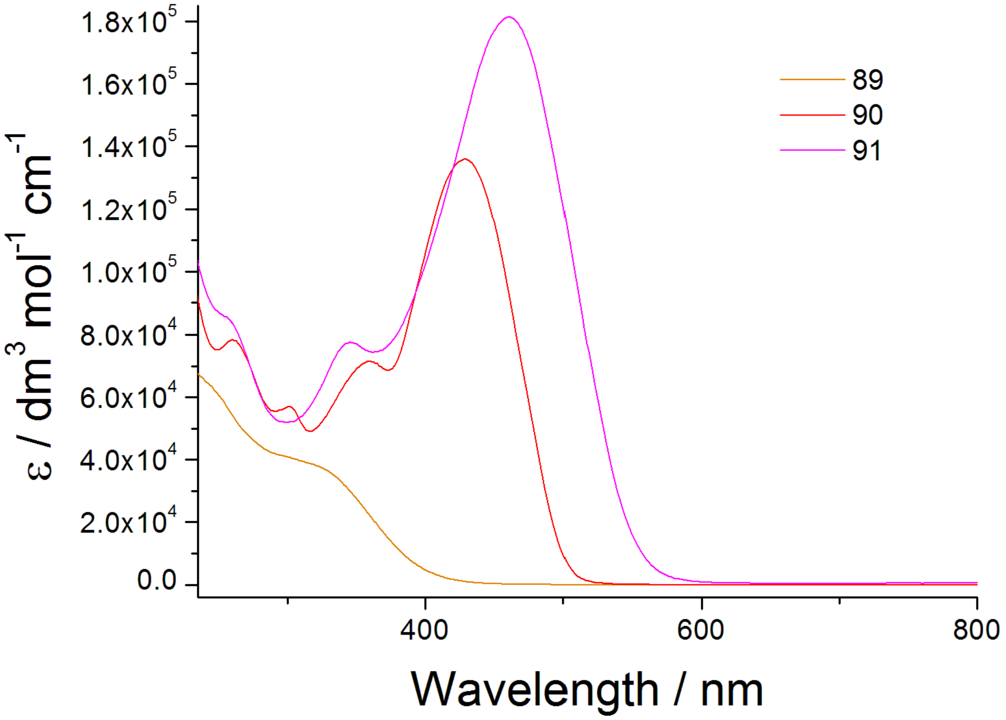

Figure 5-3 Absorption spectra for compounds **89-91**.

The absorption spectra of compounds **89-91** are shown in figure 5-2. The absorption profiles of all three molecules are dominated by the π-π* transition of the oligothiophene chains (λ_{max} and optical HOMO-LUMO gap values shown in table 5-1). This peak is redshifted as the conjugation length of the oligothiophene chain increases.

Comparison with the precursors **46**, **47** and **48** shows that the optical HOMO-LUMO gap has been increased by 0.06 eV in **89**, and 0.03 eV **90** whereas that of the bis(septithiophene) derivative **91** has demonstrated a decrease of 0.04 eV. This appears to be the beginning of a trend, with the extent of electronic communication between the conjugated oligothiophene chains decreasing with increasing chain length. Development of a nonathiophene derivative, though complex, could serve to confirm this.

Table 5-1 Absorption maxima observed for spirocyclic compounds **89**-**91**.

	λ_{max} / nm	HOMO-LUMO gap / eV[a]
89	305	3.09
90	430	2.47
91	459	2.25

[a] Optical HOMO-LUMO gap calculated from the onset of the longest wavelength absorption.

The bis(quinquethiophene) molecule **90** and the bis(septithiophene) species **91** have demonstrated incredibly high molar absorptivities, verging on almost three times those observed in their respective precursor (table 5-2). Similar spirocentric septithiophene dimers featuring a Si centre bound between four C atoms, demonstrated a two-fold increase in intensity, which was attributed to no or limited communication between the orthogonally bound oligothiophenes.[195] The three-fold increase observed with the molecules here is unprecedented and indicates much more exotic electronic behaviour.

Table 5-2 Molar extinction coefficients of oligothiophene precursors **46-48** and their respective spirobi([1,3,2]dithiagermole) dimers **89-91**.

	ε / dm^3 mol^{-1} cm^{-1}
46	19,729
47	45,327
48	61,202
89	40,274
90	135,910
91	181,279

5.4.2. Electrochemistry

The electrochemical properties of these molecules were studied using cyclic voltammetry and square-wave voltammetry; the results are shown in figure 5-4 and figure 5-5 respectively, and summarised in table 5-3.

Table 5-3 CV results for compounds **89-91**.

	E_{1ox} / V	E_{2ox} / V	E_{3ox} / V	E_{4ox} / V	E_{1red} / V	E_{2red} / V
89	+0.59/0.45^{q}	+0.88/0.71^{q}	+1.10/0.89^{q}		-1.51^{irr}	-2.21^{irr}
90	+0.29/0.25^{q}	+0.44/0.34^{q}	+0.70/0.64	+1.14^{irr}	-1.49^{irr}	
91	+0.14^{q}	+0.85^{q}	+1.00/0.96^{q}	+1.20/1.11^{q}	-1.64^{irr}	

^{q}Quasi-reversible peak. ^{irr}Irreversible peak

Bis(terthiophene) **89** displays three quasi-reversible oxidation processes, occurring at $E_{1/2}$ of +0.52, +0.80, and +1.00 V. The first of these oxidations corresponds to radical cation formation on a terthiophene chain, and the second and third to the formation of a second radical cation on the other terthiophene chain and oxidation to the dication respectively. No further processes are observed in the SWV. At reducing potentials, **89** shows two irreversible reductions at -1.51 eV and -2.21 eV corresponding to sequential radical anion formation on the two terthiophene chains.

The bis(quinquethiophene) molecule **90** demonstrates two quasi-reversible oxidation processes at $E_{1/2}$ of +0.27, and +0.39. The low potential and close proximity of these waves attributes them both to radical cation formation on the individual quinquethiophene chains. These are followed by a reversible oxidation generating a single dication at +0.67 V and a final irreversible oxidation to form a second dication at +1.14 V. There is a notable loss of peak definition upon reversal of potential, possibly due to diffusion of these large molecules into solution.

For the largest of the series, the bis(septithiophene) **91**, there is a broad quasi-reversible wave, reminiscent of that observed for the bis(septithiophene)-TTF **72** (structure shown in figure 3-1, CV in figure 3-3) and for similar spirocentric septithiophenes reported by Tour *et al.* stretching between peaks at +0.14 and +0.85 V. SWV analysis (figure 3-4) shows that this appears to be comprised of four waves with peaks at +0.14, +0.23, +0.35, and +0.59 V, prior to the much more well defined peak at +0.82 V. These early peaks are all very small. Like **72**, this molecule aggregates extensively. The fragmented nature and low potential of these early smaller peaks, indicates that they could arise from the formation of radical cations on the septithiophene chains of molecules in slightly different conformations in solution, as opposed to individual discrete 1-electron oxidations. In the CV, the quasi-reversible peaks at +0.85 V and +1.00 V are attributed to sequential dication formation on the septithiophene chains, and the final quasi-reversible oxidation with a peak at +1.20 V stems from the formation of a radical trication on at least one of the septithiophene chains.

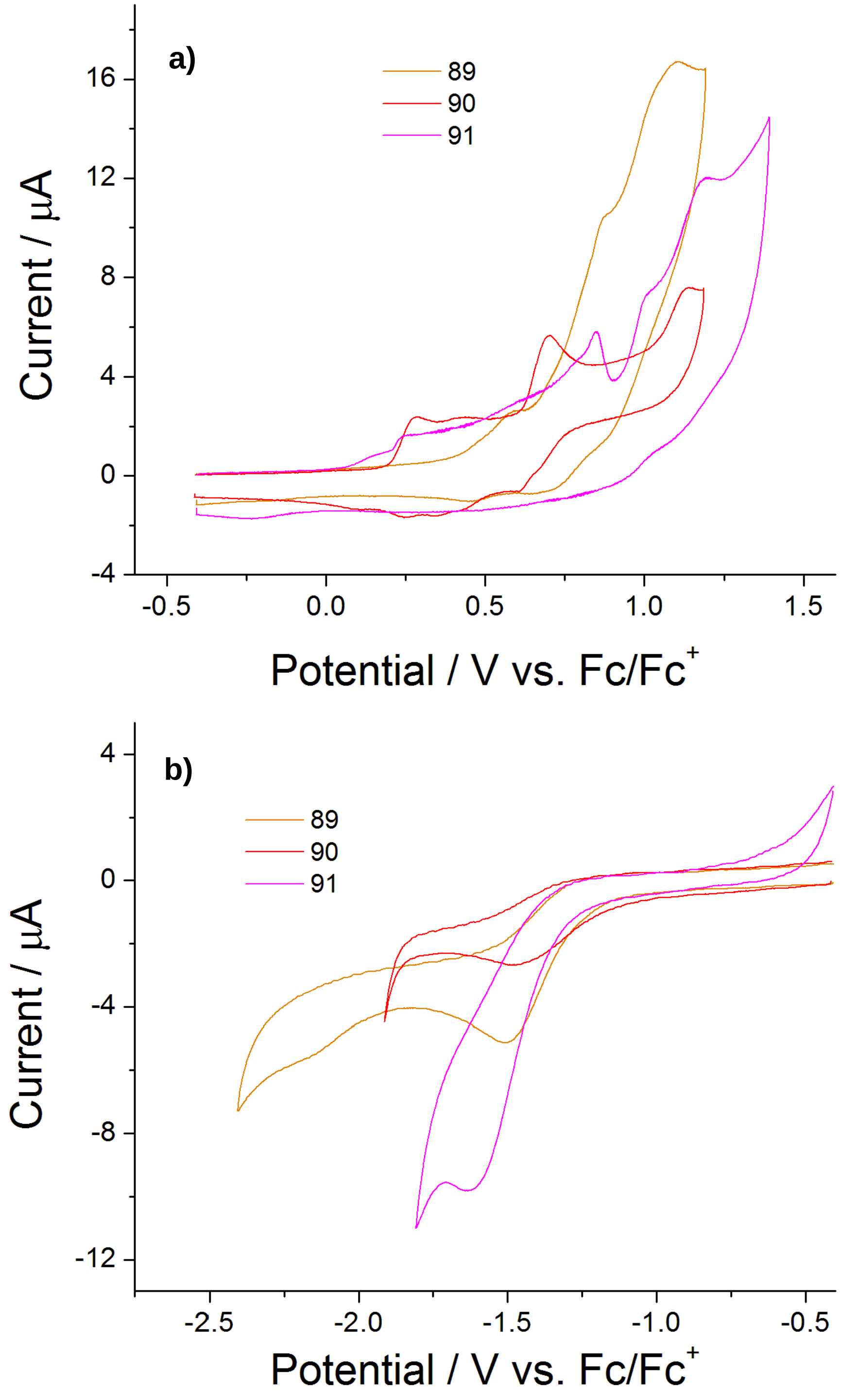

Figure 5-4 Oxidation and reduction scans for spirocyclic molecules **89**-**91**.

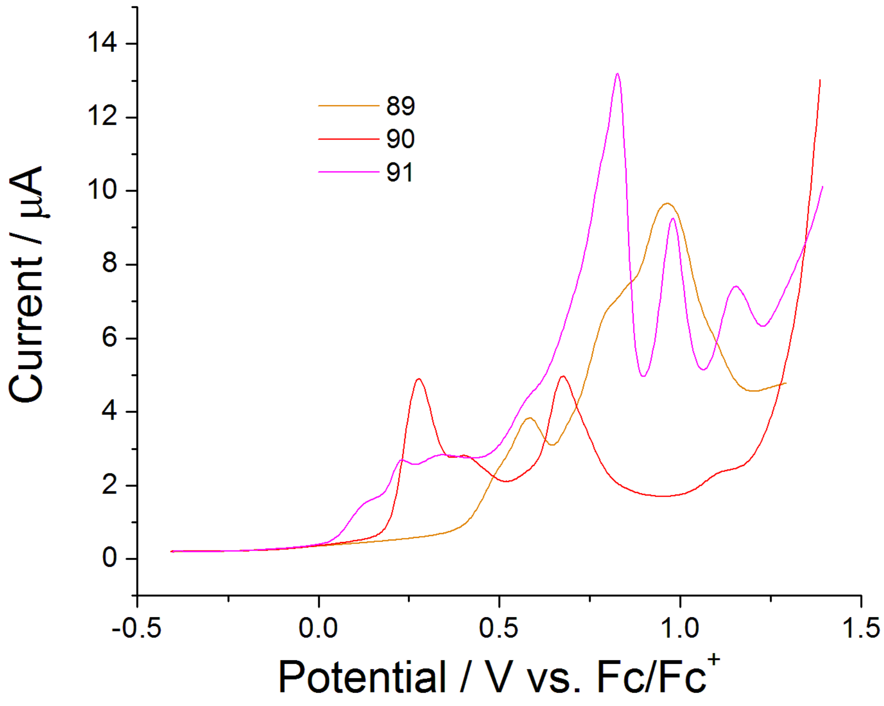

Figure 5-5 SWV results for compounds **89**-**91**.

HOMO and LUMO levels, and the electrochemical HOMO-LUMO gaps have been calculated using the combined oxidation and reduction scans (figure 5-6 and table 5-4). The electrochemical HOMO-LUMO gaps of all 3 molecules are much smaller than the optical gaps (table 5-1), indicating a greater influence of the electron rich spirobi([1,3,2]dithiagermole) centre on the redox properties than on the energy of the π-π* transition.

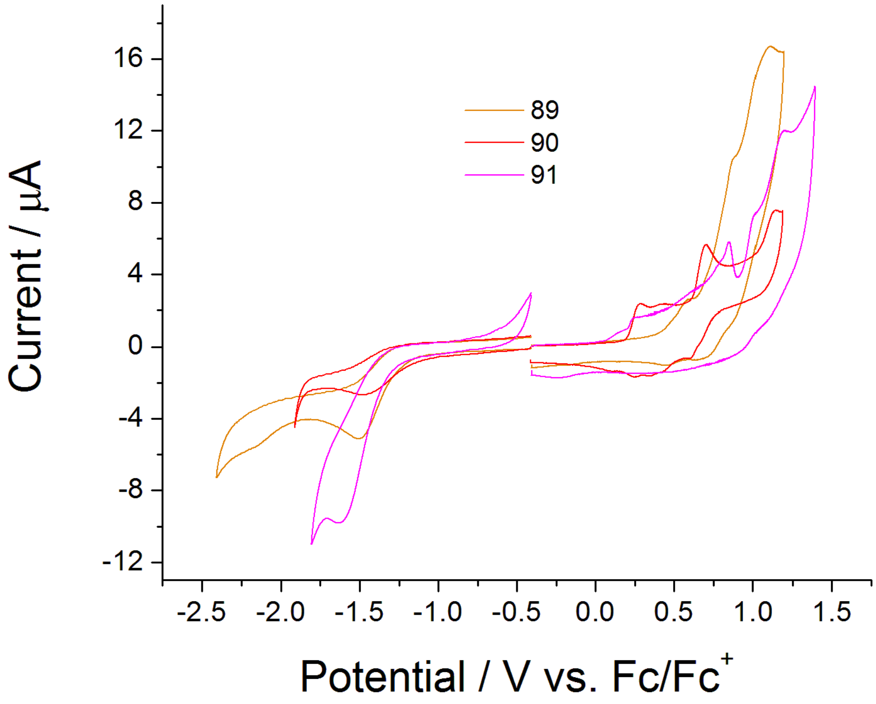

Figure 5-6 Combined oxidation and reduction scans used for HOMO and LUMO level calculation.

In comparison with precursors **46-48** (table 2-3), the introduction of the electron rich spirobi([1,3,2]dithiagermole) centre has resulted in the HOMO levels of all three compounds **89**, **90**, and **91** being raised by 0.15, 0.11, and 0.16 eV respectively, whilst the energies of the LUMOs have been lowered much more substantially by 0.74, 0.76, and 0.39 eV. This is very different to the effects noticed from the introduction of the TTF centre in compounds **70-72** where it was the HOMO levels which were raised much more substantially.

The extent to which the LUMO was lowered in the terthiophene system **89** and the quinquethiophene system **90** is particularly notable and has demonstrated the potential for the use of this structural characteristic in developing future low band gap materials.

Table 5-4 HOMO and LUMO levels and electrochemical HOMO-LUMO gaps of **89**-**91**.

	HOMO / eV[a]	LUMO / eV[a]	HOMO-LUMO gap / eV[b]
89	-5.19	-3.58	1.61
90	-5.10	-3.64	1.46
91	-5.02	-3.47	1.55

[a] HOMO and LUMO levels are calculated from the onset of the first peak of the corresponding redox wave and are referenced to ferrocene which has a HOMO of -4.8 eV. [b] Electrochemical HOMO-LUMO gap is the energy gap between the HOMO and LUMO levels.

The very large drop in the energy of LUMO has given these materials particularly low electrochemical HOMO-LUMO gaps of 1.61 eV for bis(terthiophene) **89**, 1.46 eV for bis(quinquethiophene) **90**, and 1.55 eV for bis(septithiophene) **91**. It is worth noting the unconventional trend in this series. Whilst the HOMO-LUMO gaps of **89** and **91** demonstrate the expected trend of decreasing HOMO-LUMO gap with increasing oligothiophene chain length, the intermediate chain length molecule **90** actually demonstrates the lowest HOMO-LUMO gap (by 0.09 eV) compared to the longest chain length molecule **91**, due to its particularly low LUMO level.

Unlike in all of the bis(quinquethiophene) based molecules and complexes described in previous chapters, in which the hexyl chains were expected to distort the predominantly planar structures, the orientation of the hexyl chains in the spirocentric bis(quinquethiophene) molecule **90** should allow for improved chain planarity and improved orbital overlap between adjacent molecules, contributing towards the lowering of the LUMO. X-ray crystallographic analysis of crystals obtained of both **90** and **91** will help to confirm this.

The particularly low first oxidation potentials, particularly for **90** and **91**, compared to the precursors **46-48**, indicates a more electronically delocalised structure implying that delocalisation over the spirocentre is indeed occurring.[184] These first oxidation potentials are typically lower than those observed with oligothiophenes featuring an SiC_4 spirocentre, again indicating improved spiroconjugation effects.[184, 195]

5.4.3. Spectroelectrochemistry

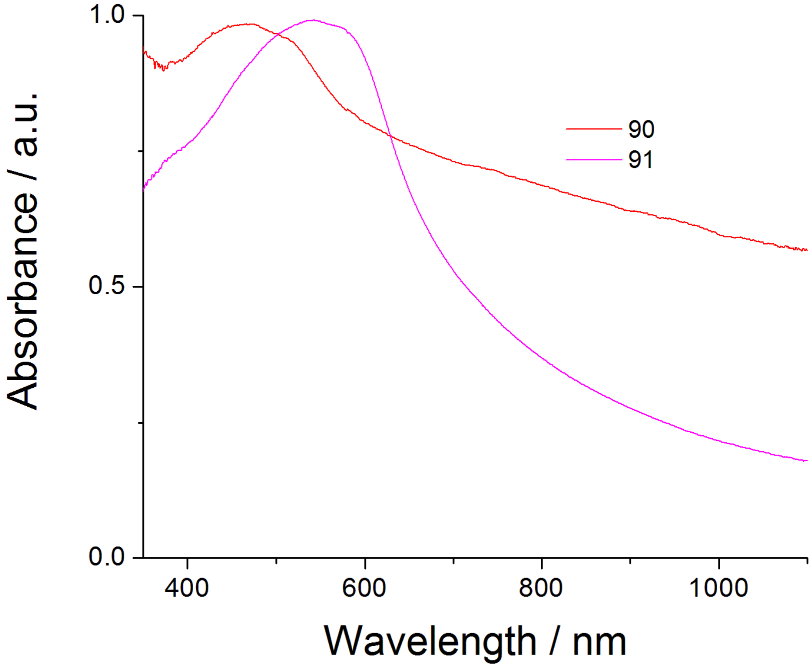

Figure 5-7 Absorption spectra of thin films of bis(quinquethiophene) **90** and bis(septithiophene) **91**.

Thin films of **90** and **91** were dropcast onto an ITO slide from dilute CH_2Cl_2 solution. Compound **89** is an oil and so no films could be obtained.

The solid state absorption spectrum of **90** (figure 5-7) demonstrates an absorption maximum at 472 nm. This is redshifted by 42 nm compared to its solution spectrum and is due to the π-π* transitions of the oligothiophene chains. The signal is also redshifted by 24 nm compared to the solid state spectrum of its precursor, the quinquethiophene **47**.

The absorption band of the solid state spectrum of **91** demonstrates an absorption maxima at 547 nm, with a shoulder at 570 nm. This broad absorption band is due to π-π* transitions of the septithiophene chains. The longest wavelength peak in the solid state spectrum of the septithiophene precursor occurs at 572 nm, very close to that seen here, though the absorption maximum is blue shifted by 52 nm. Compared to the solution spectrum, the peak maximum of **91** is red shifted by 111 nm.

The tail of the spectra of both **90** and **91** extends over the entire visible window, which, coupled with the high absorptivity, makes such molecules exciting candidates for OSC applications.

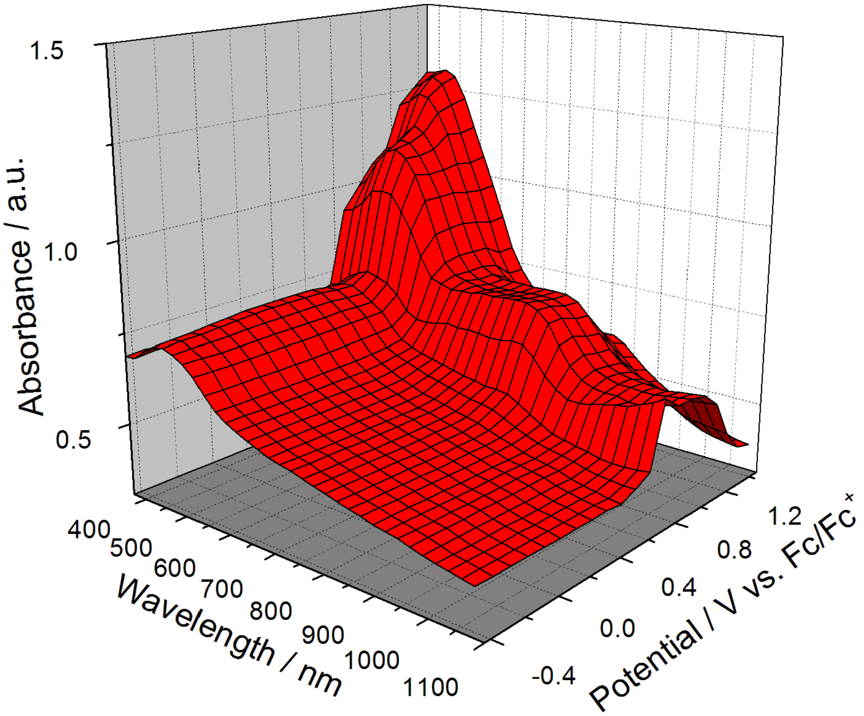

Figure 5-8 SEC of a thin film of bis(quinquethiophene) spirobi([1,3,2]dithiagermole) **90**.

The SEC plot for the film of **90** is shown in figure 5-8. When the potential is increased to +0.70 V oxidation, forming a radical cation, occurs whereupon the intensity of absorption increases across the entire visible window, with peaks at 460 and 795 nm and a NIR band at >1100 nm. If the potential is increased above +1.20 V, dication formation occurs resulting in loss of the NIR band, and a decrease in the intensity of the band at 795 nm, while the main π-π* absorption band is blueshifted to 423 nm and increases in intensity.

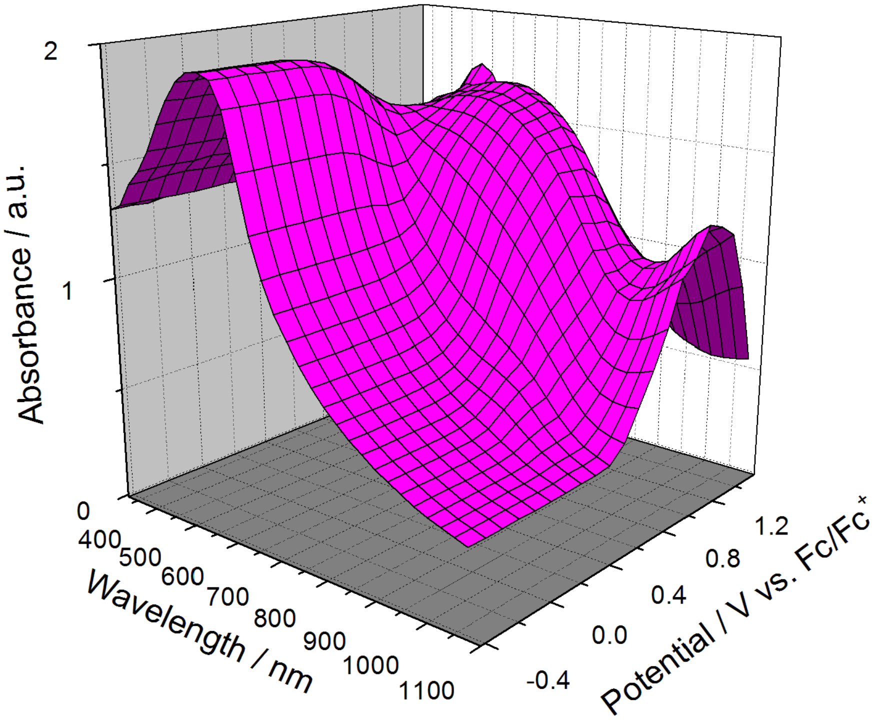

Figure 5-9 SEC of a thin film of bis(septithiophene) spirobi([1,3,2]dithiagermole) **91**.

The SEC plot for the bis(septithiophene) **91** is depicted in figure 5-9. As the potential is increased past +0.40 V, radical cation formation is observed resulting in loss of intensity of the π-π* transition, while broad and intense new peaks at 657 and >1100 nm emerge. As the potential is increased above +1.40 V, dication formation occurs resulting in sharp loss of intensity of both the peak at 657 nm and the NIR band, while the intensity of the π-π* band recovers and is blueshifted to 485 nm.

5.5. Conclusions and Further Work

The synthesis of three new methyl-capped oligothiophene dimers, featuring oligothiophene chain lengths of three, five, and seven thiophenes, bound *via* a unique electron-rich spirobi([1,3,2]dithiagermole) core, has been presented.

These molecules aggregate in solution and have demonstrated very high molar extinction coefficients with low electrochemical HOMO-LUMO gaps. The low HOMO-LUMO gaps stem from a large drop in the LUMO energy compared to the single chain precursors.

From solid state SEC studies, it has been observed that neutral films of the bis(quinquethiophene) and bis(septithiophene) compounds display absorptions which extend over the entire visible window. Upon oxidation, the excited states of these molecules have demonstrated absorptions of similar or greater intensity to the non-oxidised films. Once more, these occur over the entire visible region.

Single crystals of the bis(quinquethiophene) and bis(septithiophene) compounds have been obtained and crystallographic analysis is currently ongoing.

As a result of the solubility, high absorptivity and broad absorption profile of both the neutral and oxidised species, the study of the application of these materials in OSC devices is currently underway.

Spirocentres are known to have useful morphological properties that can improve processability, such as readily forming amorphous glassy states and good thermal stability.[183, 184] Both of these will be investigated in future work. Also unlike the highly absorbing metal complexes discussed in chapter 4, these compounds are not salts and so should demonstrate improved processability and increased film homogeneity regardless. Additionally, alongside solution processing, vapour phase techniques such as vacuum deposition may be applicable for device manufacture.

To confirm whether the large and electron rich Ge centre is improving the extent of electronic communication between the oligothiophene chains, and whether it is the cause of such high extinction coefficients, the development and study of analogues featuring C and Si spiroatoms would be very useful. The influence of the spiroatom on the observed LUMO level could also be investigated in this way. This should be achievable simply by the use of CBr_4 or $SiCl_4$ in place of $GeBr_4$ in the synthetic route detailed above. Alternatively, Sn spirocentres could be employed by the use of $SnCl_4$ and the effect of descending the group could be investigated.

Whilst developing these compounds, efforts towards the synthesis of diamagnetic, homoleptic tris(dithiolene) Sn(IV) complexes featuring terthiophene **92**, quinquethiophene **93**, or septithiophene **94** chains (figure 5-10), using methodology similar to that used for the dithiolene complexes in chapter 4 was attempted. Dithiolene complexes of Sn have rarely been studied. The few examples known have demonstrated pseudo-octahedral geometries as opposed to the trigonal prismatic geometry typically observed in tris(dithiolene) complexes.[187, 198, 199] It would be interesting to investigate the properties which result from incorporating these extended ligands into this geometry. Early attempts to synthesise these complexes as Et_4N^+ salts have proven inconclusive, though single crystals have been isolated of the tris(septithiophene) complex **94**, which will also be subjected to X-ray crystallographic analysis.

92

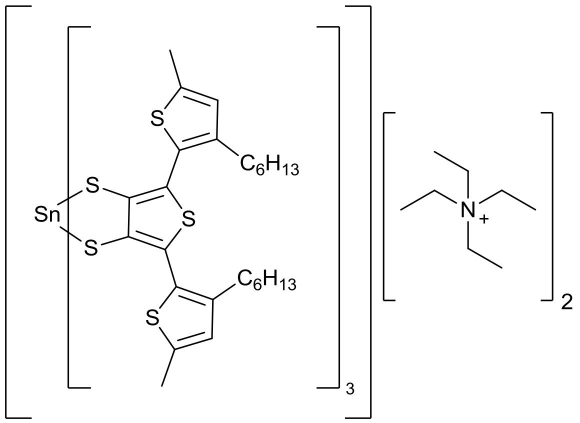

93

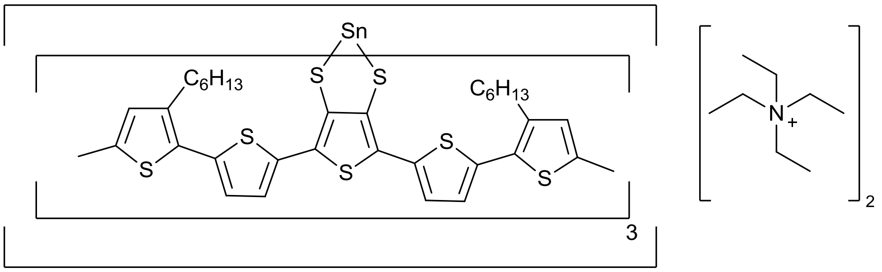

94

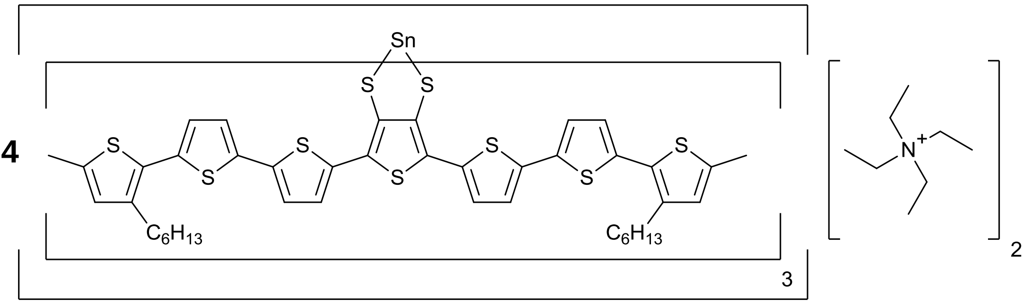

Figure 5-10 Diamagnetic Sn tris(dithiolene) complexes under development.

Chapter 6: Experimental

General Experimental

Synthesis: LDA was purchased from Sigma Aldrich and titrated against menthol with 2,2'-bipyridyl as indicator before use. NaOMe was prepared freshly before use. NBS was purchased from Sigma Aldrich, recrystallised from water and dried under vacuum, $Pd(PPh_3)_4$ was synthesised prior to use and stored under N_2. Unless otherwise stated all other reagents were sourced commercially and used without further purification. Dry solvents were obtained from a solvent purification system (SPS 400 from Innovative Technologies) using alumina as drying agent. Melting points were taken using a TA Instruments DSC Q1000 Differential Scanning Calorimeter and are uncorrected. ^1H and ^{13}C NMR spectra were recorded on a Bruker DRX 500 apparatus at 500.13 and 125.76 MHz. Chemical shifts are given in ppm; all J values are in Hz. Elemental analyses were obtained on a Perkin-Elmer 2400 analyzer. MS LDI-TOF spectra were run on a Shimadzu Axima-CFR spectrometer (mass range 1-150000 Da). TGA analysis was performed using a Perkin Elmer Thermogravimetric Analyzer TGA7 under a constant flow of helium.

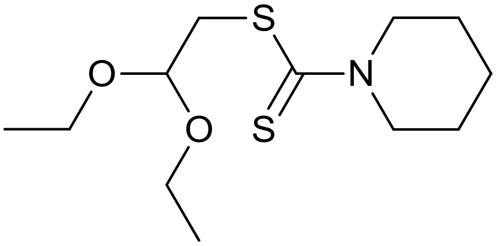

Formylmethyl piperidine-1-carbodithiolate diethyl acetal (60):[157]

NaOH pellets (80 g, 2 mol) were added portionwise over ca. 15 min to an ice-cooled, mechanically stirred solution of piperidine (198 mL, 2 mol) in EtOH (750 mL). CS_2 (120 mL, 2 mol) was then added dropwise over ca. 1 h and the reaction was left to stir for 1 h at 0 °C, whereupon the solution turned yellow and a white precipitate of sodium thiocarbamate formed, before the reaction was heated to reflux for a further 3 h. Dropwise addition of bromoacetaldehyde diethyl acetal (300 mL, 2 mol) over 0.5 hr resulted in the formation of a deep red solution which was then heated to reflux for 24 h. The mixture was allowed to cool to room temperature before addition of H_2O (1 L) and extraction of the mixture with CH_2Cl_2 (3 × 350 mL). The organic extracts were combined and washed with H_2O (3 × 250 mL), dried over $MgSO_4$ and the solvent removed under reduced pressure to give a wine red oil which solidified upon standing. Recrystallisation twice from hexane (with cooling in a freezer) afforded the product as an off white solid (405.5 g, 73.2%).

^1H NMR ($CDCl_3$): $\delta = 4.70$ (1H, t, $J = 5.50$ Hz), 4.30 (2H, bs), 3.93 (2H, bs), 3.72 (2H, dq, $J = 9.50$, $J = 7.00$), 3.64 (2H, dq, $J = 9.50$, $J = 7.00$), 3.61 (2H, d, 5.00), 1.71 (6H, bs), 1.24 (6H, t, $J = 7.25$).

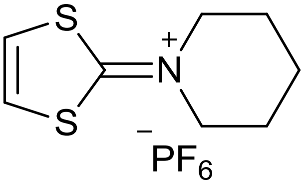

2-Piperidino-1,3-dithiolium hexafluorophosphate (61):[157]

Formylmethyl piperidine-1-carbodithiote diethyl acetal, **60**, (405.5 g, 1.47 mol) was added portionwise to ice cold H_2SO_4 (350 mL) over a period of 2 h before heating to 100 °C for 4 days. The reaction mixture was allowed to cool before being poured slowly into ice-cooled, stirred H_2O (1.5 L) containing HPF_6 (60% wt. in H_2O, 365 g, 1.5 mmol), yielding a heavy white precipitate. The precipitate was separated *via* filtration and washed with H_2O (*ca.* 2.5 L). The solid was then dissolved in CH_2Cl_2 (*ca.* 2.5 L) and the organic phase washed sequentially with H_2O (500 mL), saturated $NaHCO_3$ (500 mL) and H_2O (500 mL) before drying over $MgSO_4$. The solvent was evaporated under vacuum to the point of crystallisation, before Et_2O (500 mL) was added to precipitate the product as a grey white solid, which was collected by filtration and washed with Et_2O (500 mL) (397.2 g, 82%).

^{1}H NMR (acetone-d_6): δ = 7.75 (2H, s), 4.05 (4H, t, J = 6.00), 2.00 (4H, quintet, J = 7.00), 1.84 (2H, m).

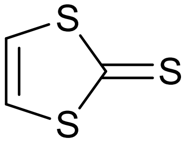

Vinylene trithiocarbonate (52):[200]

2-Piperidino-1,3-dithiolium hexafluorophosphate, **61**, (56.0 g, 169 mmol) and sodium hydrogen sulphide monohydrate (13.8 g, 186 mmol) were added portionwise to a stirred, ice cooled DMF/glacial acetic acid mixture (3:1, 300 mL) and left to stir overnight. The reaction mixture was then poured into water (300 mL) and extracted with Et_2O (4 × 175 mL). The organic extracts were combined and washed with water (3 × 175 mL), $NaHCO_3$ (3 × 175 mL), and again with water (175 mL), before drying ($MgSO_4$). The solvent was removed under reduced pressure. The crude product was dissolved in CH_2Cl_2 (200 mL) and stirred with decolourising charcoal for 15 minutes before filtering through a short silica column. The solvent was removed under reduced pressure to yield a yellow/orange solid which was stored in the fridge until required (11.23 g, 54 %).

^{1}H NMR ($CDCl_3$): $\delta = 7.10$ (s, 2H).

^{13}C NMR ($CDCl_3$): $\delta = 129.1$.

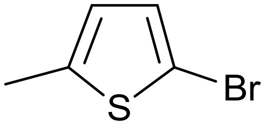

2-Bromo-5-methylthiophene (62):

Under exclusion of light, NBS (18.11 g, 101.86 mmol) was added portionwise to 2-methylthiophene (10.00 g, 101.86 mmol) in DMF (150 mL). The reaction was then stirred overnight at room temperature before being poured into water (600 mL). The suspension was extracted with Et_2O (3 × 150 mL) before the combined organic extracts were washed with brine, dried (Na_2SO_4) and the solvent removed under reduced pressure. The material was purified *via* column chromatography (silica, hexane) to give a colourless oil (14.96 g, 83%), which was used immediately to avoid any possible decomposition.

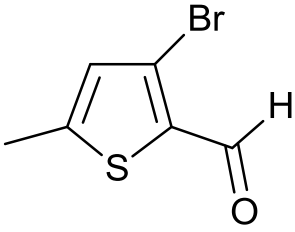

3-Bromo-5-methylthiophene-2-carbaldehyde (63):[158]

Under N_2, 2-bromo-5-methylthiophene, **62**, (14.96 g, 84.49 mmol) was dissolved in anhydrous THF and cooled to -70 °C. LDA.THF (1.5 M solution in cyclohexane, 67.6 mL, 101.39 mmol) was added dropwise and the reaction was stirred for 2 h. Dry DMF (8.58 g, 109.84 mmol) was added and the reaction was stirred at -70 °C for 30 min before being allowed to warm to room temperature and stirred overnight. The reaction mixture was poured into water and extracted with Et_2O (3 × 200 mL) before being dried (Na_2SO_4) and the solvent removed under reduced pressure. Purification was achieved by distillation under high vacuum (kugelrohr, b.p. 80 °C at 6.8×10^{-2} mbar) to give a black/brown oil, which was dissolved in CH_2Cl_2 and stirred with decolourising charcoal for 10 min before being filtered through a celite plug (eluting with CH_2Cl_2) to give a brown oil (11.00 g, 63%).

^1H NMR ($CDCl_3$): $\delta = 9.88$ (1H, s), 6.86 (1H, s), 2.56 (3H, s).

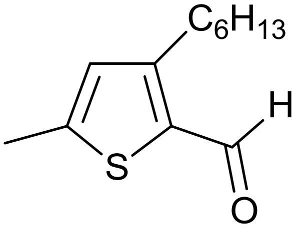

3-Hexyl-5-methylthiophene-2-carbaldehyde (49):

Under N_2, $ZnCl_2$ (11.58 g, 84.97 mmol) was suspended in dry THF (60 mL) and cooled to -60 °C. Hexyl lithium (2.3M in hexane, 33.58 mL, 77.24 mmol) was added slowly and the reaction was stirred for 30 min to generate hexylzinc chloride. The organozinc solution was then allowed to warm to room temperature before being added *via* cannula to a solution of **63** and $Pd(PPh_3)_4$ (1.55 g, 1.34 mmol) in THF (30 mL). The reaction was heated to reflux overnight then filtered prior to hydrolysis with 2N HCl (100 mL) and extraction with Et_2O (400 mL). The organic extract was washed with H_2O (2 × 150 mL), brine (2 × 150 mL), dried over $MgSO_4$ and the solvent was removed under reduced pressure. Purification was achieved by column chromatography (silica, CH_2Cl_2/hexane 2:1) to yield the desired product as a dark brown oil (7.60 g, 67 %).

^{1}H NMR ($CDCl_3$): $\delta = 9.93$ (1H, s), 6.69 (1H, m), 2.88 (2H, t, $J = 7.75$), 2.51 (3H, d, $J = 1.00$), 1.64 (2H, quintet, $J = 7.62$), 1.34 (6H, m), 0.89 (3H, t, $J = 7.00$).

^{13}C NMR ($CDCl_3$): $\delta = 181.8$, 154.0, 150.8, 136.1, 129.8, 31.8, 31.6, 29.2, 28.7, 22.7, 16.4, 14.3.

MS (MALDI): $m/z = 211$ $[M + H^+]^+$.

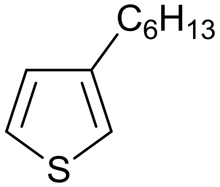

3-Hexylthiophene:[159]

To an ice cooled solution of 3-bromothiophene (25 g, 152.3 mmol) and $NiCl_2(dppp)_2$ (206 mg, 0.38 mmol) in dry Et_2O (275 mL), under N_2 was slowly added hexyl magnesium bromide (91.36 mL, 182.76 mmol). The ice bath was removed and the reaction left to stir for 3 h at room temperature. The reaction was quenched with water (*ca.* 100 mL) before removal of the organic phase. The aqueous phase was washed with Et_2O (2 × 50 mL) and the combined organic extracts dried ($MgSO_4$) before removal of solvent under reduced pressure. Purification was achieved *via* distillation under high vacuum (kugelrohr, b.p. 65 °C at 6.8×10^{-2} mbar) to obtain the product as a colourless oil (19.06 g, 74 %).

^{1}H NMR ($CDCl_3$): δ = 7.24 (1H, dd, J = 3.00, J = 5.00), 6.94 (2H, m), 2.63 (2H, t, J = 7.50), 1.64 (2H, m), 1.34 (6H, m), 0.90 (3H, t, J = 6.75).

^{13}C NMR ($CDCl_3$): δ = 143.5, 128.5, 125.2, 120.0, 31.9, 30.8, 30.5, 29.2, 22.8, 14.3.

MS (MALDI): m/z = 169 $[M + H^+]^+$.

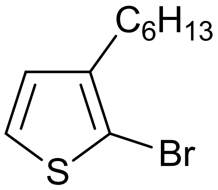

2-Bromo-3-hexylthiophene:[160]

Under exclusion of light, NBS (22.65 g, 134.58 mmol) was added portionwise to a stirred solution of 3-hexylthiophene (23.95 g, 134.58 mmol) in 1:1 chloroform/glacial acetic acid mixture (400 mL). The reaction was left to stir overnight at room temperature before being poured into H_2O (200 mL). The aqueous phase was extracted with CH_2Cl_2 (3 × 150 mL), and the combined organic phases were washed with satd. $NaHCO_3$ soln. (4 × 250 mL), and water (4 × 250 mL), before drying ($MgSO_4$), and evaporation of the solvent under reduced pressure to give the crude product as a brown oil. The oil was purified *via* distillation under high vacuum (kugelrohr, b.p. 95 °C at 6.8×10^{-2} mbar) to give a colourless oil (32.71 g, 98%).

^{1}H NMR ($CDCl_3$): δ = 7.19 (1H, d, J = 5.00), 6.80 (1H, d, J = 5.00), 2.58 (2H, t, J = 7.75), 1.60 (2H, quintet, J = 7.50), 1.33 (6H, m), 0.90 (3H, t, J = 7.00).

^{13}C NMR ($CDCl_3$): δ = 142.2, 128.5, 125.3, 109.0, 31.8, 29.9, 29.6, 29.1, 22.8, 14.3.

MS (CI): m/z = 246 $[M]^+$.

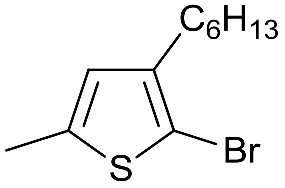

2-Bromo-3-hexyl-5-methylthiophene (64):

Under N_2, 2-bromo-3-hexylthiophene (32.71 g, 132.32 mmol) was dissolved in dry THF (150 mL) and cooled to -40 °C before dropwise addition of lithium diisopropylamide monotetrahydrofuran (LDA.THF) (1.5 M solution in cyclohexane, 88.20 mL, 132.32 mmol). The mixture was stirred at -40 °C for 30 min before dropwise addition of MeI (22.54 g, 158.79 mmol) at the same temperature. The reaction mixture was allowed to come to room temperature and stirred for 24 h, then hydrolysed with H_2O (500 mL) before extraction with Et_2O (3 × 125 mL), drying ($MgSO_4$) and removal of solvent under reduced pressure. The crude product was purified *via* distillation under high vacuum (kugelrohr, b.p. 113 °C at 6.8×10^{-2} mbar) to give a pale yellow oil (31.33 g, 91 %).

^{1}H NMR ($CDCl_3$): δ = 6.47 (1H, m), 2.48 (2H, t, J = 7.75), 2.39 (3H, d, J = 1.00), 1.54 (2H, quintet, J = 7.25), 1.31 (6H, m), 0.89 (3H, t, 7.00).

^{13}C NMR ($CDCl_3$): δ = 142.0, 139.5, 126.6, 105.3, 31.9, 29.9, 29.7, 29.1, 22.8, 15.8, 14.3.

MS (CI): m/z = 261 $[M + H^+]^+$.

Elemental Analysis: Found C, 50.06; H, 6.65; S, 11.98; Br, 29.70 Calculated: C, 50.59; H, 6.52; S, 12.27; Br, 30.62.

$Pd(PPh_3)_4$

Tetrakis(triphenylphosphine) palladium(0):

Palladium dichloride (0.50 g, 2.8 mmol) and triphenylphosphine (3.70 g, 14.10 mmol), suspended in dry DMSO (40 mL) and under N_2, were heated with rapid stirring to ca. 140 °C, whereupon complete dissolution occurs. Hydrazine monohydrate (0.56 g, 11.28 mmol) was then added rapidly *via* syringe (vigorous reaction) to produce a dark solution. The solution was cooled with the aid of a water bath until crystallisation began to occur (ca. 125 °C). The water bath was removed and the solution was then allowed to cool to room temperature without external cooling. The mixture was filtered under N_2 and the precipitate washed with MeOH (2 × 10 mL) and Et_2O (2 × 10 mL) to give the product as a bright yellow solid (3.12g, 95.7%).

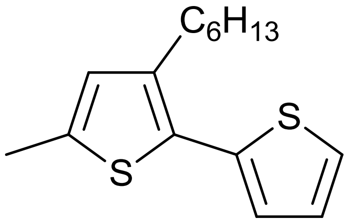

3-Hexyl-5-methyl-2,2'-bithiophene (65):

Under N_2, thiophene (5.36 g, 63.71 mmol) was dissolved in THF (50 mL) and cooled to -60 °C before dropwise addition of n-BuLi (2.5 M in hexanes) (25.5 mL, 63.71 mmol). After stirring for 30 min, a suspension of $ZnCl_2$ (8.68 g, 63.71 mmol) in THF (65 mL) was added to the lithiated thiophene *via* syringe at -60 °C before being allowed to warm to room temperature. The 2-thienylzinc bromide solution thus formed was added *via* cannula to **64** (13.87 g, 53.09 mmol) and $Pd(PPh_3)_4$ (1.54 g, 1.33 mmol) in THF (50 mL) and the mixture heated to reflux overnight, before being allowed to cool to room temperature before filtration and treatment with 2N HCl. The aqueous phase was then extracted with Et_2O (300 mL) and the combined organic phases were washed with H_2O (2 × 150 mL) and brine (2 × 150 mL) before drying ($MgSO_4$). Evaporation of the solvent under reduced pressure yielded a crude yellow oil which was purified *via* distillation under high vacuum (kugelrohr, b.p. 125 °C at 6.8 × 10^{-2} mbar) before column chromatography (silica, petroleum ether) to give **65** as a colourless oil (9.54 g, 67%).

^{1}H NMR ($CDCl_3$): δ = 7.26 (1H, dd, J = 4.50, J = 1.75), 7.05 (2H, m), 6.61 (1H, m), 2.68 (2H, t, J = 8.00), 2.46 (3H, d, J = 3.50), 1.60 (2H, quintet, J = 7.87), 1.31 (6H, m), 0.90, (3H, t, J = 7.00).

^{13}C NMR ($CDCl_3$): δ = 139.8, 138.3, 136.9, 128.5, 128.2, 127.4, 125.6, 124.9, 31.9, 30.9, 29.5, 22.8, 15.4, 14.3.

MS (CI): m/z = 265 [M + H$^+$]$^+$.

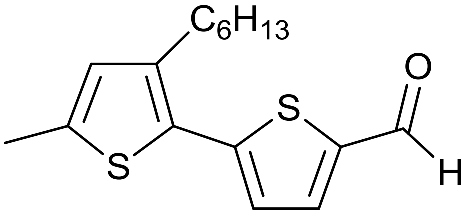

3'Hexyl-5'-methyl-[2,2'-bithiophene]-5-carbaldehyde (50):

Under N_2, 3-Hexyl-5-methyl-2,2'-bithiophene (7.39 g, 27.94 mmol) was dissolved in dry THF (100 mL) and cooled to 0 °C. *n*-BuLi (2.36 M in hexanes, 15.29 mL, 36.33 mmol) was added dropwise and the reaction was stirred for 15 min. Dry DMF (3.01 mL, 36.33 mmol) was added and the reaction was stirred overnight at room temperature. The reaction mixture was then poured into water (200 mL) and extracted with ethyl acetate (3 × 100 mL) before the combined organic extracts were washed with water (3 × 150 mL), dried over $MgSO_4$ and the solvent removed under reduced pressure. The product was purified *via* column chromatography (silica, $CHCl_3$/ hexane 3:2), followed by distillation under high vacuum (kugelrohr, b.p. 175 °C at 6.8 × 10^{-2} mbar) to give the product as a yellow oil (6.35 g, 78 %).

^{1}H NMR ($CDCl_3$): δ = 9.87 (1H, s), 7.68 (1H, d, J = 4.00), 7.15 (1H, d, J = 4.00), 6.65 (1H, d, J = 0.50), 2.75 (2H, t, J = 7.75), 2.47 (3H, d, J = 1.00), 1.64 (2H, quintet, J = 7.75), 1.36 (6H, m), 0.90 (3H, t, J = 7.00).

^{13}C NMR ($CDCl_3$): δ = 182.8, 147.3, 142.5, 141.8, 140.8, 137.1, 129.4, 127.5, 125.6, 31.2, 30.5, 29.9, 29.4, 22.8, 15.5, 14.2.

MS (MALDI): *m/z* = 291 [M - H]$^+$.

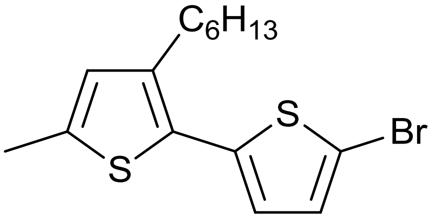

5'-Bromo-3-hexyl-5-methyl-2,2'-bithiophene (66):

Under exclusion of light, NBS (4.65 g, 26.13 mmol) was added portionwise to a stirred solution of **65** (6.91 g, 26.13 mmol) in 1:1 chloroform/glacial acetic acid mixture (200 mL). The reaction was left to stir for 3 h at room temperature before being poured into H_2O (350 mL). The aqueous phase was extracted with CH_2Cl_2 (3 × 125 mL) and the combined organic phases were washed with satd. $NaHCO_3$ soln. (3 × 200 mL) and water (3 × 200 mL) before drying ($MgSO_4$). Evaporation of the solvent under reduced pressure gave the crude product as brown oil. The oil was purified *via* distillation under high vacuum (kugelrohr, b.p. 185 °C at 6.8×10^{-2} mbar) to give a light yellow oil (8.62 g, 96 %).

^{1}H NMR ($CDCl_3$): δ = 6.99 (1H, d, J = 4.00), 6.79 (1H, d, J = 4.00), 6.59 (1H, m, J = 1.00), 2.63 (2H, t, J = 8.25), 2.44 (3H, d, J = 1.00), 1.58 (2H, quintet, J = 7.50), 1.30 (6H, m), 0.90 (3H, t, J = 7.00).

^{13}C NMR ($CDCl_3$): δ = 140.5, 138.9, 138.4, 130.3, 128.5, 127.3, 125.8, 111.3, 31.9, 30.9, 29.4, 22.8, 15.5, 14.3.

MS (CI): *m/z* = 343 [M + H$^+$]$^+$.

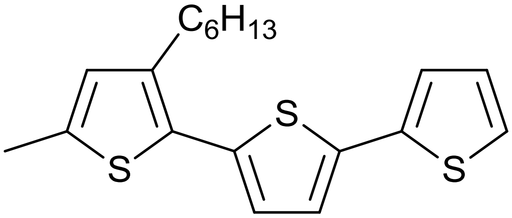

5-Methyl-3-hexyl-2,2':5',2"-terthiophene (67):

Compound **66** (4.33 g, 12.57 mmol) and Pd(dppf)Cl_2.CH_2Cl_2 (103 mg, 0.126 mmol) were placed under N_2 and dissolved in dry THF (75 mL) before being cooled to 0 °C. Thiophen-2-yl-magnesium bromide (1.0 M solution in THF, 13.83 mL, 13.83 mmol) was added slowly and the reaction mixture was stirred for 1 h at room temperature. The reaction mixture was hydrolysed with satd. NH_4Cl soln. (50 mL), which was followed by the addition of hexane (125 mL). Et_2O (400 mL) was added before the organic phase was washed with water (3 × 250 mL) and dried ($MgSO_4$). The solvent was removed under reduced pressure to give the crude product, which was purified *via* column chromatography (silica, petroleum/ CH_2Cl_2 10:1) and finally by distillation under high vacuum (kugelrohr, b.p. 240 °C at 6.8×10^{-2} mbar) to give a bright yellow oil (3.85 g, 88 %).

^1H NMR ($CDCl_3$): δ = 7.21 (1H, dd, J = 5.00, J = 1.00), 7.18 (1H, dd, J = 3.50, J = 1.00), 7.10 (1H, d, J = 3.50), 7.03 (1H, dd, J = 5.50, J = 3.00), 6.95 (1H, d, J = 3.50), 6.61 (1H, m), 2.70 (2H, t, J = 7.75), 2.46 (3H, d, J = 0.50), 1.63 (2H, quintet, J = 7.88), 1.32 (6H, m), 0.90 (3H, t, J = 6.5).

^{13}C NMR ($CDCl_3$): δ = 140.0, 138.5, 137.5, 136.7, 135.9, 128.7, 128.0, 127.7, 124.5, 124.1, 123.7, 31.9, 30.8, 29.6, 29.5, 22.8, 15.4, 14.3.

MS (MALDI): m/z = 346 $[M]^+$.

Elemental Analysis: Found C, 65.98; H, 6.32; S, 27.58 Calculated: C, 65.90; H, 6.36; S, 27.75.

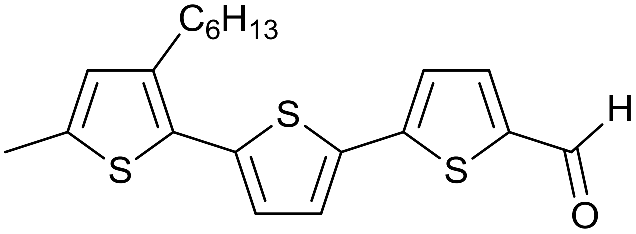

5-Methyl-3-hexyl-2,2':5',2"-terthiophene-5"-carboxaldehyde (51):

Under N_2, terthiophene **67** (3.32 g, 9.57 mmol) in dry THF (50 mL) was cooled to 0 °C. *n*-BuLi (2.5 M in hexanes, 5.0 mL, 12.43 mmol) was added dropwise and the reaction was stirred at 0 °C for 15 min. Dry DMF (909 mg, 12.43 mmol) was added and the reaction was heated to reflux for 2.5 h. The mixture was poured into water (300 mL) and extracted with ethyl acetate (3 × 200 mL), before the combined organic extracts were washed with water (3 × 200 mL), dried ($MgSO_4$) and the solvent removed under reduced pressure. Purification was achieved *via* column chromatography (silica, CH_2Cl_2/petroleum 2:1) to yield the product as, red/orange crystals which may be recrystallised from hexane (2.96 g, 83 %). m.p. 60 – 61 °C.

^{1}H NMR ($CDCl_3$): δ = 9.87 (1H, s), 7.68 (1H, d, J = 4.00), 7.30 (1H, d, J = 3.50), 7.24 (1H, d, J = 4.00), 7.01 (1H, d, J = 4.00), 6.63 (1H, m), 2.71 (2H, t, J = 7.75), 2.46 (3H, d, J = 1.00), 1.63 (2H, quintet, J = 7.62), 1.33 (6H, m), 0.89 (3H, t, 7.00).

^{13}C NMR ($CDCl_3$): δ = 182.6, 147.36, 141.6, 140.8, 139.3, 139.0, 137.6, 134.9, 128.9, 127.5, 126.7, 126.3, 124.0, 31.9, 30.7, 29.7, 29.4, 22.8, 15.5, 14.3.

MS (MALDI): m/z = 375 $[M + H^+]^+$, 397 $[M + Na^+]^+$.

Elemental Analysis: Found C, 63.76; H, 5.99; S, 25.83 Calculated: C, 64.13; H, 5.92; S, 25.68.

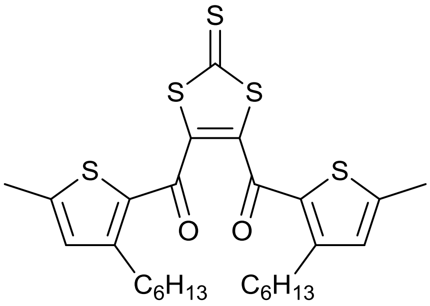

(2-Thioxo-1,3-dithiole-4,5-diyl)bis((3-hexyl-5-methylthiophen-2-yl)methanone) (53):

Under N_2, VTC (**52**) (612 mg, 4.56 mmol) was dissolved in dry THF (20 mL) at -55 °C. LDA.THF (1.5 M solution in cyclohexane, 3.34 mL, 5.02 mmol) was added and the reaction was stirred for 20 min at -55 °C. Compound **49** (1.06 g, 5.03 mmol) was added dropwise as a solution in dry THF (15 mL) before the reaction was stirred for a further 20 min at -55 °C. A second equivalent of LDA.THF (1.5 M solution in cyclohexane, 3.34 mL, 5.02 mmol) was added and the reaction was stirred for 15 min at -55 °C. The cooling bath temperature was reduced to -80 °C, and a second equivalent of **49** (1.06 g, 5.02 mmol) in dry THF (15 mL) was added. The reaction was allowed to continue until the reaction temperature warmed to -50 °C, whereupon the reaction was allowed to attain room temperature without external cooling. The reaction mixture was then poured into a solution of saturated $NaHCO_3$ (200 mL) to which KBr (20 g) was added. The product was extracted with ethyl acetate (3 × 60 mL) and the combined organic layers were dried over Na_2SO_4. The solvent was removed under reduced pressure and the residue was purified *via* column chromatography (silica, CH_2Cl_2 then ethyl acetate) to obtain the mono and diol products respectively in order of elution. After removal of solvent under reduced pressure the diol was obtained as a yellow/brown oil and was reacted immediately. The diol (3.51 g) was dissolved in CH_2Cl_2 (60 mL) and to this a ten-fold excess (w/w) of MnO_2 (35.1 g) was added portionwise (yet quickly), and the mixture stirred for 1 min at room temperature before being filtered immediately through a plug of silica (*ca.* 2.5 × 5 cm thick), eluting with CH_2Cl_2 (approx. 200 mL). The solvent was removed under reduced pressure and purification was achieved *via* column chromatography (silica, CH_2Cl_2/hexane 1:1) prior to recrystallisation from hexane to give **53** as bright yellow crystals (1.32 g, 53 %); m.p. 89 – 90 °C.

^{1}H NMR ($CDCl_3$): δ = 6.62 (2H, s), 2.68 (4H, t, *J* = 7.76), 2.43 (6H, s), 1.39 (4H, broad quintet, *J* = 7.17), 1.25 (12H, m), 0.86 (6H, t, *J* = 7.02).

^{13}C NMR ($CDCl_3$): δ = 208.5, 175.6, 154.6, 149.8, 146.8, 131.8, 131.0, 31.9, 20.5, 30.3, 29.5, 22.8, 16.0, 14.3.

MS (MALDI): *m/z* = 518 $[M - S]^+$, 549 $[M - H]^+$, 551 $[M + H]^+$.

Elemental Analysis: Found C, 58.89; H, 6.20; S, 29.27 Calculated: C, 58.87; H, 6.22; S, 29.10.

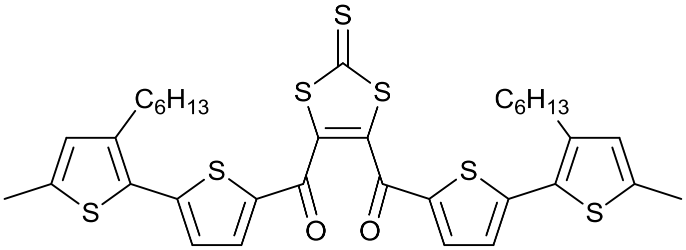

(2-Thioxo-1,3-dithiole-4,5-diyl)bis((3'-hexyl-5'-methyl-[2,2'-bithiophen]-5-yl)methanone) (54):

Under N_2, VTC (**52**) (616 mg, 4.58 mmol) was dissolved in dry THF (20 mL) at -55 °C. LDA.THF (1.3 M solution in cyclohexane, 3.87 mL, 5.04 mmol) was added and the reaction was stirred for 20 min at -55 °C. Compound **50** (1.48 g, 5.04 mmol) was added dropwise as a solution in dry THF (15 mL) before the reaction was stirred for a further 20 min at -55 °C. A second equivalent of LDA.THF (1.3 M solution in cyclohexane, 3.87 mL, 5.04 mmol) was added and the reaction was stirred for 15 min at -55 °C. The cooling bath temperature was reduced to -80 °C, and a second equivalent of **50** (1.048 g, 5.04 mmol) in dry THF (15 mL) was added. The reaction was allowed to continue until the reaction temperature warmed to -50 °C, whereupon the reaction was allowed to attain room temperature without external cooling. The reaction mixture was then poured into a solution of saturated $NaHCO_3$ (200 mL) to which KBr (20 g) was added. The product was extracted with ethyl acetate (3 × 60 mL) and the combined organic layers were dried over Na_2SO_4. The solvent was removed in vacuo and the residue was purified *via* column chromatography (silica, CH_2Cl_2 then ethyl acetate) to obtain the mono and diol products respectively in order of elution. The solvent was removed under reduced pressure and the diol was obtained as a dark red/brown oil which was reacted immediately. The diol (4.03 g) was dissolved in CH_2Cl_2 (80 mL) and to this a ten-fold excess (w/w) of MnO_2 (40.3 g) was added portionwise (yet quickly), and the mixture stirred for 1 min at room temperature before being filtered immediately through a plug of silica (*ca.* 2.5 × 5 cm thick), eluting with CH_2Cl_2 (approx. 200 mL). Purification was achieved *via* column chromatography (silica, CH_2Cl_2/petroleum ether 1:1) to give a thick red oil (1.72 g, 53 %).

^{1}H NMR ($CDCl_3$): δ = 7.62 (2H, d, J = 4.00), 7.03 (2H, d, J = 4.00), 6.61 (2H, m), 2.61 (4H, t, J = 8.00), 2.44 (6H, d, J = 1.00), 1.55 (4H, broad quintet, J = 7.50), 1.30 (12H, brm), 0.89 (6H, t, J = 7.00).

^{13}C NMR ($CDCl_3$): δ = 207.9, 175.2, 149.8, 144.4, 143.2, 141.4, 139.8, 136.1, 129.4, 127.1, 125.5, 31.6, 30.1, 29.8, 29.2, 22.6, 15.4, 14.1.

MS (MALDI): m/z = 683 $[M - S]^+$, 715 $[M]^+$.

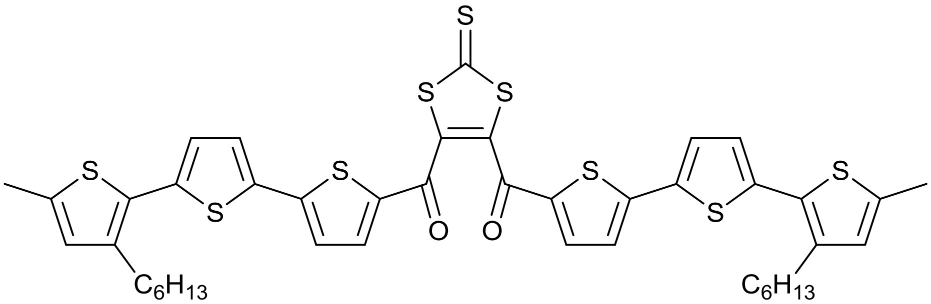

(2-Thioxo-1,3-dithiole-4,5-diyl)bis((3''-hexyl-5''-methyl-[2,2':5',2''-terthiophen]-5-yl)methanone) (55)

Under N_2, VTC (**52**) (326 mg, 2.43 mmol) was dissolved in dry THF at -55 °C. LDA.THF (1.5 M solution in cyclohexane, 1.78 mL, 2.67 mmol) was added and the reaction was stirred for 20 min at -55 °C. Compound **51** (1.00 g, 2.67 mmol) was added dropwise as a solution in dry THF (10 mL), before the reaction was stirred for a further 20 min at -55 °C. A second equivalent of LDA.THF (1.5 M solution in cyclohexane, 1.78 mL, 2.67 mmol) was added and the reaction was stirred for 15 min at -55 °C. The cooling bath temperature was reduced to -80 °C, and a second equivalent of **51** (1.00 g, 2.67 mmol) in dry THF (10 mL) was added. The reaction was allowed to continue until the reaction temperature warmed to -50 °C whereupon the reaction was allowed to attain room temperature without external cooling. The reaction mixture was thenpoured into a solution of saturated $NaHCO_3$ (60 mL) to which KBr (6 g) was added. The product was extracted with ethyl acetate (3 × 60 mL) and the combined organic layers were dried over Na_2SO_4. The solvent was removed in vacuo and the residue was purified *via* column chromatography (silica, CH_2Cl_2 then ethyl acetate) to obtain the mono and diol products respectively in order of elution. The diol was obtained as a red solid and was reacted immediately. The diol (2.19 g) was dissolved in CH_2Cl_2 (80 mL) and to this a ten-fold excess (w/w) of MnO_2 (21.9 g) was added portionwise (yet quickly), and the mixture stirred for 1 min at room temperature before being filtered immediately through a plug of silica (*ca.* 2.5 × 5 cm thick) eluting with CH_2Cl_2 (approx. 200 mL). The solvent was removed under reduced pressure to yield **55** as a deep-red tar-like solid (1.29 g, 60 %). The material was used without further purification, though an analytical sample was obtained *via* precipitation from hot CH_2Cl_2 with hexane to give a red powder; $T_g = 27.6$ °C, m.p. 82 – 83 °C.

^{1}H NMR ($CDCl_3$): $\delta = 7.62$ (2H, d, $J = 4.00$), 7.22 (2H, d, $J = 4.00$), 7.12 (2H, d, $J = 4.50$), 6.96 (2H, d, $J = 4.00$), 6.61 (2H, m), 2.67 (4H, t, $J = 7.75$), 2.44 (6H, d, $J = 0.50$), 1,60 (4H, quintet, $J = 7.75$), 1.33 (12H, m), 0.89 (6H, t, $J = 7.00$)

^{13}C NMR ($CDCl_3$): $\delta = 207.9$, 175.2, 150.1, 144.2, 141.0, 140.0, 139.7, 139.6, 136.9, 134.2, 129.0, 127.4, 127.4, 126.3, 124.2, 31.9, 30.7, 29.7, 29.4, 22.8, 15.5, 14.3.

MS (MALDI): $m/z = 879$ $[M]^+$.

Elemental Analysis: Found C, 58.69; H, 4.51; S, 32.91 Calculated: C, 58.73; H, 4.81; S, 32.82.

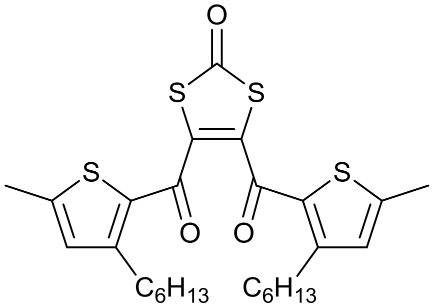

(2-Oxo-1,3-dithiole-4,5-diyl)bis((3-hexyl-5-methylthiophen-2-yl)methanone) (56):

1,3-dithiol-2-thione **53** (1.31 g, 2.38 mmol) was dissolved in 3:1 CH_2Cl_2/acetic acid (100ml). $Hg(OAc)_2$ (1.05 g, 3.33 mmol) was added and the reaction was stirred overnight at room temperature. The reaction mixture was filtered through a plug of silica before the filtrate was washed with water (2 × 200 mL) and saturated $NaHCO_3$ solution (2 × 200 mL) and the solvent was removed under reduced pressure. Purification was achieved by column chromatography (silica, CH_2Cl_2/hexane 2:1), followed by recrystallisation from hexane to give 1,3-dithiole-2-one **56** as round bright yellow crystals (1.12 g, 88 %). m.p. 54 – 55 °C.

^{1}H NMR ($CDCl_3$): δ = 6.64 (2H, s), 2.68 (4H, t, J = 7.75), 2.45 (6H, s), 1.42 (4H, broad quintet, J = 7.25), 1.29 (12H, m), 0.89 (6H, t, J = 6.90)

^{13}C NMR ($CDCl_3$): δ =187.5, 177.0, 153.9, 149.3, 137.7, 132.1, 130.6, 31.6, 30.2, 30.1, 29.3, 22.6, 15.8, 14.1.

MS (MALDI): m/z = 535 $[M + H]^+$.

Elemental Analysis: Found C, 60.54; H, 6.64; S, 23.82 Calculated: C, 60.64; H, 6.41; S, 23.98.

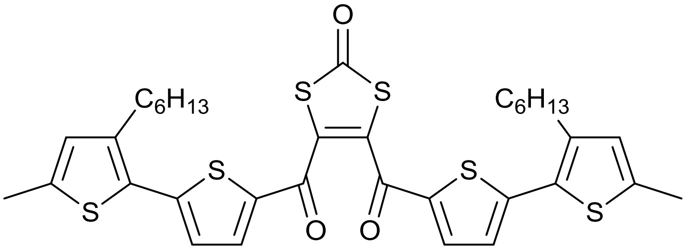

(2-Oxo-1,3-dithiole-4,5-diyl)bis((3'-hexyl-5'-methyl-[2,2'-bithiophen]-5-yl)methanone) (57):

1,3-dithiol-2-thione **54** (1.72 g, 2.41 mmol) was dissolved in 3:1 CH_2Cl_2/acetic acid (100ml), $Hg(OAc)_2$ (1.07 g, 3.37 mmol) was added and the reaction was stirred overnight at room temperature. The reaction mixture was filtered through a plug of silica before the filtrate was washed with water (2 × 250 mL) and saturated $NaHCO_3$ solution (2 × 250 mL) and the solvent was removed under reduced pressure. Purification by column chromatography (silica, CH_2Cl_2/hexane 2:1) gave 1,3-dithiole-2-one **57** as a thick red oil (1.41 g, 84 %).

^{1}H NMR (CDCl$_3$): δ = 7.59 (2H, d, J = 4.00), 7.02 (2H, d, J = 4.00), 6.61, (2H, m), 2.61 (4H, t, J = 7.75), 2.44 (6H, d, J = 1.00), 1.54 (4H, broad quintet, J = 7.63), 1.19 (12H, brm), 0.89 (6H, brm).

^{13}C NMR (CDCl$_3$): δ = 187.3, 176.9, 149.4, 143.0, 141.2, 140.1, 136.0, 135.6, 129.3, 127.1, 125.4, 31.6, 30.1, 29.8, 29.2, 22.6, 15.3, 14.1.

MS (MALDI): m/z = 699 [M]$^+$.

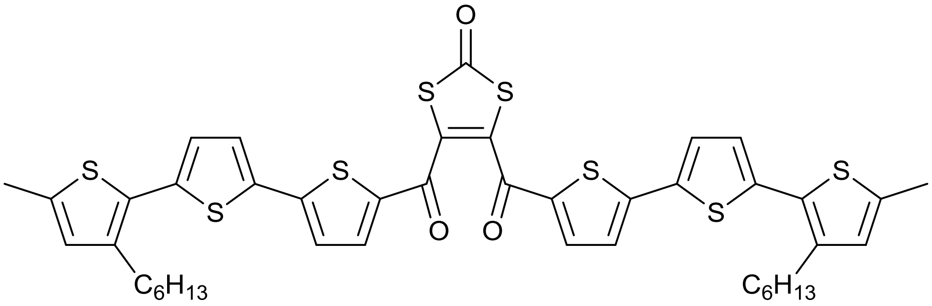

(2-Oxo-1,3-dithiole-4,5-diyl)bis((3''-hexyl-5''-methyl-[2,2':5',2''-terthiophen]-5-yl)methanone) (58)

55 (1.29g, 1.47 mmol) was dissolved in 3:1 CH_2Cl_2/glacial acetic acid mixture (150 mL) before addition of mercury(II) acetate (0.65 g, 2.05 mmol). The mixture was stirred overnight at room temperature before being filtered through a plug of silica eluting CH_2Cl_2. The filtrate was washed with water (2 × 200 mL) and saturated $NaHCO_3$ solution (2 × 200 mL) before the solvent was removed under reduced pressure. Purification was achieved *via* column chromatography (silica, CH_2Cl_2/hexane 2:1) to give a dark red tar-like solid (1.26 g, 99%). An analytical sample was obtained *via* precipitation from hot CH_2Cl_2 with hexane to give a bright red powder. T_g = 22.5 °C, m.p. 75 – 76 °C.

^{1}H NMR (CDCl$_3$): δ = 7.59 (2H, d, J = 4.00), 7.21 (2H, d, J = 4.00), 7.12 (2H, d, J = 4.00), 6.95 (2H, d, J = 3.50), 6.61 (2H, m), 2.67 (4H, t, J = 8.00), 2.44 (6H, d, J = 0.50), 1,60 (4H, quintet, J = 7.75), 1.33 (12H, m), 0.89 (6H, t, J = 7.00)

^{13}C NMR ($CDCl_3$): δ = 187.3, 176.8, 149.8, 140.9, 140.0, 139.8, 139.5, 136.8, 135.5, 134.3, 129.0, 127.4, 127.2, 126.3, 124.1, 31.8, 30.6, 29.7, 29.4, 22.8, 15.5, 14.3

MS (MALDI): *m/z* = 863 [M]$^+$

Elemental Analysis: Found C, 59.85; H, 4.68; S, 29.82 Calculated: C, 59.82; H, 4.90; S, 29.71

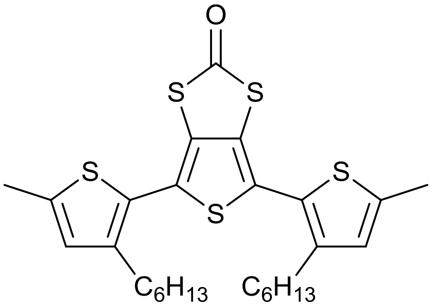

4,6-Bis(3-hexyl-5-methylthiophen-2-yl)thieno[3,4-d][1,3]dithiol-2-one (46): 1,3-Dithiole-2-one **56** (1.00 g, 1.87 mmol), P_4S_{10} (2.07 g, 4.66 mmol), and $NaHCO_3$ (786 mg, 9.35 mmol) were stirred together in 1,4-dioxane (40 mL) under N_2. The reaction was heated from 60 – 90 °C over 30 min, then stirred at 90 °C for 3 h. The reaction mixture was then allowed to cool to room temperature and water was added (10 × 10 mL portions) (**CAUTION!** H_2S and CO_2 gas evolution). The resulting suspension was heated to reflux for 1 h before being allowed to cool and stirred overnight at room temperature. The precipitate was filtered off over a glass sinter and washed with copious amounts of water before being dried under a stream of air. The precipitate was washed through the sinter with copious CS_2 before drying over Na_2SO_4 and removal of solvent under reduced pressure. Purification was achieved using column chromatography (silica, CS_2), then a further short silica column using pentane as the eluent. The product was isolated as yellow oil which solidified over time to give a brown solid (746 mg, 75 %); T_d = 345 °C, m.p. 46 – 48 °C.

^{1}H NMR ($CDCl_3$): δ = 6.65 (2H, m), 2.64 (4H, t, J = 7.83), 2.49 (6H, s), 1.60 (4H, broad quintet, J = 7.56), 1.30 (12H, m), 0.88 (6H, t, J = 6.83).

^{13}C NMR ($CDCl_3$): δ = 193.0, 142.6, 140.6, 128.3, 126.5, 126.1, 124.5, 31.6, 30.7, 29.5, 29.2, 22.6, 15.4, 14.1.

MS (MALDI): m/z = 533 $[M - H]^+$.

Elemental Analysis: Found C, 60.57; H, 6.01; S, 29.94 Calculated: C, 60.63; H, 6.41; S, 29.97.

The ^{1}H NMR spectrum for **46** is shown in figure 6-1. The aromatic region contains a single narrow multiplet at 6.65 ppm stemming from the lone proton of each of the two thiophene rings. The symmetrical nature of the molecule results in signals which overlap perfectly, resulting in increased intensity of peaks rather than increasing the number of peaks observed. This multiplet signal is observed throughout the synthetic pathways towards all of the oligothiophene dimers, and the dimers themselves. The fine splitting observed is a result of coupling with the protons of the adjacent alkyl chains.

The aliphatic region demonstrates a signal at 2.49 ppm attributable to the chain-capping methyl units; the multiplet nature arising from long-range coupling to the thienyl proton. All other peaks arise from the hexyl chains: the terminal CH_2 signal is the triplet at 2.64 ppm, and its immediate neighbour gives rise to the quintet at 1.60 ppm, the terminal CH_3 a triplet at 0.88 ppm, and the other resonances overlap extensively as a broad multiplet centred at 1.30 ppm. Broadening of the signals of long alkyl chains is common owing to the large number of hydrogen atoms in very similar environments.

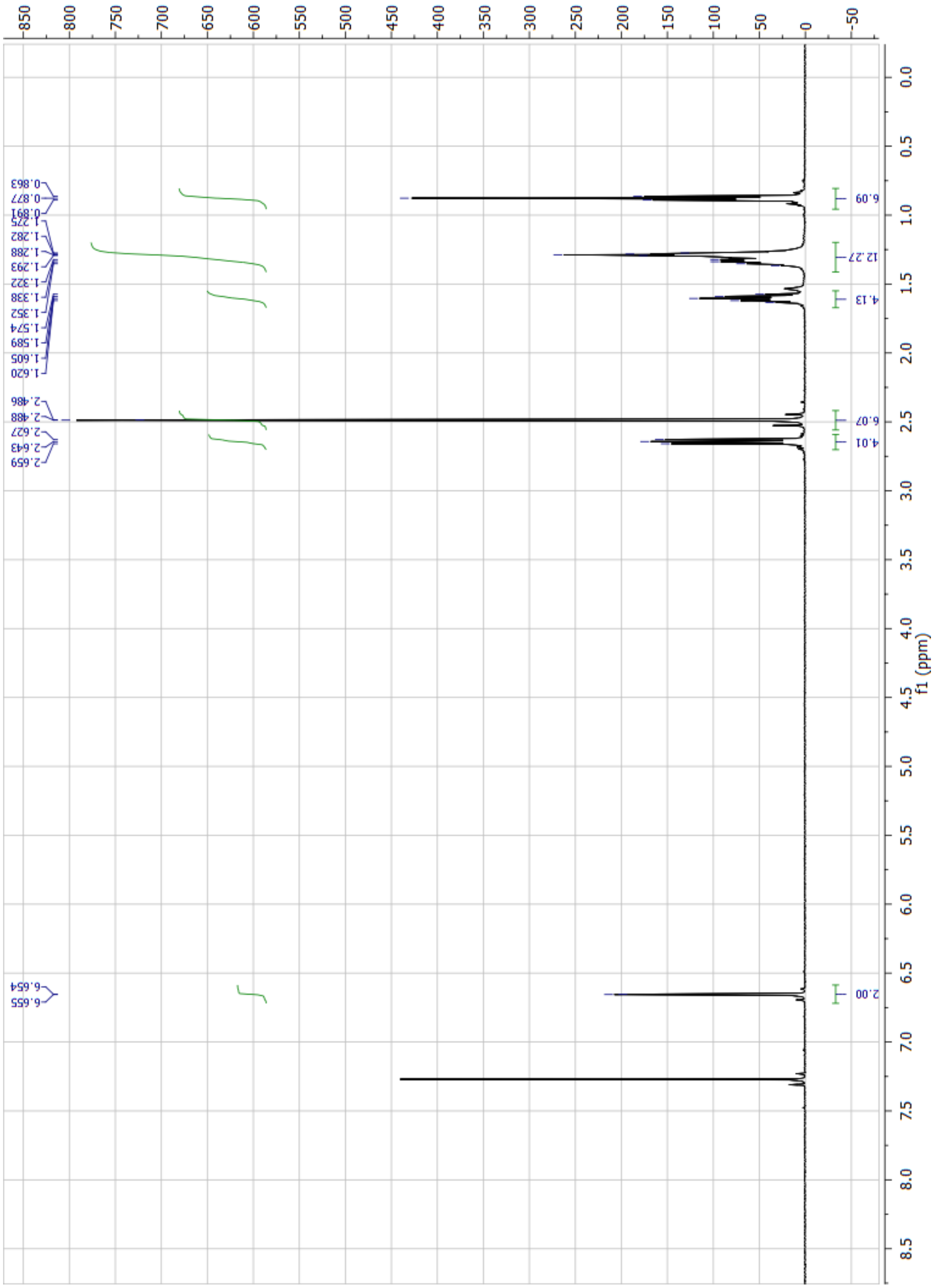

Figure 6-1 ^{1}H NMR spectrum of **46**.

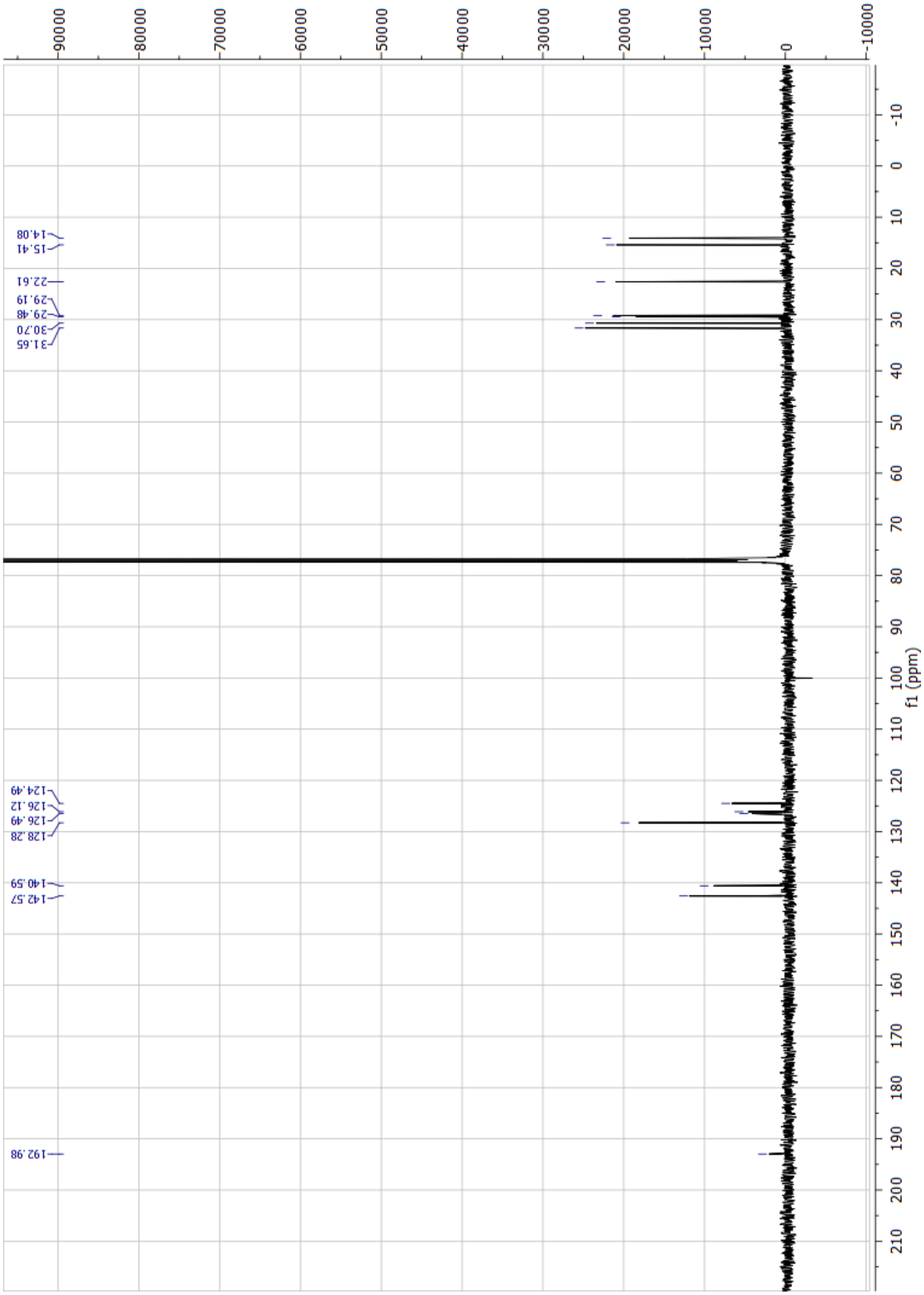

Figure 6-2 ^{13}C NMR spectrum of **46**.

The ^{13}C spectrum demonstrated in figure 6-2 shows a low intensity peak at 193.0 ppm corresponding to the central carbonyl unit. The symmetrical nature of the molecule results in the observation of only six peaks in the aromatic region stemming from the terthiophene chain, and seven peaks in the aliphatic region from the methyl and hexyl groups on the terminal thiophenes.

The mass spectrum showed the presence of the unfragmented molecular species, and the elemental analysis agreed well with the predicted results.

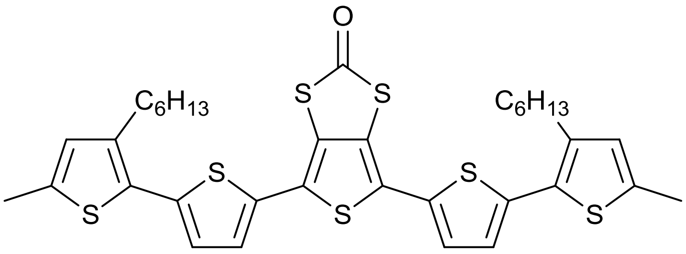

4,6-Bis(3'-hexyl-5'-methyl-[2,2'-bithiophen]-5-yl)thieno[3,4-d][1,3]dithiol-2-one (47):

1,3-Dithiole-2-one **57** (1.41 g, 2.02 mmol), P_4S_{10} (4.48 g, 10.08 mmol), and $NaHCO_3$ (848 mg, 10.08 mmol) were stirred together in 1,4-dioxane (60 mL) under N_2. The reaction was heated from 60 – 90 °C over 30 min then stirred at 90 °C for 3 h. The reaction mixture was then allowed to cool to room temperature and water was added (10 × 10 mL portions) (**CAUTION!** H_2S and CO_2 gas evolution). The resulting suspension was heated to reflux for 1 h before being allowed to cool and stirred overnight at room temperature. The precipitate was filtered off over a glass sinter and washed with copious amounts of water before being dried under a stream of air. The precipitate was washed through the sinter with copious CS_2 before drying over Na_2SO_4 and removal of solvent under reduced pressure. Purification was achieved using column chromatography (silica, CS_2), followed by recrystallisation from cyclohexane to obtain a shiny orange precipitate which was filtered and washed with cold methanol before drying in a desiccator (1.06 g, 75 %). T_d = 419 °C, m.p. 47 – 48 °C.

^{1}H NMR ($CDCl_3$): δ = 7.14 (2H, d, J = 4.00), 7.02 (2H, d, J = 3.50), 6.63 (2H, m), 2.72 (4H, t, J = 7.75), 2.47 (6H, d, J = 0.50), 1.64 (4H, broad quintet, J = 7.38), 1.35 (12H, m), 0.91 (6H, m).

^{13}C NMR ($CDCl_3$): δ = 192.0, 140.5, 139.0, 137.9, 133.2, 128.7, 127.3, 125.9, 125.4, 125.3, 124.0, 31.7, 30.6, 29.5, 29.3, 22.7, 15.3, 14.1.

MS (MALDI): m/z = 697 $[M - H]^+$, 669 $[M - CO - H]^+$.

Elemental Analysis: Found C, 60.31; H, 5.40; S, 32.43 Calculated: C, 60.13; H, 5.48; S, 32.43.

Figure 6-3 shows the ^{1}H NMR spectrum for **47**. The characteristic multiplet stemming from the lone hydrogens of the terminal thiophenes is present at 6.63 ppm. Doublets at 7.14 and 7.02 ppm are apparent, representing the four hydrogens remaining on the quinquethiophene chain. The aliphatic region is virtually identical to that of **46**, and is explained in the same manner. Similarly to **46**, the symmetrical nature of the molecule results in peaks of higher intensity rather than a greater number of peaks in both the ^{1}H and ^{13}C NMR spectra.

The ^{13}C NMR spectrum of **47** is shown in figure 6-4. At 192.0 ppm a peak corresponding to the central carbonyl is present. The aromatic carbon atoms are accounted for in the region from 140.5-124.0 ppm, as expected there are four more signals in this region than for **46**, stemming from the presence of the additional thiophene ring on both sides of the molecule. Again, the aliphatic region is virtually identical to that of **46** and can be explained in the same way.

The mass spectrum showed the presence of the unfragmented molecular species, and the elemental analysis agreed well with the predicted results.

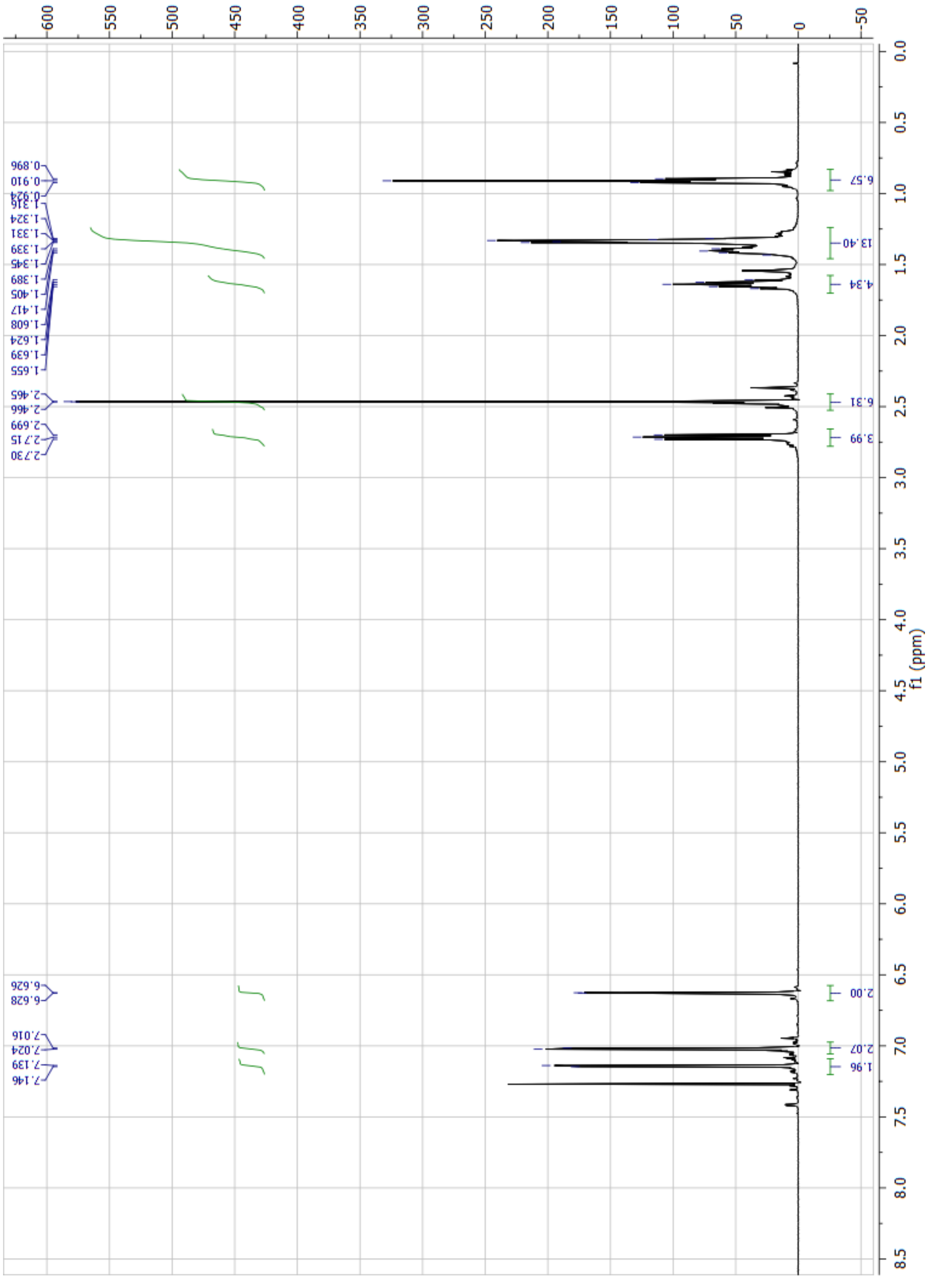

Figure 6-3 ^{1}H NMR spectrum of **47**.

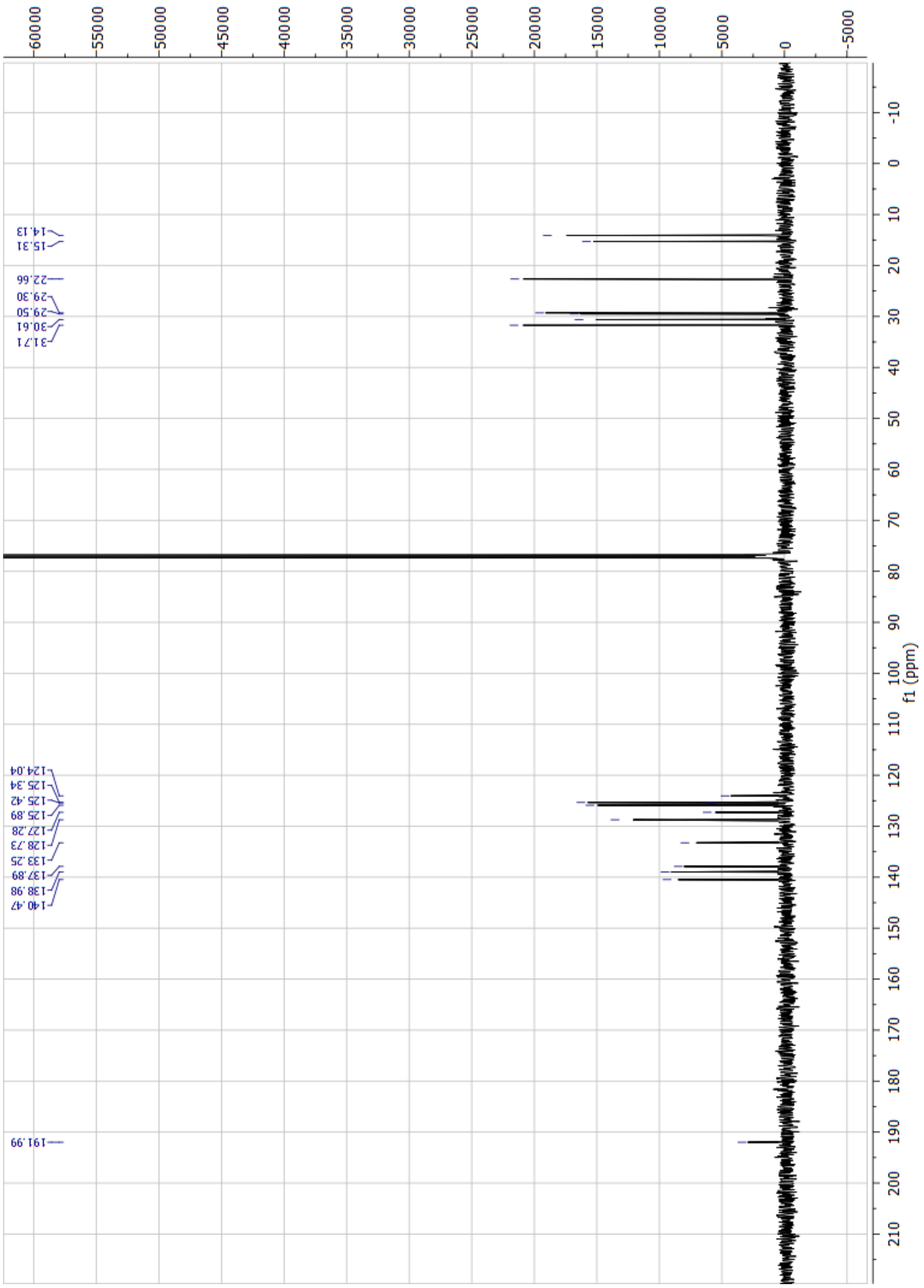

Figure 6-4 ^{13}C NMR spectrum of **47**.

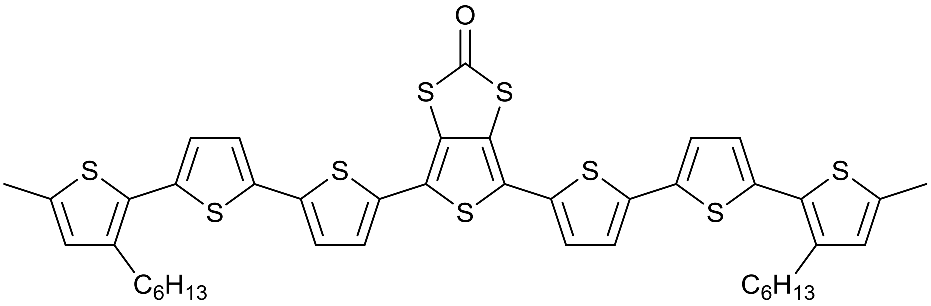

4,6-Bis(3''-hexyl-5''-methyl-[2,2':5',2''-terthiophen]-5-yl)thieno[3,4-d][1,3]dithiol-2-one (48):

Compound **58** (1.26 g, 1.47 mmol), P_4S_{10} (1.63 g, 3.67 mmol) and sodium hydrogen carbonate (616 mg, 7.33 mmol) were stirred together in 1,4-dioxane (40 mL) under N_2. The reaction was heated from 60 – 90 °C over 30 min then stirred at 90 °C for 3 h. The reaction mixture was then allowed to cool to room temperature and water was added (10 × 10 mL portions) (**CAUTION!** H_2S and CO_2 gas evolution). The resulting suspension was heated to reflux for 1 h before being allowed to cool and stirred overnight at room temperature. The precipitate was filtered off over a glass sinter and washed with copious amounts of water before being dried under a stream of air. The precipitate was washed through the sinter with copious CS_2 before drying over Na_2SO_4 and removal of solvent under reduced pressure. The crude material was purified *via* column chromatography (silica, CS_2) then precipitation from hot chloroform with hexane to give **48** as fine purple crystals with a metallic lustre (872 mg, 69 %). Recrystallisation can be achieved from dichloromethane to yield larger crystals; T_d = 400 °C, m.p. 111 – 112 °C.

^{1}H NMR ($CDCl_3$): δ = 7.12 (6H, m), 6.96 (2H, d, J = 4.00), 6.62 (2H, m), 2.70 (4H, t, J = 7.75), 2.46 (6H, bs), 1,60 (4H, quintet, J = 7.37), 1.34 (12H, m), 0.90 (6H, t, J = 7.00).

^{13}C NMR ($CDCl_3$): δ = 191.7, 139.9, 138.4, 138.1, 136.6, 135.1, 132.6, 128.6, 127.9, 125.6, 125.5, 125.3, 124.3, 124.0, 123.9, 31.7, 30.5, 29.5, 29.3, 22.7, 15.3, 14.2.

MS (MALDI): m/z = 863 $[M]^+$.

Elemental Analysis: Found C, 59.48; H, 4.65; S, 33.66 Calculated: C, 59.82; H, 4.90; S, 33.43.

Figure 6-5 shows the ^{1}H NMR spectrum for **48**. The characteristic multiplet stemming from the lone hydrogens of the terminal thiophenes is present at 6.62 ppm. A group of overlapping split signals corresponding to six of the aromatic protons is present at 7.12 ppm and the remaining two are accounted for in the doublet at 6.96 ppm. The aliphatic region can be explained in the same fashion as for the related species **46** and **47**. Again, the symmetrical nature of the molecule results in peaks of increased intensity rather than greater number.

The ^{13}C NMR spectrum of **48** is shown in figure 6-6. At 191.7 ppm the peak corresponding to the central carbonyl is present. The aromatic carbon atoms are accounted for in the region between 140.0 and 123.0 ppm. As expected there are four more signals in this region than for **47**, coming from the additional thiophene ring on both sides of the molecule. Again, the aliphatic region is virtually identical to that of **46** and **47** and can be explained in the same way.

The mass spectrum showed the presence of the unfragmented molecular species, and the elemental analysis agreed well with the predicted results.

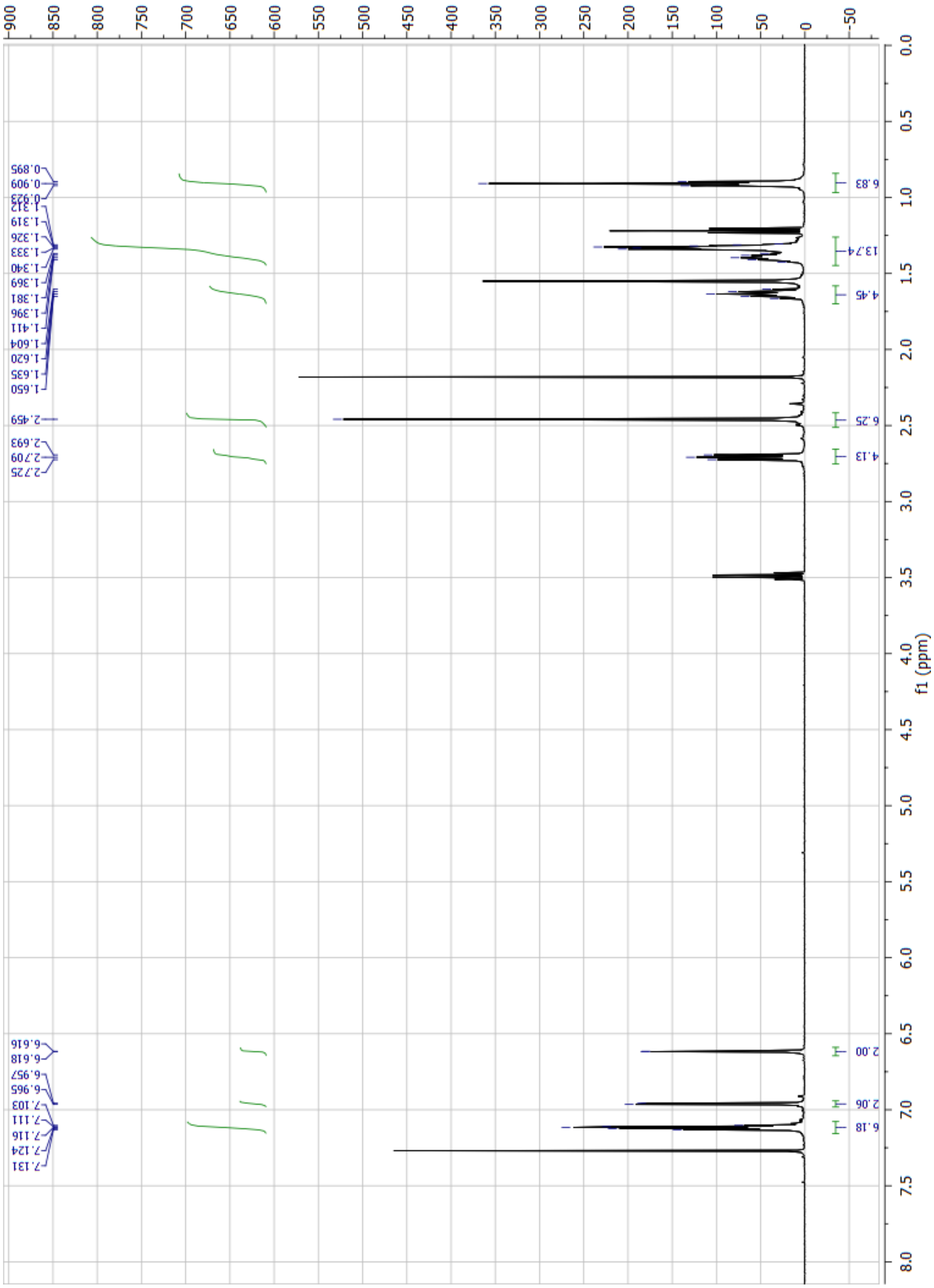

Figure 6-5 ^{1}H NMR spectrum of **48**.

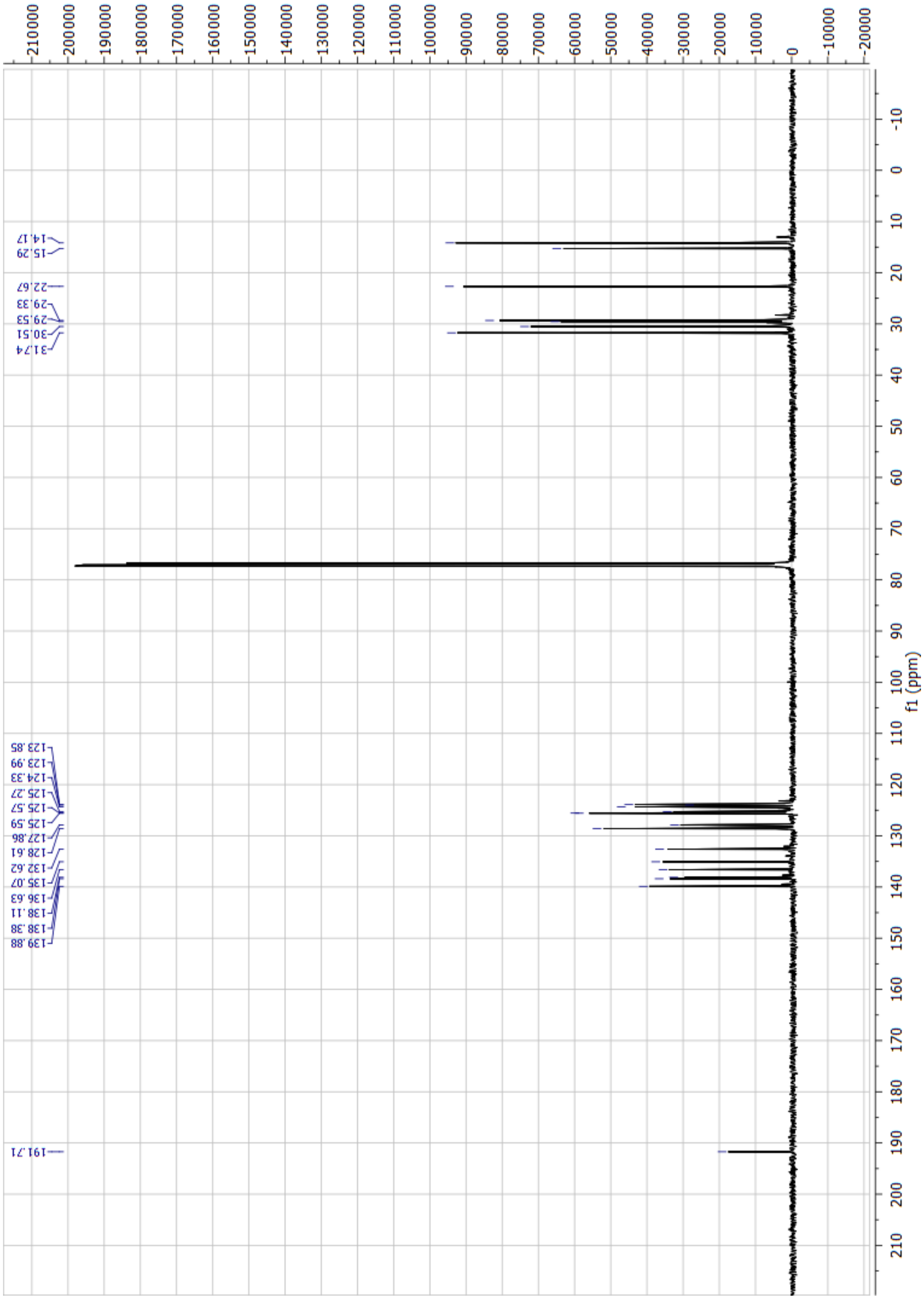

Figure 6-6 ^{13}C NMR spectrum of **48**.

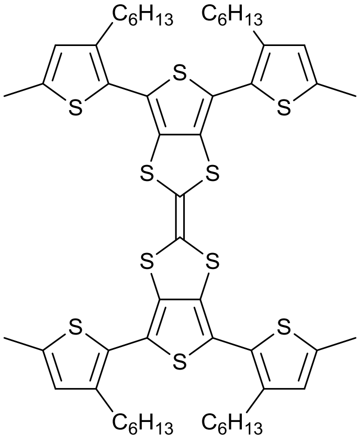

4,4',6,6'-Tetrakis(3-hexyl-5-methylthiophen-2-yl)-2,2'-bithieno[3,4-d][1,3]dithiolylidene (70):

Under N_2, 1,3-dithiole-2-one **46** (150 mg, 0.28 mmol) was dissolved in freshly distilled $P(OEt)_3$ (*ca.* 10ml) and heated at 125 °C for 4 days. After cooling to room temperature, the resulting suspension was poured into a beaker and the solvent removed under a stream of air. The residue was purified *via* recrystallisation from hexane to yield very small fine yellow crystals (112 mg, 77%); T_d = 377 °C, T_g = -43.21 °C, m.p. 120 – 125 °C.

^{1}H NMR ($CDCl_3$): δ = 6.61 (4H, m), 2.64 (8H, t, J = 7.75), 2.47 (12H, m, J = 0.5), 1.58 (8H, broad quintet, J = 7.38), 1.29 (24H, brm), 0.87 (12H, t, J = 7.00).

^{13}C NMR ($CDCl_3$): δ = 142.2, 140.1, 133.7, 128.4, 125.4, 122.3, 119.0, 31.9, 31.0, 29.7, 29.4, 22.8, 15.6, 14.3.

MS (MALDI): m/z = 1036 $[M]^+$.

Elemental Analysis: Found C, 62.20; H, 6.40; S, 30.49 Calculated: C, 62.50; H, 6.60; S, 30.90.

The ^{1}H NMR spectrum of **70** is shown in figure 6-7, and can be explained in exactly the same way as for the precursor **46**. It is notable that, despite being comprised of a combination of four signals, the peaks observed are very well defined.

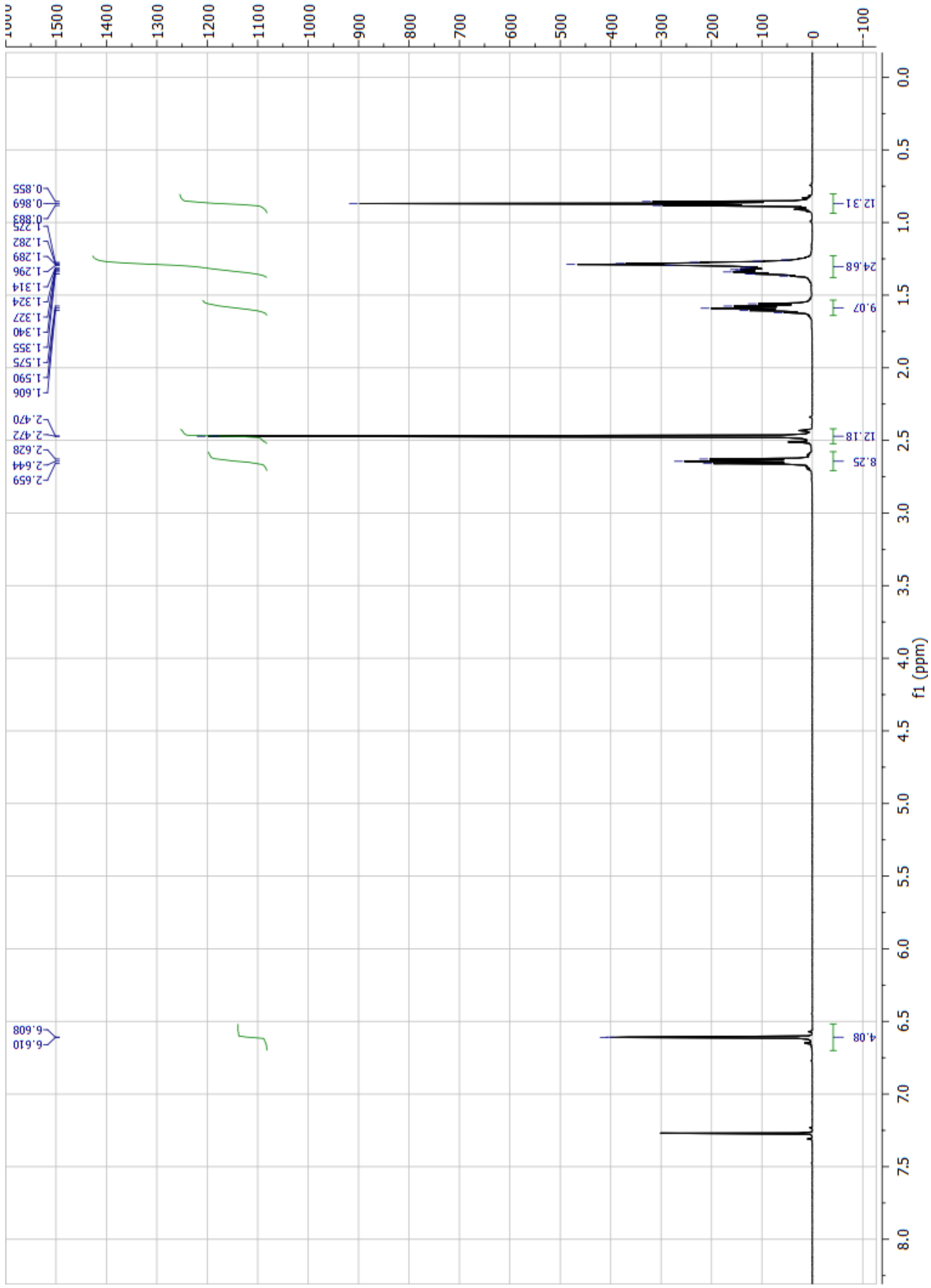

Figure 6-7 ^{1}H NMR spectrum of **70**.

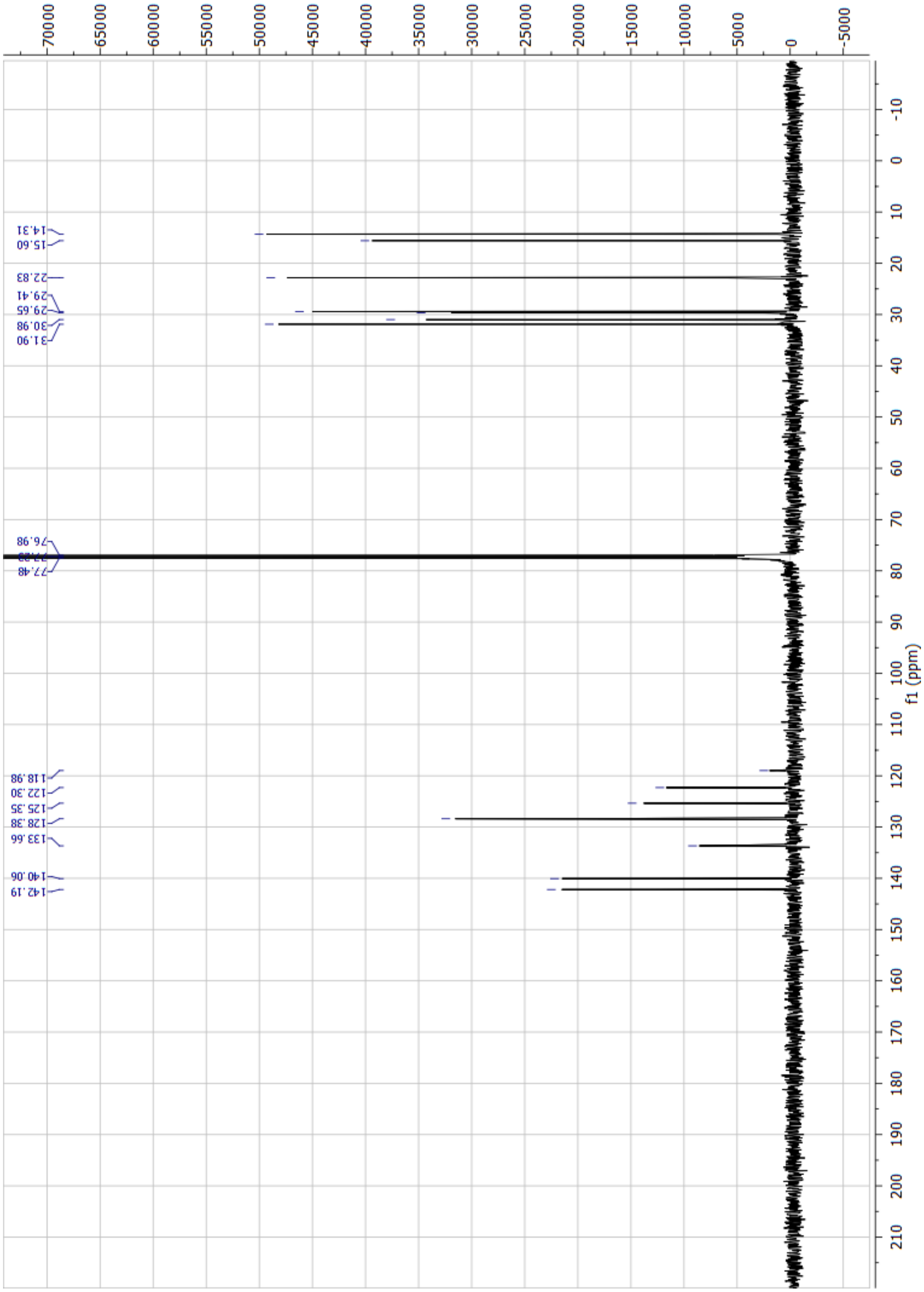

Figure 6-8 ^{13}C NMR spectrum of **70**.

The ^{13}C NMR spectrum of **70** is shown in figure 6-8. The carbonyl peak observed at 193.0 ppm in the spectrum of **46**, is no longer apparent (this indicates that the coupling has proceeded as expected) while the rest of the spectrum can be explained analogously to that of **46**.

The mass spectrum showed the presence of the unfragmented molecular species, and the elemental analysis agreed well with the predicted results.

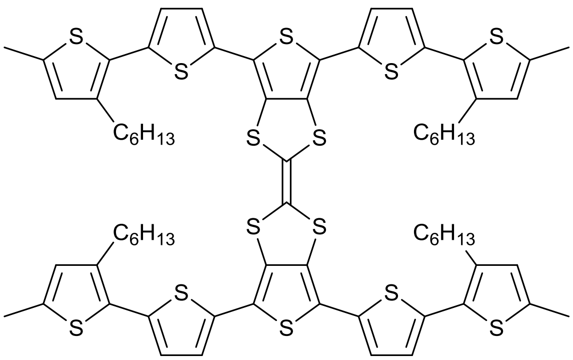

4,4',6,6'-Tetrakis(3'-hexyl-5'-methyl-[2,2'-bithiophen]-5-yl)-2,2'-bithieno[3,4-d][1,3]dithiolylidene (71):

Under N_2, 1,3-dithiole-2-one **47** (250 mg, 0.36 mmol) was dissolved in freshly distilled $P(OEt)_3$ and heated at 125 °C for 3 days. The reaction mixture was cooled to room temperature precipitating the product. The $P(OEt)_3$ was decanted off and the precipitate was washed repeatedly with methanol until the washings were colourless. The product was then dried in a desiccator (201 mg, 82 %); T_d = 436 °C, m.p. 152 – 155 °C.

^1H NMR (CD_2Cl_2/CS_2 (3:1)): δ = 7.50 (1H, d, J = 3.50), 7.44 (1H, d, J = 4.00), 7.10 (3H, m, J = 4.00), 7.01 (3H, m, J = 4.00), 6.64, (4H, m), 2.73 (8H, brm), 2.50 (12H, m), 1.66 (8H, brm), 1.36 (24H, brm), 0.90 (12H, brm).

^{13}C NMR (CD_2Cl_2/CS_2 (3:1)): δ = 140.8, 139.2, 137.9, 134.3, 132.0, 129.3, 128.3, 126.4, 125.6, 121.9, 32.5, 31.3, 30.2, 30.1, 23.5, 15.7, 14.8.

MS (MALDI): m/z = 1364 $[M]^+$

Elemental Analysis: Found C, 61.20; H, 5.29; N, 0.31; S, 30.83 Calculated: C, 61.54; H, 5.61; N, 0.00 S, 32.86.

Figures 6-9 and 6-10 demonstrate well the how the extent of aggregation affects the shape of the ^{1}H NMR spectrum for **71**. Figure 6-9 (as described in the experimental) demonstrates the spectrum at higher concentration than in figure 6-10. At higher concentrations, the effects of aggregation can be observed, whilst increasing the ratio of CS_2 to sample mass serves to largely eliminate these effects. In figure 6-9 there is more extensive overlapping of the signal pertaining to the lone proton of the terminal thiophenes at 6.66. This TTF structure is expected to be less planar than the others as unlike in **70** and **72** the hexyl chains are pointing towards each other. Accommodating these chains is expected to result in twisting of the oligothiophene chain. As these molecules are aggregating, this effect will be amplified as the molecules freedom of movement is restricted thus these protons are not equivalent and an overlapping signal is observed. Upon increasing CS_2, the effects of aggregation or overcome and the molecule can obtain its equilibrium geometry in solution and these protons become equivalent again. This results in the peak resolving as a well-defined multiplet at 6.64 ppm, as expected from observations made of the TTF precursors. The rest of the aromatic region in figure 6-9 displays two multiplets, which have a similar overlapping character to that described above, and two doublets at 7.46 and 7.52 ppm. The integrals indicate that the two multiplets are comprised of three protons each, and the two doublets of a single proton each. This may imply significant twisting of only one of the four bithiophene moieties which are bound to the central DT-TTF. Again, by increasing CS_2 concentration, this effect is lost, and instead we observe only two signals, a multiplet at 6.96 ppm, and a doublet at 7.03 ppm, both with an integral of four.

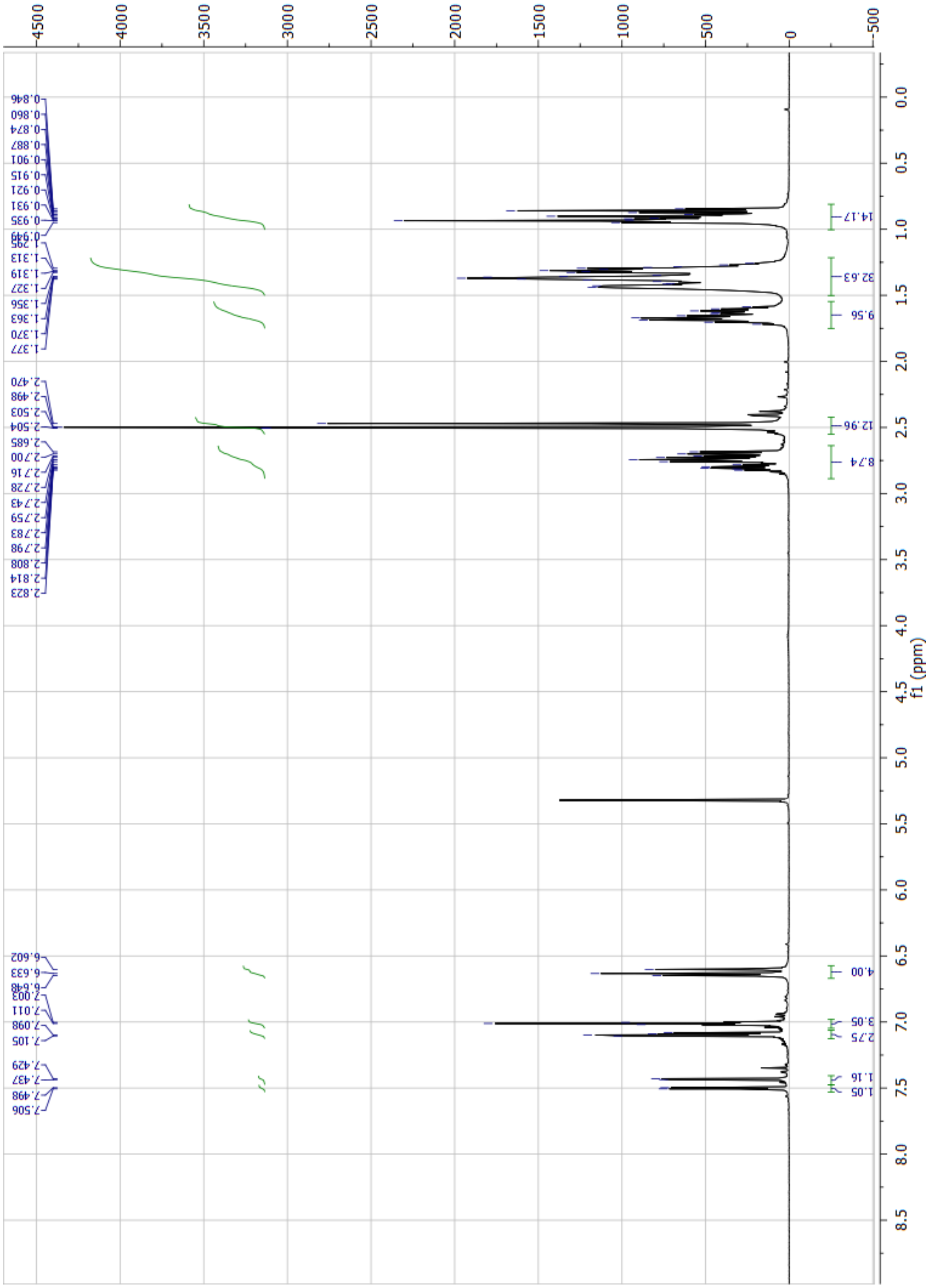

Figure 6-9 ^{1}H NMR spectrum of **71**.

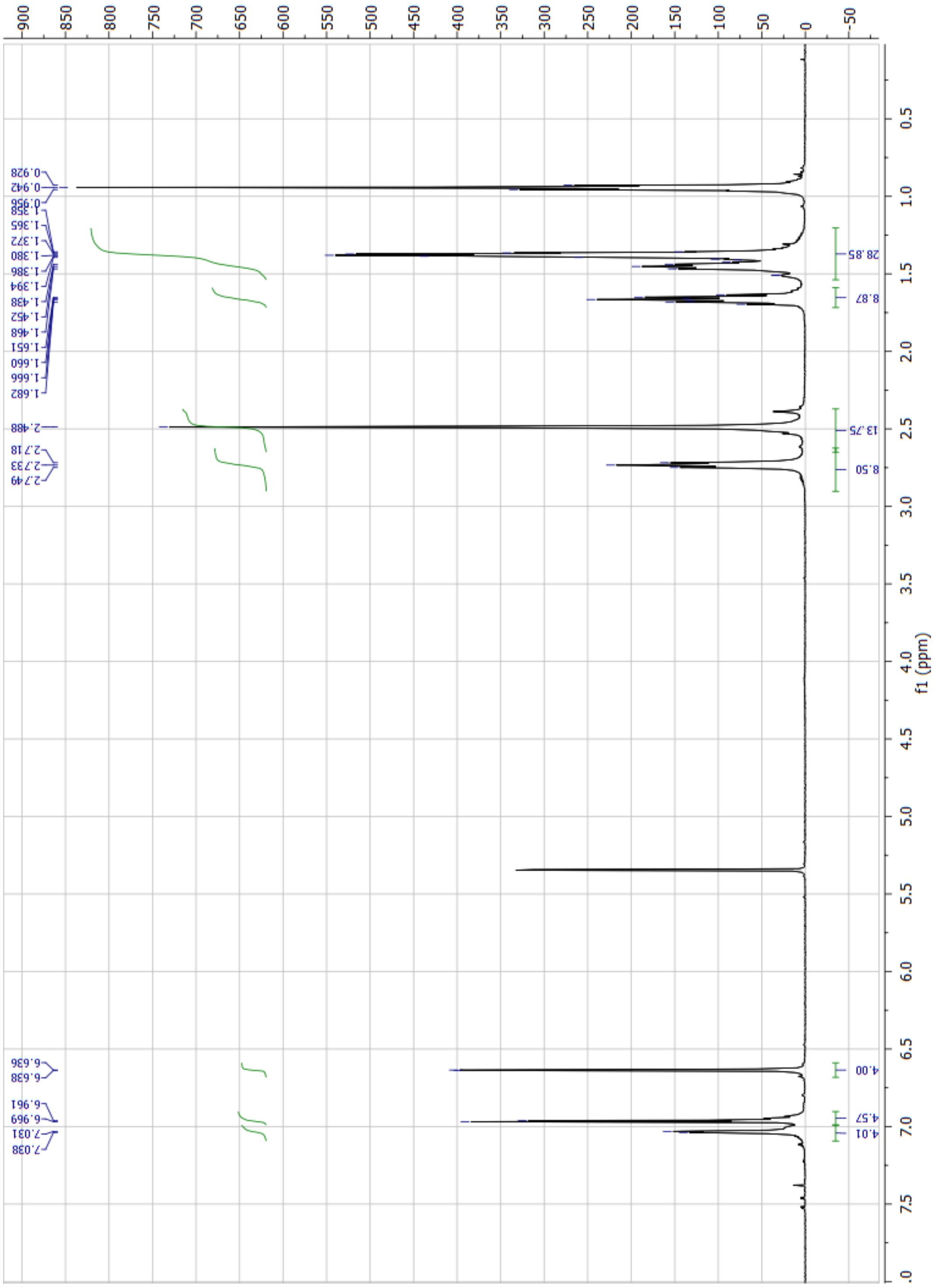

Figure 6-10 ^{1}H NMR spectrum of **71** demonstrating both the effects of aggregation upon the spectrum, and the effects induced by either increasing CS_2 concentration or further dilution.

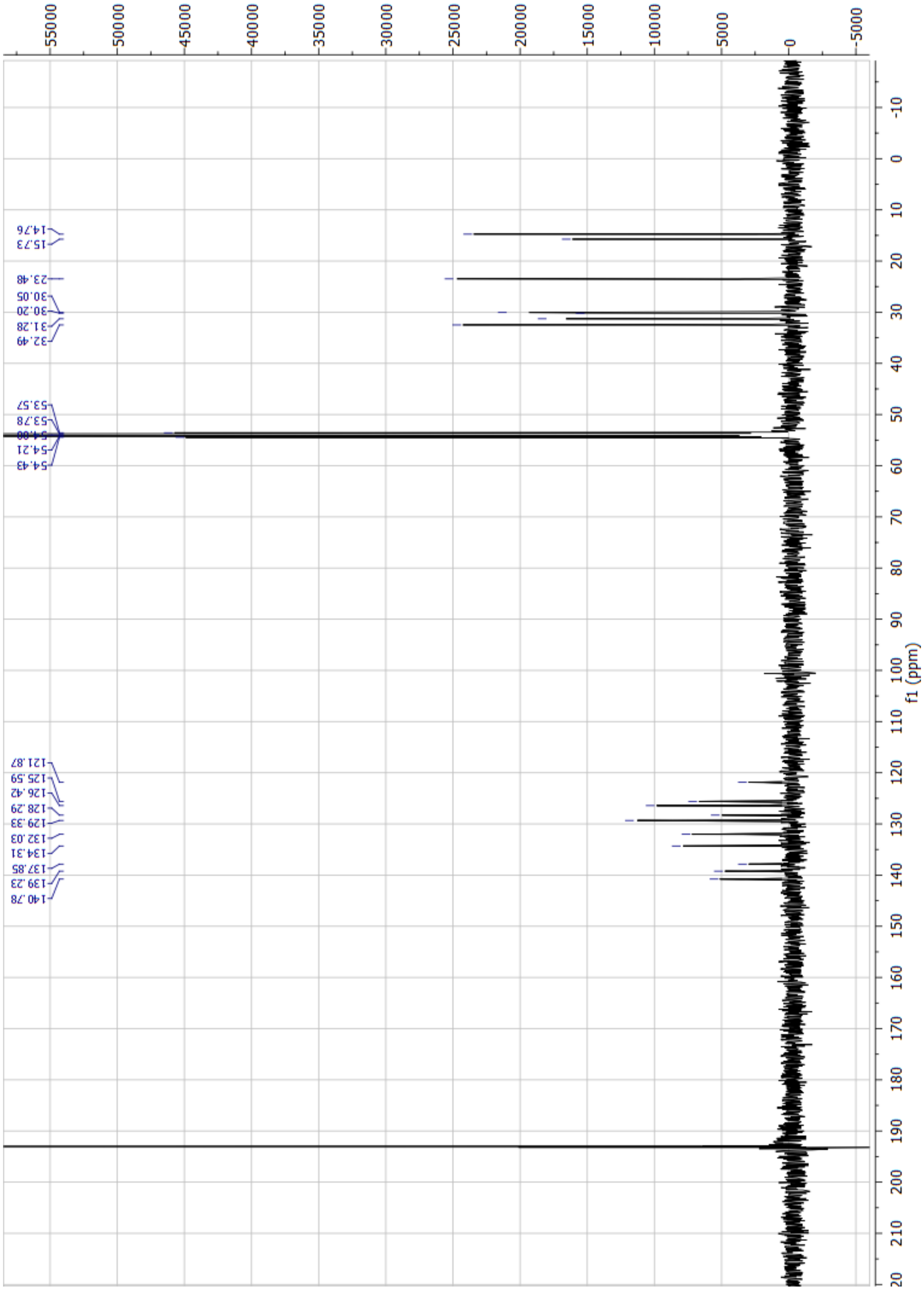

Figure 6-11 ^{13}C NMR spectrum of **71**.

The ^{13}C NMR spectrum of **71** is shown in figure 6-11. Unfortunately, any residual carbonyl peak from the precursor **47**, cannot be seen due to the presence of the CS_2 peak at *ca.* 193 ppm, however the emergence of the lower shift peak at 121.9 ppm indicates successful coupling, and the rest of the spectrum can be explained analogously to that of **47**. Resolution of one of the aromatic carbon peaks could not be obtained depite numerous attempts. This has can be attributed either to the low sample concentration, or conceivably to two peaks overlapping resulting in masking of one of the signals.

The mass spectrum showed the presence of the unfragmented molecular species.

Despite appearing pure in both the NMR and MS analysis obtaining satisfactory elemental analysis proved difficult as the results were prone to variation, indicating incomplete combustion. Careful control over combustion parameters was required in order to obtain the results given which, other than the high result for the sulfur analysis agree well with the calculated values.

It is worth noting that obtaining satisfactory elemental analysis for all of the compounds which demonstrate extensive aggregation has proven very challenging.

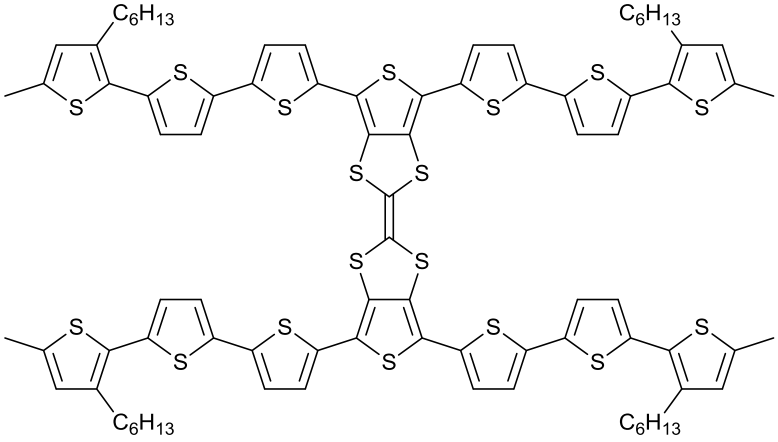

4,4',6,6'-Tetrakis(3''-hexyl-5''-methyl-[2,2':5',2''-terthiophen]-5-yl)-2,2'-bithieno[3,4-d][1,3]dithiolylidene (72):

Compound **48** (750 mg, 872 μmol) was dissolved in dry $P(OEt)_3$ (20 mL) and heated at 125 °C for 4 days. The crude product forms as a red precipitate, which was filtered then washed with hexane and dried under a stream of air. The precipitate was then washed through the sinter with CS_2 before removal of solvent under reduced pressure. The material was purified *via* column chromatography (silica, CS_2) prior to precipitation from the minimum volume of hot chloroform with hexane (286 mg, 39 %). A sample suitable for crystallographic analysis was obtained by slow evaporation of a CH_2Cl_2/CS_2 3:2 mixture; T_d = 399 °C.

^{1}H NMR (CD_2Cl_2/CS_2 (3:1)): δ = 7.48-6.55 (20H, brm), 2.74-2.44 (20H, brm), 1.64-1.60 (8H, brm), 1.40-1.32 (24H, brm), 0.95-0.91 (12H, brm).

MS (MALDI): m/z = 1694 $[M]^+$.

Elemental Analysis: Found C, 60.27; H, 4.95; S, 34.03 Calculated: C, 60.95; H, 5.00; S, 34.06.

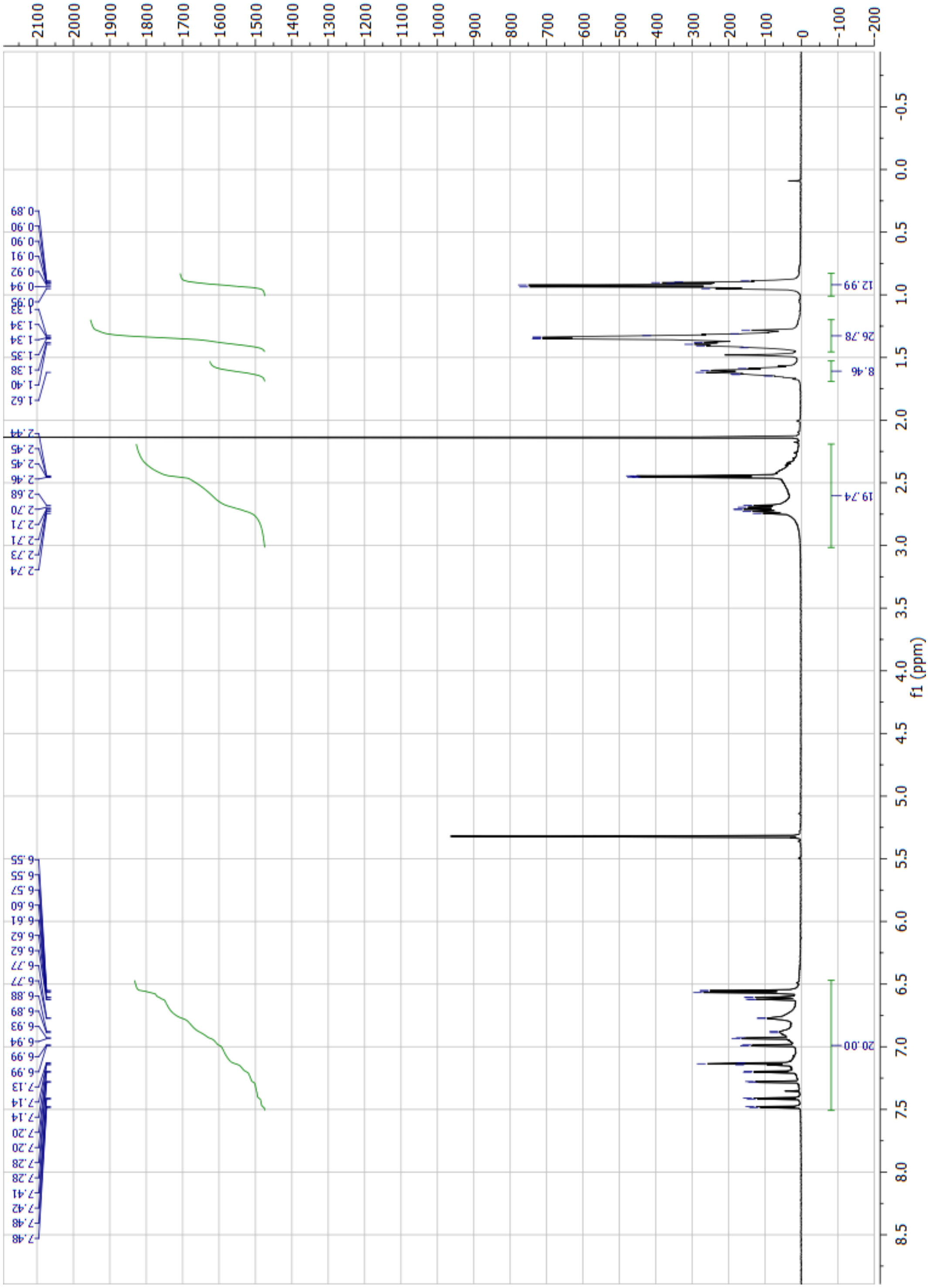

Figure 6-12 ^{1}H NMR spectrum of **72**.

The ^{1}H NMR spectrum for **72** is shown in figure 6-12. Here, the effect of aggregation between molecules on broadening of the NMR peaks is very apparent and, despite the addition of CS_2 to help overcome this, could not be eliminated from the spectrum. In the aromatic region a number of peaks, both well defined and broad peaks, converge to give a single convoluted mass of peaks stretching from 7.48-6.55 ppm. The peaks in the aliphatic region are of a similar general shape to those seen previously in the spectra of oligothiophenes **46-48**. Whilst the peaks themselves are fairly well-defined at the top, the bases of the peaks show broadening similar to that observed in the aromatic region. Unlike with the precursor **48**, the peak splitting here are less well defined, as the slightly differing geometries of the thiophene chains of aggregated molecules has resulted in overlapping of the individual multiplet characteristics, hence well defined triplets or quintets are not observed.

Provided the overlapping nature of many of these peaks is taken into consideration when calculating peak area, the magnitude of the integrals demonstrates excellent agreement with the proposed structure.

Despite numerous attempts to obtain a spectrum, the effects of aggregation on the ^{13}C NMR spectrum rendered it essentially meaningless for straightforward interpreatation. Though not shown here, no peaks attributable to a carbonyl were observed.

The mass spectrum showed the presence of the unfragmented molecular ion.

Similarly to **71**, obtaining satisfactory elemental analysis proved difficult and the results were prone to variation. Careful control over combustion parameters was again required in order to obtain the results given which, other than the slightly low result for the carbon analysis are in excellent agreement with those calculated.

The results of X-ray crystallography serve to confirm absolutely that the desired structure has been obtained.

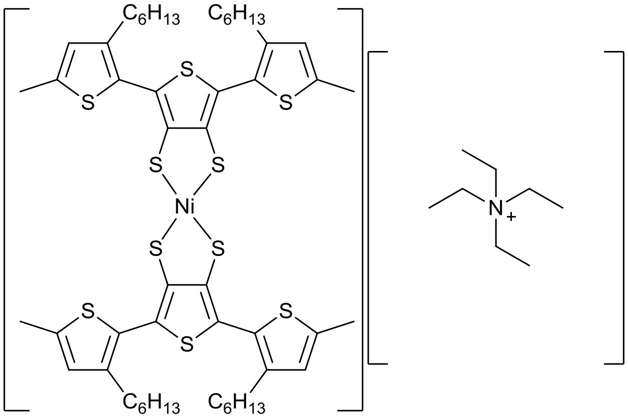

[(C$_{26}$H$_{34}$S$_5$)$_2$Ni][Et$_4$N] (80):

To a solution of 1,3-dithiole-2-one **46** (250 mg, 0.47 mmol) in dry THF (50 mL) under N$_2$, was added NaOMe (0.93 M solution in MeOH, 2.02 mL, 1.87 mmol) and the reaction was heated to reflux for 15 min. Upon cooling to room temperature, (Et$_4$N)Br (99 mg, 0.47 mmol) was added followed by NiCl$_2$.6H$_2$O (55 mg, 0.23 mmol) and the reaction mixture stirred overnight. The reaction mixture was filtered and the solvent removed under reduced pressure prior to precipitation from hot THF with ethanol to give a dull yellow/orange solid (92 mg, 33 %). Further attempts to purify led to decomposition of the complex; m.p. = blackens.

A red crystal was obtained from liquid diffusion of cyclohexane into a THF solution.

MS (MALDI): *m/z* = 1072 [M – Et$_4$N]$^-$.

Elemental Analysis: Found C, 53.59; H, 6.46; N 1.37, Calculated: C, 59.92; H, 7.38; N, 1.16.

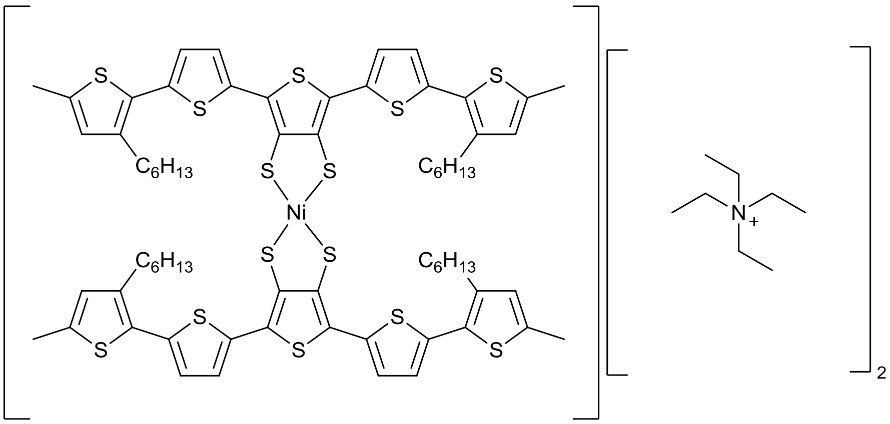

$[(C_{34}H_{38}S_7)_2Ni][Et_4N]_2$ (81):

Under N_2, 1,3-dithiole-2-one **47** (250 mg, 0.36 mmol) was dissolved in dry THF (50 mL) before addition of NaOMe (0.93 M solution in MeOH, 1.54 mL, 1.43 mmol) and the reaction mixture heated to reflux for 15 min. The reaction was then allowed to cool to room temperature and $(Et_4N)Br$ (76 mg, 0.36 mmol) was added followed by $NiCl_2.6H_2O$ (43 mg, 0.18 mmol), before the reaction was stirred overnight. The reaction mixture was filtered and the solvent removed under reduced pressure, prior to precipitation from hot THF with ethanol to give a black/red powder (208 mg, 70 %). Further attempts to purify resulted in decomposition of the complex; m.p. = 167-168 °C

Single crystals were obtained from liquid diffusion of cyclohexane into a CH_2Cl_2 solution.

MS (MALDI): *m/z* = 1400 $[M - 2Et_4N + e]^-$.

Elemental Analysis: Found C, 57.40; H, 6.26; N, 1.41 Calculated: C, 60.72; H, 7.04; N, 1.69.

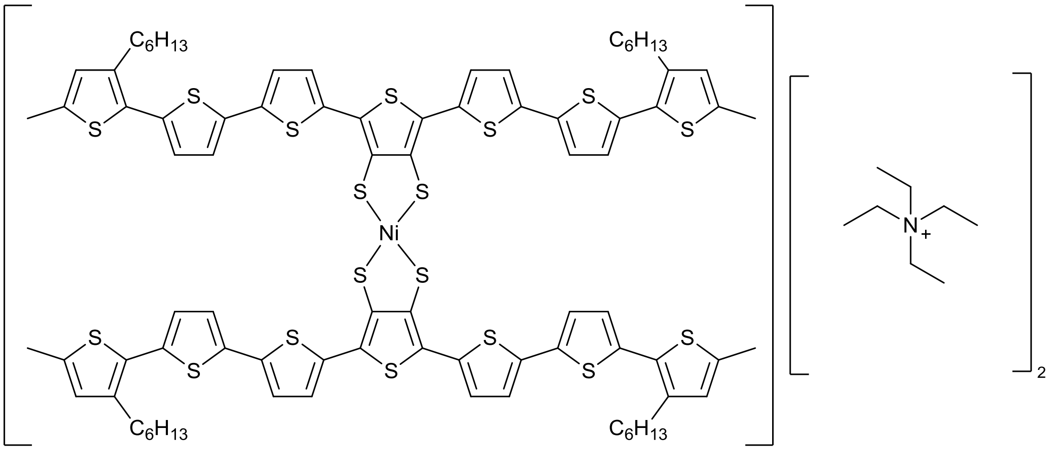

[($C_{42}H_{42}S_9$)$_2$Ni][Et_4N]$_2$ (82):

Under N_2, 1,3-dithiole-2-one **48** (250 mg, 0.29 mmol) was dissolved in dry THF (50 mL) before addition of NaOMe (0.93 M solution in MeOH, 1.25 mL, 1.16 mmol) and the reaction mixture heated to reflux for 15 min. The reaction was then allowed to cool to room temperature and (Et_4N)Br (61 mg, 0.29 mmol) was added followed by $NiCl_2.6H_2O$ (36 mg, 0.15 mmol), before the reaction was stirred overnight. The reaction mixture was filtered and the solvent removed under reduced pressure, prior to precipitation from hot THF with ethanol to give a black/purple powder (233 mg, 78 %). Further attempts to purify resulted in decomposition of the complex; m.p. = 172-174 °C. Crystals were obtained from liquid diffusion of EtOH into a THF solution.

MS (MALDI): *m/z* = 1726 $[M - 2Et_4N + e]^-$.

Elemental Analysis: Found C, 57.32; H, 5.44; N, 1.04 Calculated: C, 60.36; H, 6.28; N, 1.41.

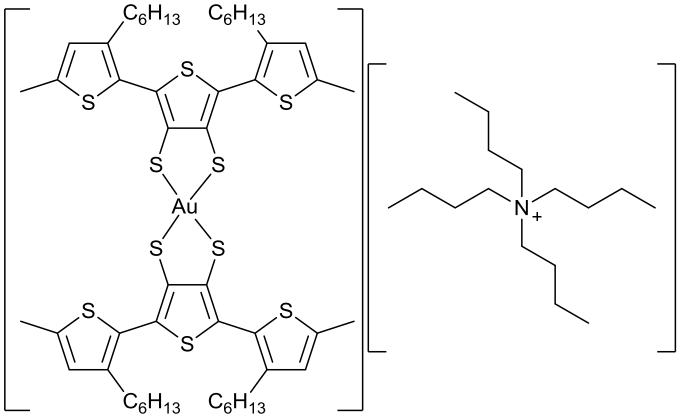

[($C_{26}H_{34}S_5$)$_2$Au][Et_4N] (83):

To a solution of 1,3-dithiole-2-one **46** (250 mg, 0.47 mmol) in dry THF (50 mL) under N_2, was added NaOMe (0.61 M solution in MeOH, 3.06 mL, 1.87 mmol) and the reaction mixture heated to reflux for 15 min. Upon cooling to room temperature, (*n*-Bu_4N)Br (152 mg, 0.47 mmol) was added, followed by $KAuCl_4$ (88 mg, 0.23 mmol) and the reaction was stirred overnight. The reaction mixture was filtered and the solvent removed under reduced pressure. The crude material was dissolved in ethyl acetate and filtered through celite to give a purple solution. The solvent was removed and the product crystallised from a THF/MeCN mixture (*ca.* 1:80) in the freezer over 14 days to give a grey/black crystalline powder (144 mg, 43 %); m.p. = 148-149 °C.

MS (MALDI): *m/z* = 1209 [M – *n*-Bu_4N]$^-$.

Elemental Analysis: Found C, 56.26; H, 7.15; N, 0.67; S, 22.18 Calculated: C, 56.20; H, 7.21; N, 0.96; S, 22.07.

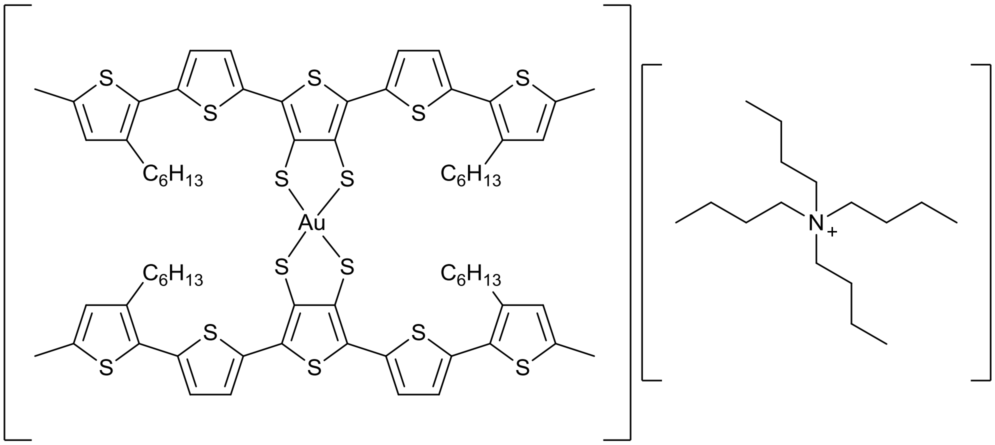

$[(C_{34}H_{38}S_7)_2Au][Et_4N]$ (84):

Under N_2, 1,3-dithiole-2-one **47** (250 mg, 0.36 mmol) was dissolved in dry THF (50 mL) before addition of NaOMe (0.61 M solution in MeOH, 2.34 mL, 1.43 mmol) and the reaction mixture heated to reflux for 15 min. The reaction was then allowed to cool to room temperature and (n-Bu_4N)Br (116 mg, 0.36 mmol) was added, followed by $KAuCl_4$ (68 mg, 0.18 mmol) before the reaction was stirred overnight. The solvent was removed under reduced pressure and the crude material was dissolved in ethyl acetate and filtered through celite to give an emerald green solution. After removal of solvent the material was crystallised *via* diffusion of MeCN into THF to give a dark green crystalline solid (153 mg, 48 %); m.p. = 104-105 °C.

MS (MALDI): $m/z = 1537$ $[M - n\text{-}Bu_4N]^-$.

Elemental Analysis: Found C, 56.45; H, 6.23; N, 0.85; S, 25.09 Calculated: C, 56.63; H, 6.34; N, 0.79; S, 25.20.

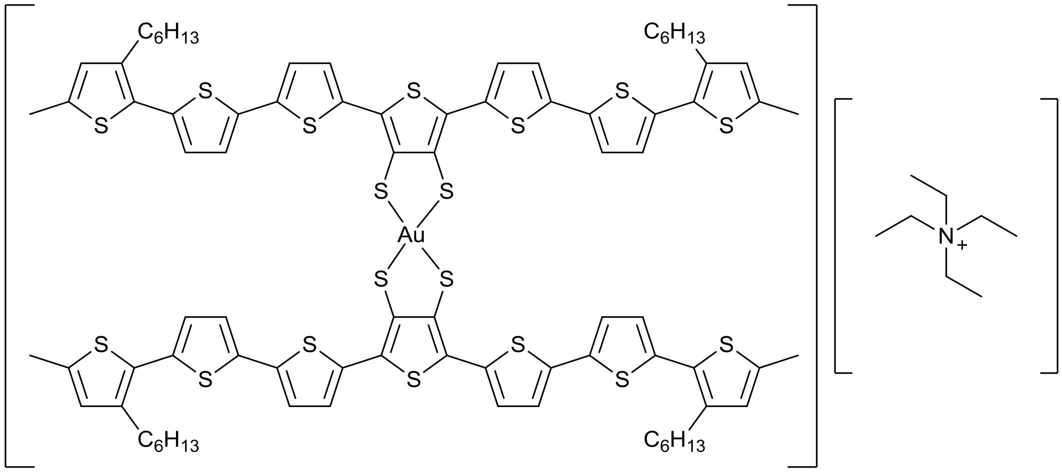

[($C_{42}H_{42}S_9$)$_2$Au][Et_4N] (85):

1,3-Dithiole-2-one **48** (250 mg, 0.29 mmol) was dissolved in dry THF (50 mL) in a N_2 atmosphere before addition of NaOMe (0.34 M solution in MeOH, 3.41 mL, 1.16 mmol) and the reaction mixture heated to reflux for 15 min. The reaction was then allowed to cool to room temperature and (Et_4N)Br (30 mg, 0.15 mmol) was added, followed by $KAuCl_4$ (57 mg, 0.15 mmol) before the reaction was stirred overnight. The reaction mixture was filtered and the solvent removed under reduced pressure prior to precipitation from hot THF with ethanol to give a brown powder (222 mg, 74 %); m.p. = 188-190 °C.

Crystals for X-ray crystallographic analysis were obtained from liquid diffusion of EtOH into a THF solution.

MS (MALDI): *m/z* = 1865 [M – Et_4N]$^-$.

Elemental Analysis: Found C, 51.60; H, 4.27; N, 0.52; S, 28.70 Calculated: C, 55.31; H, 5.25; N, 0.70; S, 28.89.

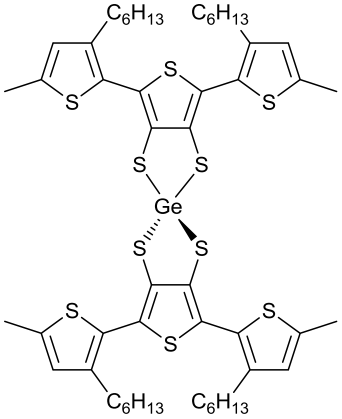

4,4',6,6'-Tetrakis(3-hexyl-5-methylthiophen-2-yl)-2,2'-spirobi[thieno[3,4-d][1,3,2]dithiagermole] (89):

Under N_2, 1,3-dithiole-2-one **46** (300 mg, 0.56 mmol) was dissolved in anhydrous THF (50 mL). NaOMe (0.72 M solution in MeOH, 2.33 mL, 1.68 mmol) was added, resulting in an immediate colour change from yellow to red/orange, and the reaction was heated to reflux for 15 min. Upon cooling to room temperature $GeBr_4$ (0.13 M solution in anhydrous THF, 2.38 mL, 0.31 mmol) was added and the reaction was left to stir overnight. 2n HCl (10 mL) was added before the reaction mixture was poured into H_2O (100 mL) and extracted with CH_2Cl_2 (3 × 50 mL) before drying over Na_2SO_4 and removal of solvent under reduced pressure. The crude material was dissolved in CH_2Cl_2 (80 mL) and stirred with decolourising charcoal for 30 min, then filtered through a silica plug and the solvent removed under reduced pressure. The pure material was then obtained by washing through a silica plug (*ca.* 5 × 10 cm thick) eluting with Et_2O to yield a thick yellow oil (219 mg, 65 %).

^{1}H NMR ($CDCl_3$): $\delta = 6.64$ (4H, m), 2.56 (8H, t, $J = 7.75$), 2.48 (12H, m), 1.57 (8H, brm), 1.28 (24H, brm), 0.86 (12H, t, $J = 6.75$).

^{13}C NMR ($CDCl_3$): $\delta = 143.5$, 143.0, 141.2, 140.5, 136.4, 131.8, 128.4, 128.3, 127.6, 127.4, 126.6, 125.2, 124.6, 31.7, 30.7, 29.3, 29.1, 22.6, 15.4, 14.1.

MS (MALDI): $m/z = 1086$ [M]$^+$.

Elemental Analysis: Found C, 59.60; H, 5.94; N, 0.00 Calculated: C, 57.49; H, 6.31; N, 0.00.

The ^{1}H and ^{13}C spectra for **89** are shown in figures 6-13 and 6-14 respectively. The general shape of the ^{1}H spectra can be rationalised in the same manner as for the precursor **46**, and the bis(terthiophene) TTF **70**, though the aromatic multiplet displays a number of splitting and minor peaks not observed previously.

There is a mismatch between the structure and its ^{13}C spectrum, specifically a surplus of aromatic C signals. The multiplet nature of the aromatic proton signal in the ^{1}H spectrum, and minor peaks observed in the aliphatic region of the ^{13}C spectrum indicates the possibility of some diastereomeric effects which should be investigated further.

The mass spectrum showed the presence of the unfragmented molecular ion.

The carbon result of elemental analysis showed considerable disparity from the calculated value. Oils are prone to retaining solvents which may be a factor in explaining this result. If possible, distillation to remove residual solvents may help to resolve this issue.

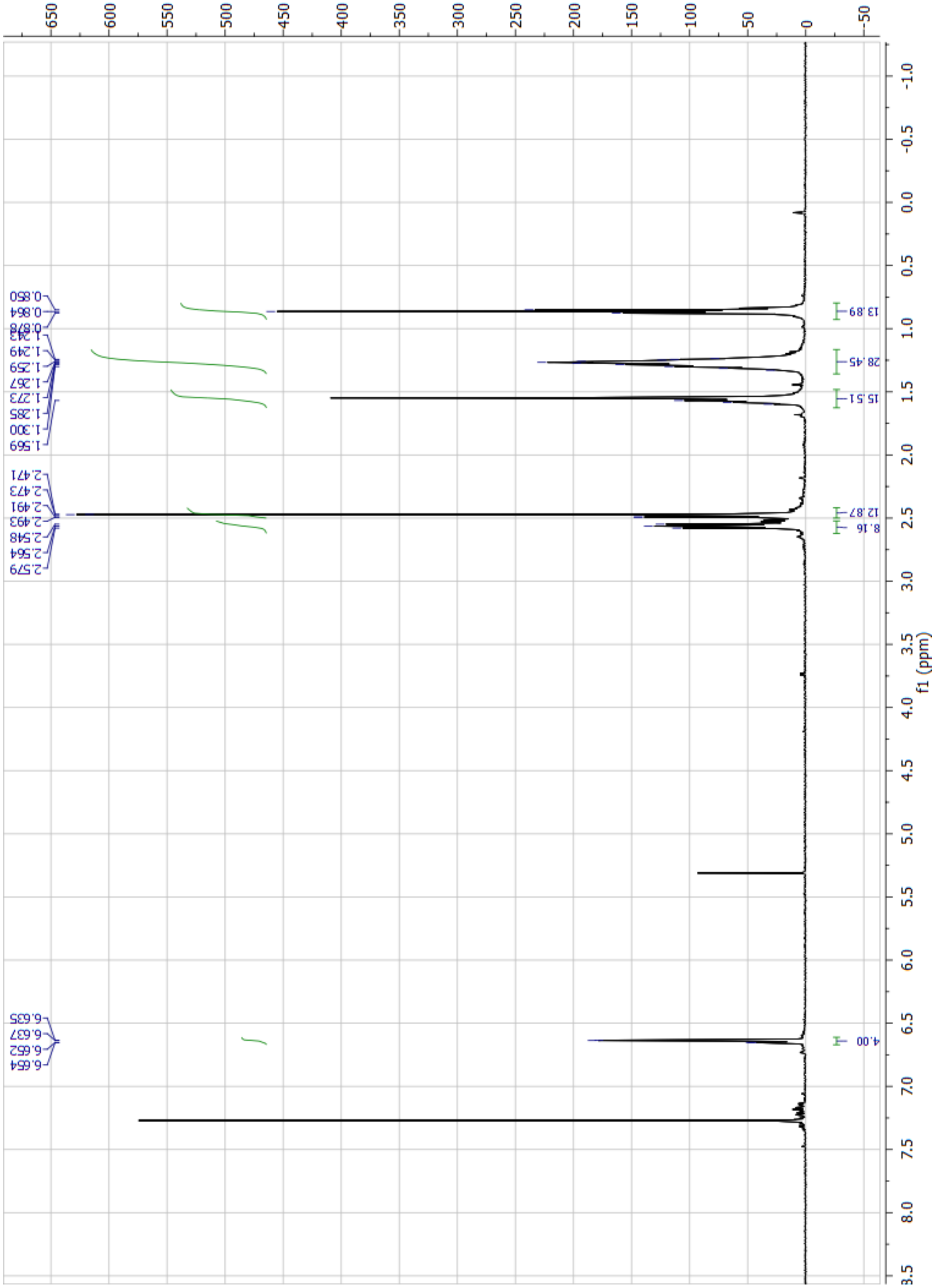

Figure 6-13 ^{1}H NMR spectrum of **89**.

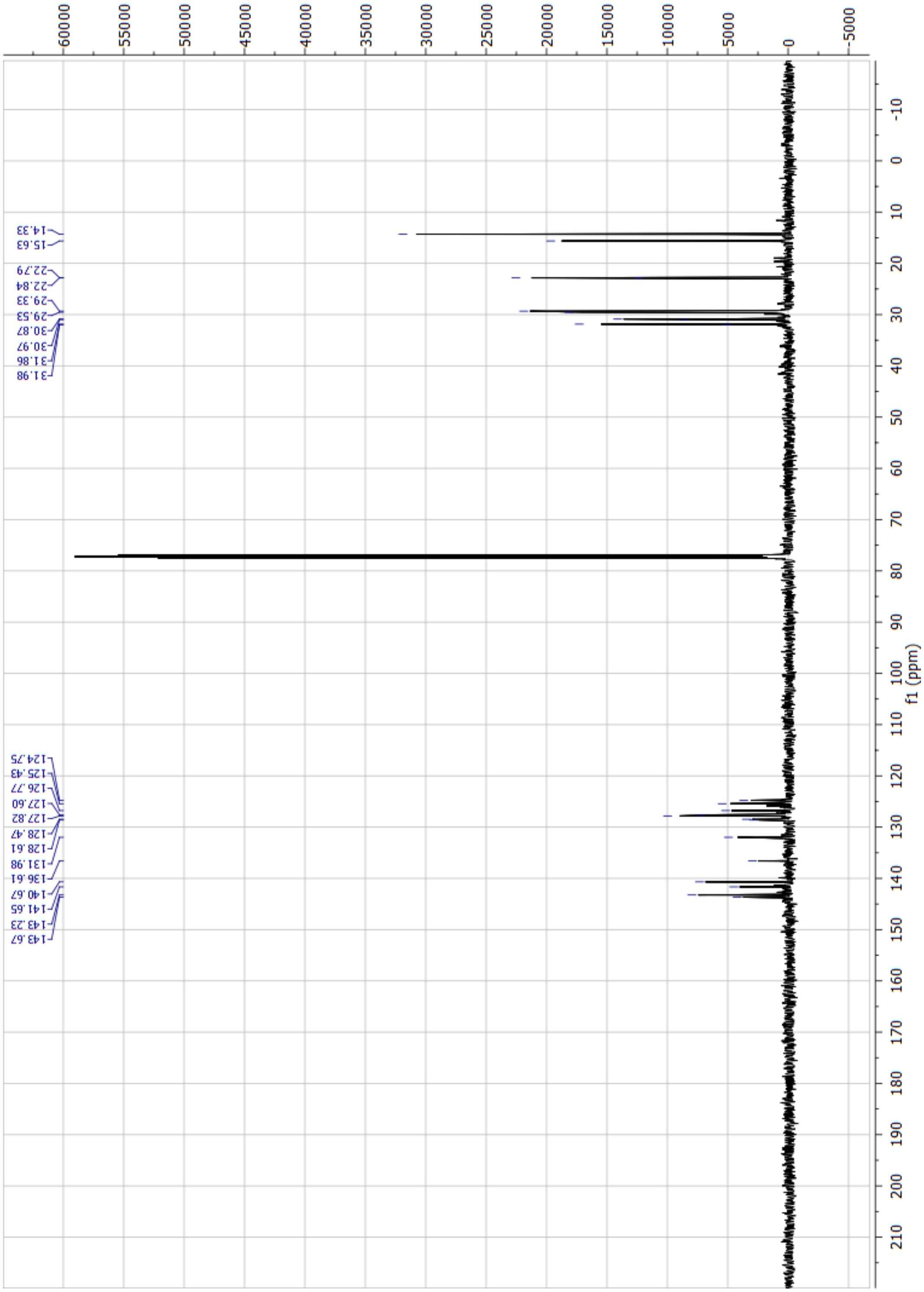

Figure 6-14 ^{13}C NMR spectrum of **89**.

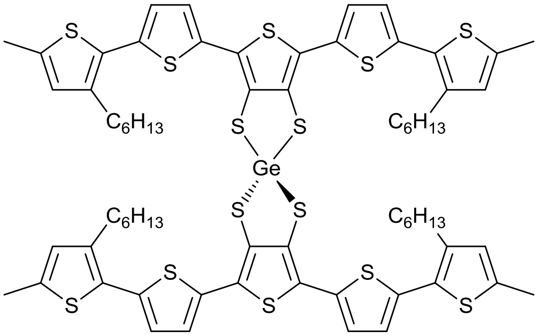

4,4',6,6'-Tetrakis(3'-hexyl-5'-methyl-[2,2'-bithiophen]-5-yl)-2,2'-spirobi[thieno[3,4-d][1,3,2]dithiagermole] (90):

Under N_2, 1,3-dithiole-2-one **47** (300 mg, 0.43 mmol) was dissolved in anhydrous THF (50 mL). NaOMe (0.72 M solution in MeOH, 1.80 mL, 1.29 mmol) was added, resulting in a colour change from orange to dark red, and the reaction was heated to reflux for 15 min then allowed to cool to room temperature. $GeBr_4$ (0.13 M solution in anhydrous THF, 1.85 mL, 0.24 mmol) was then added and the reaction was left to stir overnight. 2n HCl (10 mL) was added before the reaction mixture was poured into H_2O (100 mL) and extracted with CH_2Cl_2 (3 × 50 mL) before drying over Na_2SO_4 and removal of the solvent under reduced pressure. Purification was achieved *via* recrystallisation from cyclohexane to yield a bright orange powder (237 mg, 70 %); m.p. = 174-175 °C.

Crystals suitable for crystallographic analysis were grown *via* liquid diffusion of EtOH into a CH_2Cl_2/CS_2 solution.

^1H NMR (CD_2Cl_2/CS_2): $\delta = 7.33$ (4H, d, $J = 4.00$), 7.01 (4H, d, $J = 4.00$), 6.62 (4H, m), 2.74 (8H, t, $J = 7.75$), 2.48 (12H, s), 1.66 (8H, broad quintet, $J = 7.63$), 1.36 (24H, brm), 0.91 (12H, t, $J = 7.00$).

^{13}C NMR (CD_2Cl_2/CS_2): $\delta = 140.7$, 139.2, 137.8, 134.7, 129.3, 129.2, 128.0, 126.7, 126.4, 125.9, 32.2, 31.1, 29.9, 29.8, 23.2, 15.5, 14.4.

MS (MALDI): $m/z = 1414$ $[M]^+$.

Elemental Analysis: Found C, 57.56; H, 5.00; N, 0.00; S, 31.65 Calculated: C, 57.72; H, 5.41; N, 0.00; S, 31.73.

The ^{1}H spectrum of **90** is shown in figure 6-15, CS_2 as an additive was required in order to overcome aggregation effects. The spectrum shows the characteristic multiplet at 6.62 ppm relating to the lone proton of the terminal thiophenes, and two doublets at 7.33 and 7.01 ppm. The well-defined nature of these peaks indicates complementary geometries of the oligothiophene chains. The aliphatic region cna be explained in the same way as before, and the peak shapes and integrals here again indicate highly complementary geometry of the chains.

The ^{13}C spectrum of **90** (figure 6-16) is quite similar to that of the precursor **47**, and can be explained in the same way. Unlike with the terthiophene analogue **89**, no minor peaks are observed, and the total number of peaks matches what is expected, demonstrating again that the oligothiophene chains are equivalent.

The unfragmented molecular ion was present in the mass spectrum

The results obtained for elemental analysis agreed well with the calculated values.

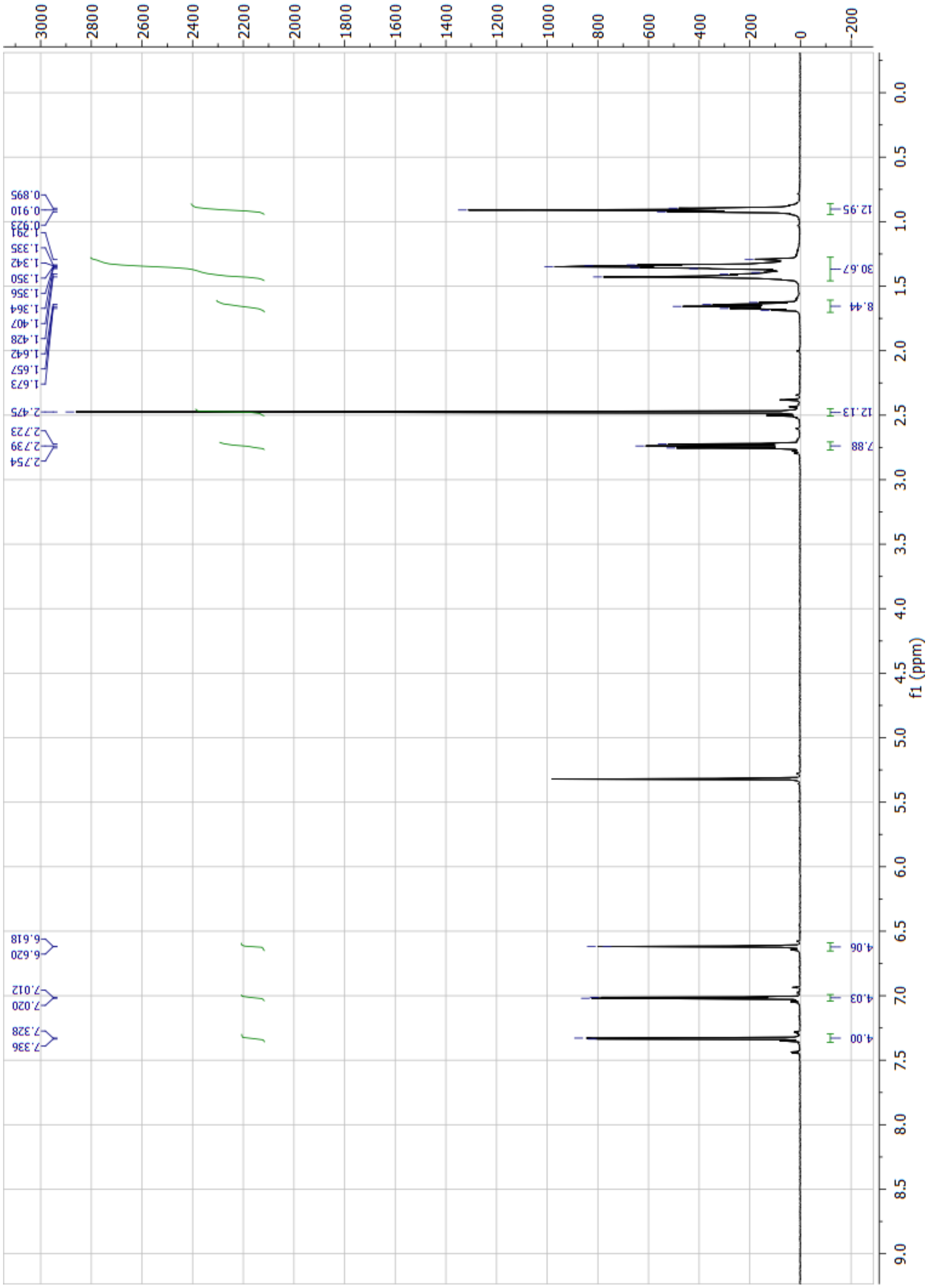

Figure 6-15 ^{1}H NMR spectrum of **90**.

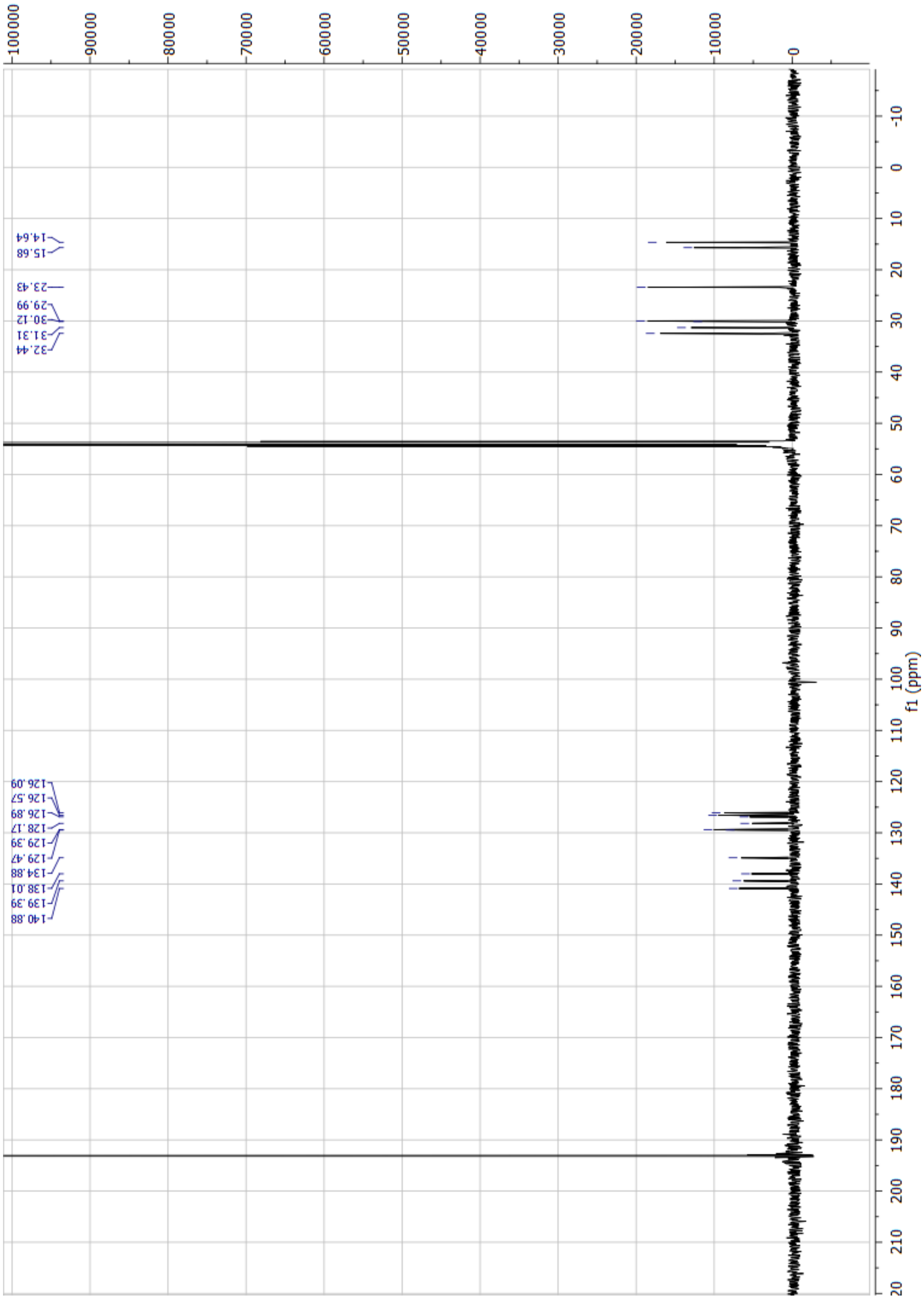

Figure 6-16 ^{13}C NMR spectrum of **90**.

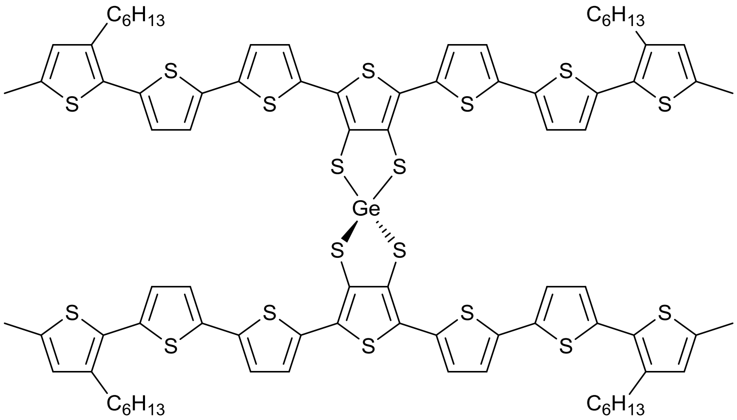

4,4',6,6'-Tetrakis(3''-hexyl-5''-methyl-[2,2':5',2''-terthiophen]-5-yl)-2,2'-spirobi[thieno[3,4-d][1,3,2]dithiagermole] (91):

Under N_2, 1,3-dithiole-2-one **48** (300 mg, 0.43 mmol) was dissolved in anhydrous THF (50 mL). NaOMe (0.72 M solution in MeOH, 1.44 mL, 1.04 mmol) was added, resulting in a colour change from red to deep violet, and the reaction was heated to reflux for 15 min then allowed to cool to room temperature. $GeBr_4$ (0.13 M solution in anhydrous THF, 1.46 mL, 0.19 mmol) was then added and the reaction was left to stir overnight. 2n HCl (10 mL) was added before the reaction mixture was poured into H_2O (100 mL) and extracted with chloroform (3 × 50 mL) before drying over Na_2SO_4 and removal of the solvent under reduced pressure. The material was purified by passing the material through a silica plug (*ca.* 5 × 10 cm thick), first eluting with CS_2 to remove unwanted starting material and by-products, then chloroform for the desired product. The material was then precipitated from THF with EtOH to give a dark red powder (212 mg, 64 %); m.p. = 196-197 °C.

Single crystals for X-ray analysis were grown by liquid diffusion of EtOH into a CH_2Cl_2/CS_2 solution.

^{1}H NMR (CD_2Cl_2/CS_2): δ = 7.43 (3H, d, J = 4.00), 7.35 (1H, s), 7.24 (3H, d, J = 3.50), 7.16 (3H, d, J = 3.50), 7.14 (2H, m), 6.95 (4H, m), 6.61 (4H, m), 2.73

(8H, m), 2.48 (12H, s), 1.65 (8H, brm), 1.40 (24H, brm), 0.94 (12H, brt, *J* = 7.00).

^{13}C NMR (CD_2Cl_2/CS_2): δ = 140.3, 138.8, 138.2, 137.0, 136.00, 134.4, 129.7, 129.2, 128.3, 127.0, 126.8, 126.3, 124.8, 124.3, 32.4, 31.2, 30.0, 29.9, 23.4, 15.6, 14.7.

MS (MALDI): *m/z* =1746 [M + H]$^+$.

Elemental Analysis: Found C, 59.32; H, 4.50; N, 0.00; S, 33.93 Calculated: C, 57.87; H, 4.86; N, 0.00; S, 33.11.

Figure 6-17 depicts the ^{1}H NMR spectrum for **91**. This molecule is prone to aggregation and the aromatic region is complicated, with a number of overlapping signals. The signal relating to the sole proton of the terminal thiophenes is present at 6.61 ppm. The other protons give a number of responses between 7.43 and 6.95 ppm with integrals ranging from 1-4. If the concentration of CS_2 in the solution drops, aggregation effects begin to further dominate the spectrum; the peak bases broaden and broad-profiled peaks emerge similarly to the effects observed in the ^{1}H NMR spectrum for the bis(septithiophene) TTF **72** (figure 6-12). Whilst the total of the integrals works out as expected, the multiplet and/or overlapping nature of many of these signals, and the range of integrals encountered may indicate some disorder along one or both of the septithiophene chains. The aliphatic region of the spectrum is quite well-defined and the integrals correlate well to the values expected. This region of the spectrum can be explained in a similar fashion to those of the molecules described previously.

The ^{13}C spectrum is shown in figure 6-18. The cluster of fourteen aromatic peaks between 140.3-124.3 ppm correlates well with the expected molecular structure. The peak at 100.4 ppm is due to impurities present in the CS_2. Similarly to the ^{1}H spectrum, the aliphatic region can be explained in the same manner as for molecules described previously.

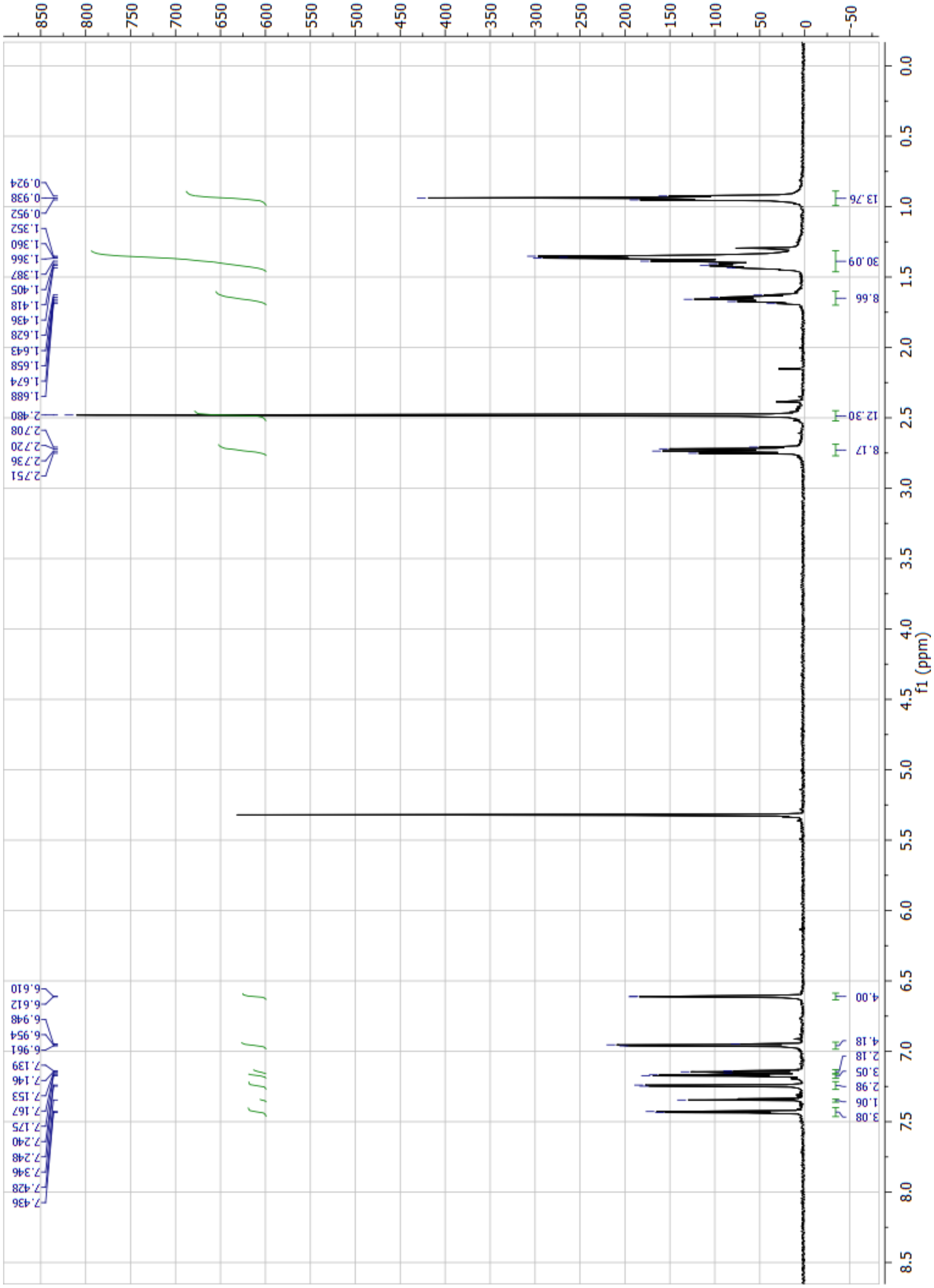

Figure 6-17 ¹H NMR spectrum of **91**.

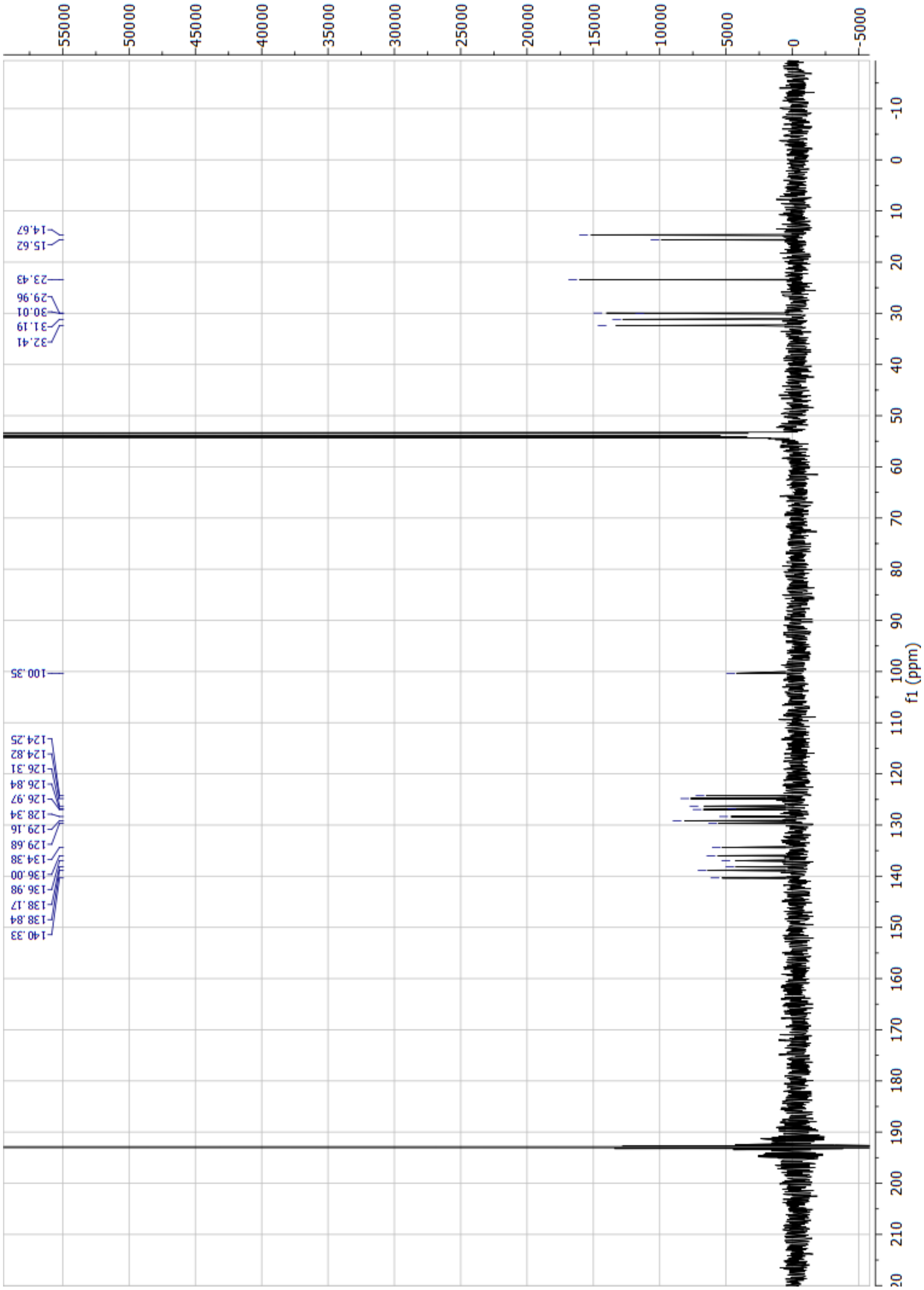

Figure 6-18 ^{13}C NMR spectrum of **91**.

The unfragmented molecular ion was present in the mass spectrum.

As mentioned previously, obtaining satisfactory results for the elemental analysis of the compounds which aggregate extensively has proven difficult. The data presented above shows some of the better results obtained, though poor reproducibility between runs indicates that this substance may not be well suited to this method of analysis.

Chapter 7: Supporting Crystal Data

7.1. 1,3-Dithiole-2-one Functionalised Septithiophene 48

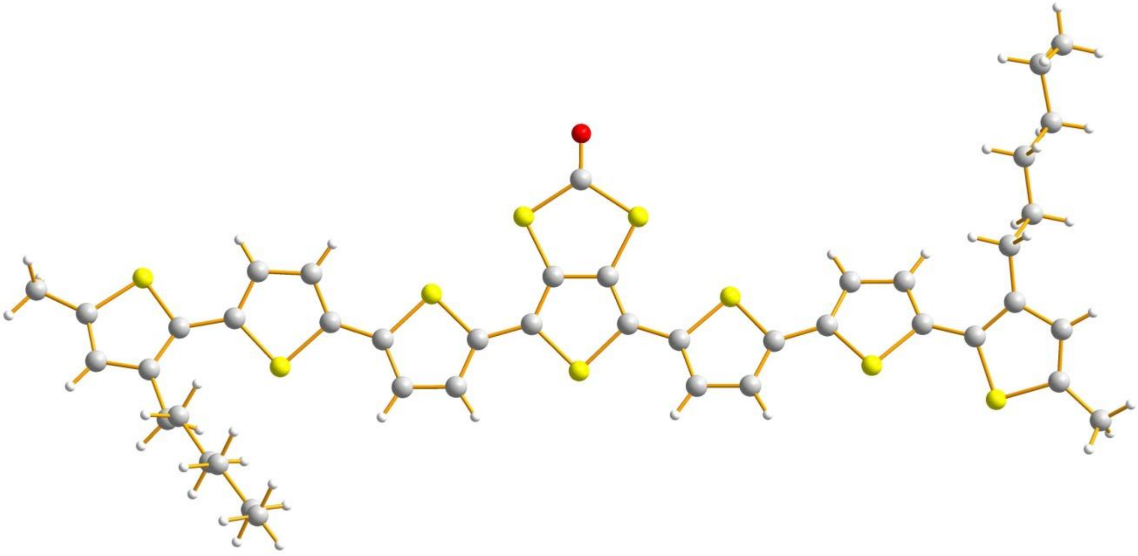

Table 1. Crystal data and structure refinement for 2009src1321r.

Identification code	2009src1321r	
Empirical formula	C43 H42 O S9	
Formula weight	863.31	
Temperature	120(2) K	
Wavelength	0.71073 Å	
Crystal system	Monoclinic	
Space group	P2(1)/c	
Unit cell dimensions	a = 18.4493(18) Å	α= 90°.
	b = 16.6052(16) Å	β= 99.196(4)°.
	c = 14.1055(12) Å	γ = 90°.
Volume	4265.7(7) Å^3	
Z	4	
Density (calculated)	1.344 Mg m^{-3}	
Absorption coefficient	0.501 mm^{-1}	
F(000)	1808	
Crystal size	0.20 x 0.04 x 0.01 mm^3	

Theta range for data collection	2.93 to 27.50°.
Index ranges	-23<=h<=23, -21<=k<=21, -18<=l<=18
Reflections collected	51176
Independent reflections	9743 [R(int) = 0.1372]
Completeness to theta =	27.50° 99.3 %
Absorption correction	Semi-empirical from equivalents
Max. and min. transmission	0.9950 and 0.9065
Refinement method	Full-matrix least-squares on F^2
Data / restraints / parameters	9743 / 0 / 482
Goodness-of-fit on F2	1.114
Final R indices [I>2sigma(I)]	R1 = 0.1478, wR2 = 0.2442
R indices (all data)	R1 = 0.2375, wR2 = 0.2903
Largest diff. peak and hole	0.635 and -0.529 e.Å^{-3}

Table 2. Atomic coordinates (x 10^4) and equivalent isotropic displacement parameters (Å^{2}x 10^3) for 2009src1321r. U(eq) is defined as one third of the trace of the orthogonalized U^{ij} tensor.

	x	y	z	U(eq)
C(1)	7112(6)	4491(6)	-463(7)	42(2)
C(2)	6143(5)	5657(6)	-683(6)	33(2)
C(3)	6445(5)	5634(6)	-1553(6)	34(2)
C(4)	5589(5)	6200(6)	-694(6)	34(2)
C(5)	6135(5)	6163(6)	-2224(6)	34(2)
C(6)	5142(5)	6382(5)	43(6)	28(2)
C(7)	4550(5)	6881(5)	-6(6)	33(2)
C(8)	4246(5)	6906(5)	846(6)	34(2)
C(9)	4609(5)	6418(6)	1555(6)	35(2)

C(10)	4456(5)	6230(6)	2504(6)	35(2)
C(11)	4725(6)	5630(7)	3107(7)	43(3)
C(12)	4414(6)	5589(6)	3944(7)	42(2)
C(13)	3882(5)	6148(6)	3990(6)	34(2)
C(14)	3495(5)	6283(6)	4808(6)	37(2)
C(15)	3176(6)	6236(6)	6461(7)	42(2)
C(16)	3190(6)	6068(6)	7523(7)	48(3)
C(17)	2669(6)	6631(6)	5825(7)	41(2)
C(18)	2846(5)	6658(6)	4874(7)	35(2)
C(19)	2360(6)	7066(7)	4070(7)	46(3)
C(20)	1909(7)	6474(7)	3373(7)	61(3)
C(21)	1579(7)	6886(9)	2435(9)	71(4)
C(22)	1069(7)	6357(8)	1756(9)	65(3)
C(23)	779(8)	6787(10)	802(10)	85(4)
C(24)	237(9)	6313(12)	143(11)	111(6)
C(25)	6243(6)	6288(6)	-3198(7)	38(2)
C(26)	5806(5)	6677(6)	-3936(6)	35(2)
C(27)	6077(6)	6619(6)	-4822(6)	39(2)
C(28)	6706(5)	6202(5)	-4776(6)	32(2)
C(29)	7159(5)	6022(6)	-5491(7)	36(2)
C(30)	7831(5)	5678(6)	-5384(7)	41(2)
C(31)	8126(6)	5639(7)	-6253(7)	54(3)
C(32)	7676(5)	5940(6)	-7032(7)	41(2)
C(33)	7796(5)	5994(6)	-8024(7)	36(2)
C(34)	7882(5)	6495(6)	-9674(7)	38(2)
C(35)	7814(7)	6964(7)	-10578(7)	53(3)
C(36)	8274(5)	5809(6)	-9427(7)	38(2)
C(37)	8244(5)	5505(6)	-8489(7)	36(2)
C(38)	8595(6)	4740(6)	-8114(7)	43(3)

C(39)	9430(6)	4810(7)	-7815(8)	48(3)
C(40)	9757(6)	4013(8)	-7409(10)	63(3)
C(41)	10592(7)	4005(9)	-7211(12)	88(5)
C(42)	10911(8)	3204(9)	-6747(14)	104(6)
C(43)	10723(8)	2478(9)	-7445(13)	104(6)
O(1)	7493(4)	3936(4)	-165(5)	51(2)
S(1)	5441(1)	6714(2)	-1789(2)	35(1)
S(2)	6480(1)	4956(2)	197(2)	36(1)
S(3)	7136(1)	4930(2)	-1615(2)	37(1)
S(4)	5336(1)	5934(2)	1161(2)	36(1)
S(5)	3775(1)	6755(2)	2978(2)	34(1)
S(6)	3885(2)	5889(2)	5905(2)	39(1)
S(7)	7000(1)	5868(2)	-3607(2)	38(1)
S(8)	6858(1)	6261(2)	-6691(2)	39(1)
S(9)	7447(2)	6803(2)	-8727(2)	41(1)

Table 3. Bond lengths [Å] and angles [°] for 2009src1321r.

C(1)-O(1)	1.193(12)	C(5)-C(25)	1.434(12)
C(1)-S(2)	1.780(10)	C(5)-S(1)	1.763(9)
C(1)-S(3)	1.789(10)	C(6)-C(7)	1.363(13)
C(2)-C(4)	1.361(13)	C(6)-S(4)	1.728(9)
C(2)-C(3)	1.428(12)	C(7)-C(8)	1.405(12)
C(2)-S(2)	1.743(9)	C(8)-C(9)	1.375(13)
C(3)-C(5)	1.350(13)	C(9)-C(10)	1.445(12)
C(3)-S(3)	1.743(9)	C(9)-S(4)	1.730(9)
C(4)-C(6)	1.458(13)	C(10)-C(11)	1.353(13)
C(4)-S(1)	1.747(9)	C(10)-S(5)	1.748(9)

C(11)-C(12)	1.394(13)	C(33)-S(9)	1.730(10)
C(12)-C(13)	1.359(13)	C(34)-C(36)	1.365(14)
C(13)-C(14)	1.468(13)	C(34)-C(35)	1.482(13)
C(13)-S(5)	1.733(9)	C(34)-S(9)	1.740(10)
C(14)-C(18)	1.366(13)	C(36)-C(37)	1.426(12)
C(14)-S(6)	1.728(9)	C(37)-C(38)	1.484(14)
C(15)-C(17)	1.357(14)	C(38)-C(39)	1.535(14)
C(15)-C(16)	1.519(13)	C(39)-C(40)	1.528(15)
C(15)-S(6)	1.729(10)	C(40)-C(41)	1.521(16)
C(17)-C(18)	1.431(13)	C(41)-C(42)	1.555(19)
C(18)-C(19)	1.491(13)	C(42)-C(43)	1.56(2)
C(19)-C(20)	1.537(15)		
C(20)-C(21)	1.527(16)	O(1)-C(1)-S(2)	123.2(8)
C(21)-C(22)	1.512(17)	O(1)-C(1)-S(3)	122.4(8)
C(22)-C(23)	1.542(17)	S(2)-C(1)-S(3)	114.4(6)
C(23)-C(24)	1.478(19)	C(4)-C(2)-C(3)	113.8(8)
C(25)-C(26)	1.372(13)	C(4)-C(2)-S(2)	129.3(7)
C(25)-S(7)	1.740(10)	C(3)-C(2)-S(2)	116.8(7)
C(26)-C(27)	1.421(12)	C(5)-C(3)-C(2)	113.9(8)
C(27)-C(28)	1.344(13)	C(5)-C(3)-S(3)	129.3(7)
C(28)-C(29)	1.440(12)	C(2)-C(3)-S(3)	116.8(7)
C(28)-S(7)	1.743(9)	C(2)-C(4)-C(6)	129.6(8)
C(29)-C(30)	1.351(13)	C(2)-C(4)-S(1)	110.2(7)
C(29)-S(8)	1.740(10)	C(6)-C(4)-S(1)	120.2(7)
C(30)-C(31)	1.420(13)	C(3)-C(5)-C(25)	131.1(9)
C(31)-C(32)	1.362(14)	C(3)-C(5)-S(1)	110.1(7)
C(32)-C(33)	1.454(13)	C(25)-C(5)-S(1)	118.6(7)
C(32)-S(8)	1.738(10)	C(7)-C(6)-C(4)	129.0(8)
C(33)-C(37)	1.395(13)	C(7)-C(6)-S(4)	110.8(7)

C(4)-C(6)-S(4)	120.2(7)	C(26)-C(25)-C(5)	129.7(9)
C(6)-C(7)-C(8)	113.6(8)	C(26)-C(25)-S(7)	110.1(7)
C(9)-C(8)-C(7)	112.9(9)	C(5)-C(25)-S(7)	120.1(8)
C(8)-C(9)-C(10)	131.0(9)	C(25)-C(26)-C(27)	112.8(9)
C(8)-C(9)-S(4)	110.6(7)	C(28)-C(27)-C(26)	114.5(9)
C(10)-C(9)-S(4)	118.3(7)	C(27)-C(28)-C(29)	131.7(8)
C(11)-C(10)-C(9)	129.4(9)	C(27)-C(28)-S(7)	110.2(7)
C(11)-C(10)-S(5)	109.9(7)	C(29)-C(28)-S(7)	118.0(7)
C(9)-C(10)-S(5)	120.4(7)	C(30)-C(29)-C(28)	129.3(9)
C(10)-C(11)-C(12)	114.2(9)	C(30)-C(29)-S(8)	110.4(7)
C(13)-C(12)-C(11)	113.9(9)	C(28)-C(29)-S(8)	120.2(7)
C(12)-C(13)-C(14)	126.0(9)	C(29)-C(30)-C(31)	113.2(9)
C(12)-C(13)-S(5)	110.2(7)	C(32)-C(31)-C(30)	114.3(10)
C(14)-C(13)-S(5)	123.6(7)	C(31)-C(32)-C(33)	129.2(9)
C(18)-C(14)-C(13)	131.7(9)	C(31)-C(32)-S(8)	109.4(8)
C(18)-C(14)-S(6)	110.9(7)	C(33)-C(32)-S(8)	121.4(8)
C(13)-C(14)-S(6)	117.5(7)	C(37)-C(33)-C(32)	127.5(9)
C(17)-C(15)-C(16)	130.0(10)	C(37)-C(33)-S(9)	112.2(7)
C(17)-C(15)-S(6)	110.6(7)	C(32)-C(33)-S(9)	119.9(8)
C(16)-C(15)-S(6)	119.4(8)	C(36)-C(34)-C(35)	128.7(9)
C(15)-C(17)-C(18)	113.5(9)	C(36)-C(34)-S(9)	109.9(7)
C(14)-C(18)-C(17)	112.5(9)	C(35)-C(34)-S(9)	121.4(8)
C(14)-C(18)-C(19)	125.7(9)	C(34)-C(36)-C(37)	115.8(9)
C(17)-C(18)-C(19)	121.8(9)	C(33)-C(37)-C(36)	110.1(9)
C(18)-C(19)-C(20)	113.2(9)	C(33)-C(37)-C(38)	126.1(9)
C(21)-C(20)-C(19)	111.6(10)	C(36)-C(37)-C(38)	123.7(8)
C(22)-C(21)-C(20)	114.2(11)	C(37)-C(38)-C(39)	113.2(9)
C(21)-C(22)-C(23)	112.2(12)	C(40)-C(39)-C(38)	110.9(9)
C(24)-C(23)-C(22)	114.0(14)	C(41)-C(40)-C(39)	113.9(10)

C(40)-C(41)-C(42)	112.9(12)
C(41)-C(42)-C(43)	111.4(14)
C(4)-S(1)-C(5)	92.0(5)
C(2)-S(2)-C(1)	96.1(5)
C(3)-S(3)-C(1)	95.9(5)
C(6)-S(4)-C(9)	92.0(4)
C(13)-S(5)-C(10)	91.8(5)
C(14)-S(6)-C(15)	92.5(5)
C(25)-S(7)-C(28)	92.3(5)
C(32)-S(8)-C(29)	92.5(5)
C(33)-S(9)-C(34)	92.1(5)

Table 4. Anisotropic displacement parameters ($Å^2$x 10^3) for 2009src1321. The anisotropic displacement factor exponent takes the form: $-2p^2[h^2a^{*2}U^{11} + ... + 2 h k a^* b^* U^{12}]$

	U^{11}	U^{22}	U^{33}	U^{23}	U^{13}	U^{12}
C(1)	52(7)	43(6)	35(5)	-3(5)	17(5)	2(5)
C(2)	36(5)	35(5)	26(5)	4(4)	4(4)	-7(4)
C(3)	31(5)	38(5)	31(5)	-6(4)	0(4)	6(4)
C(4)	42(6)	32(5)	27(5)	2(4)	2(4)	-4(4)
C(5)	42(6)	34(5)	28(5)	-12(4)	9(4)	3(4)
C(6)	36(5)	26(5)	23(4)	-2(4)	3(4)	-10(4)
C(7)	42(6)	32(5)	26(4)	1(4)	8(4)	-1(4)
C(8)	45(6)	26(5)	32(5)	-7(4)	13(4)	2(4)
C(9)	38(5)	43(6)	24(4)	-6(4)	9(4)	2(4)
C(10)	39(6)	41(6)	28(5)	-7(4)	14(4)	-3(4)
C(11)	42(6)	55(7)	33(5)	3(5)	13(5)	15(5)
C(12)	48(6)	42(6)	39(6)	9(5)	14(5)	5(5)
C(13)	34(5)	40(6)	26(5)	4(4)	0(4)	-9(4)
C(14)	40(6)	44(6)	28(5)	5(4)	8(4)	-10(5)
C(15)	55(7)	42(6)	33(5)	-6(4)	19(5)	-9(5)
C(16)	68(8)	46(6)	37(6)	3(5)	28(5)	-5(6)
C(17)	45(6)	45(6)	38(5)	-9(5)	17(5)	-4(5)
C(18)	31(5)	39(6)	36(5)	-2(4)	3(4)	-7(4)
C(19)	48(7)	55(7)	39(6)	-1(5)	19(5)	12(5)
C(20)	77(9)	67(8)	37(6)	-2(6)	7(6)	12(7)
C(21)	61(9)	85(10)	61(8)	-4(7)	-5(7)	-10(7)

C(22)	53(8)	86(10)	58(8)	6(7)	11(6)	1(7)
C(23)	73(10)	111(13)	72(9)	7(9)	14(8)	0(9)
C(24)	101(13)	148(17)	73(10)	-15(11)	-22(10)	-28(12)
C(25)	44(6)	40(6)	31(5)	-15(4)	9(4)	-7(5)
C(26)	42(6)	33(5)	31(5)	-3(4)	9(4)	2(4)
C(27)	48(6)	43(6)	26(5)	-3(4)	10(4)	-2(5)
C(28)	42(6)	33(5)	21(4)	-1(4)	5(4)	2(4)
C(29)	37(5)	39(5)	35(5)	2(4)	16(4)	-4(4)
C(30)	33(5)	60(7)	30(5)	4(5)	10(4)	1(5)
C(31)	53(7)	73(8)	38(6)	2(6)	12(5)	19(6)
C(32)	38(6)	38(6)	49(6)	-2(5)	10(5)	0(5)
C(33)	37(5)	37(5)	34(5)	2(4)	5(4)	-9(4)
C(34)	40(6)	40(6)	34(5)	-5(4)	7(4)	-10(5)
C(35)	73(8)	51(7)	38(6)	3(5)	16(6)	-5(6)
C(36)	32(5)	52(6)	34(5)	6(5)	16(4)	3(5)
C(37)	30(5)	45(6)	35(5)	-6(4)	11(4)	-1(4)
C(38)	50(7)	49(6)	33(5)	-3(5)	15(5)	7(5)
C(39)	42(6)	55(7)	53(6)	4(5)	21(5)	12(5)
C(40)	52(8)	62(8)	76(9)	13(7)	12(7)	2(6)
C(41)	55(9)	66(9)	133(14)	14(9)	-15(9)	13(7)
C(42)	48(9)	71(10)	185(19)	2(11)	-5(10)	1(8)
C(43)	64(10)	73(11)	172(18)	7(11)	12(11)	2(9)
O(1)	56(5)	47(5)	50(4)	6(4)	6(4)	15(4)
S(1)	39(1)	42(1)	25(1)	2(1)	8(1)	6(1)
S(2)	40(1)	38(1)	30(1)	5(1)	9(1)	5(1)
S(3)	40(1)	42(1)	31(1)	1(1)	7(1)	6(1)
S(4)	36(1)	48(2)	27(1)	2(1)	10(1)	7(1)
S(5)	40(1)	37(1)	26(1)	0(1)	10(1)	3(1)
S(6)	46(2)	42(1)	31(1)	3(1)	11(1)	-2(1)

S(7)	39(1)	47(2)	29(1)	1(1)	11(1)	6(1)
S(8)	40(1)	48(2)	30(1)	0(1)	11(1)	3(1)
S(9)	47(2)	42(2)	36(1)	0(1)	10(1)	2(1)

7.2. Hybrid bis(septithiophene)-TTF 72

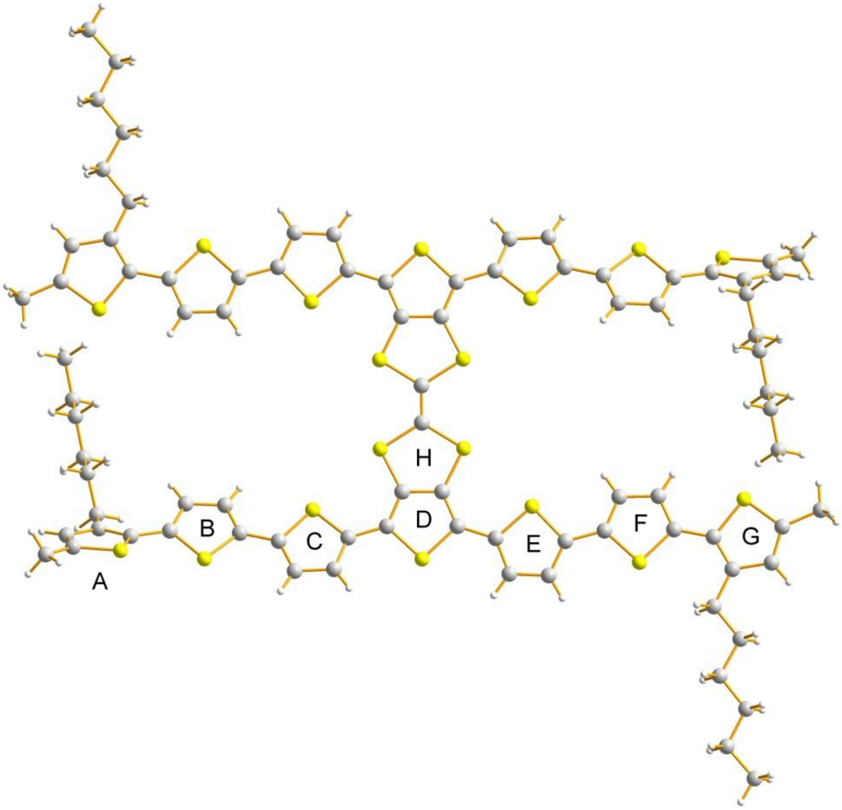

Table 1. Crystal data and structure refinement for 2010src0100.

Identification code	2010src0100	
Empirical formula	C87 H84 S20	
Formula weight	1770.74	
Temperature	120(2) K	
Wavelength	0.71073 Å	
Crystal system	Triclinic	
Space group	P-1	
Unit cell dimensions	a = 11.7929(2) Å	α = 82.8950(10)°
	b = 12.7339(3) Å	β = 74.031(2)°.
	c = 15.5721(4) Å	γ = 66.263(2)°.
Volume	2057.80(8) Å^3	

Z	1
Density (calculated)	1.429 Mg m^{-3}
Absorption coefficient	0.568 mm^{-1}
F(000)	926
Crystal size	0.20 x 0.20 x 0.06 mm^3
Theta range for data collection	2.93 to 27.50°.
Index ranges	-13<=h<=15, -16<=k<=16, -20<=l<=20
Reflections collected	37249
Independent reflections	9158 [R(int) = 0.0498]
Completeness to theta =	27.50° 96.7 %
Absorption correction	Semi-empirical from equivalents
Max. and min. transmission	0.9667 and 0.8948
Refinement method	Full-matrix least-squares on F^2
Data / restraints / parameters	9158 / 0 / 474
Goodness-of-fit on F2	1.021
Final R indices [I>2sigma(I)]	R1 = 0.0532, wR2 = 0.1385
R indices (all data)	R1 = 0.0702, wR2 = 0.1500
Largest diff. peak and hole	1.370 and -1.559 e.Å^{-3}

Table 2. Atomic coordinates (x 10^4) and equivalent isotropic displacement parameters (Å^{2}x 10^3) for 2010src0100. U(eq) is defined as one third of the trace of the orthogonalized U^{ij} tensor.

	x	y	z	U(eq)
C(44)	-5000	20000	10000	96(3)
S(10)	-3843(1)	18895(1)	9880(1)	59(1)
C(1)	5488(3)	8033(2)	3218(2)	24(1)
C(2)	5479(3)	7036(2)	3669(2)	22(1)

C(3)	6252(3)	6028(2)	3148(2)	21(1)
C(4)	6831(3)	6255(2)	2293(2)	21(1)
C(5)	5197(3)	5324(2)	4669(2)	21(1)
C(6)	4884(3)	9208(2)	3504(2)	26(1)
C(7)	5023(3)	10158(3)	3052(2)	33(1)
C(8)	4283(3)	11181(3)	3536(2)	33(1)
C(9)	3594(3)	11013(2)	4368(2)	26(1)
C(10)	2768(3)	11812(2)	5080(2)	25(1)
C(11)	2274(3)	11566(3)	5946(2)	30(1)
C(12)	1505(3)	12546(3)	6467(2)	29(1)
C(13)	1404(3)	13553(2)	6002(2)	23(1)
C(14)	637(3)	14701(2)	6349(2)	23(1)
C(15)	504(3)	15760(2)	5962(2)	25(1)
C(16)	-419(3)	16666(3)	6548(2)	29(1)
C(17)	-973(3)	16307(3)	7348(2)	29(1)
C(18)	-1942(3)	17003(3)	8123(2)	36(1)
C(19)	1208(3)	15943(3)	5028(2)	28(1)
C(20)	991(3)	17187(3)	4770(2)	32(1)
C(21)	1739(3)	17310(3)	3820(2)	31(1)
C(22)	1602(4)	18542(3)	3577(2)	36(1)
C(23)	2358(4)	18701(3)	2647(2)	41(1)
C(24)	2214(4)	19943(4)	2451(3)	54(1)
C(25)	7626(3)	5488(2)	1558(2)	23(1)
C(26)	7909(3)	5755(3)	666(2)	31(1)
C(27)	8707(3)	4786(3)	131(2)	31(1)
C(28)	9040(3)	3780(2)	610(2)	23(1)
C(29)	9847(3)	2624(2)	308(2)	23(1)
C(30)	10290(3)	1659(3)	807(2)	27(1)
C(31)	10989(3)	650(3)	303(2)	28(1)

C(32)	11098(3)	835(2)	-592(2)	26(1)
C(33)	11642(3)	4(3)	-1309(2)	30(1)
C(34)	12639(3)	-1048(3)	-1393(2)	34(1)
C(35)	12766(3)	-1611(3)	-2176(2)	39(1)
C(36)	11912(4)	-1031(3)	-2660(2)	37(1)
C(37)	11751(4)	-1399(3)	-3478(2)	47(1)
C(38)	13483(3)	-1575(3)	-769(3)	40(1)
C(39)	13150(3)	-2514(3)	-169(3)	42(1)
C(40)	14016(3)	-3104(3)	461(3)	41(1)
C(41)	13634(4)	-4004(3)	1058(3)	45(1)
C(42)	14450(4)	-4589(3)	1715(3)	51(1)
C(43)	14050(4)	-5476(4)	2307(3)	56(1)
S(1)	6451(1)	7721(1)	2142(1)	27(1)
S(2)	4662(1)	6826(1)	4752(1)	24(1)
S(3)	6306(1)	4719(1)	3663(1)	24(1)
S(4)	3840(1)	9579(1)	4546(1)	26(1)
S(5)	2276(1)	13278(1)	4902(1)	25(1)
S(6)	-373(1)	14830(1)	7413(1)	27(1)
S(7)	8353(1)	4029(1)	1737(1)	25(1)
S(8)	10340(1)	2290(1)	-815(1)	27(1)
S(9)	10889(1)	268(1)	-2169(1)	34(1)

Table 3. Bond lengths [Å] and angles [°] for 2010src0100.

C(44)-S(10)	1.5022(12)	C(1)-C(6)	1.441(4)
C(44)-S(10)#1	1.5022(12)	C(1)-S(1)	1.735(3)
C(1)-C(2)	1.376(4)	C(2)-C(3)	1.430(4)

C(2)-S(2)	1.745(3)
C(3)-C(4)	1.374(4)
C(3)-S(3)	1.743(3)
C(4)-C(25)	1.447(4)
C(4)-S(1)	1.736(3)
C(5)-C(5)#2	1.339(6)
C(5)-S(3)	1.765(3)
C(5)-S(2)	1.767(3)
C(6)-C(7)	1.367(4)
C(6)-S(4)	1.731(3)
C(7)-C(8)	1.412(4)
C(8)-C(9)	1.371(4)
C(9)-C(10)	1.449(4)
C(9)-S(4)	1.729(3)
C(10)-C(11)	1.366(4)
C(10)-S(5)	1.728(3)
C(11)-C(12)	1.404(4)
C(12)-C(13)	1.370(4)
C(13)-C(14)	1.453(4)
C(13)-S(5)	1.733(3)
C(14)-C(15)	1.373(4)
C(14)-S(6)	1.737(3)
C(15)-C(16)	1.433(4)
C(15)-C(19)	1.505(4)
C(16)-C(17)	1.357(5)
C(17)-C(18)	1.495(4)
C(17)-S(6)	1.723(3)
C(19)-C(20)	1.520(4)
C(20)-C(21)	1.524(4)
C(21)-C(22)	1.520(4)
C(22)-C(23)	1.517(5)
C(23)-C(24)	1.521(5)
C(25)-C(26)	1.369(4)
C(25)-S(7)	1.728(3)
C(26)-C(27)	1.410(4)
C(27)-C(28)	1.369(4)
C(28)-C(29)	1.447(4)
C(28)-S(7)	1.727(3)
C(29)-C(30)	1.363(4)
C(29)-S(8)	1.732(3)
C(30)-C(31)	1.409(4)
C(31)-C(32)	1.364(4)
C(32)-C(33)	1.460(4)
C(32)-S(8)	1.740(3)
C(33)-C(34)	1.374(4)
C(33)-S(9)	1.731(4)
C(34)-C(35)	1.432(5)
C(34)-C(38)	1.490(5)
C(35)-C(36)	1.344(6)
C(36)-C(37)	1.494(5)
C(36)-S(9)	1.725(3)
C(38)-C(39)	1.535(5)
C(39)-C(40)	1.524(5)
C(40)-C(41)	1.518(6)
C(41)-C(42)	1.519(5)
C(42)-C(43)	1.509(6)

S(10)-C(44)-S(10)#1	180.000(2)
C(2)-C(1)-C(6)	131.0(3)
C(2)-C(1)-S(1)	109.8(2)
C(6)-C(1)-S(1)	119.1(2)
C(1)-C(2)-C(3)	113.5(2)
C(1)-C(2)-S(2)	130.2(2)
C(3)-C(2)-S(2)	116.3(2)
C(4)-C(3)-C(2)	113.4(2)
C(4)-C(3)-S(3)	129.6(2)
C(2)-C(3)-S(3)	117.0(2)
C(3)-C(4)-C(25)	130.3(3)
C(3)-C(4)-S(1)	109.9(2)
C(25)-C(4)-S(1)	119.8(2)
C(5)#2-C(5)-S(3)	121.8(3)
C(5)#2-C(5)-S(2)	122.3(3)
S(3)-C(5)-S(2)	115.91(16)
C(7)-C(6)-C(1)	128.5(3)
C(7)-C(6)-S(4)	110.5(2)
C(1)-C(6)-S(4)	121.0(2)
C(6)-C(7)-C(8)	113.4(3)
C(9)-C(8)-C(7)	113.3(3)
C(8)-C(9)-C(10)	130.8(3)
C(8)-C(9)-S(4)	110.5(2)
C(10)-C(9)-S(4)	118.7(2)
C(11)-C(10)-C(9)	127.9(3)
C(11)-C(10)-S(5)	110.7(2)
C(9)-C(10)-S(5)	121.5(2)
C(10)-C(11)-C(12)	113.5(3)
C(13)-C(12)-C(11)	113.4(3)
C(12)-C(13)-C(14)	126.1(3)
C(12)-C(13)-S(5)	110.4(2)
C(14)-C(13)-S(5)	123.5(2)
C(15)-C(14)-C(13)	131.1(3)
C(15)-C(14)-S(6)	111.1(2)
C(13)-C(14)-S(6)	117.7(2)
C(14)-C(15)-C(16)	111.5(3)
C(14)-C(15)-C(19)	124.2(3)
C(16)-C(15)-C(19)	124.3(3)
C(17)-C(16)-C(15)	114.5(3)
C(16)-C(17)-C(18)	129.2(3)
C(16)-C(17)-S(6)	110.5(2)
C(18)-C(17)-S(6)	120.3(2)
C(15)-C(19)-C(20)	114.9(3)
C(19)-C(20)-C(21)	112.1(3)
C(22)-C(21)-C(20)	112.5(3)
C(23)-C(22)-C(21)	114.4(3)
C(22)-C(23)-C(24)	112.1(3)
C(26)-C(25)-C(4)	128.2(3)
C(26)-C(25)-S(7)	110.6(2)
C(4)-C(25)-S(7)	121.2(2)
C(25)-C(26)-C(27)	113.1(3)
C(28)-C(27)-C(26)	113.4(3)
C(27)-C(28)-C(29)	129.9(3)
C(27)-C(28)-S(7)	110.5(2)
C(29)-C(28)-S(7)	119.6(2)
C(30)-C(29)-C(28)	128.5(3)
C(30)-C(29)-S(8)	110.1(2)

C(28)-C(29)-S(8)	121.4(2)	C(37)-C(36)-S(9)	121.4(3)
C(29)-C(30)-C(31)	114.1(3)	C(34)-C(38)-C(39)	112.5(3)
C(32)-C(31)-C(30)	113.3(3)	C(40)-C(39)-C(38)	114.4(3)
C(31)-C(32)-C(33)	129.3(3)	C(41)-C(40)-C(39)	112.7(3)
C(31)-C(32)-S(8)	110.2(2)	C(40)-C(41)-C(42)	114.4(3)
C(33)-C(32)-S(8)	120.3(2)	C(43)-C(42)-C(41)	113.6(3)
C(34)-C(33)-C(32)	130.0(3)	C(1)-S(1)-C(4)	93.32(13)
C(34)-C(33)-S(9)	111.3(2)	C(2)-S(2)-C(5)	95.42(13)
C(32)-C(33)-S(9)	118.4(2)	C(3)-S(3)-C(5)	95.20(13)
C(33)-C(34)-C(35)	110.5(3)	C(9)-S(4)-C(6)	92.36(14)
C(33)-C(34)-C(38)	126.4(3)	C(10)-S(5)-C(13)	92.09(14)
C(35)-C(34)-C(38)	123.0(3)	C(17)-S(6)-C(14)	92.48(15)
C(36)-C(35)-C(34)	115.7(3)	C(28)-S(7)-C(25)	92.31(14)
C(35)-C(36)-C(37)	128.8(3)	C(29)-S(8)-C(32)	92.32(14)
C(35)-C(36)-S(9)	109.8(3)	C(36)-S(9)-C(33)	92.59(17)

Table 4. Anisotropic displacement parameters ($Å^2 \times 10^3$) for 2010src0100. The anisotropic displacement factor exponent takes the form: $-2\pi^2[h^2 a^{*2} U^{11} + ... + 2 h k a^* b^* U^{12}]$

	U^{11}	U^{22}	U^{33}	U^{23}	U^{13}	U^{12}
C(1)	26(2)	22(1)	21(1)	-3(1)	1(1)	-8(1)
C(2)	22(1)	22(1)	19(1)	-2(1)	0(1)	-8(1)
C(3)	25(2)	17(1)	19(1)	-2(1)	-3(1)	-8(1)
C(4)	23(2)	18(1)	19(1)	-4(1)	0(1)	-7(1)
C(5)	23(1)	19(1)	18(1)	-5(1)	1(1)	-7(1)
C(6)	28(2)	20(1)	22(1)	-5(1)	2(1)	-6(1)

C(7)	40(2)	23(2)	24(2)	-2(1)	7(1)	-11(1)
C(8)	40(2)	21(2)	29(2)	-2(1)	2(1)	-10(1)
C(9)	28(2)	20(1)	26(2)	-4(1)	-2(1)	-5(1)
C(10)	27(2)	17(1)	26(2)	-4(1)	-3(1)	-6(1)
C(11)	37(2)	18(1)	28(2)	-2(1)	-3(1)	-8(1)
C(12)	34(2)	25(2)	22(2)	-2(1)	-1(1)	-9(1)
C(13)	28(2)	22(1)	20(1)	-3(1)	-5(1)	-8(1)
C(14)	24(2)	21(1)	24(1)	-4(1)	-6(1)	-7(1)
C(15)	30(2)	20(1)	25(2)	-1(1)	-11(1)	-7(1)
C(16)	37(2)	19(1)	32(2)	-2(1)	-14(1)	-9(1)
C(17)	32(2)	23(2)	30(2)	-8(1)	-8(1)	-7(1)
C(18)	41(2)	25(2)	39(2)	-11(1)	-6(2)	-8(1)
C(19)	35(2)	23(2)	26(2)	-2(1)	-9(1)	-10(1)
C(20)	43(2)	27(2)	28(2)	1(1)	-11(1)	-14(1)
C(21)	41(2)	25(2)	29(2)	1(1)	-10(1)	-15(1)
C(22)	50(2)	28(2)	35(2)	5(1)	-15(2)	-18(2)
C(23)	51(2)	40(2)	37(2)	9(2)	-14(2)	-23(2)
C(24)	67(3)	51(2)	57(3)	27(2)	-29(2)	-36(2)
C(25)	24(2)	19(1)	22(1)	-4(1)	-1(1)	-7(1)
C(26)	40(2)	21(2)	22(2)	-1(1)	1(1)	-7(1)
C(27)	40(2)	26(2)	19(1)	-4(1)	1(1)	-8(1)
C(28)	26(2)	23(1)	18(1)	-7(1)	-1(1)	-9(1)
C(29)	25(2)	25(2)	19(1)	-8(1)	1(1)	-11(1)
C(30)	32(2)	25(2)	24(2)	-6(1)	-2(1)	-11(1)
C(31)	30(2)	21(1)	29(2)	-3(1)	-3(1)	-9(1)
C(32)	26(2)	20(1)	28(2)	-8(1)	4(1)	-9(1)
C(33)	33(2)	24(2)	30(2)	-11(1)	9(1)	-16(1)
C(34)	28(2)	27(2)	43(2)	-13(1)	7(1)	-14(1)
C(35)	37(2)	32(2)	42(2)	-22(2)	18(2)	-19(2)

C(36)	47(2)	30(2)	28(2)	-12(1)	13(2)	-20(2)
C(37)	66(3)	38(2)	31(2)	-18(2)	10(2)	-24(2)
C(38)	26(2)	31(2)	60(2)	-18(2)	1(2)	-11(1)
C(39)	32(2)	34(2)	59(2)	-16(2)	-6(2)	-11(2)
C(40)	31(2)	39(2)	55(2)	-16(2)	-8(2)	-11(2)
C(41)	37(2)	36(2)	66(3)	-15(2)	-19(2)	-9(2)
C(42)	42(2)	40(2)	73(3)	-16(2)	-23(2)	-8(2)
C(43)	52(3)	40(2)	81(3)	-4(2)	-36(2)	-9(2)
S(1)	34(1)	19(1)	20(1)	-2(1)	4(1)	-9(1)
S(2)	30(1)	18(1)	18(1)	-4(1)	3(1)	-7(1)
S(3)	30(1)	18(1)	19(1)	-4(1)	3(1)	-8(1)
S(4)	32(1)	17(1)	21(1)	-3(1)	3(1)	-8(1)
S(5)	31(1)	17(1)	22(1)	-2(1)	-2(1)	-7(1)
S(6)	32(1)	21(1)	25(1)	-6(1)	-1(1)	-9(1)
S(7)	31(1)	21(1)	18(1)	-5(1)	1(1)	-7(1)
S(8)	34(1)	22(1)	21(1)	-7(1)	4(1)	-10(1)
S(9)	51(1)	24(1)	22(1)	-8(1)	5(1)	-16(1)

References

1. P. Atkins and J. de Paula, *Physical Chemistry*, Oxford University Press, Oxford, 2006.
2. C. H. Hamann, A. Hamnett and W. Vielstich, *Electrochemistry*, Wiley-VCH, Weinheim, 2007.
3. M. R. Bryce, *Chem. Soc. Rev.*, 1991, **20**, 355-390.
4. V. V. Walatka, M. M. Labes and J. H. Perlstein, *Phys. Rev. Lett.*, 1973, **31**, 1139-1142.
5. R. L. Greene, G. B. Street and L. J. Suter, *Phys. Rev. Lett.*, 1975, **34**, 577-579.
6. W. D. Gill, W. Bludau, R. H. Geiss, P. M. Grant, R. L. Greene, J. J. Mayerle and G. B. Street, *Phys. Rev. Lett.*, 1977, **38**, 1305-1308.
7. C. K. Chiang, C. R. Fincher, Y. W. Park, A. J. Heeger, H. Shirakawa, E. J. Louis, S. C. Gau and A. G. MacDiarmid, *Phys. Rev. Lett.*, 1977, **39**, 1098-1101.
8. G. Sonmez, *Chem. Commun.*, 2005, 5251-5259.
9. P. M. Beaujuge, C. M. Amb and J. R. Reynolds, *Acc. Chem. Res.*, 2010, **43**, 1396-1407.
10. P. M. Beaujuge and J. R. Reynolds, *Chem. Rev.*, 2010, **110**, 268-320.
11. H. Dong, C. Wang and W. Hu, *Chem. Commun.*, 2010, **46**, 5211-5222.
12. S. Allard, M. Forster, B. Souharce, H. Thiem and U. Scherf, *Angew. Chem., Int. Ed.*, 2008, **47**, 4070-4098.
13. H. Klauk, *Chem. Soc. Rev.*, 2010, **39**, 2643-2666.
14. J. L. Delgado, P.-A. Bouit, S. Filippone, M. A. Herranz and N. Martin, *Chem. Commun.*, 2010, **46**, 4853-4865.
15. B. C. Thompson and J. M. J. Frechet, *Angew. Chem., Int. Ed.*, 2008, **47**, 58-77.
16. C. Li, M. Liu, N. G. Pschirer, M. Baumgarten and K. Müllen, *Chem. Rev.*, 2010, **110**, 6817-6855.
17. E. Bundgaard and F. C. Krebs, *Sol. Energy Mater.*, 2007, **91**, 954-985.
18. Y.-J. Cheng, S.-H. Yang and C.-S. Hsu, *Chem. Rev.*, 2009, **109**, 5868-5923.
19. A. C. Grimsdale, K. Leok Chan, R. E. Martin, P. G. Jokisz and A. B. Holmes, *Chem. Rev.*, 2009, **109**, 897-1091.

20. U. Lange, N. V. Roznyatouskaya and V. M. Mirsky, *Anal. Chim. Acta*, 2008, **614**, 1-26.
21. J. Roncali, *Chem. Rev.*, 1997, **97**, 173-205.
22. D. F. Perepichka and M. R. Bryce, *Angew. Chem., Int. Ed.*, 2005, **44**, 5370-5373.
23. D. Lehnherr and R. R. Tykwinski, *Materials*, 2010, **3**, 2772-2800.
24. J. E. Anthony, *Angew. Chem., Int. Ed.*, 2008, **47**, 452-483.
25. A. R. Murphy and J. M. J. Fréchet, *Chem. Rev.*, 2007, **107**, 1066-1096.
26. M. Bendikov, F. Wudl and D. F. Perepichka, *Chem. Rev.*, 2004, **104**, 4891-4945.
27. A. Mishra, C. Q. Ma and P. Bauerle, *Chem. Rev.*, 2009, **109**, 1141-1276.
28. T. Mori, *J. Phys.: Condens. Matter*, 2008, **20**, 184010.
29. R. E. Martin and F. Diederich, *Angew. Chem., Int. Ed.*, 1999, **38**, 1350-1377.
30. A. Tsumura, H. Koezuka and T. Ando, *Appl. Phys. Lett.*, 1986, **49**, 1210-1212.
31. G. Horowitz, D. Fichou, X. Peng, Z. Xu and F. Garnier, *Solid State Commun.*, 1989, **72**, 381-384.
32. F. Geiger, M. Stoldt, H. Schweizer, P. Bauerle and E. Umbach, *Adv. Mater.*, 1993, **5**, 922-925.
33. N. Noma, T. Tsuzuki and Y. Shirota, *Adv. Mater.*, 1995, **7**, 647-648.
34. J. Hassan, M. Sevignon, C. Gozzi, E. Schulz and M. Lemaire, *Chem. Rev.*, 2002, **102**, 1359-1469.
35. Y. Guo, G. Yu and Y. Liu, *Adv. Mater.*, 2010, **22**, 4427-4447.
36. F. Mariano, M. Mazzeo, Y. Duan, G. Barbarella, L. Favaretto, S. Carallo, R. Cingolani and G. Gigli, *Appl. Phys. Lett.*, 2009, **94**, 063510.
37. I. F. Perepichka, D. F. Perepichka, H. Meng and F. Wudl, *Adv. Mater.*, 2005, **17**, 2281-2305.
38. M. Mazzeo, V. Vitale, F. Della Sala, M. Anni, G. Barbarella, L. Favaretto, G. Sotgiu, R. Cingolani and G. Gigli, *Adv. Mater.*, 2005, **17**, 34-39.
39. G. Gigli, O. Inganas, M. Anni, M. De Vittorio, R. Cingolani, G. Barbarella and L. Favaretto, *Appl. Phys. Lett.*, 2001, **78**, 1493-1495.
40. J. Roncali, *Acc. Chem. Res.*, 2009, **42**, 1719-1730.
41. A. B. Tamayo, B. Walker and T. Q. Nguyen, *J. Phys. Chem. C*, 2008, **112**, 11545-11551.

42. K. Schulze, C. Uhrich, R. Schuppel, K. Leo, M. Pfeiffer, E. Brier, E. Reinold and P. Bauerle, *Adv. Mater.*, 2006, **18**, 2872-2875.
43. J. Roncali, *Chem. Soc. Rev.*, 2005, **34**, 483-495.
44. C. R. Newman, C. D. Frisbie, D. A. da Silva, J. L. Bredas, P. C. Ewbank and K. R. Mann, *Chem. Mater.*, 2004, **16**, 4436-4451.
45. J. Zaumseil and H. Sirringhaus, *Chem. Rev.*, 2007, **107**, 1296-1323.
46. P. Sonar, S. P. Singh, P. Leclere, M. Surin, R. Lazzaroni, T. T. Lin, A. Dodabalapur and A. Sellinger, *J. Mater. Chem.*, 2009, **19**, 3228-3237.
47. A. B. Tamayo, M. Tantiwiwat, B. Walker and T. Q. Nguyen, *J. Phys. Chem. C*, 2008, **112**, 15543-15552.
48. G. Ulrich, R. Ziessel and A. Harriman, *Angew. Chem., Int. Ed.*, 2008, **47**, 1184-1201.
49. A. Ajayaghosh, *Chem. Soc. Rev.*, 2003, **32**, 181-191.
50. A. Kreyes, S. Ellinger, K. Landfester, M. Defaux, D. A. Ivanov, A. Elschner, T. Meyer-Friedrichsen and U. Ziener, *Chem. Mater.*, 2010, **22**, 2079-2092.
51. H. Akamatu, H. Inokuchi and Y. Matsunaga, *Nature*, 1954, **173**, 168-169.
52. D. S. Acker and W. R. Hertler, *J. Am. Chem. Soc.*, 1962, **84**, 3370-3374.
53. L. R. Melby, R. J. Harder, W. R. Hertler, W. Mahler, R. E. Benson and W. E. Mochel, *J. Am. Chem. Soc.*, 1962, **84**, 3374-3387.
54. F. Wudl, G. M. Smith and E. J. Hufnagel, *Chem. Commun.*, 1970, 1453-1454.
55. J. Ferraris, V. Walatka, J. H. Perlstein and D. O. Cowan, *J. Am. Chem. Soc.*, 1973, **95**, 948-949.
56. J. Singleton, *J. Solid State Chem.*, 2002, **168**, 675-689.
57. P. Cassoux, L. Valade, H. Kobayashi, A. Kobayashi, R. A. Clark and A. E. Underhill, *Coord. Chem. Rev.*, 1991, **110**, 115-160.
58. K. Bechgaard, C. S. Jacobsen, K. Mortensen, H. J. Pedersen and N. Thorup, *Solid State Commun.*, 1980, **33**, 1119-1125.
59. K. Bechgaard, K. Carneiro, F. B. Rasmussen, M. Olsen, G. Rindorf, C. S. Jacobsen, H. J. Pedersen and J. C. Scott, *J. Am. Chem. Soc.*, 1981, **103**, 2440-2442.
60. G. Saito, T. Enoki, K. Toriumi and H. Inokuchi, *Solid State Commun.*, 1982, **42**, 557-560.
61. H. Mori, *J. Phys. Soc. Jpn.*, 2006, **75**, 51003.

62. A. M. Kini, U. Geiser, H. H. Wang, K. D. Carlson, J. M. Williams, W. K. Kwok, K. G. Vandervoort, J. E. Thompson, D. L. Stupka, D. Jung and M. H. Whangbo, *Inorg. Chem.*, 1990, **29**, 2555-2557.
63. J. M. Williams, A. M. Kini, H. H. Wang, K. D. Carlson, U. Geiser, L. K. Montgomery, G. J. Pyrka, D. M. Watkins, J. M. Kommers, S. J. Boryschuk, A. V. S. Crouch, W. K. Kwok, J. E. Schirber, D. L. Overmyer, D. Jung and M. H. Whangbo, *Inorg. Chem.*, 1990, **29**, 3272-3274.
64. H. Taniguchi, M. Miyashita, K. Uchiyama, K. Satoh, N. Mori, H. Okamoto, K. Miyagawa, K. Kanoda, M. Hedo and Y. Uwatoko, *J. Phys. Soc. Jpn.*, 2003, **72**, 468-471.
65. J. S. Brooks, *Chem. Soc. Rev.*, 2010, **39**, 2667-2694.
66. G. N. Schrauzer, *Acc. Chem. Res.*, 1969, **2**, 72-80.
67. S. Dalgleish and N. Robertson, *Coord. Chem. Rev.*, 2010, **254**, 1549-1558.
68. B. S. Lim, D. V. Fomitchev and R. H. Holm, *Inorg. Chem.*, 2001, **40**, 4257-4262.
69. K. Ray, T. Petrenko, K. Wieghardt and F. Neese, *Dalton Trans.*, 2007, 1552-1566.
70. N. Robertson and L. Cronin, *Coord. Chem. Rev.*, 2002, **227**, 93-127.
71. M. L. Kirk, R. L. McNaughton and M. E. Helton, in *Prog. Inorg. Chem.*, John Wiley & Sons Inc, New York, 2004, vol. 52, pp. 111-212.
72. G. Steimecke, R. Kirmse and E. Hoyer, *Zeit. Chem.*, 1975, **15**, 28-29.
73. R. Kato, *Chem. Rev.*, 2004, **104**, 5319-5346.
74. P. Cassoux, *Coord. Chem. Rev.*, 1999, **185-6**, 213-232.
75. L. Valade, M. Bousseau, A. Gleizes and P. Cassoux, *Chem. Commun.*, 1983, 110.
76. L. Brossard, M. Ribault, L. Valade and P. Cassoux, *Physica B+C*, 1986, **143**, 378-380.
77. M. Mas-Torrent and C. Rovira, *J. Mater. Chem.*, 2006, **16**, 433-436.
78. M. Mas-Torrent and C. Rovira, *Chem. Soc. Rev.*, 2008, **37**, 827-838.
79. X. K. Gao, W. F. Qiu, Y. Q. Liu, G. Yu and D. B. Zhu, *Pure Appl. Chem.*, 2008, **80**, 2405-2423.
80. T. Hasegawa and J. Takeya, *Sci. Technol. Adv. Mater.*, 2009, **10**, 024314.
81. Y. Yamashita, *Sci. Technol. Adv. Mater.*, 2009, **10**, 24313.

82. V. C. Sundar, J. Zaumseil, V. Podzorov, E. Menard, R. L. Willett, T. Someya, M. E. Gershenson and J. A. Rogers, *Science*, 2004, **303**, 1644-1646.
83. J. Takeya, M. Yamagishi, Y. Tominari, R. Hirahara, Y. Nakazawa, T. Nishikawa, T. Kawase, T. Shimoda and S. Ogawa, *Appl. Phys. Lett.*, 2007, **90**, 102120.
84. M. Mas-Torrent, M. Durkut, P. Hadley, X. Ribas and C. Rovira, *J. Am. Chem. Soc.*, 2004, **126**, 984-985.
85. M. Leufgen, O. Rost, C. Gould, G. Schmidt, J. Geurts, L. W. Molenkamp, N. S. Oxtoby, M. Mas-Torrent, N. Crivillers, J. Veciana and C. Rovira, *Org. Electron.*, 2008, **9**, 1101-1106.
86. M. Mas-Torrent, S. Masirek, P. Hadley, N. Crivillers, N. S. Oxtoby, P. Reuter, J. Veciana, C. Rovira and A. Tracz, *Org. Electron.*, 2008, **9**, 143-148.
87. M. Mas-Torrent, P. Hadley, S. T. Bromley, X. Ribas, J. Tarres, M. Mas, E. Molins, J. Veciana and C. Rovira, *J. Am. Chem. Soc.*, 2004, **126**, 8546-8553.
88. M. Mas-Torrent, P. Hadley, S. T. Bromley, N. Crivillers, J. Veciana and C. Rovira, *Appl. Phys. Lett.*, 2005, **86**, 012110.
89. X. Chen and R. L. Elsenbaumer, *Tetrahedron Lett.*, 2009, **50**, 3750-3752.
90. X. Chen, N. R. de Tacconi and R. L. Elsenbaumer, *J. Org. Chem.*, 2009, **74**, 9188-9190.
91. P. J. Skabara, D. M. Roberts, I. M. Serebryakov and C. Pozo-Gonzalo, *Chem. Commun.*, 2000, 1005-1006.
92. P. J. Skabara, R. Berridge, E. J. L. McInnes, D. P. West, S. J. Coles, M. B. Hursthouse and K. Mullen, *J. Mater. Chem.*, 2004, **14**, 1964-1969.
93. R. Berridge, P. J. Skabara, C. Pozo-Gonzalo, A. Kanibolotsky, J. Lohr, J. J. W. McDouall, E. J. L. McInnes, J. Wolowska, C. Winder, N. S. Sariciftci, R. W. Harrington and W. Clegg, *J. Phys. Chem. B*, 2006, **110**, 3140-3152.
94. A. L. Kanibolotsky, L. Kanibolotskaya, S. Gordeyev, P. J. Skabara, I. McCulloch, R. Berridge, J. E. Lohr, F. Marchioni and F. Wudl, *Org. Lett.*, 2007, **9**, 1601-1604.
95. P. Basu, A. Nigam, B. Mogesa, S. Denti and V. N. Nemykin, *Inorg. Chim. Acta*, 2010, **363**, 2857-2864.

96. T. T. Bui, B. Garreau-de Bonneval and K. Ching, *New J. Chem.*, 2010, **34**, 337-347.
97. C. Pozo-Gonzalo, R. Berridge, P. J. Skabara, E. Cerrada, M. Laguna, S. J. Coles and M. B. Hursthouse, *Chem. Commun.*, 2002, 2408-2409.
98. P. J. Skabara, C. Pozo-Gonzalo, N. L. Miazza, M. Laguna, E. Cerrada, A. Luquin, B. Gonzalez, S. J. Coles, M. B. Hursthouse, R. W. Harrington and W. Clegg, *Dalton Trans.*, 2008, 3070-3079.
99. K. L. Marshall, G. Painter, K. Lotito, A. G. Noto and P. Chang, *Mol. Cryst. Liq. Cryst.*, 2006, **454**, 47-79.
100. W. F. Guo, X. B. Sun, J. Sun, X. Q. Wang, G. H. Zhang, Q. Ren and D. Xu, *Chem. Phys. Lett.*, 2007, **435**, 65-68.
101. P. Deplano, L. Pilia, D. Espa, M. L. Mercuri and A. Serpe, *Coord. Chem. Rev.*, 2010, **254**, 1434-1447.
102. T. D. Anthopoulos, S. Setayesh, E. Smits, M. Colle, E. Cantatore, B. de Boer, P. W. M. Blom and D. M. de Leeuw, *Adv. Mater.*, 2006, **18**, 1900-1904.
103. G. C. Anyfantis, G. C. Papavassiliou, N. Assimomytis, A. Terzis, V. Psycharis, C. P. Raptopoulou, P. Kyritsis, V. Thoma and I. B. Koutselas, *Solid State Sci.*, 2008, **10**, 1729-1733.
104. J. Y. Cho, B. Domercq, S. C. Jones, J. Yu, X. Zhang, Z. An, M. Bishop, S. Barlow, S. R. Marder and B. Kippelen, *J. Mater. Chem.*, 2007, **17**, 2642-2647.
105. S. P. Tiwari, W. J. Potscavage, T. Sajoto, S. Barlow, S. R. Marder and B. Kippelen, *Org. Electron.*, 2010, **11**, 860-863.
106. M. O. Wolf, *J. Inorg. Organomet. Polym. Mater.*, 2006, **16**, 189-199.
107. C. Moorlag, B. C. Sih, T. L. Stott and M. O. Wolf, *J. Mater. Chem.*, 2005, **15**, 2433-2436.
108. C. L. Kean and P. G. Pickup, *Chem. Commun.*, 2001, 815-816.
109. C. L. Kean, D. O. Miller and P. G. Pickup, *J. Mater. Chem.*, 2002, **12**, 2949-2956.
110. T. Anjos, S. J. Roberts-Bleming, A. Charlton, N. Robertson, A. R. Mount, S. J. Coles, M. B. Hursthouse, M. Kalaji and P. J. Murphy, *J. Mater. Chem.*, 2008, **18**, 475-483.
111. S. Dalgleish, C. A. Morrison, D. S. Middlemiss, A. R. Mount, A. Collins, L. Pilia, A. Serpe, M. L. Mercuri, S. J. Roberts-Bleming, A. Charlton, P. Deplano, P. J. Murphy and N. Robertson, *J. Mater. Chem.*, 2009, **19**, 6194-6200.

112. S. Dalgleish and N. Robertson, *Chem. Commun.*, 2009, 5826-5828.
113. D. Belo, H. Alves, E. B. Lopes, M. T. Duarte, V. Gama, R. T. Henriques, M. Almeida, A. Perez-Benitez, C. Rovira and J. Veciana, *Chem.-Eur. J.*, 2001, **7**, 511-519.
114. D. Belo, M. J. Figueira, J. Mendonca, I. C. Santos, M. Almeida, R. T. Henriques, M. T. Duarte, C. Rovira and J. Veciana, *Eur. J. Inorg. Chem.*, 2005, 3337-3345.
115. D. Belo and M. Almeida, *Coord. Chem. Rev.*, 2010, **254**, 1479-1492.
116. G. Schukat and E. Fanghänel, *Sulfur Reports*, 2003, **24**, 1-190.
117. K. B. Simonsen and J. Becher, *Synlett*, 1997, 1211-1220.
118. N. Svenstrup, K. M. Rasmussen, T. K. Hansen and J. Becher, *Synthesis*, 1994, 809-812.
119. D. C. Green, *J. Org. Chem.*, 1979, **44**, 1476-1479.
120. C. S. Wang, A. Ellern, V. Khodorkovsky, J. Bernstein and J. Y. Becker, *Chem. Commun.*, 1994, 983-984.
121. A. I. F. Vogel, B.S. Hannaford, A.J. Smith, P.W.G. Tatchell, A.R., *Vogel's Textbook of Practical Organic Chemistry 5th Edition*, Longman Scientific & Technical, Essex, 1989.
122. D. H. Williams and I. Fleming, *Spectroscopic Methods in Organic Chemistry*, McGraw-Hill, Maidenhead, 1995.
123. A. J. Bard and L. R. Faulkner, *Electrochemical Methods Fundamentals and Applications*, John Wiley & Sons Inc., New York, 2001.
124. F. Settle, *Handbook of Instrumental Techniques for Analytical Chemistry*, Prentice Hall, New Jersey, 1997.
125. C. G. Zoski, *Handbook of Electrochemistry*, Elsevier, Amsterdam, 2007.
126. J. F. Rusling and S. L. Suib, *Adv. Mater.*, 1994, **6**, 922-930.
127. G. Gritzner and J. Kuta, *Pure Appl. Chem.*, 1984, **56**, 461-466.
128. J. C. Lindon, G. E. Tranter and J. L. Holmes, *Encyclopedia of Spectroscopy and Spectrometry*, Academic Press, London, 2000.
129. C. J. Brabec, S. Gowrisanker, J. J. M. Halls, D. Laird, S. J. Jia and S. P. Williams, *Adv. Mater.*, 2010, **22**, 3839-3856.
130. G. Dennler, M. C. Scharber and C. J. Brabec, *Adv. Mater.*, 2009, **21**, 1323-1338.
131. G. Yu, J. Gao, J. C. Hummelen, F. Wudl and A. J. Heeger, *Science*, 1995, **270**, 1789-1791.

132. Y. Cao, G. Yu, C. Zhang, R. Menon and A. J. Heeger, *Synth. Met.*, 1997, **87**, 171-174.
133. F. Padinger, R. S. Rittberger and N. S. Sariciftci, *Adv. Funct. Mater.*, 2003, **13**, 85-88.
134. http://www.solarmer.com/news.php.
135. A. W. Hains, Z. Q. Liang, M. A. Woodhouse and B. A. Gregg, *Chem. Rev.*, 2010, **110**, 6689-6735.
136. B. Oregan and M. Gratzel, *Nature*, 1991, **353**, 737-740.
137. M. Gratzel, *Acc. Chem. Res.*, 2009, **42**, 1788-1798.
138. M. K. Nazeeruddin, F. De Angelis, S. Fantacci, A. Selloni, G. Viscardi, P. Liska, S. Ito, T. Bessho and M. Gratzel, *J. Am. Chem. Soc.*, 2005, **127**, 16835-16847.
139. Y. Chiba, A. Islam, Y. Watanabe, R. Komiya, N. Koide and L. Y. Han, *Jpn. J. Appl. Phys. Part 2 - Lett. Express Lett.*, 2006, **45**, L638-L640.
140. U. Mitschke and P. Bauerle, *J. Mater. Chem.*, 2000, **10**, 1471-1507.
141. F. Carpi and D. De Rossi, *Optics And Laser Tech.*, 2006, **38**, 292-305.
142. M. A. Baldo, D. F. O'Brien, M. E. Thompson and S. R. Forrest, *Phys. Rev. B*, 1999, **60**, 14422-14428.
143. M. R. Andersson, O. Thomas, W. Mammo, M. Svensson, M. Theander and O. Inganas, *J. Mater. Chem.*, 1999, **9**, 1933-1940.
144. B. W. D'Andrade and S. R. Forrest, *Adv. Mater.*, 2004, **16**, 1585-1595.
145. K. T. Kamtekar, A. P. Monkman and M. R. Bryce, *Adv. Mater.*, 2010, **22**, 572-582.
146. R. J. Mortimer, A. L. Dyer and J. R. Reynolds, *Displays*, 2006, **27**, 2-18.
147. G. Sonmez, C. K. F. Shen, Y. Rubin and F. Wudl, *Angew. Chem.-Int. Edit.*, 2004, **43**, 1498-1502.
148. G. Sonmez, H. B. Sonmez, C. K. E. Shen and F. Wudl, *Adv. Mater.*, 2004, **16**, 1905-1908.
149. B. C. Thompson, P. Schottland, K. W. Zong and J. R. Reynolds, *Chem. Mater.*, 2000, **12**, 1563-1571.
150. M. Mazzeo, D. Pisignano, L. Favaretto, G. Barbarella, R. Cingolani and G. Gigli, *Synth. Met.*, 2003, **139**, 671-673.
151. C. R. Mason, P. J. Skabara, D. Cupertino, J. Schofield, F. Meghdadi, B. Ebner and N. S. Sariciftci, *J. Mater. Chem.*, 2005, **15**, 1446-1453.
152. R. Berridge, P. J. Skabara, R. Andreu, J. Garin, J. Orduna and M. Torra, *Tetrahedron Lett.*, 2005, **46**, 7871-7875.

153. A. L. Kanibolotsky, J. C. Forgie, S. Gordeyev, F. Vilela, P. J. Skabara, J. E. Lohr, B. M. Petersen and J. O. Jeppesen, *Macromol. Rapid Commun.*, 2008, **29**, 1226-1230.
154. J. C. Forgie, P. J. Skabara, I. Stibor, F. Vilela and Z. Vobecka, *Chem. Mater.*, 2009, **21**, 1784.
155. P. J. Skabara, R. Berridge, I. M. Serebryakov, A. L. Kanibolotsky, L. Kanibolotskaya, S. Gordeyev, I. F. Perepichka, N. S. Sariciftci and C. Winder, *J. Mater. Chem.*, 2007, **17**, 1055-1062.
156. P. J. Skabara, I. M. Serebryakov, I. F. Perepichka, N. S. Sariciftci, H. Neugebauer and A. Cravino, *Macromolecules*, 2001, **34**, 2232-2241.
157. A. J. Moore and M. R. Bryce, *Synthesis*, 1997, 407-409.
158. J. Frohlich, C. Hametner and W. Kalt, *Monatsh. Chem.*, 1996, **127**, 325-330.
159. P. A. Chaloner, S. R. Gunatunga and P. B. Hitchcock, *J. Chem. Soc.-Perkin Trans. 2*, 1997, 1597-1604.
160. J. P. Lere-Porte, J. J. E. Moreau and C. Torreilles, *Eur. J. Org. Chem.*, 2001, 1249-1258.
161. M. Sato and H. Kamine, *Chem. Lett.*, 2009, **38**, 924-925.
162. A. Bilge, A. Zen, M. Forster, H. B. Li, F. Galbrecht, B. S. Nehls, T. Farrell, D. Neher and U. Scherf, *J. Mater. Chem.*, 2006, **16**, 3177-3182.
163. F. Gerson and W. Huber, *Electron Spin Resonance Spectroscopy of Organic Radicals*, Wiley-VCH, Weinheim, 2003.
164. C. W. Chu, J. Ouyang, H. H. Tseng and Y. Yang, *Adv. Mater.*, 2005, **17**, 1440-1443.
165. H. Sirringhaus, P. J. Brown, R. H. Friend, M. M. Nielsen, K. Bechgaard, B. M. W. Langeveld-Voss, A. J. H. Spiering, R. A. J. Janssen, E. W. Meijer, P. Herwig and D. M. de Leeuw, *Nature*, 1999, **401**, 685-688.
166. A. J. Mozer, G. Dennler, N. S. Sariciftci, M. Westerling, A. Pivrikas, R. Osterbacka and G. Juska, *Phys. Rev. B*, 2005, **72**, 035217.
167. K. Kaneto, K. Hatae, S. Nagamatsu, W. Takashima, S. S. Pandey, K. Endo and M. Rikukawa, *Jpn. J. Appl. Phys. Part 2 - Lett.*, 1999, **38**, L1188-L1190.
168. G. J. McEntee, P. J. Skabara, F. Vilela, S. Tierney, I. D. W. Samuel, S. Gambino, S. J. Coles, M. B. Hursthouse, R. W. Harrington and W. Clegg, *Chem. Mater.*, 2010, **22**, 3000-3008.

169. A. J. Mozer, C. Q. Ma, W. W. H. Wong, D. J. Jones, P. Bauerle and G. G. Wallace, *Org. Electron.*, 2010, **11**, 573-582.
170. T. C. Chao, K. T. Wong, W. Y. Hung, T. H. Hou and W. J. Chen, *Tetrahedron Lett.*, 2009, **50**, 3422-3424.
171. A. L. Kanibolotsky, R. Berridge, P. J. Skabara, I. F. Perepichka, D. D. C. Bradley and M. Koeberg, *J. Am. Chem. Soc.*, 2004, **126**, 13695-13702.
172. K. M. Omer, A. L. Kanibolotsky, P. J. Skabara, I. F. Perepichka and A. J. Bard, *Journal Of Physical Chemistry B*, 2007, **111**, 6612-6619.
173. G. Tsiminis, Y. Wang, P. E. Shaw, A. L. Kanibolotsky, I. F. Perepichka, M. D. Dawson, P. J. Skabara, G. A. Turnbull and I. D. W. Samuel, *Appl. Phys. Lett.*, 2009, **94**.
174. Y. Wang, G. Tsiminis, Y. Yang, A. Ruseckas, A. L. Kanibolotsky, I. F. Perepichka, P. J. Skabara, G. A. Turnbull and I. D. W. Samuel, *Synth. Met.*, 2010, **160**, 1397-1400.
175. U. T. Mueller-Westerhoff, B. Vance and D. I. Yoon, *Tetrahedron*, 1991, **47**, 909-932.
176. Q. Dai, X. F. Chen, H. Chen, X. Gao, X. P. Zhang and Z. S. Cheng, *Supramol. Sci.*, 1998, **5**, 531-536.
177. Y. Kobayashi, B. Jacobs, M. D. Allendorf and J. R. Long, *Chem. Mater.*, 2010, **22**, 4120-4122.
178. D. Belo, H. Alves, S. Rabaca, L. C. Pereira, M. T. Duarte, V. Gama, R. T. Henriques, M. Almeida, E. Ribera, C. Rovira and J. Veciana, *Eur. J. Inorg. Chem.*, 2001, 3127-3133.
179. C. M. Amb and S. C. Rasmussen, *Synth. Met.*, 2009, **159**, 2390-2393.
180. K. Ray, T. Weyhermuller, F. Neese and K. Wieghardt, *Inorg. Chem.*, 2005, **44**, 5345-5360.
181. N. C. Schiodt, P. Sommerlarsen, T. Bjornholm, M. F. Nielsen, J. Larsen and K. Bechgaard, *Inorg. Chem.*, 1995, **34**, 3688-3694.
182. S. Kokatam, K. Ray, J. Pap, E. Bill, W. E. Geiger, R. J. LeSuer, P. H. Rieger, T. Weyhermuller, F. Neese and K. Wieghardt, *Inorg. Chem.*, 2007, **46**, 1100-1111.
183. T. P. I. Saragi, T. Spehr, A. Siebert, T. Fuhrmann-Lieker and J. Salbeck, *Chem. Rev.*, 2007, **107**, 1011-1065.
184. R. Pudzich, T. Fuhrmann-Lieker and J. Salbeck, *Adv. Polym. Sci.*, 2006, **199**, 83-142.

185. U. Bach, D. Lupo, P. Comte, J. E. Moser, F. Weissortel, J. Salbeck, H. Spreitzer and M. Gratzel, *Nature*, 1998, **395**, 583-585.
186. H. J. Snaith, A. J. Moule, C. Klein, K. Meerholz, R. H. Friend and M. Gratzel, *Nano Lett.*, 2007, **7**, 3372-3376.
187. C. L. Beswick, in *Prog. Inorg. Chem.*, John Wiley & Sons Inc, New York, 2004, vol. 52, pp. 55-110.
188. E. Cadoni, E. Perra, C. Fattuoni, G. Bruno, M. G. Cabiddu, S. De Montis and S. Cabiddu, *Tetrahedron*, 2009, **65**, 2279-2284.
189. K. Ueda, M. Yamanoha, T. Sugimoto, H. Fujita, A. Ugawa, K. Yakushi and K. Kano, *Chem. Lett.*, 1997, 461-462.
190. K. Ueda, M. Iwamatsu, T. Sugimoto, T. Tada and K. Nishimura, *Acta Crystallogr. Sect. C-Cryst. Struct. Commun.*, 2000, **56**, E160-E161.
191. U. Herzog, U. Bohme and G. Rheinwald, *J. Organomet. Chem.*, 2000, **612**, 133-140.
192. J. Pfeiffer, M. Noltemeyer and A. Meller, *Z. Anorg. Allg. Chem.*, 1989, **572**, 145-150.
193. F. H. Fink, J. A. Turner and D. A. Payne, *J. Am. Chem. Soc.*, 1966, **88**, 1571-1572.
194. D. A. Payne and F. H. Fink, *J. Chem. Educ.*, 1966, **43**, 654-656.
195. J. Guay, A. Diaz, R. L. Wu and J. M. Tour, *J. Am. Chem. Soc.*, 1993, **115**, 1869-1874.
196. W. Wu, Y. Liu and D. Zhu, *Chem. Soc. Rev.*, 2010, **39**, 1489.
197. N. Allard, R. B. Aich, D. Gendron, P. L. T. Boudreault, C. Tessier, S. Alem, S. C. Tse, Y. Tao and M. Leclerc, *Macromolecules*, 2010, **43**, 2328-2333.
198. T. Akasaka, M. Nakano, H. Tamura and G. E. Matsubayashi, *Bull. Chem. Soc. Jpn.*, 2002, **75**, 2621-2628.
199. F. de Assis, Z. H. Chohan, R. A. Howie, A. Khan, J. N. Low, G. M. Spencer, J. L. Wardell and S. Wardell, *Polyhedron*, 1999, **18**, 3533-3544.
200. F. S. Guziec, J. M. Russo, F. F. Torres, G. C. Long and M. R. Tellez, *J. Chem. Soc., Perkin Trans. 1*, 1989, 1068-1070.